UNIVERSIDAD DE CONCEPCIÓN
DIRECCIÓN DE POSGRADO
FACULTAD DE CIENCIAS FÍSICAS Y MATEMÁTICAS
PROGRAMA DE DOCTORADO EN CIENCIAS FÍSICAS

Calibration Strategies for Millimeter/Submillimeter Observation Instruments

By: Lilian Basoalto Salazar

Thesis presented to the Facultad de Ciencias Físicas y Matemáticas of Universidad de Concepción to qualify for the academic degree of Doctor in Physical Sciences

Advisor: Ph.D. Rodrigo Reeves Díaz

April 25, 2025
Concepción, Chile

With love to my dear Ayleen, $+ \dot{-}$ o $-$, and the others.

Acknowledgements

To my Mom, Liliana, a fundamental pillar in my life, whose love and strength were the driving force that encouraged me every day to keep moving forward. Without her presence and trust, this journey would not have been possible. To my partner and friend, Mario, for standing by my side through every challenge, supporting me in the most difficult moments. His patience, encouragement, and ability to help me see obstacles with greater clarity were an invaluable source of strength. To my friend, Fernando, with whom I shared a significant part of my university life, both academically and personally. His enthusiasm, companionship, and unwavering support were essential in the early stages of my research projects, always encouraging me to turn ideas into reality. To my thesis advisor, for his guidance, patience, and willingness to answer my questions, often dedicating more time than expected. I am also grateful for the space provided in CePIA and the opportunity to explore astronomy from the field of calibration through my collaboration in the COMAP and LLAMA projects. To my fellow team members who worked with me on calibration loads, those who were involved from the beginning and those who joined along the way. Their dedication, enthusiasm, and commitment were essential in bringing it to completion. To the Universidad de Concepción and the Chilean National Agency for Research and Development (ANID) for making my doctoral studies possible through their scholarship programs. To Tía Marce, for her kindness and for offering me a space within the Department of Astronomy to complete the writing of this thesis. To my companions at CePIA, especially those who founded the group, for making my early years as a doctoral student more enjoyable.

Abstract

Data calibration is a critical process in astronomical observations as it enables the correction of systematic errors and ensures the reliability of measurements. This aspect is particularly crucial in radio-astronomy experiments such as COMAP and LLAMA, which aim to detect faint astronomical signals with high precision. In these projects, both instrumental and observational challenges, including the perturbation of weak signals by the atmosphere and receiving systems, introduce uncertainties that must be understood and mitigated to ensure accurate results. This research focuses on developing calibration strategies for instruments in the millimeter and submillimeter bands, addressing the factors influencing data integrity. The study concentrates on two main components: the COMAP experiment and the LLAMA calibration loads.

Within the framework of the LLAMA Project, a Calibration Loads sub-system for the LLAMA radio-telescope was developed and characterized. This ultra-wideband system allows the various single-pixel receivers planned for LLAMA to calibrate their intensity scales in antenna temperature using the Y-factor technique. We have developed a closed-loop temperature control system based on FPGAs, along with ACS control software, which was integrated into the LLAMA middleware to implement thermal monitoring and control for the Calibration Loads. The characterization of the loads included infrared and radiometric measurements performed on both the prototype and the final loads. Infrared measurements demonstrated thermal stability over time, with standard deviations of less than 1°C for all loads. In radiometric measurements, the calculated brightness temperatures exhibited a linear correlation with the physical temperatures evaluated between 40°C and 70°C. Discrepancies between the physical and the brightness temperatures increased with a rise in T_{ph}. For the prototype, in which power was measured with a 93 GHz heterodyne receiver operated alongside an FPGA-based automated system, the percentage difference reached up to 1% in Kelvin scale at 70°C. In the final loads, power was manually determined using a 93 GHz direct detection receiver, the maximum difference was 5% on the Kelvin scale at 70°C, corresponding to one of the large loads. These variations are attributed to the geometric design and thermal properties of the loads. At 70°C, the stabilization time of the brightness temperature from ambient temperature was 8 minutes for the small load and 17 and 28 minutes for the blue and red large

loads, respectively. The loads remained within the allowed error margin of 1%, validating their stability and accuracy as calibration tools.

In the context of the COMAP Project, a radiometric and atmospheric study for the OVRO site at COMAP frequencies was executed. The performance of the receiver was evaluated using a series of scans taken on different dates and times. The Y-factor technique was applied to determine the receiver temperature, incorporating spillover and atmospheric emission modeled with the AM radiative transfer model and MERRA-2 atmospheric database. The results showed that T_{Rx} remained stable, with 95% of the values falling between 10 and 31 K and a mean of 17.7 K. The system temperature was calculated by adapting the methodology of O'Neil [40], explicitly including the simulated sky temperature from the AM model using the MERRA-2 database. It was observed that T_{sys} ranged between 28 and 56 K for 95% of the data, showing dependence on PWV and the elevation angle. As expected, conditions of reduced PWV resulted in lower values of T_{sys}, highlighting the relevance of these factors in the accuracy of the measurements. COMAP's sensitivity was found to vary between 146 and 260 mK for 95% of the data, with a mean of 203 mK, evaluated at a $\Delta\nu$ of 2 MHz and a data sampling rate of 20 ms. The temporal stability of the data ranges between 5 and 22 seconds with a mean of 14 seconds, as evaluated through Allan variance, confirming the presence of gain fluctuations in all analyzed files. The aperture efficiency results showed a decrease with increasing frequency, ranging from 0.27 to 0.51 with a mean of 0.38, evaluated at the central frequencies of COMAP.
In the observational framework of the COMAP Project, a validation study of the MERRA-2 atmospheric database model was carried out through an atmospheric analysis at the OVRO site on March 25, 2019, at 15:00 GMT. This analysis compared radiometric measurements obtained by the COMAP instrument with atmospheric simulations generated using the AM radiative transfer model based on the MERRA-2 database for the specific date and time. We determined a PWV content of 5.753 mm for that moment, calculated through vertical integration of the layered model provided by the MERRA-2 database. This value was retrieved by executing the AM radiative transfer model using the same dataset with an error of less than 1%. Additionally, we conducted a radiometric study for OVRO on March 25, 2019, between 14:18 and 14:26 UTC. We analyzed the COMAP

Level-1 long skydip power data recorded at elevation angles between 30° and 86.5° during this period and estimated its atmospheric brightness temperature at different elevation angles. We compared the derived radiometric temperature with simulations from the AM radiative transfer software, based on the MERRA-2 atmospheric database model, and found strong consistency. During the data processing, we observed an excess temperature when the elevation angle decreased, which could be attributed to spillover effects. This excess temperature ranged between approximately 6 K and 8 K at an azimuthal angle of -30°. As a key scientific outcome of this atmospheric study at the OVRO site, a zenith opacity spectrum was obtained by fitting brightness temperature data across the entire COMAP frequency range, revealing excellent agreement with simulations, with a percent error of only 4%. The same procedure was applied to a more restricted subset of skydip power data, spanning elevation angles between 40° and 60° within the same evaluated file. The percent error between the calculated and simulated zenith atmospheric opacity is only 4.4%, confirming that short skydips can effectively characterize atmospheric contributions.

Contents

List of Tables

List of Figures

Chapter 1

Introduction

One of the most critical aspects of any astronomical observation is the calibration of the obtained data. This process compensates for systematic errors in the observed flux astronomical sources, ensuring reliable measurements. Ideally, multiple scans of the same source should yield consistent power readings; however, this is difficult to achieve in practice. Power measurements often fluctuate due to unwanted contributions from observational and instrumental factors. These factors cannot be entirely removed as they are intrinsic to the observation process, making it essential to understand and characterize their behavior throughout the observation to attempt a potential correction for their effects.

The Earth's atmosphere plays a significant role in the observational factors affecting signals from space. In the microwave frequency range, between 1 and 300 GHz, atmospheric absorption is primarily dominated by water vapor, oxygen, and ozone [55]. Particularly in the millimeter-wave region, water vapor, a highly variable atmospheric constituent both in time and space, strongly absorbs this radiation, significantly impacting astronomical observations [50]. Water vapor introduces atmospheric opacity, a measure of the atmospheric conditions affecting observations, and directly correlates with meteorological factors such as column density of the atmospheric constituents, precipitation, cloud cover, and humidity. The atmospheric water content is the primary indicator of the effectiveness of millimeter-wave observations, as it is directly associated with lower atmospheric opacity [36]. The concept of precipitable water vapor (PWV) quantifies the atmospheric water content more precisely and comparatively. The PWV is the

amount of integral water vapor within a vertical column of air extending from the Earth's surface to the top of the atmosphere, typically expressed as the equivalent height of liquid water in millimeters [49]. Water vapor density generally decreases almost exponentially with altitude, so the highest PWV concentration is near the sea level. According to Ross and Elliott [48] approximately 90% of PWV resides within the 500 mbar pressure level, underscoring the importance of elevation in astronomical site selection.

The Chajnantor area in Chile, situated over 5000 meters above sea level, in the Chilean Andes, and approximately 50 km east of San Pedro de Atacama, represents one of the most prominent high-altitude sites for millimeter and submillimeter astronomical observations. The amount of PWV at this altitude is much lower than at sea level, so the impact on astronomical signals should be minor. Long-term assessments of the PWV column in this region have consistently demonstrated its extreme aridity, with a year-round median of 1 mm PWV [23]. Extensive atmospheric studies ([18]; [45]; [22]; [23]; [53]; [50]) underscore the site's suitability for cutting-edge astronomical research. It accommodates key facilities such as the Atacama Large Millimeter/submillimeter Array (ALMA) and serves as a candidate location for forthcoming initiatives like the Leighton Chajnantor Telescope (LCT) led by CePIA, Universidad de Concepción.

Atmospheric water vapor is quantified using radiometers, which measure PWV through the rotational spectral emission lines at 22 GHz and 183 GHz. Tipping radiometers determine the sky brightness temperature by calibrating power data obtained during skydip scans across different elevation angles. Subsequently, the "tipping curves" are fitted to these sky temperatures, facilitating the determination of the zenith atmospheric opacity. This parameter directly correlates with PWV, as inferred from ground-based meteorological data, as shown by [45] and [22]. Additionally, atmospheric simulation tools based on radiative transfer models, such as the Atmospheric Model (AM) [42] and the Atmospheric Transmission at Microwaves (ATM) model [43], simulate conditions at specified sites using atmospheric models like MERRA-2 [26]. Validation of these models against observations from diverse instruments enhances their accuracy, contributing to more precise atmospheric characterizations.

The site of primary interest in this study is Owens Valley, California, home to the Owens Valley Radio Observatory (OVRO). Situated at an altitude of 1,222

meters above sea level, this location was selected in 1950 for its flat terrain, low radio frequency interference, and minimal wind conditions, ensuring the mechanical stability of the observatory's structure [20]. At the time, the influence of tropospheric water vapor was not considered, as its impact on observations was not fully understood [31]. Consequently, conducting atmospheric studies at this site would make significant contributions to improving the quality of the data collected by the various projects operating in this location.

The Carbon Monoxide Mapping Array Project (COMAP) operates at the OVRO site and has recently published a series of articles focusing on the validation of its technology and the methodologies implemented to achieve its objectives. Its primary goal is to utilize carbon monoxide (CO) line intensity mapping to trace the distribution and global properties of galaxies throughout cosmic history, extending back to the Epoch of Reionization (EoR) [19]. While these studies introduced the receiver and outlined scientific objectives, atmospheric analysis was less emphasized, though Foss et al. [25] noted that atmospheric contributions to data add 15-25 K. In this context, Chapter 4 provides an in-depth atmospheric study for OVRO. It adopts a methodology similar to that outlined in Cortés et al. [22], which employed brightness temperature measurements from a tipping radiometer at 350 μm to derive zenith atmospheric opacity for the Chajnantor region. Building upon this approach, the study in this thesis calibrates power data from the COMAP receiver, operating between 26–34 GHz, to determine zenith atmospheric opacity specific to OVRO. The results are subsequently compared with AM model simulations based on MERRA-2 atmospheric data, enabling an assessment of the reliability of these models for evaluating potential astronomical observing sites.

Instrumental factors play a critical role in the quality of the signals received by astronomical observatories such as ALMA and OVRO, and will be equally important for upcoming projects like LCT and LLAMA. These systems generally consist of a primary antenna that collects radiation and a receiver that converts this signal into measurable digital counts, enabling analysis. Each receiving system's design is adapted to its scientific objectives, determining elements such as the antenna size and receiver electronics. Before reaching the receiver, signals from space interact with the atmosphere and pass through the receiving system,

with the receiver itself contributing a substantial amount of baseline noise due to its electronic components. This baseline is characterized by a quantity called the receiver temperature, measured in kelvin, which defines the receiver's noise. A lower receiver temperature is preferred, as it enhances the sensitivity required to detect faint signals, such as the CO line at around 1 μK [25] [37] that COMAP aims to observe. Receiver temperature can fluctuate over time, often as a result of changes in the gain of active components, such as low-noise amplifiers (LNAs), whose performance decreases as they heat up. Therefore, maintaining receiver stability requires cryogenic cooling systems, periodic calibration with known physical temperature loads, and constant checks to evaluate receiver performance through figures of merit such as receiver temperature, system temperature, sensitivity, aperture efficiency, and receiver stability by means of Allan variance. In this context, the first research of Chapter 4 examines the COMAP receiver's performance, assessing these metrics.
The mentioned figures of merit are determined using calibration sources with known temperatures, periodically presented to the receiver(s) during observations. This process enables the comparison between sky power readings and the calibrators, forming the basis for data calibration. The power data is subsequently converted into antenna temperature and, consequently, into brightness temperature. This concept, essential in radio astronomy, allows physical interpretation of the power data for the targeted astronomical source. Brightness temperature represents the radiation intensity emitted by an astronomical source, expressed on a temperature scale in Kelvin. Notably, this value does not usually correspond to the physical temperature unless an ideal blackbody is observed, a standard assumption for calibration instruments.

The ALMA observatory, for instance, calibrates its data with two specially designed loads developed by Thomas Keating Ltd., primarily composed of silicone and epoxy resin layers [58] (left panel of Figure 1). One load operates at ambient temperature, while the other is maintained at 70°C. The ALMA team conducted thorough testing with multiple materials and configurations before arriving at this final design ([29];[7];[8];[35]). The COMAP project uses two calibration sources as well. One consists of RAM tiles at ambient temperature (right panel of Figure 1), while the other is the sky itself when looking at the zenith, allowing the receiver to capture the contributions of cosmic microwave background (CMB), the

atmosphere and the spillover. From an industrial perspective, several reputable companies manufacture calibration loads for scientific and military applications. Notable examples include *TK Instruments* in the United Kingdom [6], *Emmerson & Cumming Anechoic Chambers* in Belgium [5], *Rutherford Appleton Laboratory* (RAL Space) in the United Kingdom [3], and *Zax Millimeter Wave Corporation* in the USA [4].

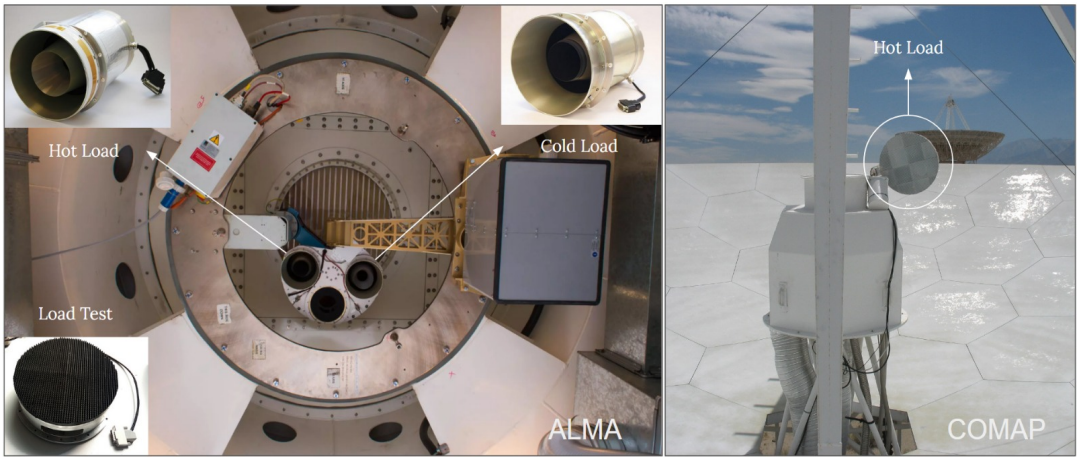

Figure 1: Examples of calibration loads currently used in certain observatories. ALMA's hot and cold calibration loads are shown on the left, implemented atop the receiver cabin [1]. On the right is COMAP's ambient-temperature calibration load positioned over the primary reflector and together to receiver [19].

Notably, each of these devices operates at a fixed temperature, either ambient or elevated. This specificity establishes the foundation for further research detailed in Chapter 5. The initial phase of this research was documented in author's undergraduate thesis [14], which encompassed two key aspects: (1) conceptual design of a calibration load prototype, and (2) preliminary infrared testing performed on this prototype. This doctoral work extends that foundational research, emphasizing the design and fabrication of the calibration loads intended for LLAMA. Furthermore, it provides an in-depth analysis of the radiometric characterization of these blackbody sources, underscoring their critical role within the telescope's calibration system.

1.1 Objectives

The primary objective of this thesis is to investigate calibration strategies for millimeter and submillimeter observational instruments through the implementation of power calibration techniques. This goal is addressed from two perspectives: an instrumental approach focused on the Calibration Load Project to establish precise calibration standards and an observational approach within the framework of the COMAP Project, aiming to enhance both atmospheric and instrumental calibration accuracy.

Calibration Loads Project

1. Develop and characterize three ultra-wideband calibration loads, three of which will be dedicated to calibrating data from the LLAMA radio telescope.
   - 1.1 Outline the requirements of the LLAMA Project.
   - 1.2 Define the objectives of the Calibration Load Project.
   - 1.3 Detail the thermo-mechanical development of the calibration loads.
   - 1.4 Present and analyze infrared measurements of the calibration loads.
   - 1.5 Present and evaluate radiometric measurements of the calibration loads.
   - 1.6 Characterize the calibration loads by establishing the relationship between their brightness temperature and physical temperature.

COMAP Project

1. Evaluate the performance of the COMAP receiver by examining critical operational parameters, including receiver temperature, system temperature, minimum detectable temperature, aperture efficiency, and Allan variance.
2. Validate the MERRA-2 atmospheric model database for radio astronomy sites by comparing its predictions with COMAP radiometric measurements.
   - 2.1 Extract precipitable water vapor value from MERRA-2 atmospheric data for the OVRO site on a specific day.

2.2 Derive the zenith atmospheric opacity across the COMAP frequency range at the OVRO site using skydip power measurements and atmospheric simulations based on MERRA-2 and the AM model.

2.3 Validate MERRA-2 data by comparing simulated and calculated zenith atmospheric opacities.

2.4 Conduct a long-term atmospheric study of the OVRO site using precipitable water vapor.

Chapter 2

Radioastronomy Projects Involved

2.1 The COMAP Project

The CO Mapping Array Project (COMAP) is part of a program called "The First Billion Years: A Technical Development Program for Spectral Line Observations" under the Keck Institute for Space Studies. Kieran Cleary is the Principal Investigator of COMAP and the Associate Director of the Owens Valley Radio Observatory (OVRO) at Caltech. The COMAP Project aims to use carbon monoxide (CO) line intensity mapping to trace the distribution and global properties of galaxies across cosmic time, extending to the Epoch of Reionization (EoR) [19]. The Project is divided into COMAP Pathfinder and COMAP-EoR. The Pathfinder operates in the 26–34 GHz band, detecting CO(J=1-0) (rest frame 115 GHz) within a redshift range of z = 2.4–3.4, with a weaker contribution from CO(J=2-1) (rest frame 230 GHz) at z = 6–8. In the future, COMAP-EoR's frequency coverage is expected to expand to 12–20 GHz to explore the CO(1-0) line during the Epoch of Reionization.

Panel (a) of Figure 2.1.1 provides a general layout of the COMAP instrument, highlighting key components. The receiver is a focal plane array of 19 single-polarization feeds deployed on a 10.4 m Cassegrain telescope at OVRO, California, USA. The first down-conversion stage shifts the RF band from 26-34 GHz to a first intermediate frequency (1st IF) of 2-10 GHz. The second down-conversion stage occurs within the telescope's side cabin, where the 2-10 GHz band from each feed is split into two 4 GHz-wide bands, each quadrature-converted to produce an IQ signal at a second IF of 0-2 GHz. Each IQ pair is fed into a "ROACH-2"

FPGA-based spectrometer. Custom FPGA code on each ROACH-2 separates upper sidebands (USB) and lower sidebands (LSB), resulting in four 2 GHz-wide sidebands from each feed, each containing 1024 spectral channels with a spectral resolution of $\sim$ 2 MHz. To process the 8 GHz bandwidth from each of the 19 feeds, 38 ROACH-2 spectrometers are required. Spectra are recorded every 20 ms and sent via Ethernet to a storage machine in a nearby control building [19].

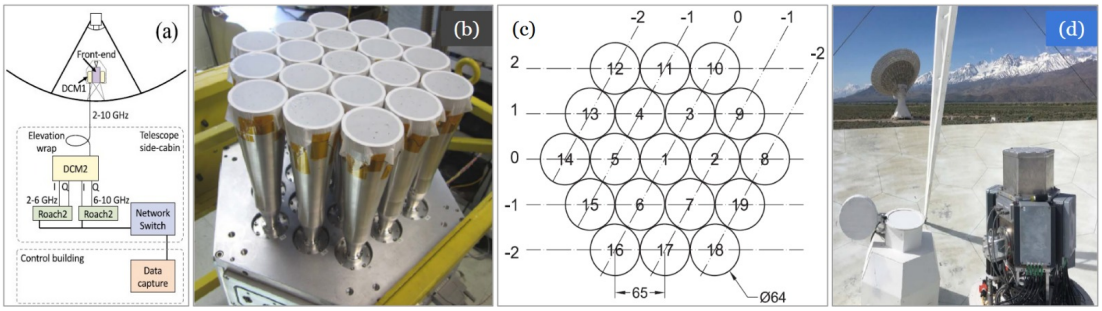

Figure 2.1.1: Panel (a) shows the general layout of the COMAP instrument and its key components. Panel (b) presents the array of 19-feed horns at the receiver's front-end. Panel (c) displays the feed horns layout from the receiver's front view. Panel (d) illustrates the calibration system, with a circular white load on the left and the receiver on the right, mounted on the primary collector. Credits: [19], [34].

Panel (b) presents the 19-feed horns forming the hexagonal array of the COMAP receiver. Below the horns is the DCM1 module, mounted at the secondary focus, shown as the front-end in panel (a). Each of these horns captures the left-handed circular polarization of the signal in the Pathfinder frequency range, between 26 and 34 GHz. Panel (c) displays a diagram of the array viewed from the front of the receiver. The central number helps identify the feeds throughout the data processing up to the final maps, which are referred to as pixels. The central number helps identify the elements throughout the data processing up to the final maps, where these are referred to as pixels. Each has a diameter of 64 mm, and the distance between centers is 65 mm. This diagram is crucial, as it will serve as a reference in the COMAP data analysis, where the procedure for some pixels, such as pixel 1, will be illustrated. The left side of panel (d) shows a microwave-absorbing material, painted white at ambient temperature, used as a Vane calibrator, placed over the cryostat, which is mounted on the DCM1 module, shown on the right side of the panel.

It is essential to understand the general data processing workflow to contextualize the level at which the COMAP data will be analyzed. This process begins with

Level 1 data, which consists of raw instrument recordings, including pointing and maintenance information. The main processing step generates calibrated and refined data stored as **Level 2**. From there, a list of observations is curated based on statistical criteria and subsequently transformed into sky temperature maps for each frequency channel through **mapmaking** techniques. These maps ultimately enable the estimation of the **CO power spectrum**. This study focuses on Level 1 data, specifically working with COMAP's raw data files. These files, formatted in HDF5, are organized into the following groups:

1.- Spectrometer: Contains raw power data recorded as digital counts across 1024 spectral channels for the 19 array pixels in four bands, along with timestamps in MJD format. It also includes azimuth and elevation position coordinates for the pixels. The bands are divided into A and B, each further split into LSB and USB, covering specific frequency ranges: A:LSB (26-28 GHz), A:USB (28-30 GHz), B:LSB (30-32 GHz), and B:USB (32-34 GHz), thereby encompassing the entire COMAP frequency range.

2.- Housekeeping: Stores system control records corresponding to the observation period. This group includes the VANE subgroup, which provides calibration source data, such as the temperature and position of the load during scans. It also contains the Weather subgroup, which provides atmospheric data, including barometric pressure in millibars, relevant for this study.

3.- Pointing: Includes boresight orientation data, which pertains to the array as a whole rather than individual pixels.

This detailed framework establishes a structured and precise approach to analyzing raw data, forming the foundation for the objectives of this research.

This project is essential for the development of the Chapter titled "Radiometric and Atmospheric Study for OVRO at COMAP frequencies" (Chapter 4), as it enables the assessment of the COMAP receiver performance. Additionally, a second section presents an atmospheric study of the site, supporting the validation of the MERRA-2 atmospheric database.

2.2 The LLAMA Project

The Large Latin American Millimeter Array (LLAMA) project represents a scientific and technological collaboration between Argentina and Brazil to establish a radio observatory in Alto Chorillos, northwest Argentina. Located at an altitude of 4820 meters above sea level, the site is approximately 16 kilometers from San Antonio de los Cobres and 180 kilometers southeast of ALMA, as shown in Figure 2.2.

Figure 2.2.1: Geographic location of the LLAMA instrument on the map

The LLAMA telescope, constructed by Vertex Antennen Technik GmbH, consists of a 12-meter diameter Cassegrain antenna with a surface accuracy of 15 microns and a pointing accuracy of ∼2 arcseconds. Equipped with two Nasmyth cabins in addition to the Cassegrain cabin, LLAMA will utilize receivers similar to those used in ALMA, operating across the 35–950 GHz frequency range. While initially functioning as an independent facility, it is expected to join a Very Long Baseline Interferometry (VLBI) network in Latin America in the future.

LLAMA's scientific objectives encompass a wide range of topics, including: 1) The molecular composition and evolution of the Universe; 2) Black holes, accretion disks, and relativistic jets; 3) Star formation and its evolution across cosmic scales; 4) Structure of the Milky Way; 5) Solar studies; 6) Planetary atmospheres; 7)

Extragalactic astronomy

Currently, LLAMA has installed its containers on-site and assembled the 12-meter Vertex antenna, as shown in the upper panel of Figure 2.2.2. The lower left panel of Figure 2.2.2 shows the Cassegrain Support Structure (CASS), one of the main components of the Nasmyth Cabin Optical System (NACOS), manufactured by the ALFA company in Araraquara, São Paulo.

Figure 2.2.2: A view of the current LLAMA site is shown in the top panel, highlighting the Vertex antenna already positioned on site. In the bottom left panel, the Cassegrain Support Structure (CASS) is depicted, while the right panel presents the robotic arm that will hold the three calibration loads developed and reported in this thesis [2].

NACOS is an optoelectro-mechanical system that channels incident light into the Nasmyth focus cabins, directing radiation toward the specific receiver [47]. In the

upper section, robotic arms will be installed, as shown in the right panel of Figure 2.2.2, to support the calibration loads developed by CePIA.
The development of LLAMA is integral to Chapter titled "Development of Ultra-Broadband Calibration Loads for the LLAMA Radio Telescope" (Chapter 5), highlighting the importance of calibration systems tailored for this observatory.

Chapter 3

Background in Radio Astronomy

This chapter presents the theoretical and scientific foundations necessary to understand the research developments discussed in Chapters 4 and 5 of this thesis. It begins by examining the theoretical basis of the signal originating in space and its interaction with the medium before detection by a radio telescope. Subsequently, the chapter explores the theoretical interaction between the signal and the receiving instrument, along with the instrument's own behavior. It also addresses atmospheric water vapor, one of the primary contaminants affecting the target signal, describing methods for measuring this interference from an instrumental perspective and through modeling techniques.

3.1 Specific Intensity and Spectral Flux

In the study of astronomical sources, astronomers measure the intensity of radiation as a function of sky direction (through mapping), frequency (via spectroscopy), and additional variables like time and polarization. Two main concepts are essential for quantifying this intensity: brightness and flux. Both describe the radiation emitted by a source but differ in their characterization.

Spectral brightness, I_ν, or spectral intensity, quantifies the energy per unit of projected area, per unit of time, per unit of frequency, and per unit of solid angle arriving from a specific direction. Figure 3.1 illustrates this concept: if a detector on Earth with area $d\sigma$ detects energy dE from an astronomical source within a solid angle $d\Omega$, the energy passing through a projected area (determined by

angle θ between the zenith, the detector, and the source) over time interval dt and bandwidth $d\nu$ is expressed as:

$$dE = I_\nu \cdot \cos\theta d\sigma d\Omega dt d\nu \tag{3.1.1}$$

The energy flux per unit time defines power dP in watts as:

$$dP = \frac{dE}{dt} = I_\nu \cdot \cos\theta d\sigma d\Omega d\nu \tag{3.1.2}$$

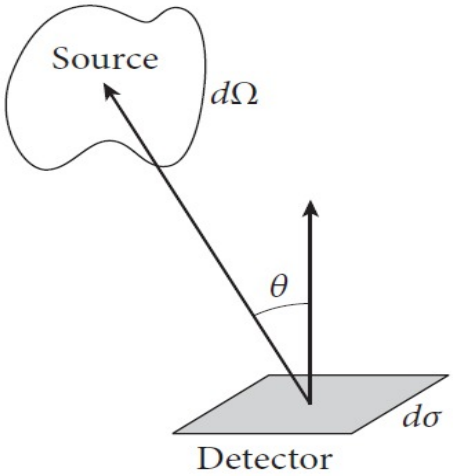

Figure 3.1.1: Specific intensity from an astronomical source of area $d\Omega$ measured by a detector with area $d\sigma$ whose normal forms an angle θ with respect to the line of sight (Image credit: Condon and Ransom [21]).

Brightness is formally defined as the intensity of radiation per unit of projected area, per unit of solid angle, and per unit of frequency, measured in $Wm^{-2}Hz^{-1}sr^{-1}$. It can be expressed as:

$$I_\nu = \frac{dP}{\cos\theta d\sigma d\nu d\Omega} \tag{3.1.3}$$

Specific intensity has two important properties: (1) brightness remains independent of the distance to the source, as radiation observed per unit area and solid angle stays constant regardless of distance, and (2) brightness can represent both energy flowing from the source and energy directed towards the detector. Consequently, in Figure 3.1, the physics holds even if the positions of the detector

and source are reversed.

Upon establishing spectral intensity, the concept of flux density can be introduced. Whereas brightness specifies energy arriving from a source per unit area and solid angle, flux density measures the total energy received over an area, irrespective of source direction or angular size. In the case of an astronomical source observed by a terrestrial telescope, the measurement encompasses not only the radiation intensity from a particular direction but also the entire energy flux over the detector's area. This flux varies with the distance between the source and the observer: as distance increases, energy disperses, lowering detected flux.
Formally, flux density, or spectral flux, is defined as the total energy arriving at a detector per unit area and time, integrated across all possible directions from the source. Thus, spectral flux density S_ν at a frequency ν is given by:

$$S_\nu = \int_{d\Omega} I_\nu\big(\theta, \phi\big) \cdot \cos\theta d\Omega \tag{3.1.4}$$

where S_ν is measured in $Wm^{-2}Hz^{-1}$. Spectral flux density is often expressed in Janskys (Jy), with 1 Jy $= 10^{-26}Wm^{-2}Hz^{-1}$. Typically, in astronomical cases, the source's angular size is $\ll 1$ radian, making $\cos\theta \approx 1$ and simplifying spectral flux density calculation.

This information was investigated from Condon and Ransom [21] and Burke et al. [17].

3.2 Radiative Transfer: Absorption and Emission

In free space, the specific intensity I_ν of radiation remains constant along a ray:

$$\frac{dI_\nu}{ds} = 0 \tag{3.2.1}$$

where s represents the coordinate along the ray from the source to the detector. However, when a medium is present between positions s_{in} and s_{out}, radiation undergoes changes through absorption and emission due to interactions with particles within the medium.
The fraction of specific intensity lost due to absorption over an infinitesimal

distance ds along the ray is expressed as:

$$\frac{dI_\nu}{I_\nu} = -\kappa ds \tag{3.2.2}$$

where κ is the linear absorption coefficient, with units of inverse length, m^{-1}. This coefficient derives from a probabilistic model, where radiation is treated as photons moving through a medium, some of which are absorbed by its particles. Considering absorption across an incremental distance ds that a photon is absorbed over ds is given by $dP = \kappa ds$, where κ denotes the medium's absorption capacity per unit distance. If κ is large, the medium quickly reduces radiation intensity; conversely, a small κ suggests transparency, allowing radiation to propagate with minimal energy loss.
Integrating both sides of the previous Equation 3.2 along the absorbing path yields the output-specific intensity as a fraction of the input-specific intensity:

$$\frac{I_\nu\big(s_{out}\big)}{I_\nu\big(s_{in}\big)} = exp\Big[-\int_{s_{in}}^{s_{out}} \kappa\big(s'\big)ds'\Big] \tag{3.2.3}$$

where,

$$\tau \equiv -\int_{s_{out}}^{s_{in}} \kappa\big(s'\big)ds' \tag{3.2.4}$$

is the optical depth or opacity of the absorber medium. Inverting the integration direction along the line of sight ensures $\tau > 0$ and increases when observing deeper into an absorbing object. If $\tau \ll 1$, the medium is optically thin; if $\tau \gg 1$, it is optically thick.

The intervening medium can also emit photons. While absorption reduces intensity due to particle interaction, emission enhances it by generating photons that add to the radiation beam. The emission within a medium is described by the emission coefficient j_ν, representing the amount of radiation emitted per unit volume ($dsd\sigma$), frequency (ν), and solid angle ($d\Omega$). Generally, the emission is isotropic, meaning radiation disperses equally in all directions from an infinitesimal volume. This process, combined with absorption, leads to the radiative transfer equation:

$$\frac{dI_\nu}{ds} = -\kappa I_\nu + j_\nu \tag{3.2.5}$$

accounting for intensity loss due to absorption, κI_ν, and gain due to emission, j_ν.

In thermodynamic equilibrium (TE), where $dI_\nu/ds = 0$, a relationship exists between absorption and emission, reflecting their interdependence, as shown by Kirchhoff's law:

$$\frac{j_\nu(T)}{\kappa(T)} = B_\nu(T) \tag{3.2.6}$$

where $B_\nu(T)$ is the blackbody radiation at temperature T given by the Planck function (Section 3.3). This law links the properties of the medium to the equilibrium radiation, allowing one coefficient to be determined if the other is known. Furthermore, Kirchhoff's law is also applicable under local thermodynamic equilibrium (LTE).

3.2.1 Modeling Atmospheric Effects on Radio Observations

In the context of radio astronomy, understanding the absorption and emission of radio waves in the Earth's atmosphere is essential, particularly regarding how atmospheric opacity impacts radio observations. Above 1 GHz, atmospheric absorption notably affects the accuracy of flux density measurements, while atmospheric emission contributes additional signal plus noise that interferes with data collection.

The primary approach for analyzing the atmosphere in radio astronomy involves atmospheric opacity. The relationship between the observed spectral brightness B_ν and the brightness temperature T_b is critical. According to the Rayleigh-Jeans approximation, $I_\nu = B_\nu$ holds when $T_b = T$ where T denotes the physical temperature of the source. Consequently, spectral brightness is proportional to brightness temperature, described by the equation:

$$T_b = \frac{I_\nu c^2}{2k\nu^2} \tag{3.2.7}$$

Here, $k = 1.380649 \cdot 10^{-23}$ J/K is Boltzmann's constant and $c = 3 \cdot 10^8$ m/s represents the speed of light. This relationship indicates that T_b varies with frequency, demonstrating that brightness temperature is a convenient measure for describing radiation power in thermal terms. This approach is particularly useful since radio telescopes are often calibrated using absorbers or "loads" of known temperature. It is important to clarify that brightness temperature does not directly correspond to physical temperature. Thermal sources generally exhibit brightness temperatures lower than their physical temperatures when they are

semi-transparent (e.g., the atmosphere) or partially reflective (e.g., the Moon). Even true blackbody radiators achieve $T_b = T$ only in the low-frequency limit $h\nu \approx kT$.

Modeling the effects of emission and absorption incorporates several assumptions into the radiative transfer equation. Four key factors are acknowledged: 1) the Earth's atmosphere is approximately isothermal, 2) Kirchhoff's law holds in local thermodynamic equilibrium (LTE) as $j_\nu = \kappa B_\nu(T_{atm})$, where T_{atm} is the kinetic temperature of the atmosphere measured by a standard thermometer, 3) the Rayleigh-Jeans approximation for $B_\nu(T_{atm})$, and 4) the path length through a plane-parallel atmosphere is proportional to the zenith angle z. By applying these assumptions to the radiative transfer equation, the brightness temperature of atmospheric emission as a function of zenith angle can be expressed as:

$$T_b = T_{atm}\left[1 - e^{-\tau(z)\cdot\sec(z)}\right] \tag{3.2.8}$$

In this equation, $\tau(z)$ denotes zenith opacity, while $\sec(z)$ accounts for the increased path length through the atmosphere at varying zenith angles. This formulation models how brightness temperature changes with the zenith angle z, providing a basis for estimating atmospheric opacity. In practical applications, radio astronomers determine the zenith opacity by fitting the observed brightness temperature data to Equation 3.2.8. This procedure enables the correction of flux density measurements to account for atmospheric absorption. Moreover, Equation 3.2.8 not only aids in calculating opacity but also establishes a direct connection between brightness temperature measurements and the thermodynamic properties of the atmosphere.

3.2.2 Kirchhoff Law for Opaque Bodies

In the study of radiation and its interaction with matter, understanding the characteristics of opaque bodies is fundamental. A body is defined as opaque when its opacity is sufficiently high to prevent photons from penetrating it. Consequently, upon the incidence of electromagnetic radiation, an opaque body can only absorb or reflect photons, without transmitting them. This behavior is critical in radio astronomy, where the interaction of radiation with various media influences observations.

For an opaque body, two fundamental coefficients are defined: 1) the absorption coefficient, $a(\nu)$ representing the probability that a photon of frequency ν is absorbed by the body, and 2) the reflection coefficient $r(\nu)$, indicating the probability that the photon is reflected. Given that each photon can either be absorbed or reflected, the fundamental relationship is established:

$$a(\nu) + r(\nu) = 1 \tag{3.2.9}$$

This implies that an ideal black body, which absorbs all incident radiation, has $a(\nu) = 1$ and thus $r(\nu) = 0$.
The emission coefficient $e(\nu)$ is defined as the ratio of the spectral power emitted per unit area at frequency ν compared to the power of a black body at the same temperature. This coefficient is interconnected with the absorption and reflection coefficients. In a local thermodynamic equilibrium (LTE) system, Kirchhoff established that:

$$e(\nu) = a(\nu) = 1 - r(\nu) \tag{3.2.10}$$

This constitutes Kirchhoff's law for opaque bodies, indicating that in thermodynamic equilibrium, the amount of radiation emitted by a body is proportional to its absorption coefficient $a(\nu)$. Essentially, the emission coefficient describes the efficiency with which a body emits radiation at a specific frequency. Physically, $e(\nu)$ compares the actual amount of radiation emitted by the object with the amount expected if it were a black body. Under thermal equilibrium conditions, the opaque body's spectral power absorbed equals the power it emits. Thus, the brightness temperature $T_b(\nu)$ of an opaque body in LTE is expressed as:

$$T_b(\nu) = a(\nu) \cdot T = \big(1 - r(\nu)\big) \cdot T \tag{3.2.11}$$

This equation emphasizes that, since $a \leq 1$, the brightness temperature will never exceed the physical temperature of the body, T. Notably, if $a(\nu) = 1$ then $T_b = T$, which is a characteristic of a perfect black body.

This information was investigated from Condon and Ransom [21], Wilson et al. [56] and Burke et al. [17].

3.3 Blackbody Radiation

A black body is an ideal object that absorbs all incident electromagnetic radiation without reflecting or transmitting any, thereby acting as a perfect emitter of radiation across all frequencies. According to Kirchhoff's law, the amount of radiation emitted by a black body depends solely on its temperature, independent of its composition. The concept of black body radiation is essential for understanding how thermal energy is emitted and distributed across different frequencies. This emission is quantitatively described by the Rayleigh-Jeans Law, Planck's Law, and Wien's Displacement Law, which will be discussed in the following sections.

Aproximación de Rayleigh-Jeans

Before the development of quantum mechanics, physicists sought to describe black body radiation using classical physics. One such approximation was developed by Lord Rayleigh and Sir James Jeans in the early twentieth century, known as the Rayleigh-Jeans approximation. The Rayleigh-Jeans Law arises from applying classical physics principles to the problem of electromagnetic radiation emitted by a black body. According to this approximation, the spectral intensity of black body radiation at low frequencies is proportional to the square of the frequency and temperature. The Rayleigh-Jeans formula for black body radiation in the radio region is:

$$B_\nu(T) = \frac{2kT\nu^2}{c^2} = \frac{2kT}{\lambda^2} \tag{3.3.1}$$

where $k = 1.380649 \cdot 10^{-23}$ J/K is Boltzmann's constant, T is the source temperature, ν is the frequency, λ is the wavelength, and $c = 3 \cdot 10^8$ m/s represents the speed of light.

Equation 3.3.1 allows for the calculation of the flux density S_ν of a discrete radio source with temperature T subtending a solid angle Ω_S. In the Rayleigh-Jeans limit, integrating over the solid angle of the source gives:

$$S_\nu(T) = \frac{2k}{\lambda^2} \int_{\Omega_S} T(\theta, \phi) d\Omega \tag{3.3.2}$$

If the brightness temperature of the source is uniform across Ω_S, the integral $\int_{\Omega_S} T(\theta, \phi) d\Omega = T\Omega_S$. It is important to emphasize that Equation 3.3.1 performs

well at low frequencies, predicting that the emitted radiation increases quadratically with frequency. However, this formula fails as frequencies increase, predicting an indefinite rise in spectral intensity. This failure is termed the "ultraviolet catastrophe," as classical theory predicts that a black body would emit infinite energy at high frequencies, which is physically impossible.
The issue with the Rayleigh-Jeans approximation was resolved when Max Planck formulated his Radiation Law in 1900, introducing the concept of quantized energy.

Planck's Radiation Law

To address the shortcomings of classical theories in describing black body radiation, such as the failure of the Rayleigh-Jeans approximation at high frequencies, German physicist Max Planck proposed a solution absent from classical physics: energy quantization. Planck's Law describes how the intensity of radiation emitted by a black body (i.e., the amount of energy emitted per unit area, per unit solid angle, per unit frequency) varies with frequency at a given temperature, expressed as:

$$B_\nu(T) = \frac{2h\nu^3}{c^2} \frac{1}{exp\left(\frac{h\nu}{kT}\right) - 1} \tag{3.3.3}$$

where $h = 6.6260 \cdot 10^{-34}$ Js is the Planck constant, $k = 1.3806 \cdot 10^{-23}$ J/K is Boltzmann's constant, T is the source temperature, ν is the frequency, λ is the wavelength, and $c = 3 \cdot 10^8$ m/s represents the speed of light. The quantum term $e^{h\nu/kT} - 1$ corrects the divergence at high frequencies. Consequently, this law accurately describes black body radiation across the entire range of frequencies and temperatures. Figure 3.3.1 illustrates Planck's spectrum for black bodies at different temperatures, represented by each curve. As the temperature of the black body increases, the shape of the curve changes; the wavelengths at which radiation is most intense shift toward shorter wavelengths, and the height of the curves also increases, indicating that the black body emits more radiation at higher temperatures. Note that at 0 K, the black body does not emit radiation.
It is important to highlight that Planck's Law represents a fundamental shift in the understanding of thermal radiation due to the formulation that energy is quantized in discrete packets called quanta, implying that energy is emitted or absorbed in discrete units of $h\nu$, marking the birth of quantum mechanics.

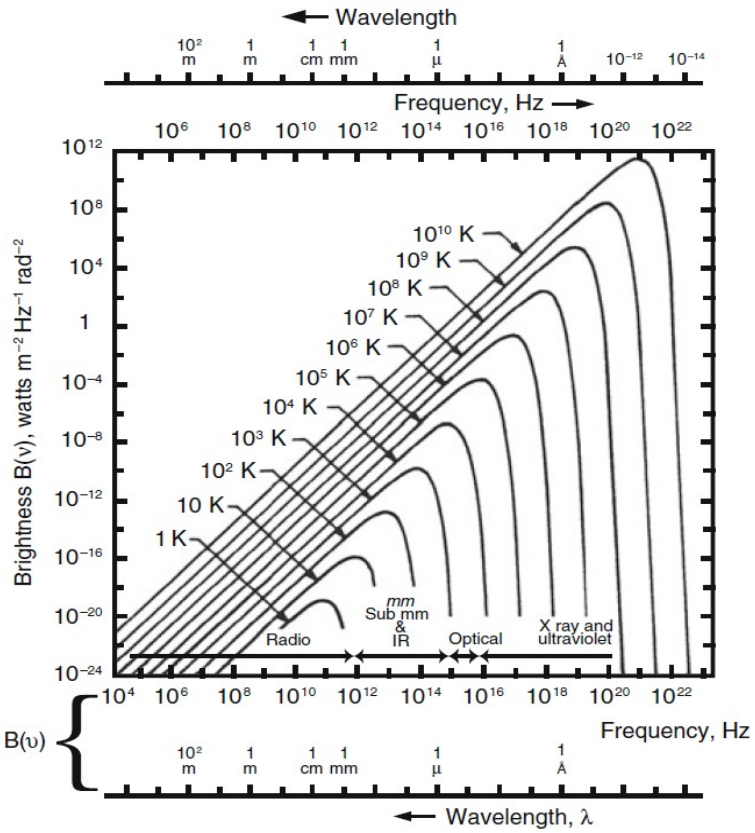

Figure 3.3.1: The Planck spectrum for black bodies at different temperatures is shown. Each curve corresponds to a different temperature; as the black body's temperature increases, the curve's shape changes, shifting leftward and increasing in intensity (Credit:Wilson et al. [56]).

Wien's Displacement Law

Wien's Law was proposed by Wilhelm Wien in 1893, based on principles of thermodynamics and classical electromagnetic theory, prior to the emergence of quantum radiation theory. Later, Wien's Law was theoretically justified by Planck's Law for high frequencies. This law describes how the wavelength at which a black body emits maximum energy shifts with changing temperature. By maximizing the spectral density with respect to wavelength in Equation 3.3.3, Wien's Displacement Law is mathematically expressed as:

$$\lambda_{max} T = b \tag{3.3.4}$$

where λ_{max} is the wavelength at which the black body emits the greatest amount

of energy (the peak of the radiation spectrum). T is the absolute temperature of the body in kelvins (K), and b is Wien's displacement constant, approximately 0.29 cm K. Equation 3.3 indicates that at higher temperatures, the black body emits more radiation, causing the peak emission to move toward shorter wavelengths, as depicted in Figure 3.3.1. This signifies that hot bodies (such as stars) emit more radiation in shorter wavelength ranges, including visible light and even ultraviolet radiation.

This information was investigated from Condon and Ransom [21] and Wilson et al. [56].

3.4 Johnson Noise and Nyquist Approximation

Johnson noise, also known as thermal noise, arises from the thermal agitation of electrons within a resistor. When a resistor is at a temperature above 0 K, the random movement of electrons generates current fluctuations, producing inherent electrical noise. This phenomenon, discovered by John B. Johnson in 1926, depends solely on temperature and the resistor's electrical resistance, making it independent of the material itself.
Harry Nyquist extended Johnson's work by deriving an expression that directly relates the noise power to temperature and other system parameters. Johnson noise can be understood as adhering to the equipartition theorem, which also underlies the Rayleigh-Jeans law for blackbody radiation at low frequencies. The average thermal energy of a frequency mode in the system is proportional to the temperature, meaning that noise increases linearly with temperature.

The Nyquist approximation states that the noise power generated by a resistor in thermal equilibrium can be expressed as:

$$P_\nu = kT \tag{3.4.1}$$

where P_ν is the noise power per unit frequency, $k = 1.3806 \cdot 10^{-23}$ J/K is Boltzmann's constant, and T is the resistor's temperature. This relation holds for low frequencies, where the Rayleigh-Jeans law accurately describes the system's behavior. Additionally, thermal noise has a flat spectrum, with constant power density across all frequencies.

3.5 Antenna Response

Antennas are passive devices that interact with electromagnetic waves, either converting them into electrical signals or radiating energy in a waveform. In applications such as radio astronomy, where very weak signals from astronomical sources are detected, thermal noise plays a crucial role, as antennas capture both the source radiation and background noise generated by the environment. This behavior can be modeled using principles akin to Johnson noise in resistors, where an antenna surrounded by thermal radiation acts as if it is "heated" by this radiation, generating a noise signal proportional to the surrounding temperature. Thus, the antenna temperature (T_A) characterizes the thermal noise power received and is measured in Kelvin, facilitating comparison with receiver-generated noise. Although the term might suggest a relation to the antenna's physical temperature, it actually represents an equivalent noise power that would be received by an ideal resistor at the same temperature. The relation between antenna temperature and power per unit frequency is expressed as:

$$T_A = \frac{P_\nu}{k} \tag{3.5.1}$$

where P_ν is the power per unit frequency and $k = 1.3806 \cdot 10^{-23}$ J/K is Boltzmann's constant. This expression aligns with the Nyquist approximation (Equation 3.4) previously introduced.

In radio astronomy, antenna temperature is a convenient way to describe the captured signal, as it is calibrated in Kelvin units, which simplifies comparison with receiver noise. Moreover, using temperature rather than power in watts is more practical, as 1 Kelvin of antenna temperature corresponds to a small amount of power per unit bandwidth. This approach enables the performance of an antenna to be expressed independently of its physical shape, which is useful when comparing antenna systems with different configurations.

In addition to temperature, another key concept in assessing antenna performance is its effective area (A_e), which describes how much electromagnetic radiation it can capture from a distant source. When oriented toward a radiation source, the power received depends not only on the antenna temperature but also on the antenna's geometry and efficiency. The total power received per unit frequency, P_ν, is related to the flux density S_ν of an unpolarized source and the effective

area of the antenna by:

$$P_\nu = \frac{A_e S_\nu}{2} \tag{3.5.2}$$

This expression is useful for point sources of radiation, such as stars or galaxies, where the power captured is proportional to the product of the antenna's effective area and the source's radiation. Applying this concept to Equation 3.5.1, the antenna temperature for a point source relates to the effective area and flux density by:

$$T_A = \frac{A_e S_\nu}{2k} \tag{3.5.3}$$

This equation is valid when the source has a small brightness distribution compared to the antenna beam, and A_e represents the antenna's effective area in the direction of the source.

For more complex sources or those with an extended distribution across the sky, the relationship between captured power and radiation must include considerations of the antenna's radiation pattern and how it interacts with the source's brightness distribution.
For an antenna receiving radiation from an extended source, the total power per unit frequency (P_ν) is expressed as an integral over the total solid angle, where the antenna's effective area ($A_e(\theta, \phi)$) and the incident radiation intensity ($I_\nu(\theta, \phi)$) vary as a function of direction:

$$P_\nu = \frac{1}{2} \int_{4\pi} A_e(\theta, \phi) I_\nu(\theta, \phi) d\Omega \tag{3.5.4}$$

This integral accounts for all directions in the sky, weighting the received power by the antenna's spatial response. Expressing this power (Equation 3.5) n terms of antenna temperature T_A and using the Nyquist approximation in Equation 3.5.1, the thermal power received can be related to the source brightness temperature using Equation 3.3.1. A general relationship between antenna temperature and brightness temperature is given by:

$$T_A = \frac{1}{\lambda^2} \int_{4\pi} A_e(\theta, \phi) T_b(\theta, \phi) d\Omega \tag{3.5.5}$$

The antenna temperature also varies according to the type of source detected. For an extended source where the radiation does not concentrate at a single point, the antenna must account for the spatial variation of brightness over the entire solid

angle. For instance, the cosmic microwave background spans the antenna's full field of view, making the antenna temperature equal to the source's brightness temperature, which is the equivalent blackbody temperature that would emit the same power per unit area, frequency, and solid angle:

$$T_A = T_b \tag{3.5.6}$$

For compact sources that occupy only a fraction of the antenna's solid angle, the antenna temperature is:

$$T_A = T_b \frac{\Omega_s}{\Omega_A} \tag{3.5.7}$$

This relationship shows that the antenna temperature is proportional to the source's brightness temperature and the portion of the beam that the source occupies.

This information was investigated from Condon and Ransom [21], Wilson et al. [56] and O'Neil [40]

3.6 Radiometers and Noise Detection

Radiometers are highly sensitive instruments designed to measure noise power from radio waves, including emissions from the cosmic microwave background (CMB), astronomical objects, and terrestrial sources like the atmosphere. This broadband, random noise is challenging to distinguish from the thermal noise generated by the receiver electronics. To measure this random noise, radiometers average the power of the incoming noise signal over time.

The detection process begins with voltage fluctuations in the noise signal, which follow a Gaussian distribution with a zero mean, typical of thermal noise. These voltage fluctuations occur on extremely short time scales, usually in the nanosecond range, due to the inverse relationship with bandwidth $\Delta\nu$. A radiometer uses a square-law detector to square the incoming noise voltage signal, converting the voltage fluctuations to noise power. This step is essential, as power is always positive, enabling accurate measurement of the average noise power over time, which remains stationary on longer time scales (seconds to hours).

3.6.1 Nyquist-Shannon Theorem

The noise voltage exhibits a Gaussian distribution with a zero mean. The Nyquist-Shannon sampling theorem provides a framework for effective noise measurement. According to the theorem, any signal with finite bandwidth $\Delta\nu$ and duration τ can be represented by $N = 2\Delta\nu\tau$ independent samples, which must be taken at intervals of $(2\nu)^{-1}$. Increasing the number of samples N reduces the uncertainty in measuring the average noise power, expressed as:

$$\frac{1}{\sqrt{N/2}} = \frac{1}{\sqrt{\Delta\nu\tau}} \tag{3.6.1}$$

Thus, increasing the bandwidth $\Delta\nu$ or the integration time τ reduces measurement uncertainty, which is crucial for detecting weak radio sources that only marginally increase the total noise power.

3.6.2 Radiation Sources Captured by a Radio Telescope

Radiation detected by a radio telescope originates from multiple sources, not solely from the observed astronomical object. Several noise sources contribute to the system noise temperature T_{sys}, a crucial parameter in radiometer observations. This parameter defines the equivalent temperature of the total noise power from all sources at the input of a radiometer connected to a radio telescope's output. Contributions include:

$$\begin{aligned} T_{sys} &= T_{Rx} + T_{Ant} \\ &= T_{Rx} + T_{cmb} + T_{Atm} + T_{source} + T_{spill} + ... \end{aligned} \tag{3.6.2}$$

where T_{Rx} is the receiver noise temperature associated with noise from the radiometer itself. All radiometers generate noise, and each can be represented by an equivalent circuit consisting of a noiseless radiometer with an input connected to a resistor at temperature T_{Rx}. Reducing radiometer noise often involves cooling the radiometer to cryogenic temperatures. T_{Ant} is the antenna temperature, which includes $T_{cmb} \approx 2.73$ K, the temperature of the cosmic microwave background (CMB); T_{source}, the emission from the observed astronomical source, typically $T_{source} \ll T_{sys}$; T_{Atm}, the atmospheric noise known as atmospheric emission brightness within the telescope beam, previously derived in Section 3.2.1, Equation 3.2.8; and T_{spill}, representing noise from the antenna's surroundings, such as ground

or foliage, mainly captured by the antenna radiation pattern side lobes.
Studying, characterizing, and minimizing these noise sources is essential for enhancing radio telescope sensitivity and enabling the detection of faint astronomical signals.

This information was investigated from Wilson et al. [56], O'Neil [40] and Perepelitsa [44]

3.7 Ideal Radiometer Equation

The ideal radiometer equation describes the system's sensitivity and its ability to detect faint signals, linking key parameters such as bandwidth $\Delta\nu$, integration time τ, and system noise temperature T_{sys}. In a simple total-power radiometer, the goal is to measure the average power across a defined radio frequency range. This power results from thermal noise fluctuations and observed signals within the frequency band, with a receiver covering from $\nu_{RF} - \Delta\nu/2$ to $\nu_{RF} + \Delta\nu/2$, where ν_{RF} represents the central frequency.

This type of radiometer comprises four main stages: 1) a bandpass filter, which selects only the noise within the desired frequency range, excluding out-of-band signals; 2) a square-law detector that squares the input voltage, transforming it into noise power proportional to the square of the voltage; 3) an integrator or averager, smoothing the detector's output to reduce rapid fluctuations; and 4) a voltage meter, recording the smoothed output proportional to the average noise power. After passing through the filter, the noise voltage is confined to the bandwidth. This setup allows the radiometer to integrate noise samples, and by applying the radiometer equation, the minimum detectable temperature change of the system σ_T (or ΔT_{min}) can be determined as follows:

$$\sigma_T = \frac{T_{sys}}{\sqrt{\Delta\nu\tau}} \tag{3.7.1}$$

where T_{sys} represents the system noise temperature, $\Delta\nu$ the bandwidth, and τ the integration time. This result is fundamental because it shows that radiometer sensitivity improves with increased bandwidth and integration time. A wider bandwidth captures more noise within the frequency range, raising the number of independent noise samples ($N = 2\Delta\nu\tau$). At the same time, extended integration

time reduces fluctuations in the average power measurement, enhancing accuracy and allowing for the detection of very weak signals.
The radiometer equation provides a solid foundation for calculating these instruments' theoretical sensitivity and estimating the minimum detectable noise. However, actual sensitivity is affected by gain variations and atmospheric emission fluctuations.

3.8 Gain Fluctuations in Radiometers

Although the ideal radiometer equation suggests that observation sensitivity indefinitely improves with longer integration times ($\tau^{1/2}$), various practical factors limit this enhancement. One of the primary challenges in operating real radiometers is receiver gain fluctuations, which introduce systematic errors in measurements.

Radiometers contain amplifiers to elevate the weak input signals ($P_{in} = k\Delta\nu T_{sys}$) to manageable levels (within the mW range). The total gain G of these amplifiers is crucial, as the radiometer's output signal is proportional to the input power multiplied by the gain ($P_{out} = k\Delta\nu T_{sys}G$). When gain is not stable, gain fluctuations $\Delta G/G$ generate spurious signals indistinguishable from thermal noise fluctuations, thus degrading measurement accuracy. The noise temperature associated with a gain fluctuation can be modeled as:

$$\sigma_G = T_{sys}\left(\frac{\Delta G}{G}\right) \tag{3.8.1}$$

where T_{sys} represents the total system noise temperature, and $\Delta G/G$ indicates the fractional gain variation. Since gain fluctuations and thermal noise are independent random processes, the variances of both contributions add up, yielding $\sigma_T^2 = \sigma_{noise}^2 + \sigma_G^2$. The total variance in the radiometer's output is then expressed as:

$$\sigma_T \approx T_{sys}\left[\frac{1}{\Delta\nu\tau} + \left(\frac{\Delta G}{G}\right)^2\right]^{1/2} \tag{3.8.2}$$

This result demonstrates that, despite increasing bandwidth or integration time, gain fluctuations will limit sensitivity unless the gain fluctuation fraction meets

the condition:

$$\frac{\Delta G}{G} \ll \frac{1}{\Delta \nu \tau} \tag{3.8.3}$$

To preserve sensitivity, gain fluctuations within timescales up to several seconds must remain minimal. Achieving this is challenging, as gain fluctuations generally exhibit a $1/f$ power spectrum, meaning they increase over longer integration times. This phenomenon implies that radiometer output fluctuations intensify as τ extends.

3.9 Gain Stability

3.9.1 $1/f$ Noise

Gain stability in radiometer systems is essential for achieving accurate measurements, yet it is affected by $1/f$ noise. Also known as flicker or low-frequency noise, $1/f$ noise describes a gain fluctuation that becomes increasingly significant over longer timescales. Unlike white noise, which has a flat frequency distribution, $1/f$ noise increases as frequency decreases, presenting a challenge for long-duration integrations in radiometers.

This type of noise can limit a radio telescope's ability to detect faint signals. While increased integration time reduces noise uncertainty (as prescribed by the ideal radiometer equation), gain fluctuations due to $1/f$ noise tend to increase the measurement variance. Consequently, the knee frequency, or $1/f_{knee}$ (f_k), is defined as the point in the frequency spectrum where $1/f$ noise begins to dominate over white noise. For integrations exceeding $1/2\pi f_k$, gain fluctuations increase, thus affecting sensitivity.

3.9.2 Allan Variance

Allan variance (or modified two-sample variance) is a statistical tool that assesses signal stability over time, aiding in detecting $1/f$ noise behavior. Unlike standard variance, which grows with longer integrations, Allan variance calculates the average deviation between consecutive pairs of measurements at specified time intervals. This method evaluates how fluctuations change as observation time extends and is especially effective for analyzing system stability in the presence of $1/f$ noise, as it reveals when the system becomes dominated by low-frequency

fluctuations. Mathematically, the Allan variance for an integration time τ is defined as:

$$\sigma_A^2(\tau) = \frac{1}{2(N-1)} \sum_{i=1}^{N-1} (y_{i+1} - y_i)^2 \tag{3.9.1}$$

where y_i represents the average gain in the i-th time interval τ. As τ increases, one can observe if noise decreases (indicating stability) or begins to rise due to $1/f$ noise.

In radiometers, maintaining low levels of $1/f$ gain noise and evaluating gain stability through Allan variance are essential for maximizing sensitivity. If the knee frequency is low and the Allan variance starts to increase at longer intervals, this indicates that $1/f$ noise is adversely impacting measurements.

The information was studied from Wilson et al. [56], Krauss [33], Ossenkopf, V. [41] and Mittaz [39].

3.10 Aperture Efficiency

The aperture efficiency η_A quantifies how effectively an antenna or radio telescope transforms the energy from an electromagnetic wave incident on its surface into a usable signal. This efficiency depends on various factors: (1) surface irregularities in the dish may reduce efficiency by deflecting part of the signal, (2) misalignment between the dish and receiver can cause signal loss or dispersion, and (3) supporting structures (such as the receiver mount) may obstruct portions of the incoming signal.

Aperture efficiency is defined as the ratio between the effective aperture of the antenna A_e and the geometric aperture A_g:

$$\eta_A = \frac{A_e}{A_g} \tag{3.10.1}$$

where $A_g = \pi D^2/4$ for a circular aperture with diameter D. Considering an antenna that receives a power per unit frequency P_ν when observing a randomly polarized radio source with an effective flux density S_ν over an effective area A_e, the power is given by Equation 3.5.2 presented earlier. Conversely, for an ideal scenario where flux density is captured by the antenna's geometric area A_g, the

power per unit frequency P_g is:

$$P_g = \frac{A_g S_\nu}{2} \tag{3.10.2}$$

The difference between the power values in Equations 3.5.2 and 3.10.2 indicates that the received power using the effective aperture P_e is lower than the incident power P_g associated with the geometric aperture, meaning that A_e is always less than A_g.
The factor η_A is a dimensionless parameter between 0 and 1.0, measuring the fraction of incoming power that is effectively captured by the physical aperture. In a perfectly efficient antenna, all radio power falling within its physical aperture would convert to electrical energy delivered to the connected output load, resulting in $A_e = A_g$ and an aperture efficiency of 1.0. This ideal scenario does not hold in practice; all antennas incur losses such as power dissipation as heat in the resistive elements, reflector spillover, and errors due to surface roughness, among other factors.

In practical astronomical data analysis, studying aperture efficiency involves measuring the detected power increase when the telescope points toward a known point-source flux, such as Jupiter. As indicated in Woody [57], calculating η_A requires knowledge of the antenna temperature (T_{Ant}), sensitivity (σ), and the flux of a source (S_λ):

$$\eta_A = \frac{T_{Ant} \cdot \sigma_{ideal}}{S_\lambda} \tag{3.10.3}$$

where T_{Ant} is computed as outlined in Equation 22 from O'Neil [40], depending on the output power of a point source at its peak, the surrounding sky's output power, and the system temperature:

$$T_{ant}[K] = T_{sys} \cdot \frac{(P^J_{on} - P^J_{off})}{P^J_{off}} \tag{3.10.4}$$

The ideal sensitivity σ_{ideal} assumes all radiation from the sky is received by the antenna and that the receiver uses its entire capacity to capture that radiation. Therefore, σ_{ideal} depends on the antenna radius (R) and Boltzmann's constant (k), and is measured in Jansky per Kelvin:

$$\sigma_{ideal}(Jy/K) = \frac{2k}{\pi R^2} \cdot 10^{26} \tag{3.10.5}$$

where the factor 10^{26} corresponds to the equivalence $1Jy = 10^{-26} \cdot W \cdot m^{-2} \cdot Hz^{-1}$. The amount of energy in Jansky arriving from the source is known as spectral flux density (S_λ), provided by Equation 3.3.2 when the temperature is uniform.

The information was studied from Wilson et al. [56], O'Neil [40] and Woody [57].

3.11 Radiometer Noise Measurement

Due to its effectiveness and simplicity, the Y-factor method is widely used in radio astronomy to characterize noise in radiometric systems. This method measures the radiometer noise temperature, establishing a direct relationship between detector output voltage and generated noise power.
By accounting for gain fluctuations, the Y-factor method evaluates system response to two known temperatures, typically termed "hot load" and "cold load" (at temperatures T_H and T_C, respectively). The Y-factor is mathematically defined as:

$$Y = \frac{P_H}{P_C} \tag{3.11.1}$$

where P_H and P_C are the powers measured when the radiometer targets a hot and cold source, respectively. In practice, the hot load is usually a black body at ambient temperature ($\approx 290K$), while the cold load is a resistor immersed in liquid nitrogen ($\approx 77K$). This procedure reduces the impact of gain instability in the characterization of radiometer noise if done quickly, in a timescale shorter than the gain fluctuations intrinsic timescale, providing an effective approach to determine the radiometer noise temperature T_{Rx}, which is the main noise component within T_{sys}.

Procedure for the Y-factor Method. Power P_H is recorded when the radiometer observes the hot load, and P_C when it observes the cold load. According to Nyquist's theorem (3.4), which states $P_\nu = kT$ for low frequencies, these voltages are expressed in terms of effective input temperature:

$$P_H = k(T_H + T_{Rx})\Delta\nu G \tag{3.11.2}$$

$$P_C = k(T_C + T_{Rx})\Delta\nu G \tag{3.11.3}$$

where $k = 1.3806 \cdot 10^{-23}$ J/K is Boltzmann's constant, $\Delta\nu$ the bandwidth, and G the system gain. $\Delta\nu$ is included since a broadband radiometer covers an entire

frequency range receiving thermal noise, and G is incorporated as it amplifies the received power to a detectable level, crucial in calibrating thermal noise in terms of amplified power. Applying Equation 3.11.1 to the powers defined in Equations 3.11.2 and 3.11.3 gives:

$$Y = \frac{T_H + T_{Rx}}{T_C + T_{Rx}} \tag{3.11.4}$$

The terms $k\Delta\nu G$ cancel since gain, bandwidth, and k are constants for a given time. Rearranging Equation 3.11.4 provides the receiver noise temperature T_{Rx}:

$$T_{Rx} = \frac{T_H - YT_C}{Y - 1} \tag{3.11.5}$$

where T_H and T_C are the known blackbody temperatures. Accurately determining T_{Rx} in radio astronomy is crucial to calibrate system sensitivity and ensure noise measurements exclude significant spurious contributions. This method is vital in heterodyne systems, which use multiple amplification stages to measure weak signals, where well-characterized radiometer noise is essential for reliable results.

The first part of Chapter 4 presents a performance analysis of the COMAP receiver, evaluating several previously discussed concepts: T_{sys}, T_{Rx}, ΔT_{min}, η, and Allan variance. A prior evaluation by the COMAP team exists; this section aims to provide hands-on experience with raw receiver data. Lamb et al. [34] reports a system temperature of 44 K, while Foss et al. [25] indicates that receiver temperature, contributing most to T_{sys}, ranges from 10-30 K, with atmospheric contributions adding 15-25 K. Lamb et al. [34] also reports a ground contribution of 5-6 K and an efficiency of 97.5%. In contrast, Lunde [37] notes a COMAP minimum detectable temperature $\sigma = 0.228$ K for $T_{sys} = 45$ K at a sampling interval $\tau = 20$ ms.

The information was studied from Condon and Ransom [21] and Wilson et al. [56].

3.12 Atmospheric Effects: Water Vapour

Fluctuations in the gain of receivers can lead to variations in signal output, causing the measured noise to resemble thermal noise. This situation becomes particularly critical in humid environments, where atmospheric water vapor introduces additional noise. The non-uniform distribution of water vapor in

the atmosphere generates emission fluctuations that affect receiver sensitivity. These fluctuations contribute to background noise, complicating the detection of weak signals.

3.12.1 The Water Vapor Molecule and Its Importance in Observations

The water molecule is asymmetric, consisting of two hydrogen atoms and one oxygen atom, with a bond angle of approximately 104.5° as depicted at the top of Figure 3.12.1. Its "V"-shaped structure allows for a permanent dipole moment, enabling effective interaction with electromagnetic radiation in the microwave range through its rotational modes. These modes facilitate the absorption and emission of radiation at lower frequencies, particularly in the radio and microwave spectrum. Spectral lines occur at key frequencies such as 22 GHz and 183 GHz, which are crucial for studying the Earth's atmosphere and radio astronomical observations.

In particular, the water molecule exhibits three fundamental rotational modes: torsional mode, rotation about the minor axis, and rotation about the major axis. Panel a) of Figure 3.12.1 illustrates rotation about the major axis. In this mode, the molecule rotates around its major axis, generating a dipole oscillation in space. This movement is responsible for the absorption in the 22 GHz band and is particularly relevant in microwave astronomy, as this line is utilized to study both the Earth's atmosphere and molecular clouds in space. Panel c) of Figure 3.12.1 depicts rotation about the minor axis. In this second mode, the rotation occurs around an axis perpendicular to the first. This rotation generates another absorption frequency, such as the 183 GHz line, which is significant for measuring the amount of water vapor in the atmosphere and studying atmospheric opacity. Panel b) of Figure 3.12.1 shows the torsional mode, a mixed mode where the molecule oscillates in a combined manner, involving changes in orientation along both principal directions. Although less specific in producing individual microwave lines, this movement contributes to the amplification of the overall rotational spectrum and is essential for the continuous absorption observed in the microwave range.

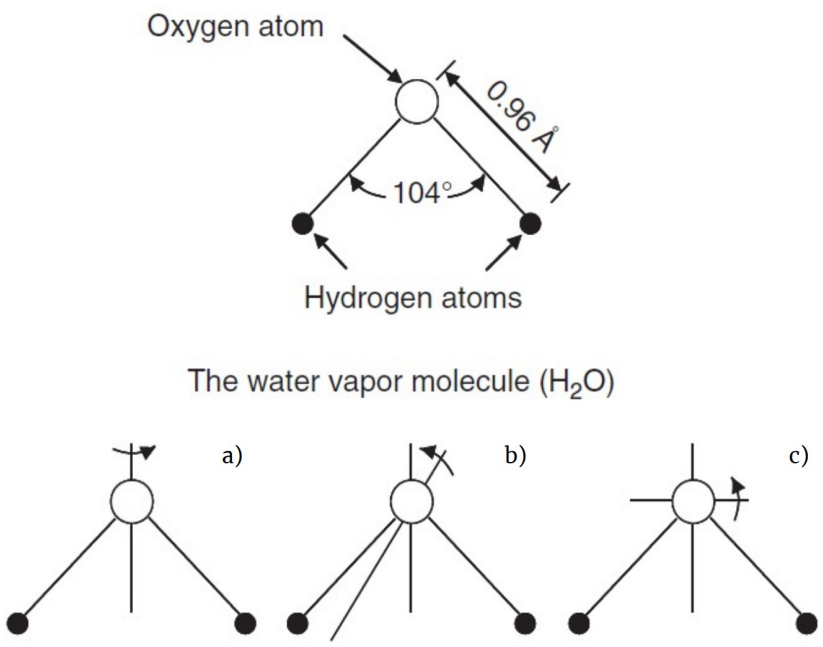

Figure 3.12.1: Water molecule and its rotational modes (Credit: Elachi and van Zyl [24]).

The absorption and emission of radiation at microwave frequencies, facilitated by the rotational modes of the water molecule, play a crucial role in the atmosphere. This effect contributes to atmospheric opacity, especially at frequencies of interest for radio astronomy, where the variability of water vapor with altitude impacts observations. Water vapor in the atmosphere decreases exponentially with altitude, exhibiting a non-homogeneous distribution largely dependent on ocean and land surface temperatures, thereby creating variations in water vapor content that affect radiometry and precision in radio frequency measurements.
The majority of atmospheric water vapor is concentrated in the troposphere, extending from the surface to approximately 10-12 km, where the primary sources of evaporation occur. Furthermore, this layer is limited in height by the thermal inversion layer closest to the Earth's surface. It has been found that approximately 90% of the Precipitable Water Vapor resides between the Earth's surface and the 500 mbar pressure level [48], highlighting the importance of elevation when selecting observation sites.

The equation describing the exponential behavior of water vapor is based on the

water vapor density as a function of altitude and can be represented as:

$$\rho(h) = \rho_0 e^{-\alpha h} \tag{3.12.1}$$

where $\rho(h)$ is the water vapor density at altitude h, ρ_0 is the density at ground level, and α is a scale factor dependent on local atmospheric temperature and pressure. This model is useful for simulations and predictions of atmospheric conditions at astronomical observation sites, allowing estimates of total vapor content based on altitude and adjustments for local climates or specific seasons.

Given its predominant distribution in the troposphere and high variability, atmospheric water vapor affects signal transparency. To quantify this absorption at a specific observation site, the concept of Precipitable Water Vapor (PWV) is employed, which evaluates the total vapor content in a column of air and allows predictions of atmospheric conditions for astronomy. The PWV, in its standard definition, represents the amount of water vapor integrated within a vertical column of air extending from the Earth's surface to the upper atmosphere, typically expressed as the equivalent liquid water height in millimeters [49]. Mathematically, the expression for PWV is given by [51]:

$$PWV = \frac{1}{g} \int_{P_0}^{P_{sup}} q(p) dp \tag{3.12.2}$$

where $q(p)$ is the specific humidity in (Kg/Kg), dp is the atmospheric pressure in Pascal, and g is the gravitational acceleration, 9.80665 (m/s^2). In this case, integration is performed over a pressure column rather than an altitude column. This approach proves useful in global atmospheric studies and applications that consider the atmosphere in terms of pressure, such as large-scale meteorological analyses and reanalysis models, where the atmospheric pressure structure is utilized to describe vapor content in each layer.

Due to the significance of PWV in site characterization and the evaluation of atmospheric conditions for astronomical observations, it is essential to rely on tools that facilitate precise monitoring and analysis. In this context, reanalysis products like MERRA-2 provide high-resolution temporal and spatial data on water vapor content, allowing detailed analysis of its variations in relation to time and atmospheric pressure. Additionally, radiative transfer models such as Scott

Paine's AM model [42] are employed to simulate atmospheric opacity, offering crucial estimates regarding the influence of water vapor on radio astronomical signals under different atmospheric conditions.

The information was studied from Hall and Dowling [28], Braun and Smirnov [16], Elachi and van Zyl [24], Tsidu et al. [51],Wan et al. [54], Salby [49] and [42].

3.12.2 MERRA-2 Reanalysis Atmospheric Data

The Modern-Era Retrospective Analysis for Research and Applications, Version 2 (MERRA-2), developed by NASA's Global Modeling and Assimilation Office (GMAO), delivers atmospheric and climate analyses from 1980 to the present. Its goal is to offer a detailed, continuous view of global climate, addressing limitations in the original MERRA, such as improved aerosol, greenhouse gas, and essential atmospheric variable representations critical for radiation and humidity applications.
MERRA-2 incorporates advanced assimilation techniques, such as the Incremental Analysis Update (IAU), to ensure consistency across temporal data evolution, combined with modern satellite inputs that enhance simulation precision. NASA's GES DISC interface enables near real-time access to multiple specific data collections, including moisture and aerosols, supporting applications in meteorology and global atmospheric studies.

The reanalysis process of MERRA-2 utilizes the GEOS-5 data assimilation model, with a spatial resolution of approximately $0.625° \times 0.5°$ in latitude and longitude (about a 50 km grid). This model encompasses the atmosphere across 72 pressure levels (native grid), distributed on a cubed-sphere structure, providing consistent global coverage—advantageous for studies demanding detailed resolution across atmospheric layers. The 72 levels allow for comprehensive modeling from the surface to the upper atmosphere, offering critical data on humidity, temperature, and other parameters affecting atmospheric dynamics. MERRA-2 also provides data on a 42-level interpolated pressure grid, suitable for studies requiring less vertical detail. Data are organized in various file collections based on research objectives. Each file includes a unique identifier specifying data contents and attributes.

This thesis (Chapter 4) selected two types of files for the OVRO site: M2I3NPASM

and M2IMNPASM, both using the 42-level interpolated pressure grid, denoted "NP". This grid was chosen as it provides atmospheric data at levels closer to OVRO's altitude than the native grid. The "I3" in the first file denotes time-averaged meteorological fields every three hours, whereas "IM" in the second file represents monthly averages. Both files include essential atmospheric variables for this study, particularly specific humidity (QV), which can be converted to PWV by estimating pressure thickness (DELP). The detailed atmospheric data provided by MERRA-2 supply essential configurations for conducting atmospheric simulations over OVRO. The AM model employs MERRA-2 data as a foundation to simulate atmospheric absorption and emission, enabling precise estimates of PWV and other atmospheric parameters impacting astronomical signals.
A more detailed description of this file format and others can be found in the MERRA-2 file specification document [15].

3.12.3 The Atmospheric Model *am*

The atmospheric model AM, developed by Scott Paine [42], is widely used in radio astronomy to simulate the Earth's atmosphere, predicting how it absorbs and emits electromagnetic radiation under various atmospheric conditions. Initially created for studies in the Atacama Desert, home to numerous high-altitude observatories, AM analyzes the effects of water vapor and other atmospheric gases on observations across a wide frequency range, from near-infrared to microwaves.

Some main features of AM include: 1) calculating atmospheric absorption and emission based on temperature, pressure, water vapor concentration, and other gases, providing precise estimates of atmospheric effects on astronomical signals as a function of altitude and local conditions; 2) enabling researchers to input custom atmospheric profiles, like MERRA-2 reanalysis data, allowing tailored simulations that predict real-time PWV and other atmospheric parameters, thus improving observational planning and accuracy; and 3) adjusting to model specific atmospheric conditions with input files that contain detailed profiles of temperature, pressure, and humidity across different altitude levels, making AM ideal for generating detailed absorption profiles in studies on radiotelescope noise and calibration, especially in high-frequency bands sensitive to water vapor content.

AM performs calculations of optical depth, radiative transfer, and refraction

over microwave to submillimeter wavelengths for radiation paths modeled as atmospheric layers or user-defined segments. Since this study of Chapter 4 focuses on Earth's atmosphere, AM applies a hydrostatic equilibrium model. Model layers are treated as hydrostatic, plane-parallel (horizontal strata) layers with boundaries defined in vertical pressure coordinates, as shown in Figure 3.12.2. This hydrostatic model assumes that layer temperatures should be defined at the boundaries, the mass of atmospheric constituents is conserved between pressure boundaries and that absorption coefficients remain constant within each layer.

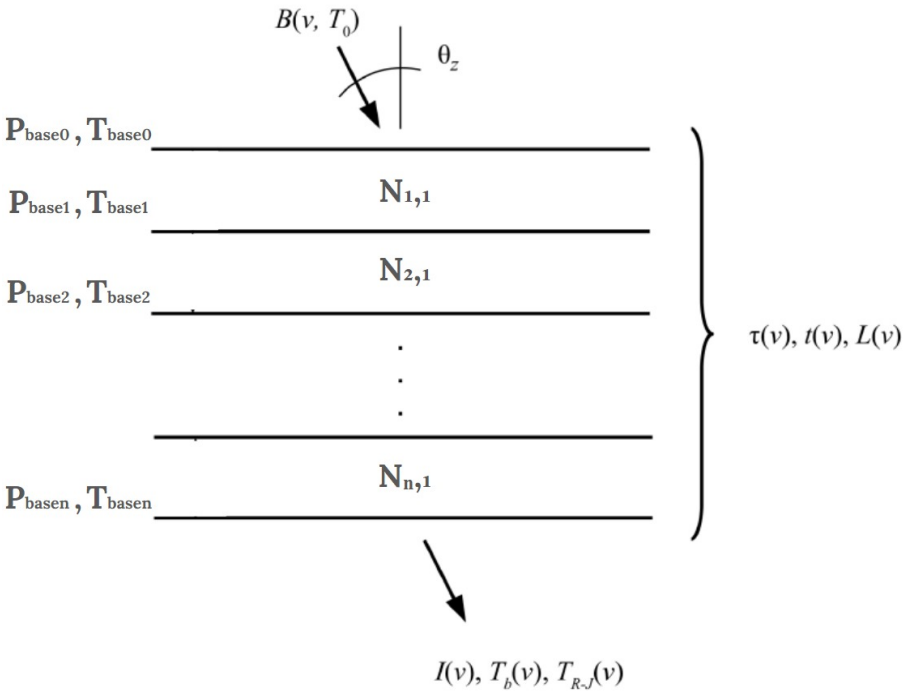

Figure 3.12.2: Hydrostatic model in the AM layer model. The layers in the model represent horizontal strata and are represented by vertical pressure coordinates for the layer boundaries. Layer temperatures are defined using base temperatures. Absorption coefficients are calculated at the layer midpoint temperatures and pressures and are assumed to be constant throughout the layer. (Credit: Modified from Paine [42]).

The atmosphere is parameterized in layers, where each layer acts as a propagation segment with a thickness defined by pressure P. The number of layers depends on the required output precision and the user's computational capabilities. Each layer can contain a mix of absorbing species (molecules) between the layer boundaries,

with the most influential for radio wavelengths being water vapor (H_2O) and ozone (O_3). The amount of each molecule per layer determines its density, allowing for the column density above the observer and at varying zenith angles if needed.
The model simulates key variables of interest, such as atmospheric brightness temperature $T_b(\nu)$, atmospheric opacity $\tau(\nu)$ and atmospheric transmittance $t(\nu)$. The radiative transfer model in AM simplifies calculations by assuming local thermodynamic equilibrium (LTE), meaning molecular collisions maintain the equality of molecular excitation and kinetic gas temperatures. Additionally, multiple scattering is neglected, and radiation is assumed to be unpolarized.
Each layer defines its own opacity, or optical depth $\tau(\nu)$ as the sum of all j column opacities defined in the layer:

$$\tau_i(\nu) = \sum_j \tau_{i,j}(\nu) \tag{3.12.3}$$

The opacity's shape depends on the type of column. Generally, opacity is proportional to the column density product, and for a plane-parallel layer, the secant of the propagation angle is measured through the layer.
Since both temperature and pressure must be considered at layer boundaries, the spectral radiance $B(\nu, T)$ follows the Planck function, as shown in Equation 3.3.3 in the Radiative Transfer section. Notably, under defined conditions, the Planck function varies linearly with optical depth across the layer, known as the linear-in-τ approximation. This allows exact integration of radiative transfer through a layer, resulting in spectral radiance:

$$I_i(\nu) = B(\nu, T_{base_i})p(\tau_i(\nu)) + B(\nu, T_{base_{i-1}})q(\tau_i(\nu)) + I_{i-1}(\nu)e^{-\tau_i(\nu)} \tag{3.12.4}$$

where,

$$p(\tau) = 1 - \frac{1 - e^{-\tau}}{\tau} \quad , \quad q(\tau) = \frac{1 - e^{-\tau}}{\tau} - e^{-\tau} \tag{3.12.5}$$

When $\tau \to \infty$, the optically thick limit, $p(\tau) \to 1$ and $q(\tau) \to 0$, with emergent spectral radiance as, $I_i(\nu) = B(\nu, T_{base_i})$. Conversely, for the optically thin limit $\tau \to 0$, $p(\tau)$ and $q(\tau)$ expand as Taylor series, approximating the effective Planck function as the layer's average Planck functions.

Radiative transfer calculations through all layer stacks proceed iteratively. AM's

default propagation is top-down, from layer 1 to the base. Spectral opacity $\tau_i(\nu)$ is first calculated for each layer (Eq. 3.2), initializing spectral radiance as $I_0(\nu) = B(\nu, T_0)$. Equation 3.12.4 then sequentially applies across layers to compute emergent spectral radiance $I(\nu) = I_n(\nu)$ and total optical depth or opacity by summing all $\tau_i(\nu)$ values.

Spectral radiance and opacity can produce several output spectra such as the brightness temperature $T_b(\nu)$, and the transmittance $t(\nu)$, which are of interest in this thesis along with opacity $\tau(\nu)$, although the model can also produce the Rayleigh-Jean temperature $T_{R-J}(\nu)$ and the excess propagation delay $L(\nu)$.
The spectral brightness temperature $T_b(\nu)$, derived from Planck's blackbody radiance $B(\nu, T)$ (Eq. 3.3.3) with $I(\nu) = B(\nu, T)$, is:

$$T_b(\nu) = \frac{h\nu}{k \ln\left(1 + \dfrac{2h\nu^2}{c^2 I(\nu)}\right)} \tag{3.12.6}$$

At frequency ν, $T_b(\nu)$ corresponds to the temperature at which a perfect blackbody emits spectral radiance $I(\nu)$. In configuration and output files, $T_b(\nu)$ is called Planck brightness temperature with the symbol Tb.
Another variable of interest is transmittance $t(\nu)$ a measure of the atmosphere's ability to allow electromagnetic radiation to pass through without significant absorption or scattering. Also, it is generally used to evaluate the atmospheric performance of astronomical sites. This parameter is derived from spectral opacity $\tau(\nu)$:

$$t(\nu) = e^{-\tau(\nu)} \tag{3.12.7}$$

In the atmospheric study of OVRO discussed in Chapter 4, the atmosphere serves as a blackbody covering the COMAP antenna's main lobe. MERRA-2 reanalysis data, specifically for the site at a given day and time, serves as input parameters for AM, yielding zenithal brightness temperature and simulated zenithal atmospheric opacity over COMAP's frequency range. The simulated zenithal brightness temperature calibrates COMAP skydip power data to brightness temperature at different elevation angles. The brightness temperature undergoes an exponential fit, as presented by Cortés et al. [22], providing OVRO's zenithal opacity. Simulated and calculated opacities are then compared to validate MERRA-2 data as reliable for radio astronomical site characterization.

Chapter 4

Radiometric and Atmospheric Study for OVRO at COMAP frequencies

This chapter presents a detailed analysis of calibration approaches relevant to the COMAP project, focusing on both instrumental and observational factors that influence the detection of the astronomical signal of interest. Instrumental factors are examined through an evaluation of receiver performance by analyzing specific sky scans conducted by the radio telescope on particular dates and times. Section 4.2 includes the study parameters such as T_{Rx}, T_{sys}, T_{min}, aperture efficiency, and Allan variance. Conversely, observational factors are addressed through an atmospheric evaluation centered on the OVRO site, where the COMAP project was developed. The goal is to understand the atmospheric impact on the data acquired by the radio telescope. Since the COMAP receiver is specifically designed to measure carbon monoxide (CO) signals and is not equipped to derive atmospheric variables, this instrument cannot conduct direct atmospheric studies. To address this limitation, Section 4.3 presents the validation of MERRA-2 atmospheric data (Section 3.12.2) using COMAP skydip power data for specific dates and times. This approach facilitates the use of MERRA-2 database at OVRO and other sites of radio astronomical interest.

4.1 Presentation of COMAP Data

To analyze the performance of the receiver, the study examines six Level-1 telescope scans conducted on different dates and times: obsid4386, obsid6863,

obsid8899, obsid8983, obsid10611, and obsid11582. Table 4.1.1 provides a general description of these scans, including the observation numbers and the corresponding observational targets. Two scans focus on co7, corresponding to the second patch of the HETDEX spring field. Two others are dedicated to radio sources used as calibrators, such as the planet Jupiter and the Cygnus A elliptical galaxy. An additional scan targets the North Celestial Pole (NCP), while another conducts a general sweep of the sky, varying elevation angles. Column 3 shows the scan types representing the radio telescope's motion during the observations. These include a skydip or continuous elevation sweep, a circular scan, two raster scans, a Lissajous pattern, and a stationary scan (Figure 4.1.1). Column four details the elevation angle ranges covered by the radio telescope's motion (Figure 4.1.2), and column five presents each scan date and time.
The analysis includes receiver temperature, system temperature, and sensitivity for all scans. The aperture efficiency evaluation is limited to obsid10611, while the Allan variance calculation applies exclusively to obsid11582.

Table 4.1.1: Basic information for COMAP five scans. The identification number, observed source, scan type, elevation angle, and observation date are presented.

obsid	Target	Scan Type	Elevation (degrees)	Date start time - end time
4386		ambient load, sky dip, ambient load in	30 to 87	2019-03-25 14:18:49 - 14:26:47
6863	co7	circular scan, T_{sys}	52.2 to 63.7	2019-07-13 20:32:04 - 21:36:25
8899	Cyg A	raster, T_{sys}, engineering test	55.0 to 59.1	2019-11-06 21:51:42 - 22:07:41
8983	co7	Lissajous, T_{sys}	60.9 to 69.7	2019-11-10 13:32:07 - 14:39:16
10611	Jupiter	raster, T_{sys}	26.1 to 28.3	2020-01-19 17:22:37 - 17:37:02
11582	NCP	stationary, T_{sys}	37.34 to 37.55	2020-02-29 11:09:42 - 12:11:35

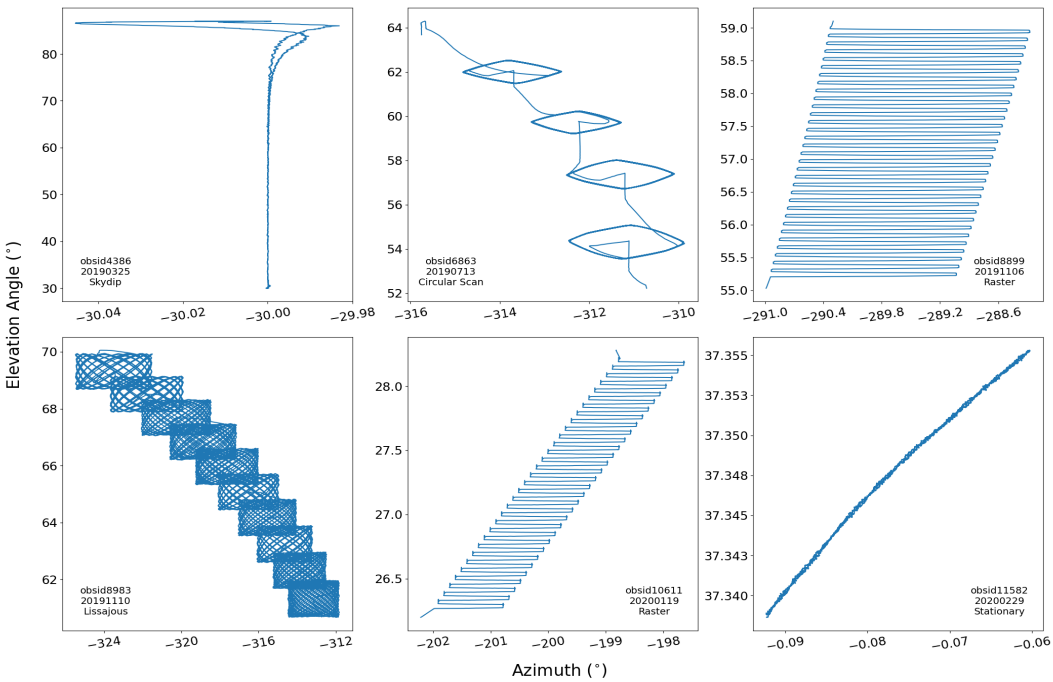

Figure 4.1.1: Six types of scans from separate observations on different dates, as detailed in Table 4.1.1, are presented. Each panel's bottom displays the observation ID, date, and scan type

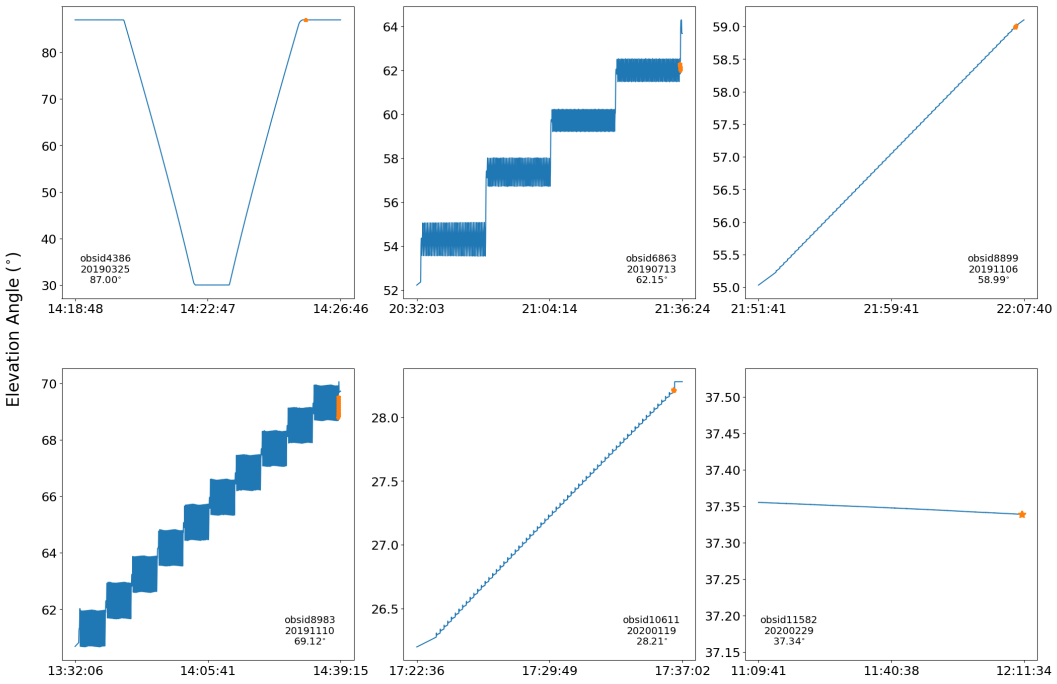

Figure 4.1.2: The elevation angles for each analyzed scan are shown. Orange sections indicate the selected elevation angle used for simulating sky brightness temperature via the AM model. The observation ID, date, and chosen elevation angle are noted at the bottom of each panel

4.2 COMAP Receiver Performance Evaluation

4.2.1 Receiver Temperature

An effective method for evaluating the instrumental impact on data involves analyzing the receiver temperature. This parameter is determined using the Y-factor technique (Equation 3.11.1), which relies on calibrators with established temperatures. Each calibrator is associated with a specific power level when presented to the COMAP receiver. As previously discussed, the COMAP system employs two calibration sources: the sky and an ambient temperature calibration load. In an ideal scenario, when the sky serves as the calibrator, the telescope should ideally point towards the zenith or as close to it as possible. However, in practice, this ideal scenario is not strictly followed. COMAP calibrations are typically conducted by measuring the calibration load at the start and end of the observation while viewing the sky without pointing the radio telescope directly at the zenith, as demonstrated by the elevation angle ranges in Table 4.1.1 and graphically in Figure 4.1.2.

The methodology employed to analyze the COMAP data and derive the receiver temperature is detailed below. For illustrative purposes, the explanation focuses on a single pixel, spectral channel, and band within a specific file; however, the same procedure is systematically applied across all pixels, channels, and bands in the complete dataset. The upper panel of Figure 4.2.1 displays the power associated to spectral channel 500 for pixel 1 across the four bands for obsid10611. Pixel 1 is located in the center of the array (Figure 2.1.1), and the channel has a different frequency depending to the band: 27.025 GHZ for A:LSB band, 28.975 GHz for A:USB, 31.025 GHz and 32.975 GHz for B:LSB and B:USB band, respectively. The bottom panel illustrates the calibration status during the scan: status 0.0 signifies that the calibration load does not cover the feeds represented by brown dots (Left Panel of Figure 4.2.2), status 1.0 indicates full coverage by the load shown in yellow dots (Right Panel of Figure 4.2.2), status 2.0 reflects the load moving toward the feeds in green dots, and status 3.0 corresponds to the load departing from the feeds in red dots. A distinct alignment between the calibration status and the power behavior is observed. Specifically, when the calibration status progresses from 0.0 to 2.0, indicating the movement of the calibration load toward the array, a pronounced and rapid increase in power is observed uniformly

across all bands. In contrast, as the status transitions to 3.0, corresponding to the departure of the load from the array's field of view, the power exhibits a marked and abrupt decline. Subsequently, at status 0, the array resumes its observation of the sky.

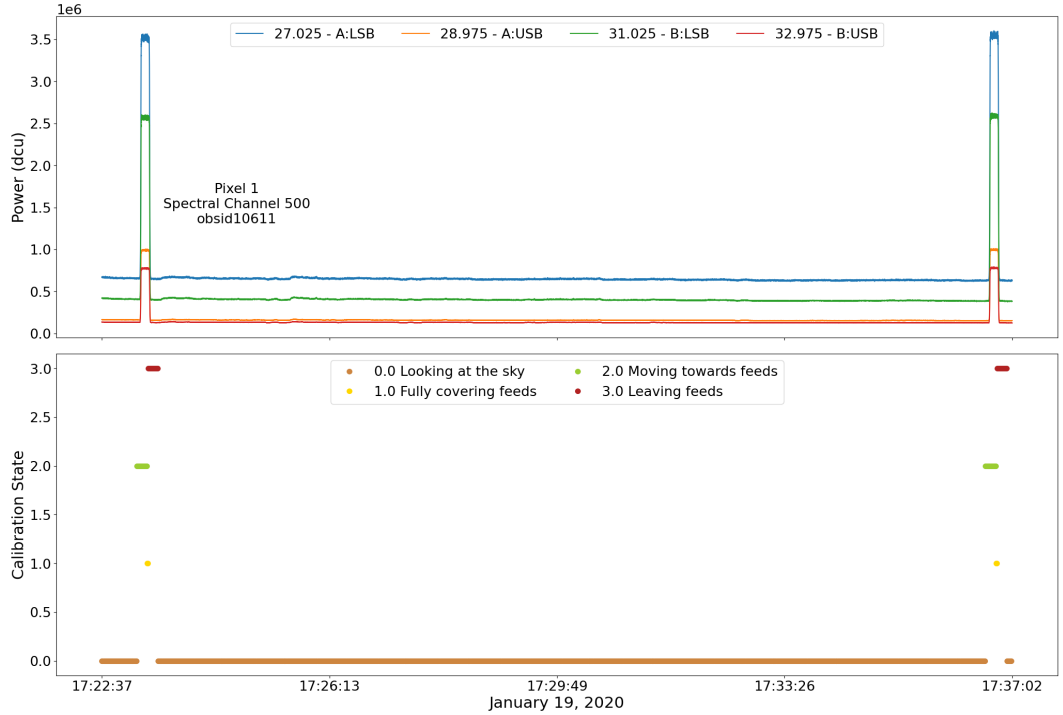

Figure 4.2.1: The upper panel presents the power measured for pixel 1 of spectral channel 500 across the four bands for obsid10611. The lower panel shows the calibration status recorded during the calibration process, corresponding to the same dataset.

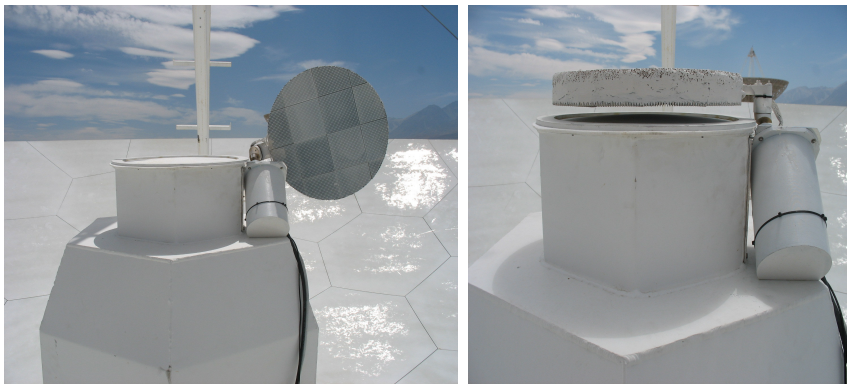

Figure 4.2.2: The calibration load is mounted on the side of the COMAP receiver. The left panel illustrates the load positioned outside the field of view of the 19-pixel array (calibration state 0.0), while the right panel displays the load placed in its calibration position (calibration state 1.0).

There are some channels, such as 1, 513, and 1024 are excluded[1] from the analysis because the power of these channels in some pixels does not respond as expected.

1.- Power associated with the calibrators. The COMAP calibration load consists of Radar Absorbing Material (RAM) tiles maintained at ambient temperature. The load is mounted on the receiver side of the telescope antenna and is painted white, as depicted in Figure 4.2.2. The calibration load data are referred to as *vane* in the *HK* group in the COMAP dataset. Figure 4.2.3 provides an enlarged view of the upper panel of Figure 4.2.1, and so is the power of the second calibration process of pixel 1 for the spectral channel 500 in the four bands for obsid10611.

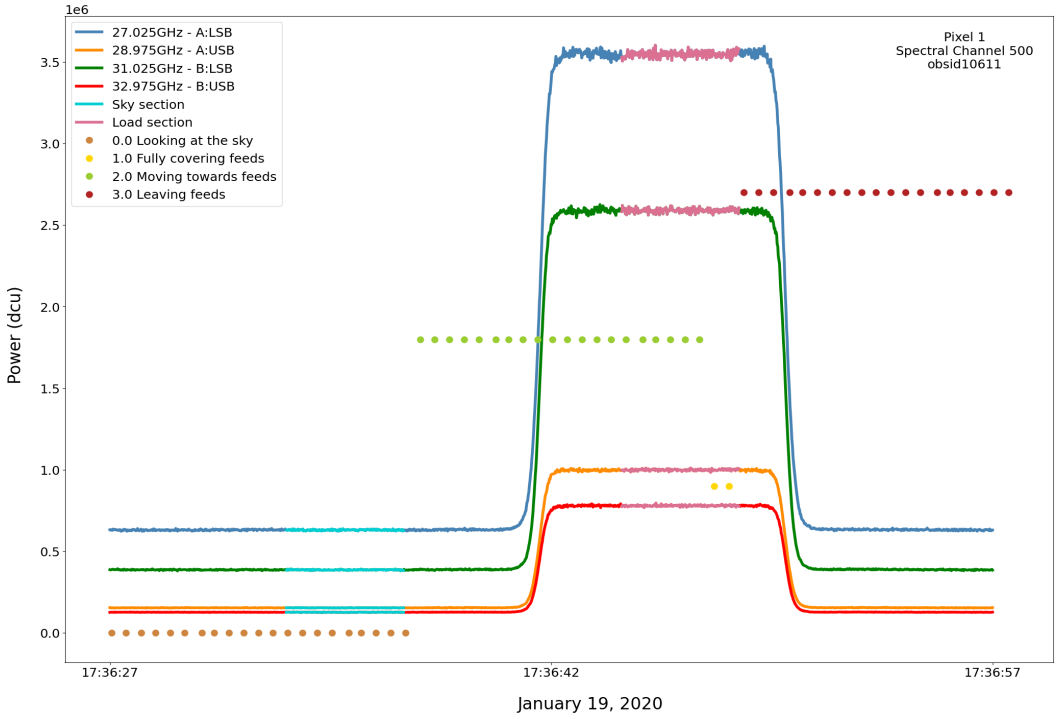

Figure 4.2.3: An enlarged view of the power during the second calibration process is presented for pixel 1 across all four bands of spectral channel 500 from the obsid10611 scan. Simultaneously, the calibration states (0.0, 1.0, 2.0, and 3.0) are plotted to illustrate the variations in power observed during calibration. Yellow and green markers indicate calibration states 1.0 and 2.0, respectively, which were utilized to select the load power sections depicted as pink regions in the curves for each band. The sky power sections, corresponding to calibration state 0.0, are represented by light blue points, with brown markers denoting the calibration state reference.

[1]Excluded frequencies 26.001953GHz, 26.9998047GHz, 28.GHz, 29.001953GHz, 29.998047GHz, 30.001953GHz, 30.998047GHz, 32.GHz, 33.001953GHz, and 33.998047GHz.

The calibration states previously introduced in the lower panel of Figure 4.2.1 are superimposed onto the power. The changes in power are more clearly observed here, particularly when the load approaches the receiver at the green points and when it moves away at the red points. Additionally, it is evident that the load power stabilizes before the load reaches its position in front of the array, as indicated by the yellow points. To select the section of load power to be used in the analysis, the stabilization of the load's power will be utilized in both state 1.0 and part of state 2.0, as shown in the pink section. This section will be averaged to derive a single load power value, referred to as P_{load}. The A:LSB band is chosen to display the T_{rx} calculation. Therefore, the load average power for pixel 1 in spectral channel 500 for that band is $P_{load}^{A:LSB} = 3547093.8$ dcu.
When the sky is used as a calibrator, the power is selected based on calibration state 0.0, represented by the brown points in Figures 4.2.1 and 4.2.3. Since the scan obsid10611 was performed within an elevation range of 26° to 28° (Table 4.1.1), a segment corresponding to the highest elevation, 28°, has been chosen. This section is depicted in orange in Figure 4.1.2 and, for this file, is located in the central panel of the second row. Table 4.2.1 shows the choice of elevation angles chosen for each scan in column 3. Once the elevation angle within the scan is determined, it is associated with the power measured when the array observes the sky. This power is represented by the light blue section in Figure 4.2.1. The chosen section will be averaged to derive the value of the sky power, which will be referred to as P_{sky}. Therefore, the sky average power for pixel 1 in spectral channel 500 for the A:LSB band is $P_{sky}^{A:LSB} = 630304.8$ dcu.

3.- Obtain Y-factor (Y). The Y-factor is calculated by dividing the power data of the load by that of the sky, as defined in Equation 3.11.1. For pixel 1, at spectral channel 500 within the A:LSB band, corresponding to obsid10611, the computation yields:

$$Y^{A:LSB} = \frac{P_{load}^{A:LSB}}{P_{sky}^{A:LSB}} = \frac{3547093.8\, dcu}{630304.8\, dcu} = 5.627585 \tag{4.2.1}$$

This method is consistently applied across all pixels, spectral channels, and frequency bands for every scan.

4.- Determine the Calibrators Temperatures. 1) Calibration load. Upon determining the position of P_{load}, it is linked to the load temperature recorded as

T_{vane} corresponding to sensors embedded in the load, which is mounted on the side of the receiver (Figure 4.2.2). The load temperature, T_{load}, is then derived from T_{vane} using Equation:

$$T_{load}\,(K) = \frac{T_{vane}}{100} + 273.15 \tag{4.2.2}$$

Figure 4.2.4 illustrates the variation of the load temperature throughout the entire obsid10611 scan. The orange markers specifically represent the temperature data corresponding to the same position as the load power. This dataset is utilized to compute the average calibration load temperature, yielding $T_{load} = 275.32$ K for the obsid10611. Table 4.2.1 provides the load temperature values for all six scans in the second column. Note that T_{load} is unique for all bands.

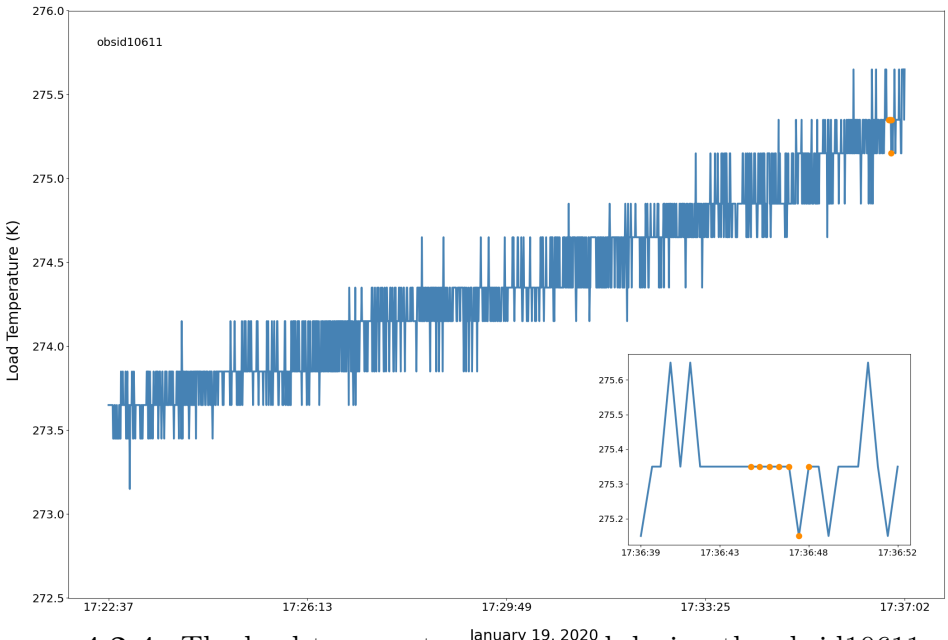

Figure 4.2.4: The load temperature measured during the obsid10611 scan is depicted. Orange markers denote the selected load temperature, which is correlated with the load power.

2) Sky as calibrator. Precise determination of sky temperature depends on frequency, atmospheric air mass, spillover contribution, and atmospheric conditions. It is defined as follows:

$$T_{SKY}(\nu,\theta) = T_{CMB} + T_{SP}(\nu,\theta) + T_{ATM}(\nu,\theta) \tag{4.2.3}$$

where $T_{CMB} = 2.73$ K represents the cosmic microwave background (CMB), while

$T_{SP}(\nu, \theta)$ accounts for spillover effects as a function of frequency and elevation angle. At lower elevation angles, the interaction with secondary lobes intensifies, increasing its contribution to the observed temperature. Meanwhile, $T_{ATM}(\nu, \theta)$ denotes the atmospheric brightness temperature, which quantifies the atmosphere's impact on the observed signal.

The atmospheric contribution to sky temperature depends on frequency, and is influenced by air mass variations with elevation angle, expressed as $am = 1/\cos(90 - \theta)$. At zenith ($\theta = 90$), air mass is minimized ($am = 1$), leading to the lowest atmospheric contribution to received power. At lower elevation angles, increased air mass extends the optical path of incident radiation, enhancing interactions with the atmosphere and raising its impact on the registered temperature. Moreover, temporal factors such as observation date and time must be considered, as atmospheric water vapor significantly affects brightness temperature. As observed at the OVRO site, where COMAP operates, atmospheric brightness temperature varies throughout the day and across seasons due to fluctuations in water vapor content, precluding its treatment as a constant parameter.

Before proceeding, it is important to clarify that the explicit derivation of sky brightness temperature and spillover contribution will be addressed in the next section titled "Validation of MERRA-2 Data Through COMAP Skydip Measurements" (Sections 4.3), while in this section, only the results will be applied directly. The simulation of $T_{ATM}(\nu, \theta)$ is derived from the AM radiative transfer model utilizing data from the MERRA-2 atmospheric database (described in Sections 3.12.2, 3.12.3 and analyzed in Section 4.3.1). Initially, the sky temperature used as a calibrator was assumed to correspond to a 7 K contribution across COMAP's entire spectral range, originating from the atmosphere and the CMB, without considering spillover. The results obtained in Section 4.3 validated the use of the AM radiative transfer model within COMAP's frequency range, providing more accurate spectral channel and elevation angle values for $T_{ATM}(\nu, \theta)$ compared to previous estimations. The modeling considers the day, time, and elevation angle corresponding to each scan. Figure 4.2.5 depicts the simulated atmospheric brightness temperature using the AM radiative transfer model for all analyzed scans, applying the elevation angles listed in column four of Table 4.1.1. As expected, the simulated curve varies both in shape and magnitude as a function of the PWV corresponding to the day and time of the scan.

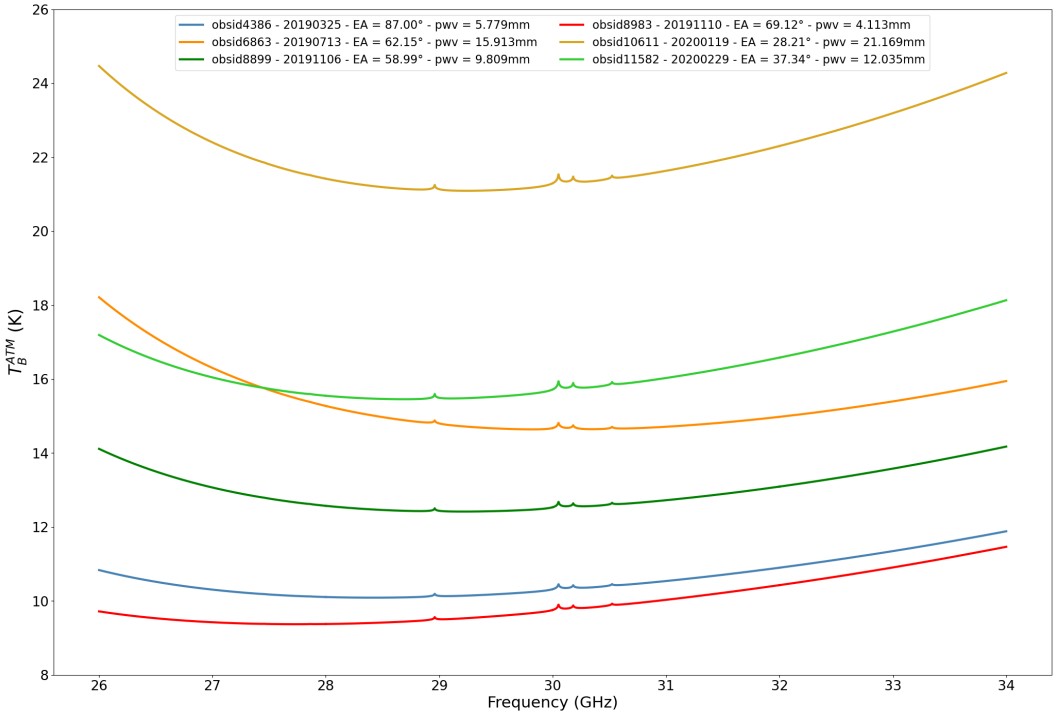

Figure 4.2.5: Simulated brightness temperature from AM model and its respective precipitable water vapor value.

As expected, the simulated curve varies both in shape and magnitude as a function of the PWV corresponding to the day and time of the scan. A direct relationship exists between the simulated temperature and PWV, such that an increase in one results in a proportional rise in the other and vice versa. Furthermore, the temperature slope at lower frequencies, ranging from 26 to 28 GHz, becomes increasingly pronounced due to the influence of the water line at 22 GHz, particularly when the PWV reaches higher values. Lastly, peaks near 29 and 30 GHz are identified, corresponding to the presence of the ozone molecule. The spillover value, obtained from an exponential model defined by Equation 4.3.13, is derived from the calibration of power data converted to temperature units, as detailed in Section 4.3.3. This model accounts for spillover contributions at elevation angles between 30° and 86.5°, referencing the 6 K value at zenith reported by Lamb et al. [34]. The resulting spillover temperature, specified in column 4 of Table 4.2.1, is evaluated at the elevation angle listed in column 3. The integrated application of both models within the procedure for determining the sky temperature as a calibrator ensures a more accurate and robust characterization of COMAP's system behavior.

Table 4.2.1: Relevant information used to calculate T_{rx}. The columns corresponding to the scan identification number (obsid), the load temperature (T_{load}), the spillover temperature (T_{SP}) calculated from the spillover model, and the mean elevation angle used in the T_{ATM} simulation and T_{SP}.

obsid	Load Temperature (K)	Spillover Temperature (K)	Mean Elevation Angle (degrees)
4386	273.15	5.99	87.0
6863	343.15	6.46	62.154
8899	292.15	6.56	58.990
8983	267.21	6.27	69.119
10611	275.32	8.76	28.212
11582	272.89	7.79	37.338

5.- Evaluate Receiver Temperature (T_{Rx}). The receiver temperature for pixel 1, at spectral channel 500 in the A:LSB band corresponding to frequency 27.025 GHz, derived from observation obsid10611, is determined using $T_{load} = 275.32$ K, associated with P_{load} for this observation. The T_{sky} value, equal to 31.13 K, is obtained as the sum of $T_{ATM} = 22.37$ K, corresponding to spectral channel 500 in the simulated yellow curve in Figure 4.2.5, and $T_{SP} = 8.76$ K, specific to the same observation. Incorporating these along with $Y = 5.627585$ from Equation 4.2.2 into Equation 3.11.5 produces:

$$\begin{aligned} T_{Rx}^{A:LSB} &= \frac{T_{load} - Y \cdot T_{sky}}{Y - 1} \\ &= \frac{275.32\ K - 5.627585 \cdot 31.13\ K}{5.627585 - 1} \\ &= 21.64\ K \end{aligned} \tag{4.2.4}$$

The same approach is employed to evaluate the receiver temperature for all pixels, spectral channels, and frequency bands in the dataset.

For the calculation of T_{Rx}, the 19 pixels from the obsid6863 and obsid4386 scans are considered. However, for the remaining scans, pixels 18 and 19 are excluded since, across all spectral channels in the four bands, these pixels exhibit significant noise and fail to respond either to sky scans or calibration procedures. It should also be

noted that spectral channels 1, 513, and 1024 are omitted because they produce spectral peaks across all bands, are common to all pixels, and are associated with the DC component and its Nyquist alias (Lamb et al. [34]). The receiver temperature is determined for the remaining pixels and spectral channels across all analyzed scans, and the results are presented in the histogram of Figure 4.2.6.

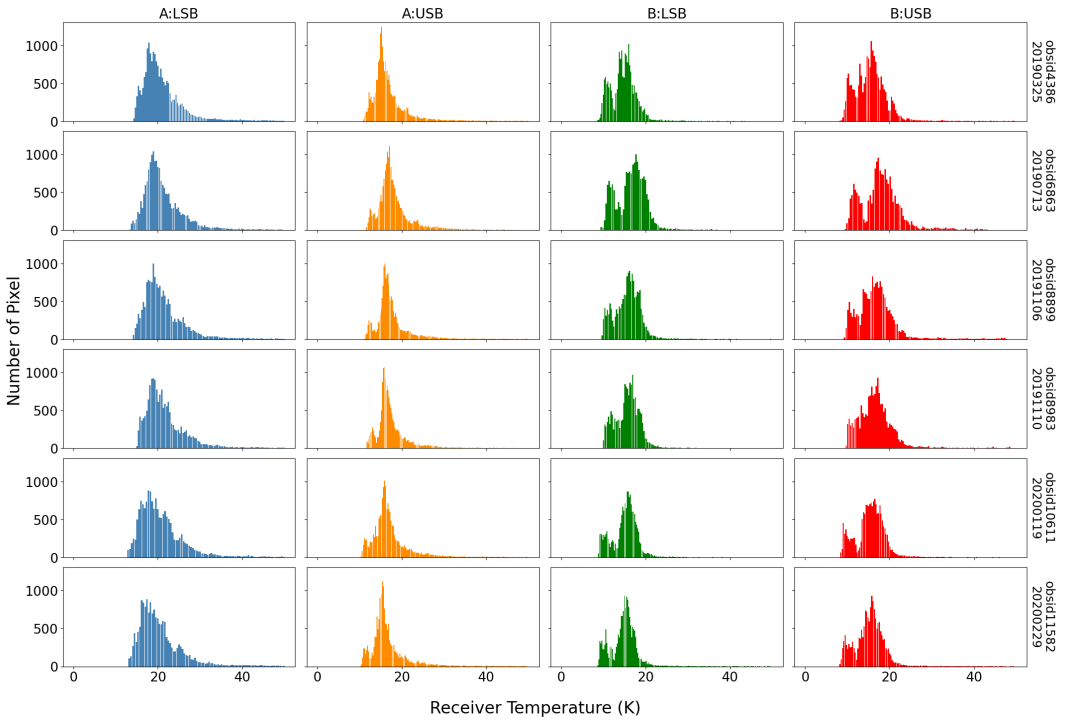

Figure 4.2.6: Histograms of the receiver temperature per band are displayed without averaging the spectral channels for each analyzed file. Each row corresponds to a specific scan, and each column represents a spectral band corresponding to the COMAP frequencies.

This histogram displays T_{Rx} values constrained between 0 and 50 K. The right vertical axis specifies the analyzed scans alongside their corresponding observation dates, while the left vertical axis specifies the total count of spectral channels corresponding to each interval of T_{Rx} values, illustrating the absolute frequency of these occurrences. The upper horizontal axis illustrates the four frequency bands employed by COMAP. For Band A, the histogram exhibits a well-defined bell-shaped distribution when considering all scans. The mean in the LSB band ranges from 20.53 K to 22.08 K, whereas the mean in the USB band spans from 16.94 K to 19.00 K. In contrast, Band B demonstrates a more pronounced peak alongside a smaller peak evident across all scans at lower T_{Rx} values. An analysis

of the power corresponding to the pixels and spectral channels exhibiting this behavior revealed no erratic power fluctuations (further information should be reviewed in related papers). Considering the more prominent peak, the mean in the LSB band ranges from 14.84 K to 17.15 K, while for the USB band, it spans from 15.35 K to 18.53 K.

Figure 4.2.7 presents the histogram of receiver temperature based on the analysis of six scans. The assessment indicates that 95% of the T_{Rx} values fall within the range of 10 to 31 K, with a mean of 17.7 K. These results align closely with those reported by Foss et al. [25], who documented T_{Rx} values between 10 and 30 K. Appendix B called "COMAP Performance Receiver" provides the receiver temperature across the entire spectral frequency range of COMAP for each individual scan.

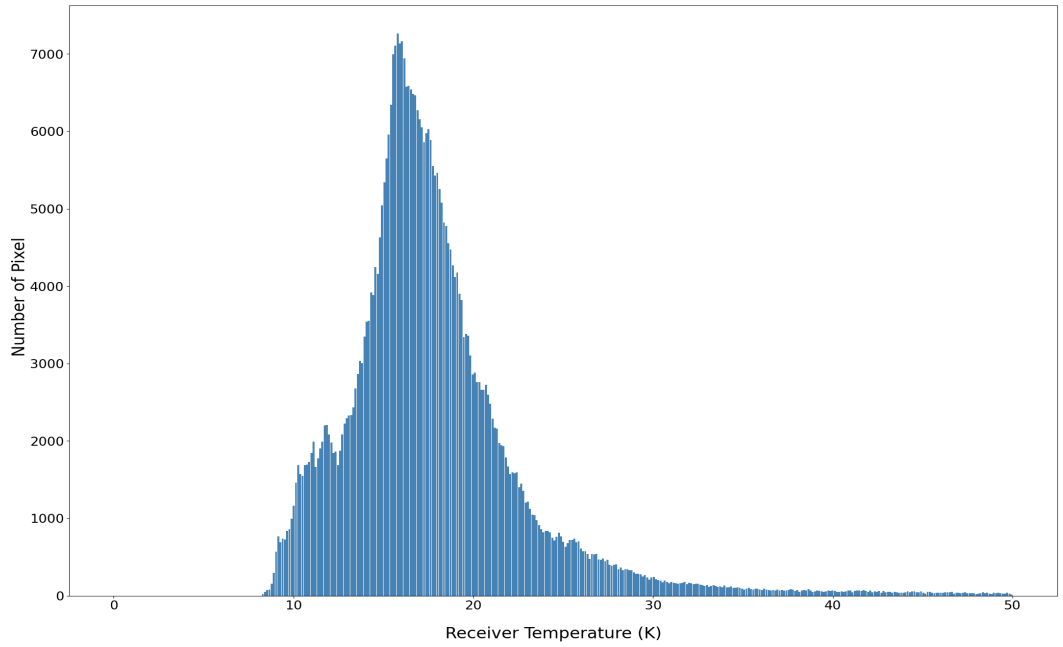

Figure 4.2.7: Receiver temperature histogram per spectral channel and per band, including the six scans.

4.2.2 System Temperature

The system temperature, T_{sys}, is determined using Equation 22 from O'Neil [40], derived from the mathematical formulation of the general power equation when observing the sky and a noise source. In that study, the contribution of sky temperature is deemed negligible compared to the noise source, as the latter exceeds T_{sky} by several orders of magnitude. However, in this analysis, T_{sky} is

explicitly incorporated into the calculation of T_{sys}. Consequently, the equation employed to compute T_{sys} is:

$$T_{sys} = \frac{P_{sky}}{P_{load} - P_{sky}} \cdot \Big(T_{load} - T_{sky}\Big) \tag{4.2.5}$$

This expression differs slightly from Equation 23 in Foss et al. [25], where T_{sys} is computed considering only T_{CMB} as T_{sky}. In contrast, the present analysis accounts for T_{sky} as defined in Equation 4.2.3, ensuring a more comprehensive representation of the sky contribution. All parameters required in the equation are already known and were obtained in the previous section 4.2.1. Note that the power values are specific to each pixel and spectral channel across all bands. In contrast, T_{sky}, representing the sky temperature simulated using the AM model, has a distinct value for each spectral channel within every frequency band. Meanwhile, T_{load} remains constant for all pixels and spectral channels in a given band. Following the example described above, the values are substituted in equation 4.2.5 to compute T_{sys} for the spectral channel 500 of pixel 1 in band A:LSB of obsid10611:

$$\begin{aligned} T_{sys}^{A:LSB} &= \frac{630304.8\ dcu}{3547093.8\ dcu - 630304.8\ dcu} \cdot \Big(275.32\ K - 31.13\ K\Big) \\ &= 52.77\ K \end{aligned}$$

In this analysis, the same pixels and spectral channels previously selected for the calculation of T_{Rx} were utilized, maintaining the exclusion criteria already detailed. Figure 4.2.8 presents histograms of the system temperature corresponding to all the scans evaluated in the four frequency bands. The system temperature values were limited to a range of 20 and 70 K after reviewing the T_{sys} temperature graph across the full COMAP spectral range, presented in Appendix B, where the tendency of T_{sys} values is visible. The right vertical axis shows four lines in each row, specifying the analyzed scans, their respective observation dates, the amount of precipitable water vapor (PWV) present at that moment derived from the AM model in the atmospheric brightness temperature simulation, and the respective elevation angle at which the simulation was performed. The left vertical axis shows the total spectral channels per T_{sys} interval, representing the absolute frequency. The upper axis shows the four frequency bands utilized by COMAP. In general, when examining all scans and bands, it is evident that T_{sys} strongly

depends on the PWV present at the time of observation.

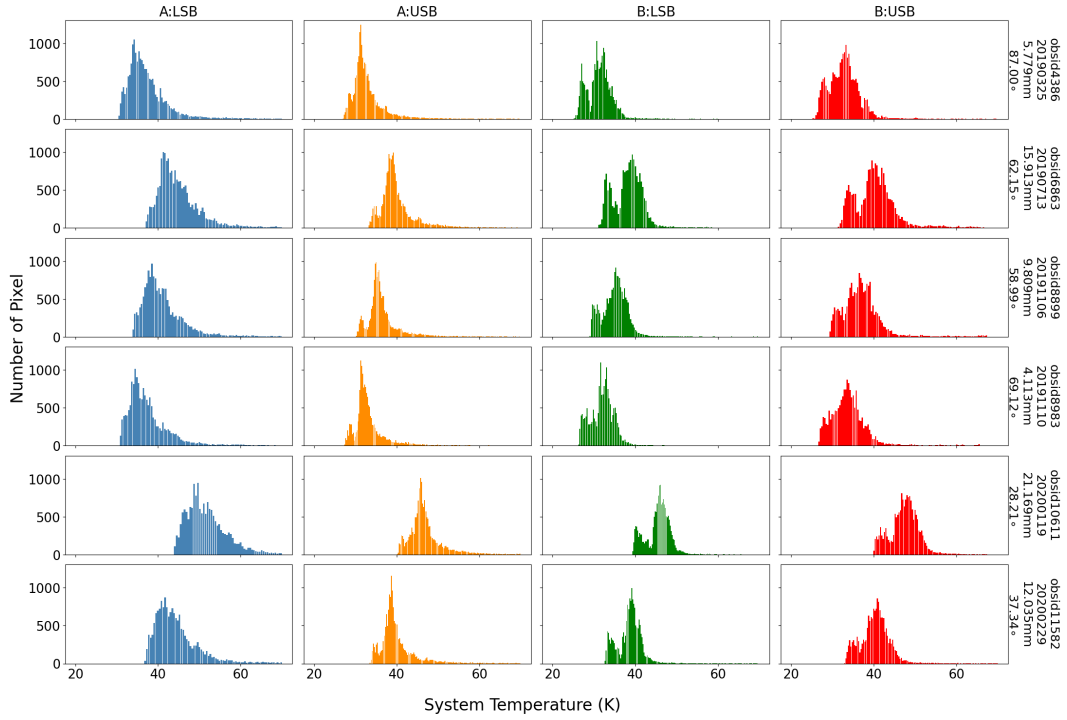

Figure 4.2.8: Histograms of the system temperature per band are displayed without averaging the spectral channels for each analyzed file. Each row corresponds to a specific scan, and each column represents a spectral band corresponding to the COMAP frequencies.

This is evident since the scans with the lowest mean values of T_{sys} correspond to those with lower PWV, and conversely. For instance, the scan identified as obsid8983, located in the fourth row, shows mean values of T_{sys} ranging from 32.23 to 37.70 K in the four bands, with an associated PWV of 4.113 mm. The obsid4386 scan, positioned in the first row, exhibits mean values of T_{sys} between 31.41 and 37.41 K, corresponding to a PWV of 5.779 mm. On the other hand, the obsid10611 scan, located in the fifth row, shows the highest mean values of T_{sys} across all four bands of all scans, ranging from 45.64 and 51.71 K, with an associated PWV of 21.169 mm at the observation time. It is determined that 95% of the T_{sys} data, including all six scans, ranges from 28 to 56 K. This is comparable to the findings of Foss et al. [25], who reported T_{sys} values between 34 and 60 K, with a mean of 44 K. In this analysis, a single mean was not identified due to the influence of PWV on the calibration process.

4.2.3 Sensitivity

The sensitivity is determined using Equation 3.7.1, incorporating the previously calculated system temperature, the COMAP IF bandwidth of 2 MHz, and the evaluation period of 20 ms, which corresponds to the COMAP data recording rate. An example calculation of sensitivity, for a single-pixel receiver, is provided for the spectral channel 500 of pixel 1 in band A:LSB for obsid10611:

$$\begin{aligned}\sigma_{20ms}^{A:LSB} &= \frac{T_{sys}^{A:LSB}}{\sqrt{\Delta\nu \cdot \tau}} \\ &= \frac{52.77\ K}{\sqrt{2 \times 10^6\ Hz \cdot 0.02\ s}} \\ &= 263.85\ mK \end{aligned} \tag{4.2.6}$$

For the COMAP 19-pixel array, the sensitivity is reduced in a factor of 6.57, then $\sigma_{20ms}^{A:LSB} = 40.15$mK. Figure 4.2.9 presents a histogram of sensitivity for all scans across the four frequency bands for a single-pixel receiver. Sensitivity values were constrained between 100 and 400 mK, with the 95% of the data in the range of 165-282 mK.

Clearly, the sensitivity behavior is directly influenced by the system temperature of each scan. To enhance the detection of weak signals, increasing the integration time is effective. For instance, in scan obsid8983, which observes a sky region containing CO for approximately one hour (3600 seconds), with a constant bandwidth and a system temperature of $T_{sys} = 35$ K, the noise uncertainty decreases to $\sigma_{3600s} = 412.48\mu$K, representing a 99.7% reduction compared to σ_{20ms}. In the implementation of the 19-pixel, the sensitivity is $\sigma_{3600s} = 94.63\mu$K, reducing in a factor of 4.36.

To detect the cosmological CO signal, which is around 1μK [25], determining the required observation time is crucial. According to the radiometer equation, a single receiver would necessitate an integration time of $\tau = 6.125\times10^8$s $\approx$ 19 years for a single receiver is required. This time is reduced to 373 days for the 19-pixel array of COMAP. In practice, COMAP data analysis employs frequency bins of $\Delta\nu$ =31.25 MHz [19], broader than the individual spectral channel width of approximately ∼2 MHz. This approach reduces the integration time per receiver to 1.2 years. Furthermore, since COMAP operates as a 19-pixel array, the system's sensitivity improves by a factor of $\sqrt{19} \approx 4.36$, thereby shortening the required

integration time to approximately 24 days.

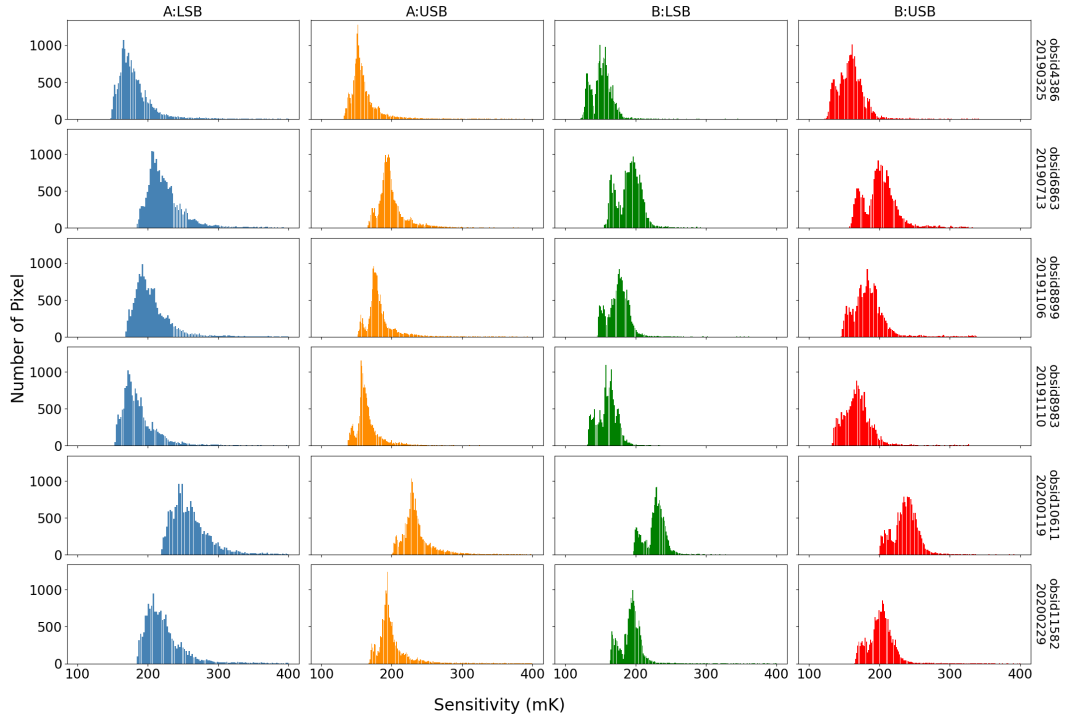

Figure 4.2.9: Histograms of sensitivity per band are displayed without averaging the spectral channels for each analyzed file. Each row corresponds to a specific scan, and each column represents a spectral band corresponding to the COMAP frequencies.

4.2.4 Allan Variance

The Allan variance is an essential tool for assessing signal stability in the time domain. This analysis enables the identification of white noise within specific intervals, allowing for the determination of optimal integration limits and enhancing the quality of radio astronomical observations. The Python library allantools was employed to calculate the normalized Allan variance. The input parameters consist of: 1) the TOD power of spectral channel 500, segmented by band and pixel for the obsid11582 scan, representing a stationary-type observation; and 2) the sampling rate of the COMAP data, set at 20 milliseconds.

Figure 4.2.10 presents a plot of the power of pixel 1 in the A:LSB band. For the analysis, only the power highlighted in orange, located in the embedded graph at the center, is selected. This segment corresponds to the time interval during which the radio telescope observed the sky at an elevation of approximately 37° over

the course of one hour, as recorded in the calibration state data. Two calibration points, one at the beginning and another at the end of the scan, are excluded from the analysis.

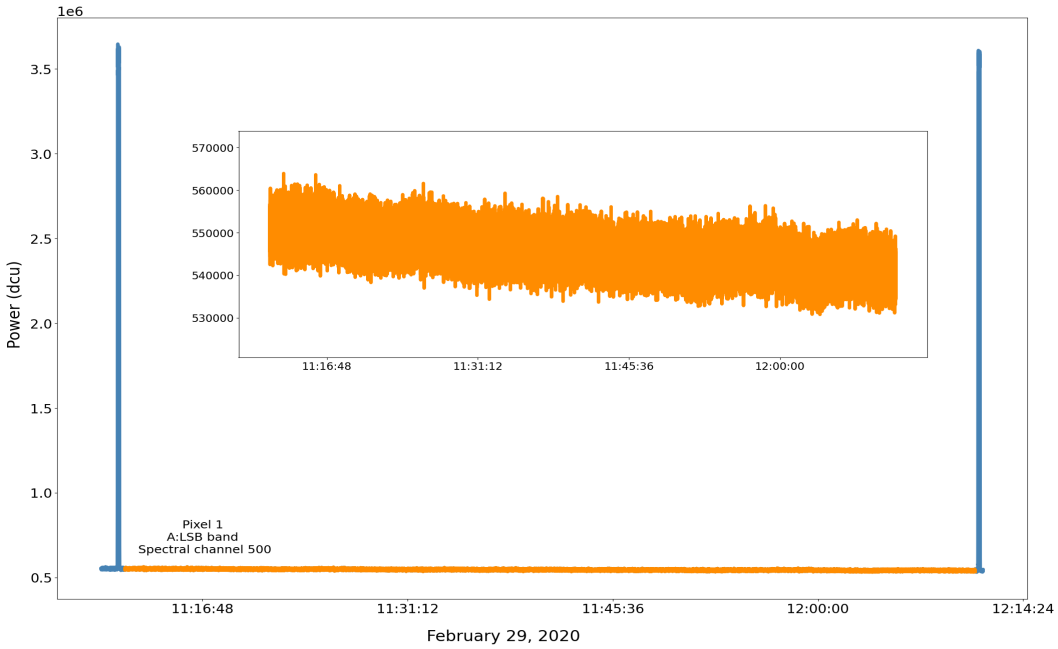

Figure 4.2.10: The power of spectral channel 500 for pixel 1 in the A:LSB band from file obsid11582, which records a stationary observation, is displayed. The section used in the Allan variance analysis is highlighted in orange.

Figure 4.2.11 illustrates the results of applying the normalized Allan variance to the power data from pixel 1 across the four bands. The resulting curves exhibit linear behavior for shorter time intervals. As time increases, the curves adopt a concave shape with a minimum point known as the Allan time, measured in seconds. This parameter represents the interval during which the measurements are influenced exclusively by white noise.
Additionally, alongside the variances, the radiometer equation is presented as a blue line, derived from Equation 1 by Kooi et al. [32]:

$$\sigma = \frac{\langle S(t) \rangle}{\sqrt{B \cdot T}} \tag{4.2.7}$$

In this expression, σ represents the standard deviation of the signal, $S(t)$ corresponds to the analyzed power data, in this case, from spectral channel 500 of pixel 1 across the four bands. The parameter B refers to the IF bandwidth

of COMAP, equivalent to 2 MHz, and T indicates the integration time derived from the Allan variance calculation for each band. The plot displays the radiometer equation exclusively for the A:LSB band, as identical results are obtained for the other bands. The inclusion of the radiometer equation aims to highlight the ideal behavior of the power data under the exclusive influence of white noise. In such a scenario, it would be possible to perform radio astronomical observations with indefinite integration times. In practice, however, the data are continuously subject to additional $1/f$ noise sources. Foss et al. [25] identifies three primary contributors to this noise affecting COMAP: gain variations in the LNA amplifiers, atmospheric fluctuations, and time-dependent standing waves.

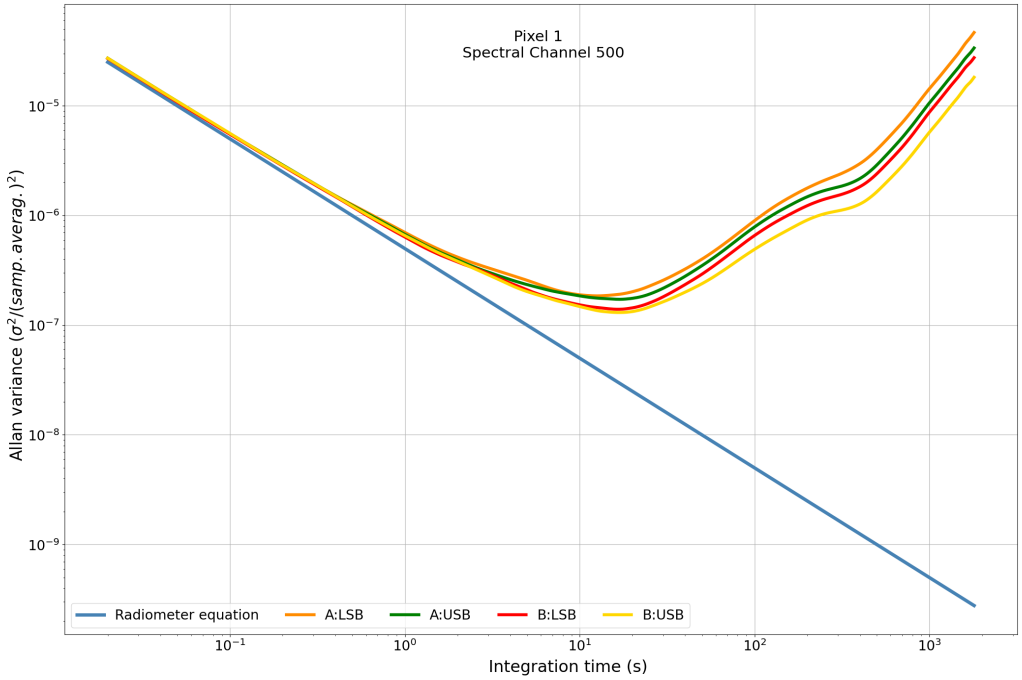

Figure 4.2.11: The normalized Allan variance for the spectral channel 500 of pixel 1 in the four bands is also displayed. The Allan times are 12.44, 16.92, 16.54, and 16.6 seconds for bands A:LSB, A:USB, B:LSB, and B:USB, respectively. The radiometer equation is represented by a blue dashed line.

Figure 4.2.12 depicts the Allan time values for each pixel across different bands for spectral channel 500. The temporal stability of the data ranges between 5 and 22 seconds, confirming the presence of low-frequency noise in all analyzed files. No correlation is observed between pixels or across bands.

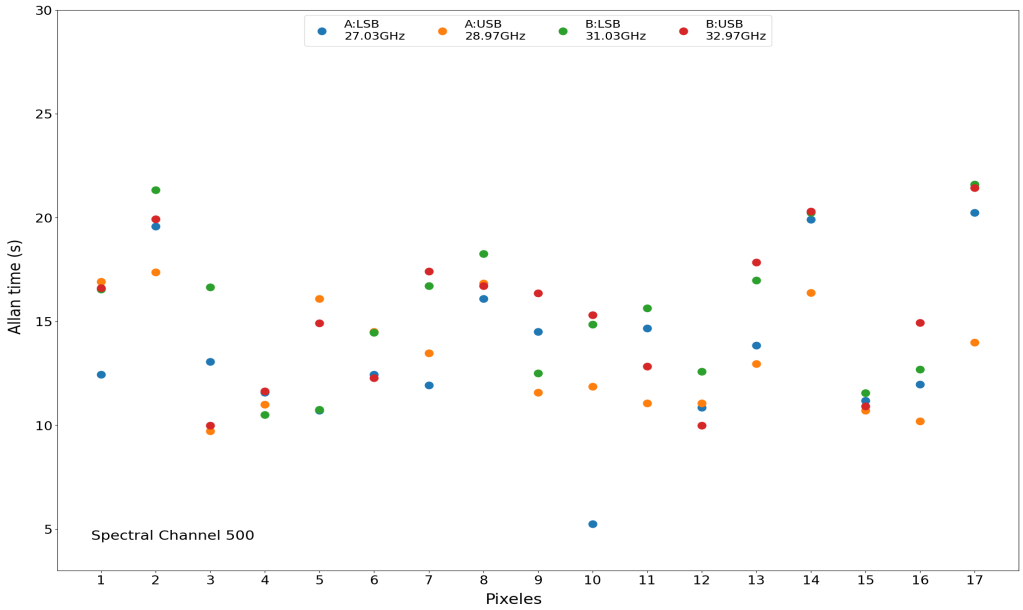

Figure 4.2.12: The Allan time for each pixel and band is presented.

4.2.5 Aperture Efficiency

The method proposed by Woody [57] is subsequently implemented to compute the aperture efficiency (Section 3.10) for all pixels in the obsid10611 scan, corresponding to the observation of planet Jupiter. This method is applied to the central frequencies of COMAP's four bands: 27 GHz, 29 GHz, 31 GHz, and 33 GHz. The procedure is detailed for pixel 1 in the A:LSB band, averaging 1021 spectral channels while excluding channels 1, 513, and 1024. Figure 4.2.13 displays the power of the spectral channels considered for this pixel in that band, with a selected time interval between 17:29:10 and 17:30:22 UTC containing Jupiter's data, which are used for the analysis. Averaging the spectral channels reduces measurement noise and enhances the visibility of Jupiter's power peaks, as shown in the embedded graph within the figure. After averaging, six peaks corresponding to Jupiter are identified, significantly influenced by variations in gain. For this reason, Woody's method proves to be an effective choice for determining aperture efficiencies, as each peak is calculated individually while disregarding gain variations. The procedure for determining the aperture efficiency (η) is described as follows:

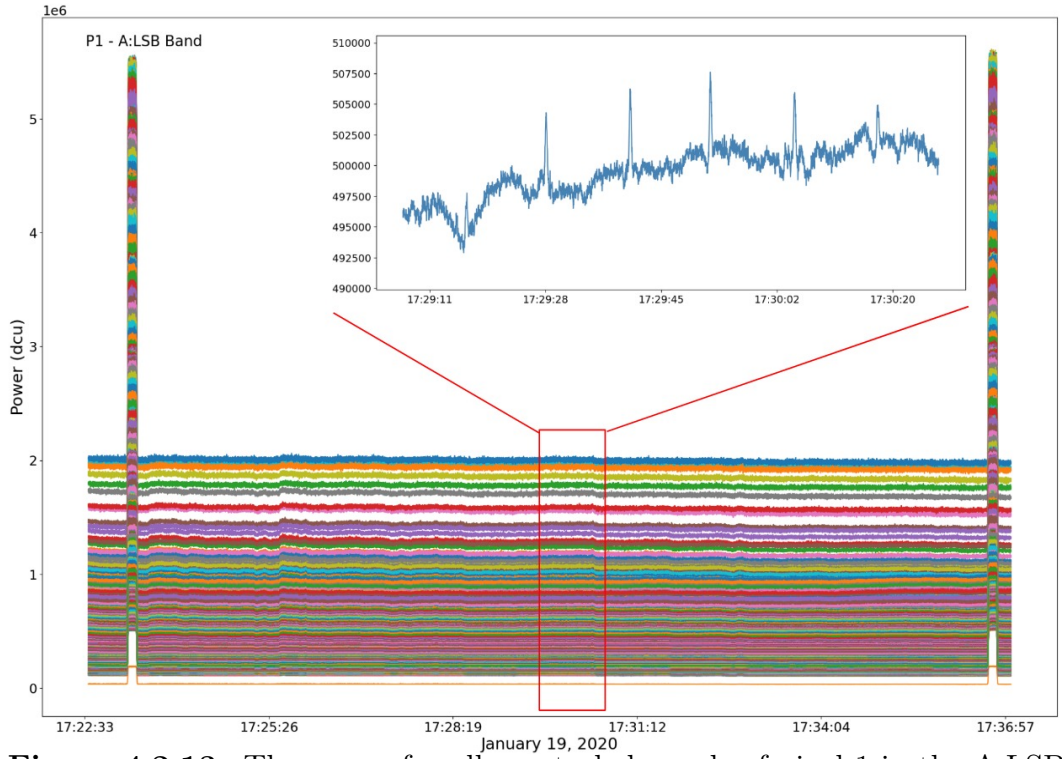

Figure 4.2.13: The power for all spectral channels of pixel 1 in the A:LSB band of the obsid10611 scan is shown. The section of Jupiter peaks is presented in the embedded graph, which was obtained by averaging the spectral channels to minimize noise and increase peak size.

1.- Determine the antenna temperature of Jupiter (T^J_{ant}). This parameter is calculated using Equation 3.10.4, which employs the power of Jupiter (P^J_{on}), recorded when the radiotelescope performs a sweep over the planet. It also utilizes the sky power (P^J_{off}) measured immediately before and after the radiotelescope's transit over Jupiter, as well as the system temperature (T_{sys}).

The T_{sys} was already estimated in Section 4.2.2 for each spectral channel of every pixel across the four bands, considering all scans. However, for this evaluation, the spectral channels are averaged by band, resulting in four T_{sys} values per pixel. Specifically, for pixel 1, the calculated values are 55.32 K for the A:LSB band, 47.99 K for the A:USB band, 43.23 K for the B:LSB band, and 46.63 K for the B:USB band. According to powers, although there are six Jupiter power peaks for pixel 1 in the A:LSB band, the T^J_{ant} analysis will include only the four most prominent peaks, which correspond to the central ones shown in Figure 4.2.14. These peaks are selected because they offer the highest possibility of achieving better aperture efficiency. The orange peaks correspond to Jupiter's power, and the green-light data refer to the sky's power used for the calculation.

Figure 4.2.14: Power section contains Jupiter data of pixel 1, A:LSB band from obsid10611 file is shown. Jupiter's section is shown in the orange line, and the sky's section is illustrated in the light green line.

The T^J_{ant} calculation is performed individually for each peak. Consequently, the procedure to determine the power values for Jupiter and the sky is presented for a single peak, specifically the third one in Figure 4.2.14, with the understanding that the same method applies to the remaining peaks. Figure 4.2.15 displays Jupiter's data points in orange, fitted to a Gaussian function represented by an orange line. The green marker indicates the maximum value of the Gaussian fit, which provides the most accurate representation of Jupiter's power, P^J_{on}. The blue points correspond to sky power data, adjusted with a linear function depicted by a blue line. The chosen sky power, P^J_{off}, marked in red, matches the sky power value at the same time position as P^J_{on}. It is essential to note that using only one section of sky power data: either to the left or right of the Jupiter peak, is insufficient because variations in receiver gain clearly affect the sky power data. Thus, by applying Equation 3.10.4, the T^J_{ant} calculations are performed as previously described for the four peaks of pixel 1 in the A:LSB band:

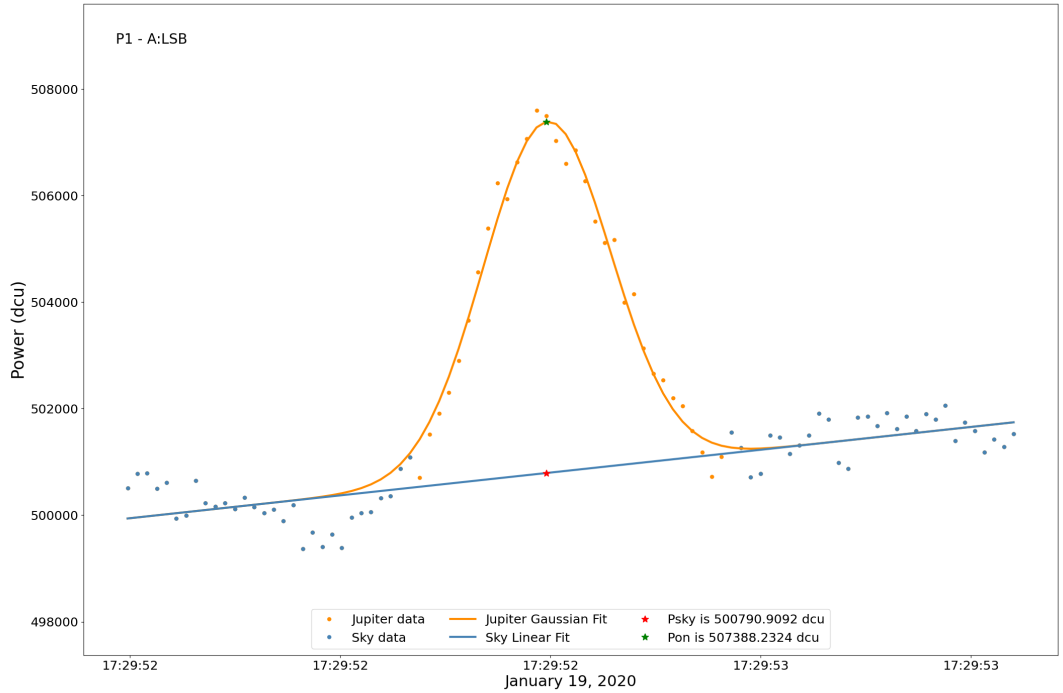

Figure 4.2.15: The third power peak of Jupiter for pixel 1 in the A:LSB band from obsid10611 scan is shown. The orange line corresponds to the Gaussian fit applied to Jupiter's peak; the green mark refers to Jupiter's maximum power value. The blue line represents the linear fit to the sky power data; the red mark is the power sky chosen for calculation.

For peak 1:

$$\begin{aligned} T_{ant}^{J_{peak1}} &= T_{sys}^{A:LSB} \cdot \frac{\left(P_{on}^{J_{peak1}} - P_{off}^{J_{peak1}}\right)}{P_{off}^{J_{peak1}}} \\ &= 55.32\ K \cdot \frac{\left(504051.48\ dcu - 498613.32\ dcu\right)}{498613.32\ dcu} \\ &= 0.60K \end{aligned} \tag{4.2.8}$$

For peak 2:

$$\begin{aligned} T_{ant}^{J_{peak2}} &= 55.32\ K \cdot \frac{\left(506060.02\ dcu - 499515.47\ dcu\right)}{499515.47\ dcu} \\ &= 0.72K \end{aligned} \tag{4.2.9}$$

For peak 3:

$$T_{ant}^{J_{peak3}} = 55.32\ K \cdot \frac{\left(507388.23\ dcu - 500790.91\ dcu\right)}{500790.91\ dcu} = 0.73K \tag{4.2.10}$$

For peak 4:

$$T_{ant}^{J_{peak4}} = 55.32\ K \cdot \frac{\left(505987.47\ dcu - 500475.51\ dcu\right)}{500475.51\ dcu} = 0.61K \tag{4.2.11}$$

The third Jupiter peak provides the highest antenna temperature, reaching 0.73 K in the A:LSB band for pixel 1. It is anticipated that in the remaining three bands of the same peak, the antenna temperatures will also exceed those of the other peaks, a prediction confirmed by the obtained results. The recorded T_{ant}^{J} values for the third peak are 0.82 K for the A:USB band, 0.93 K in the B:LSB band, and 0.99 K for the B:USB band.

2.- To calculate the flux density of Jupiter (S_J). This parameter derives from Equation 3.3.2, which considers the planet's uniform brightness temperature T_B^J, subtended by a solid angle $\Omega_{J,rad}$ in radians[2] at a specific frequency. In this case, the calculation employs the central frequencies of each COMAP band, expressed in wavelength (λ).

It must be noted that the solid angle $\Omega_{J,rad}$ depends on the observation date, which for this analysis corresponds to January 19, 2020, and the angular diameter d_J, equal to 31.987 arcsecs or $7.753{\cdot}10^{-5}$ rad, obtained using Python's ephem package. For simplicity, it considers the solid angle as the Jupiter's area:

$$\Omega_{J,rad} = \pi \cdot \left(\frac{d_{J,rad}}{2}\right)^2 = \pi \cdot \left(\frac{7.753 \cdot 10^{-5}\ rad}{2}\right)^2 = 1.88 \cdot 10^{-8}\ rad^2 \tag{4.2.12}$$

The wavelengths used in this calculation correspond to the central frequencies

[2] $\Omega = A/d^2$, where A is the area of the source observed and d is the distance between the observer and source.

of COMAP, with values of $\lambda_{27} = 0.01110342$ m, $\lambda_{29} = 0.01033767$ m, $\lambda_{31} = 0.00967072$ m, and $\lambda_{33} = 0.00908462$ m.

In the Woody method Woody [57], Jupiter's brightness temperature is assumed to be 140 K at 30 GHz. Karim et al. [30] provides a table with brightness temperature values for Jupiter over a frequency range from 27.688 to 34.688 GHz, with increments of 0.5 GHz. A linear interpolation is performed on these data to determine the brightness temperatures at the central frequencies of COMAP. Specifically, a temperature of 140.91 K is obtained for 27 GHz, 143.65 K for 29 GHz, 146.29 K for 31 GHz, and 149.37 K for 33 GHz.

By implementing Equation 3.3.2 for the central frequencies:

$$S_{J_{27,29,31,33}} = \frac{2 \cdot k \cdot \Omega_{J,rad} \cdot T_B^{J_{27,29,31,33}}}{\lambda^2_{27,29,31,33}} \cdot 10^{26} \tag{4.2.13}$$

where, $k = 1.3806 \times 10^{-23}\ J/K$ is the Boltzmann constant. The number 10^{26} multiplies the equation to correctly transform to Jansky units. A constant value is $2 \cdot k \cdot \Omega_{J,rad} \cdot 10^{26} = 0.0005215521\ J/K\ rad^2$. Applying the previously indicated values, the following results are obtained.

For 27 GHz:

$$\begin{aligned} S_{J_{27\,GHz}} &= \frac{140.91\ K \cdot 0.0005215521\ J/K\ rad^2}{\lambda^2_{27\,GHz}} \\ &= \frac{7.349446 \times 10^{-29}\ J\ rad^2}{0.01110342^2\ m^2} \\ &= 59.53\ Jy \end{aligned} \tag{4.2.14}$$

For 29 GHz:

$$\begin{aligned} S_{J_{29\,GHz}} &= \frac{143.65\ K \cdot 0.0005215521\ J/K\ rad^2}{\lambda^2_{29\,GHz}} \\ &= \frac{7.492256 \times 10^{-29}\ J\ rad^2}{0.01033767^2\ m^2} \\ &= 70\ Jy \end{aligned} \tag{4.2.15}$$

For 31 GHz:

$$\begin{aligned} S_{J_{31\,GHz}} &= \frac{146.29\ K \cdot 0.0005215521\ J/K\ rad^2}{\lambda^2_{29\,GHz}} \\ &= \frac{7.629836 \times 10^{-29}\ J\ rad^2}{0.00967072^2\ m^2} \\ &= 81.47\ Jy \end{aligned} \tag{4.2.16}$$

For 33 GHz:

$$\begin{aligned} S_{J_{33\,GHz}} &= \frac{149.37\ K \cdot 0.0005215521\ J/K\ rad^2}{\lambda^2_{33\,GHz}} \\ &= \frac{7.790497 \times 10^{-29}\ J\ rad^2}{0.00908462^2\ m^2} \\ &= 94.29\ Jy \end{aligned} \tag{4.2.17}$$

Note that these flux values are used for all pixels of the obsid10611 scan according to the band.

3.- Determinate the COMAP ideal sensitivity (σ_{ideal}). This parameter is defined as the total flux collected by the radio telescope antenna under ideal conditions, excluding losses. The σ_{ideal} is calculated using Equation 3.10.5, based on the radius of the COMAP radio telescope antenna, which is 5.2 m. Subsequently:

$$\begin{aligned} \sigma_{ideal} &= \frac{2 \cdot k}{\pi \cdot R^2} \cdot 10^{26} \\ &= \frac{2 \cdot 1.3806 \times 10^{-23}\ J/K}{5.2^2\ m^2} \cdot 10^{26} \\ &= 32.50\ Jy/K \end{aligned} \tag{4.2.18}$$

This value is unique for all frequencies used in the η calculation.

4.- Determine the aperture efficiency (η). This parameter serves as an indicator of the antenna's ability to convert received radiation into a detectable signal. This parameter, ranging from 0 to 1, is calculated using Equation 3.10.1 by applying the values of T_{ant}, S_J and σ at the central frequencies of COMAP. Then, for pixel 1 in the 4 bands:

For 27 GHz:

$$\begin{aligned}\eta_{27} &= \frac{\sigma_{ideal} \cdot T_{ant_{27}}^{J_{peak3}}}{S_{J_{27}}} \\ &= \frac{32.50\ Jy/K \cdot 0.73\ K}{59.53\ Jy} \\ &= 0.40 \end{aligned} \tag{4.2.19}$$

For 29 GHz:

$$\begin{aligned}\eta_{29} &= \frac{\sigma_{ideal} \cdot T_{ant_{29}}^{J_{peak3}}}{S_{J_{29}}} \\ &= \frac{32.50\ Jy/K \cdot 0.81\ K}{70\ Jy} \\ &= 0.38 \end{aligned} \tag{4.2.20}$$

For 31 GHz:

$$\begin{aligned}\eta_{31} &= \frac{\sigma_{ideal} \cdot T_{ant_{31}}^{J_{peak3}}}{S_{J_{31}}} \\ &= \frac{32.50\ Jy/K \cdot 0.93\ K}{81.47\ Jy} \\ &= 0.37 \end{aligned} \tag{4.2.21}$$

For 33 GHz:

$$\begin{aligned}\eta_{33} &= \frac{\sigma_{ideal} \cdot T_{ant_{33}}^{J_{peak3}}}{S_{J_{33}}} \\ &= \frac{32.50\ Jy/K \cdot 0.99\ K}{94.26\ Jy} \\ &= 0.34 \end{aligned} \tag{4.2.22}$$

As the frequency increases, the efficiency tends to decrease, a behavior observed in almost all pixels. Figure 4.2.16 illustrates the aperture efficiency for each central frequency of COMAP, assigning an eta value to every pixel. The values were multiplied by 100 to express the vertical axis in percentages. Different markers were used to highlight the rings of the 19-pixel array. pixel 1, located at the center of the array, is identified with a star. The first ring, including pixels 2 to 7, is marked with triangles, while the outer ring, consisting of pixels 8 to 17, is

represented by circles.

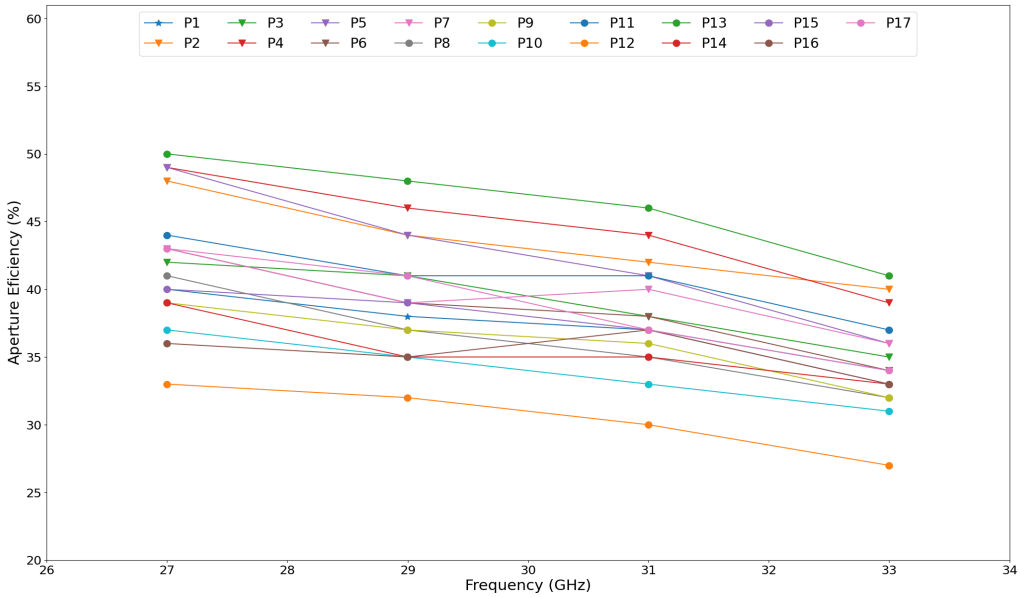

Figure 4.2.16: The aperture efficiency at each central frequency of COMAP is presented for the 17 pixels in scan obsid10611.

With increasing frequencies, a reduction in efficiency becomes apparent. This trend, observed in most of the pixels in the array, can be attributed to factors such as coma, an optical aberration that primarily affects pixels farther from the optical axis, causing an asymmetric distribution of radiation in the focal plane. For instance, pixel 1 shows an efficiency of 0.397 at 27 GHz, 0.379 at 29 GHz, 0.372 at 31 GHz, and 0.335 at 33 GHz. However, Pixels 7 and 16 deviate slightly from this trend, displaying a somewhat higher efficiency at 31 GHz compared to the others. For example, Pixel 7 records efficiency values of 0.43, 0.39, 0.40, and 0.36 for 27, 29, 31, and 33 GHz, respectively. Additionally, Figure 4.2.17 presents the aperture efficiency for all useful pixels in the obsid10611 scan. Each pixel is represented by four points corresponding to the central frequencies of COMAP. It is evident that the eta values range between 0.27 and 0.5, aligning with the findings reported by Lamb et al. [34].

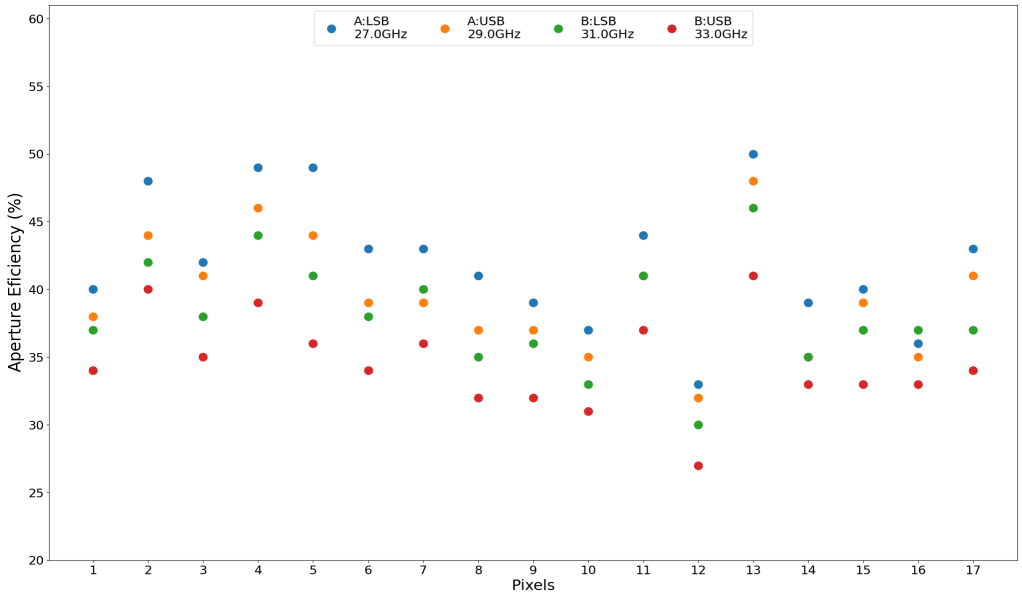

Figure 4.2.17: The aperture efficiency for the 17 pixels at the central frequencies of COMAP is shown.

4.3 MERRA-2 data validation through of COMAP skydips measurements

The MERRA-2 data validation is comprised of four major steps: 1) The preparation of MERRA-2 atmospheric data for the OVRO site. 2) The successful execution of AM configuration file with MERRA-2 data to obtain simulated atmospheric opacity and brightness temperature across the COMAP frequency range at different elevation angles, 3) The calibration of skydip power data to brightness temperature using the simulated zenith brightness temperature from the AM model. 4) The calculation of zenith spectral opacity within the COMAP frequency range.
From this procedure, some results naturally emerged that were not initially anticipated but provide valuable insights into the study of calibration strategies. These include the estimation of a spillover model for different elevation angles within the COMAP frequency range and the direct retrieval of precipitable water vapor at specific moment and over extended periods for the OVRO site.

4.3.1 Working with MERRA-2 Data

This section explains how the MERRA-2 data must be treated to calculate the precipitable water vapor over OVRO site. The methodology is enumerated as follows.

1.- Obtaining MERRA-2 atmospheric data on OVRO site. Downloading the appropriate atmospheric data type from the MERRA-2 platform is essential for conducting accurate atmospheric analysis. A file containing 3-hour averaged data of the primary variables distributed across 38 vertical pressure layers on OVRO site is downloaded. The short name file is M2I3NPASM, specifically from March 25, 2019, at 15:00 GMT, as close as possible to the timing of the COMAP data.OVRO is in the Owens Valley at $\sim$ 1.2 km above sea level (a.s.l.), its coordinates are $(37.23, -118.282)$ and the pressure registered in Weather group of obsid4386 file is 883.04 mbar. The following grid around OVRO is proposed: (-118.653, 36.426), (-118.653,37.757), (-116.830, 36.426) and (-116.830,37.757) as shown in red triangles on Figure 4.3.1. The objective is to find a point within the MERRA-2 data that closely corresponds to the observatory's location and pressure to simulate the atmospheric conditions as accurately as possible. Within

the grid, there are six points (blue triangles). The point satisfying all conditions is the blue triangle at the Valley with coordinates (36.5,-118.0) near Owens Lake. This point is at 900 mbar of pressure, $\sim$ 85 km from OVRO and $\sim$ 1.2 km a.s.l. Another potentially useful point is located at coordinates (37.0, -118.0), but is excluded despite having a pressure of 811 mbar. This exclusion is due to its location in the mountains, making it not adequately representative of the valley's climate.

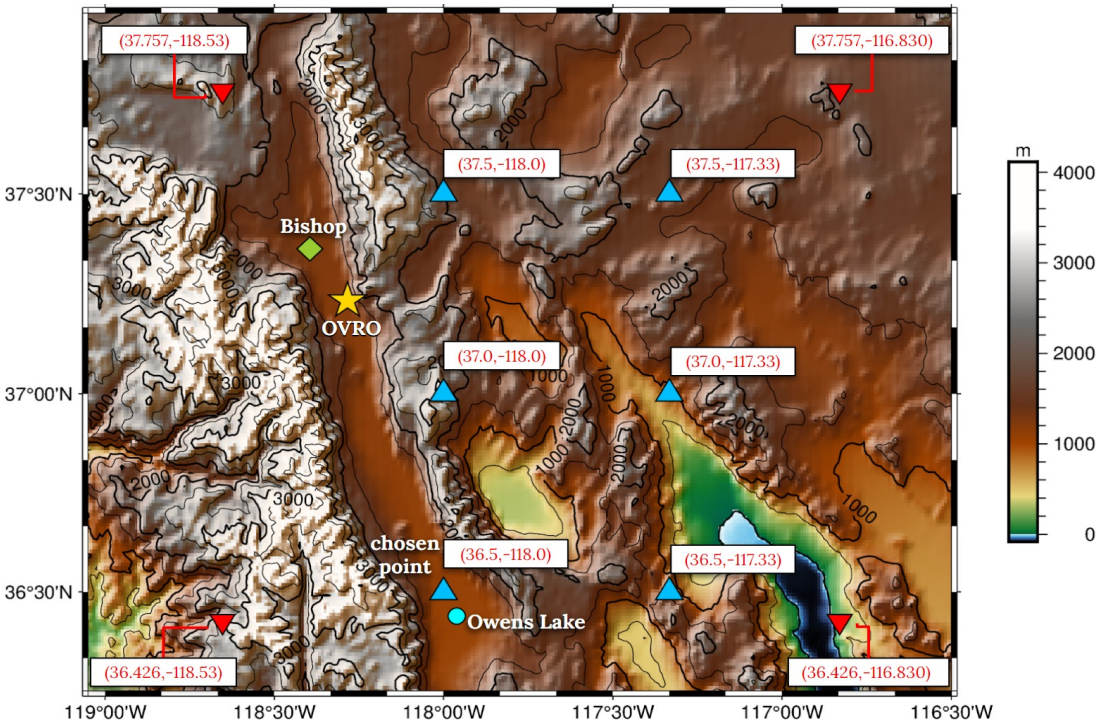

Figure 4.3.1: The red triangles indicate the four coordinates entered in the MERRA-2 platform to download the atmospheric .nc file for the region surrounding the OVRO site (yellow star). Six coordinates extracted from the file are shown as light blue triangles. Among them, the coordinate adjacent to Owens Lake (light blue circle) was selected for further analysis, as it exhibits pressure and geographic conditions similar to those of the OVRO site. The location of the Bishop meteorological station is also displayed.

2.- Identifying and to prepare the variables for atmospheric study. Once the file was obtained, the relevant variables were identified by their names: pressure layer edges as lev, temperature as T, specific humidity as QV and ozone as O3. It has already been mentioned the data are distributed in 38 vertical pressure layers which has units of Pascal (hPa). T has units of Kelvin (K), QV and O_3 have units of Kg/Kg which indicates a mass mixing ratio (mmr) between desired

gas mass quantity and dry air mass quantity.

Atmospheric profiles and the AM model require converting QV to water molecules (H_2O) in a volume mixing ratio (vmr). Besides, O_3 must also be converted to vmr. The transformation of QV to H_2O and O_3 both in vmr are given by:

$$H_2O_{vmr} = \frac{QV_{mmr}}{1.0 - QV_{mmr}} \cdot \frac{28.964}{18.015} \tag{4.3.1}$$

$$O_{3_{vmr}} = O_{3_{mmr}} \cdot \frac{28.964}{47.9982} \tag{4.3.2}$$

where 18.015 is the water molecular mass, 47.9982 is the ozone molecular mass, and 28.964 is the dry air molecular mass. All in units of grams/mol. The variables in the atmospheric profiles are correctly expressed in parts per million (ppm), therefore, the equations 4.3.1 and 4.3.2 must be multiplied by $1{\cdot}10^6$. An important final consideration is that the pressure should be expressed in mbar rather than Pa, where 1 mbar = 100 Pa.

3.- Constructing the MERRA-2 atmospheric profiles. The profiles for the selected point at the OVRO site on March 25, 2019, at 15:00 GMT are shown in Figure 4.3.2. The temperature, water vapor, and ozone profiles are plotted directly at the edge of the pressure layers in the left, center, and right panels, respectively. The edge layers are indicated as *lev* parameter in MERRA-2 file. The data are represented in blue points and varies in pressure between 0.1 and 900 mbar divided in 38 layers.

4.- Preparing the AM configuration file. As mentioned in the section 4.3.1, the configuration file expresses the atmosphere behavior on the site study, in this case, the OVRO site. To prepare the file, it is necessary to consider: 1) the OVRO pressure of 883.044 mbar, 2) the initial pressure of $P_0 = 0.01$ hPa, which is the same in all MERRA-2 grids, 3) the temperature data at the edges of the pressure layer, and 4) the specific humidity and ozone data at a point in the middle of the pressure layers *pl*. Since these layers are not in the MERRA-2 file, it is necessary to create them. Reinecker 2007 (citarlo) indicates that *pl* is obtained as follows:

$$pl_n = ple_n \pm delp_n/2 \tag{4.3.3}$$

where, *ple* is edge-layer pressure n and $delp_n = ple_{n+1} - ple_n$ is the difference between one layer n and the next $n + 1$. The $\pm$ symbol indicates the upper or

lower mid-point of the edge of a pressure layer n. To calculate the mid-points required for this study it is necessary to find the upper mid-points, therefore the minus symbol will be used. It must also be included P_0 at the beginning of lev.

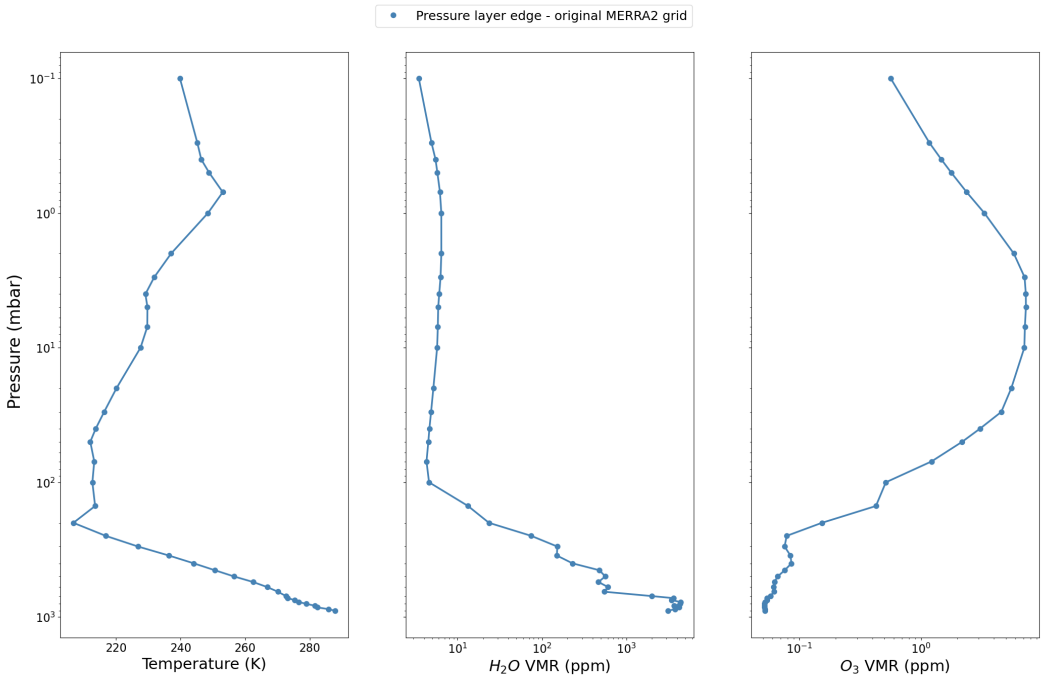

Figure 4.3.2: Temperature, water vapor and ozone profiles using the MERRA-2 original grid. The pressure range varies from 0.1 up to 900 mbar.

The penultimate layer is at 875 mbar, so the OVRO pressure of 883.044 mbar must be added, making it the lowest edge of the pressure layers instead of 900 mbar. Therefore, the edge-layer pressures now ranges between 0.01 and 883.044 mbar, denoted as lev_{new}, which corresponds to ple in equation 4.3.3. This new pressure will be utilized as the pressure layers in the configuration file. The $delp$ calculation is performed using lev_{new}. By applying equation 4.3.3, the pressure layers mid-points pl are determined, varying between 0.05 and 879.022 mbar.
Since two points were added to lev_{new}, a first-degree spline interpolation is conducted to find these two data points for each variable. Specifically, the *scipy.interpolate* package within the SciPy module of Python is utilized. The routine *interpolate.splrep* is employed to determine the spline coefficients. The data sets (x,y) used are from the original MERRA-2 grid. The y variables include T, H_2O_{vmr} derived from QV_{mmr}, and O3, while the x variable represents the pressure in lev. Additionally, *interpolate.splev* is applied to compute the spline based

on the obtained coefficients, which are then evaluated at lev_{new} or pl pressure, depending on the variable. Consequently, the variables T, H_2O_{vmr} and O3 are not the same as their original MERRA-2 grid values, therefore, they will now be referred to as T_{new}, $H_2O^{new}_{vmr}$ and $O3_{new}$. These new interpolated values will be entered into each layer of the AM configuration file.

Figure 4.3.3 displays the temperature, water vapor and ozone profiles incorporating the new data. Each panel provides an extended view to better visualize the final layers. The blue dotted line represents the original MERRA-2 grid up to 900 mbar of pressure, corresponding to the lev parameter in the file.

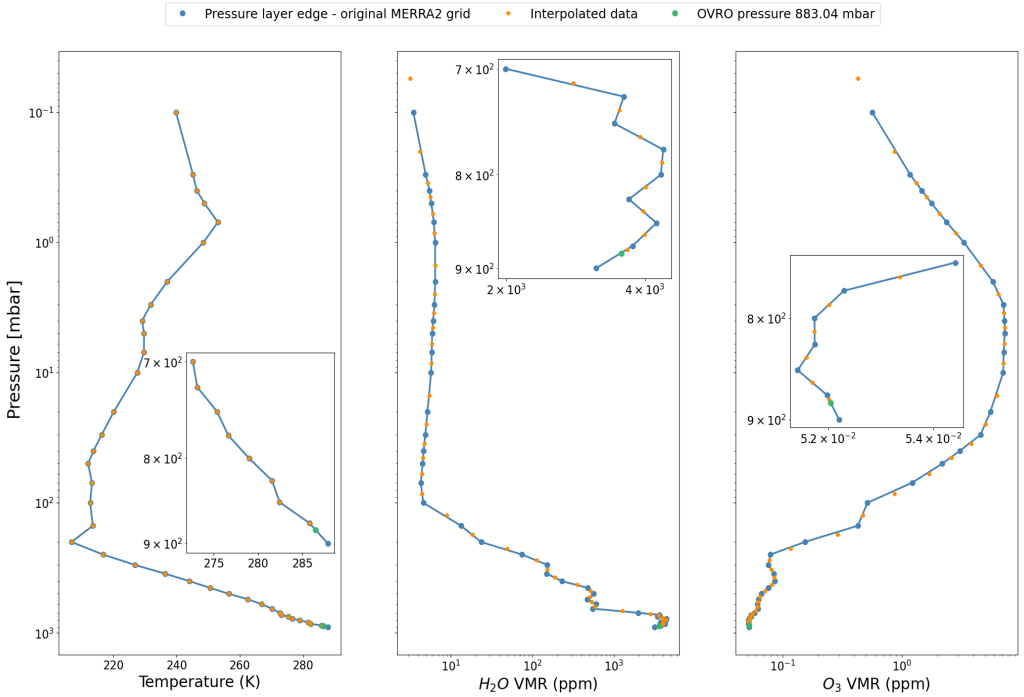

Figure 4.3.3: Temperature, water vapor, and ozone profiles are derived using the original MERRA-2 grid (blue dotted lines) and the newly interpolated data (orange dots). The pressure values at the edges and the corresponding interpolated variable values will be utilized in the AM configuration file.

The orange dots indicate the interpolated points for the three variables. In the temperature panel, these points represent the pressure layer edge using lev_{new} pressure and the values of the interpolated temperature. For the water vapor and ozone panels, these points illustrate the pressure layers mid-points pl and the values calculated with the interpolation method. The OVRO pressure is depicted as a green dot in each panel.

As a result of applying this procedure to the water vapor profile, it becomes possible to determine the precipitable water vapor (PWV) over the OVRO site, which is discussed in the following section. The AM configuration file must have .amc format. Its structure is presented in Figure 4.3.4. The upper left side provides an example of how to enter the input parameters when executing the configuration file.

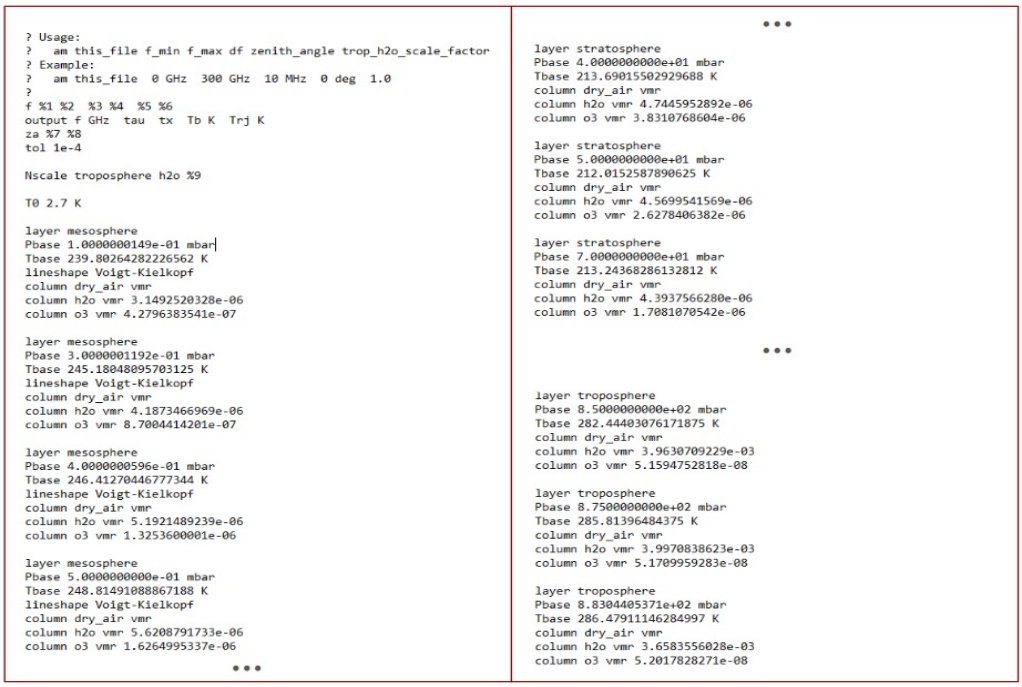

Figure 4.3.4: The configuration file of the AM Model is detailed. The top-left section demonstrates how to execute the file in the command line. Below, the frequency lines f, the zenith angle za, the tropospheric scaling factor, and the CMB temperature are provided. In addition, the paragraphs list the atmospheric layers to which their respective pressure, temperature, water, and oxygen content are associated, derived from the data provided by MERRA-2 for OVRO.

In this atmospheric study, the radiation impacting the atmosphere from space is the CMB, so its temperature should be considered as "T0 2.7 K". The atmospheric layers are then constructed using the new variables obtained through the previous procedure. The layer name can be the mesosphere, stratosphere, or troposphere; "Pbase", corresponding to lev_{new}; "Tbase", referring to T_{new}; the "column h2o vmr" corresponding to $H_2O^{new}_{vmr}$; the "column o3 vmr" referring to $O3_{new}$; and the "column dry_air vmr" indicating the air molecular mass. Additionally, a line labeled "lineshape Voigt-Kielkopf" is applied only at the mesosphere. It is important to mention that the configuration file is executed for the COMAP

frequency range between 26 and 34 GHz with a spectral resolution of 1.953125 MHz at $\theta_z = 0°$ (zenith), and with $nsacle = 1.0$ for the OVRO site on March 25, 2019. The configuration file is executed for seven more zenith angles: 3.5°, 10°, 20°, 30°, 40°, 50° y 60° in equivalence with elevation angles from COMAP skydip: 86.5°, 80°, 70°, 60°, 50°, 40° and 30°.

Explaining the implementation of the configuration file in this investigation is not as crucial as presenting its results. Therefore, section 4.3.1 provides detailed information on this. Two output files are generated in .err and .out formats from the configuration file. Figure 4.3.5 presents the main sections of the .err file obtained upon executing the AM configuration file. This file contains crucial information about the model's execution and its success.

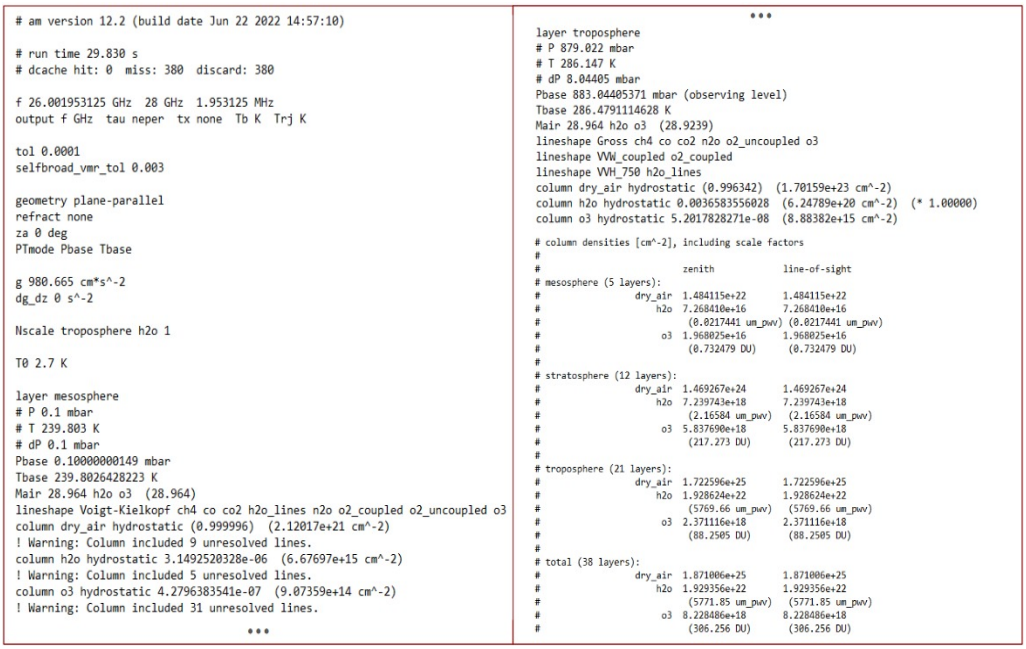

Figure 4.3.5: Description of the AM model .err output file. The top-left section displays the AM software version and the execution time of the configuration file. It then outlines the utilized frequencies and the output variables listed in the .out file: frequency f, opacity tau, transmittance tx, brightness temperature tb, and Rayleigh-Jeans temperature trj. The file sequentially details the execution of each pressure layer, along with corresponding temperature values and molecule quantities per layer. The lower-right section includes a relevant measurement: the total water vapor molecules per cm^2, converted into precipitable water vapor (pwv), presented at the zenith angle and at the line-of-sight angle, which may coincide.

It verifies if the input frequency, resolution, output parameters, and their sequence

in the .out file are accurate. The zenith angle evaluated by the model and the *nscale* used are also displayed. Subsequently, the atmospheric layers are shown in blocks, starting from the lower pressure at higher altitudes and progressing downward. The ellipsis indicates that 36 additional layers are included in the complete file. Each block provides essential details included in the .amc file, such as the base temperature (Tbase) and pressure (Pbase), as well as new information like the pressure thickness (dP) and the molecular content of water vapor and ozone per layer. This example only displays the first and last block. At the end, the file summarizes the total molecules at the zenith and along the line of sight. At the bottom right side appears an important parameter called "um_pwv", which indicates the amount of PWV obtained through this method. Figure 4.3.6 illustrates a little section of the .out file obtained upon executing the AM configuration file. This file lists the spectral parameters under study. It presents five columns: the first is the frequency (f GHz), the second is the atmospheric opacity (tau), the third is the atmospheric transmittance (tx), the fourth is the atmospheric brightness temperature (Tb K) and the fifth is the atmospheric Rayleigh-Jeans temperature (Trj K). This work will analyze the frequency, atmospheric brightness temperature, and opacity across the mentioned zenith angles.

```
2.7898438e+01 2.850253e-02 9.718998e-01 1.010547e+01 9.450787e+00
2.7900391e+01 2.850167e-02 9.719007e-01 1.010521e+01 9.450491e+00
2.7902344e+01 2.850084e-02 9.719015e-01 1.010497e+01 9.450200e+00
2.7904297e+01 2.850002e-02 9.719023e-01 1.010473e+01 9.449914e+00
2.7906250e+01 2.849923e-02 9.719030e-01 1.010449e+01 9.449632e+00
2.7908203e+01 2.849846e-02 9.719038e-01 1.010426e+01 9.449355e+00
2.7910156e+01 2.849770e-02 9.719045e-01 1.010403e+01 9.449082e+00
2.7912109e+01 2.849696e-02 9.719052e-01 1.010380e+01 9.448812e+00
2.7914062e+01 2.849624e-02 9.719060e-01 1.010358e+01 9.448547e+00
2.7916016e+01 2.849553e-02 9.719066e-01 1.010336e+01 9.448285e+00
```

Figure 4.3.6: A segment of the .output file generated in this atmospheric study is shown.

4.3.2 Precipitable Water Vapor at Specific Time

As mentioned in the previous section, determining the amount of precipitable water vapor at the OVRO site is a result of the procedure used to construct the AM configuration file. The pwv can be derived using Equation 3.12.2. The previously introduced variables are employed; *delp* corresponds to the difference between layers, such $delp_n$ in Equation 4.3.3. To determine the specific humidity

qv, the reverse process is applied by using the Equation 4.3.1 on the interpolated $H_2O_{vmr}^{new}$ data. By integrating the specific humidity data across all pressure layers, the pwv is calculated to be 5.753 mm at the OVRO site. This value can be directly compared with the PWV obtained from the .err output file when the configuration file is executed. In this case, the PWV amount is 5.772 mm, resulting in a difference of 0.0181 mm between two methods. It is important to emphasize that the water vapor profile in Figures 4.3.2 and 4.3.3 will not exhibit the same behavior across the pressure range if the amount of PWV varies. This variation could be clearly visible in the pressure layers nearer to the site, indicating that the water vapor profiles change depending on the day and time.

4.3.3 Power Data Calibration to Brightness Temperature

This section constitutes the core of the MERRA-2 data validation. It outlines the procedure implemented to determine atmospheric opacity at the OVRO site and evaluates it against the simulated opacity derived from the AM model using MERRA-2 data, previously introduced in Section 4.3.1.
The analysis relies on a COMAP file, obsid4386 (Table 4.1.1), which includes a skydip scan suitable for this study. Figure 4.3.7 illustrates the skydip power data recorded for the 19 pixels on March 25, 2019, between 14:18 and 14:26 UTC. This file was selected due to its inclusion of power measurements at various elevation angles and loaddata, both essential for determining the antenna temperature. The scan sequence begins with an ambient load placement, followed by an atmospheric sweep of the radio telescope in elevation, another ambient load, a second atmospheric sweep, and a final ambient load. The skydip motion spans elevation angles of $30.^\circ < \theta_{ea} < 86.5^\circ$, oscillating at an azimuth angle of -30.°.
The power measurements $P(\nu, \theta)$ in the scan are described by the general power equation (Section 3.11), which depends on the frequency ν and the elevation angle θ, varying over time. Each of the 19 pixels, across four frequency bands and 1024 spectral channels, follows:

$$P(\nu, \theta) = k \cdot \Delta\nu \cdot G \cdot \left[T_{Rx}(\nu) + T_{Ant}(\nu, \theta)\right] \tag{4.3.4}$$

where k represents the Boltzmann constant, $\Delta\nu$ the system's bandwidth, and G the system's gain, considered invariant over short time intervals. The term $k \cdot \Delta\nu \cdot G$ remains constant but is not directly available in the data.

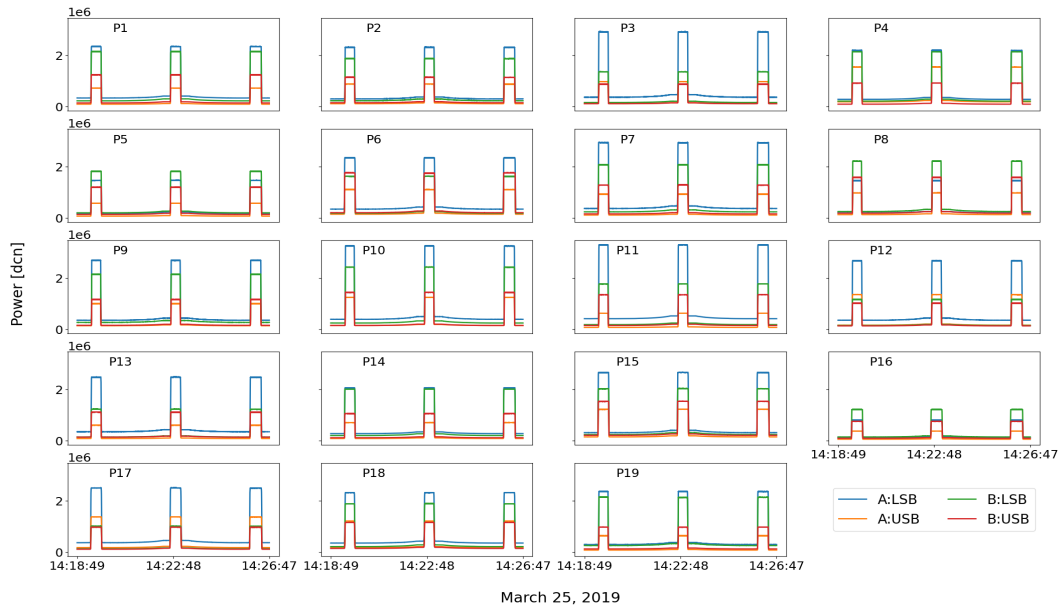

Figure 4.3.7: Power of 19-pixels, 4 bands from obsid4386 file are shown. The A:LSB, A:USB, B:LSB, and B:USB bands are presented in blue, orange, green, and red lines. For each pixel and band, all useful spectral channels are averaged. The sky scan between 30° and 86° elevation takes about 8 minutes, including three calibrations.

The system temperature, $T_{Sys} = T_{Rx}(\nu) + T_{Ant}(\nu, \theta)$ where the receiver temperature, $T_{Rx}(\nu)$, is estimated using the Y-factor method (Equation 3.11.1), previously described in Section 4.2.1. The antenna temperature, $T_{Ant}(\nu, \theta)$, is defined as:

$$T_{Ant}(\nu, \theta) = T_{CMB}(\theta) + T_{ATM}(\nu, \theta) + T_{sp}(\nu, \theta) \tag{4.3.5}$$

where T_{CMB} =2.73 K corresponds to the cosmic microwave background (CMB), while T_{ATM} and T_{sp} represent the atmospheric brightness temperature and spillover contribution, respectively. Both are unknown variables, making $T_{Ant}(\nu, \theta)$ the primary focus of the analysis. Notably, Equation 4.3.5 excludes an astronomical source contribution (T_{source}), present in Equation 3.6.2 of Section 3.6.2. This omission is justified since the study aims to examine atmospheric effects through a skydip scan, incorporating atmospheric information within the power data recorded in obsid4386 file. Equation 4.3.4 cannot be directly solved due to the presence of two unknowns. Consequently, the antenna temperature is determined using two reference points:

1. The load system temperature and power ($P_{load}(\nu), T^{sys}_{load}$), available in the

housekeeping and TOD power data, respectively:

$$P_{load}(\nu) = k \cdot \Delta\nu \cdot G \cdot \left[T_{Rx}(\nu) + T_{load}\right] \tag{4.3.6}$$

2. The sky system temperature and power at a specific elevation angle $(P_{sky}(\nu,\theta), T^{sys}_{sky}(\nu,\theta))$, where only the sky power is included in the TOD power data:

$$P_{sky}\,(\nu,\theta) = k \cdot \Delta\nu \cdot G \cdot \left[T_{Rx}(\nu) + T_{sky}\,(\nu,\theta)\right] \tag{4.3.7}$$

The radio telescope records power data up to an elevation of 86.5° (or 3.5° from the zenith), the angle at which the parameter $P_{sky}\,(\nu,\theta)$ is extracted. Since the sky temperature is not directly available in the data, it must be inferred through atmospheric model at the same elevation angle. In this case, $T_{sky}\,(\nu,\theta)$ results from the combined contributions of atmospheric noise, the Cosmic Microwave Background (CMB), and spillover effects, as described in Equation 4.3.5. The atmospheric brightness temperature at an elevation of 86.5° is simulated using the AM radiative transfer model (Sections 3.12.3 and 4.3.1), represented by the blue line in Figure 4.3.8.

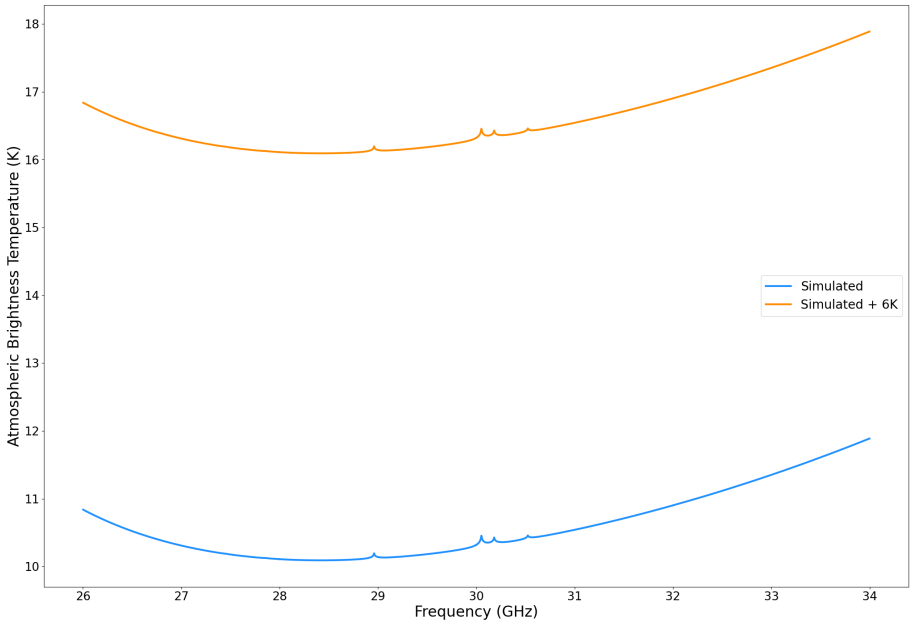

Figure 4.3.8: Simulated atmospheric brightness temperature at 86.5° elevation from AM radiative transfer model is shown in the blue line, for a pwv of 5.7 mm. The simulated temperature plus 6 K of spillover is shown in the orange line.

The CMB contribution is already included in this model. The spillover effect at the zenith corresponds to a fixed value of 6 K, which has been added to the simulated atmospheric brightness temperature values, shown by the orange line in Figure 4.3.8. This 6 K excess noise was measured by Lamb et al. [34] through system noise comparisons with and without the secondary installed in the initial receiver system configuration. Additionally, Foss et al. [25] state that most of this noise originates from illumination spillover around the primary reflector, with a secondary contribution arising from ground signal reflections off the secondary support legs.

Continuing with Equations 4.3.6 and 4.3.7, both are linear, and the only unknown parameter, $k \cdot \Delta\nu \cdot G$, remains constant over a short time interval, corresponding to the slope. By leveraging this linearity, a first-degree polynomial fit[3] is applied to the reference points, determining the slope (m) and y-intercept (P_0). Using these coefficients, a general power equation is derived:

$$P(\nu, \theta) = m \cdot \left[T_{Rx}(\nu) + T_{Ant}(\nu, \theta_{za})\right] + P_0 \tag{4.3.8}$$

where the only unknown variable is the antenna temperature. Solving for $T_{Ant}(\nu, \theta)$ yields:

$$T_{Ant}(\nu, \theta) = \frac{P(\nu, \theta) - P_0}{m} - T_{Rx}(\nu) \tag{4.3.9}$$

where $P(\nu, \theta)$ represents the skydip power data per pixel, frequency band, and spectral channel, varying with elevation over time, as recorded in obsid4386 file. Additionally, $T_{Rx}(\nu)$, the receiver temperature, is computed for each pixel, band, and spectral channel. It is important to highlight that obtaining $T_{Ant}(\nu, \theta)$ constitutes the *calibration to temperature units from power units* and corresponds to the antenna temperature of each power measurement within the skydip section of the analyzed file.

Figure 4.3.9 presents, as an example, the power sections for spectral channel 550 of pixel 1 in the four frequency bands employed to apply the previously described procedure. Determining the coefficients of the first-degree polynomial fit requires both load and sky power values, represented by the light blue and light green lines,

[3]Polynomial fitting in Python using np.polyfit: fits a polynomial $p(x) = p[0] \cdot x^{deg} + ... + p[deg]$ of degree deg to data points (x, y). The function returns a vector of coefficients that minimizes the squared error $E = \sum_{j=0}^{k} |p(x_j) - y_j|^2$.

respectively. To obtain a single value, 100 load power data points are averaged, following the same approach for the sky power data. From the housekeeping records, the load temperature corresponding to the same time instant as the load power measurement is retrieved, yielding T_{load} =273.14 K.

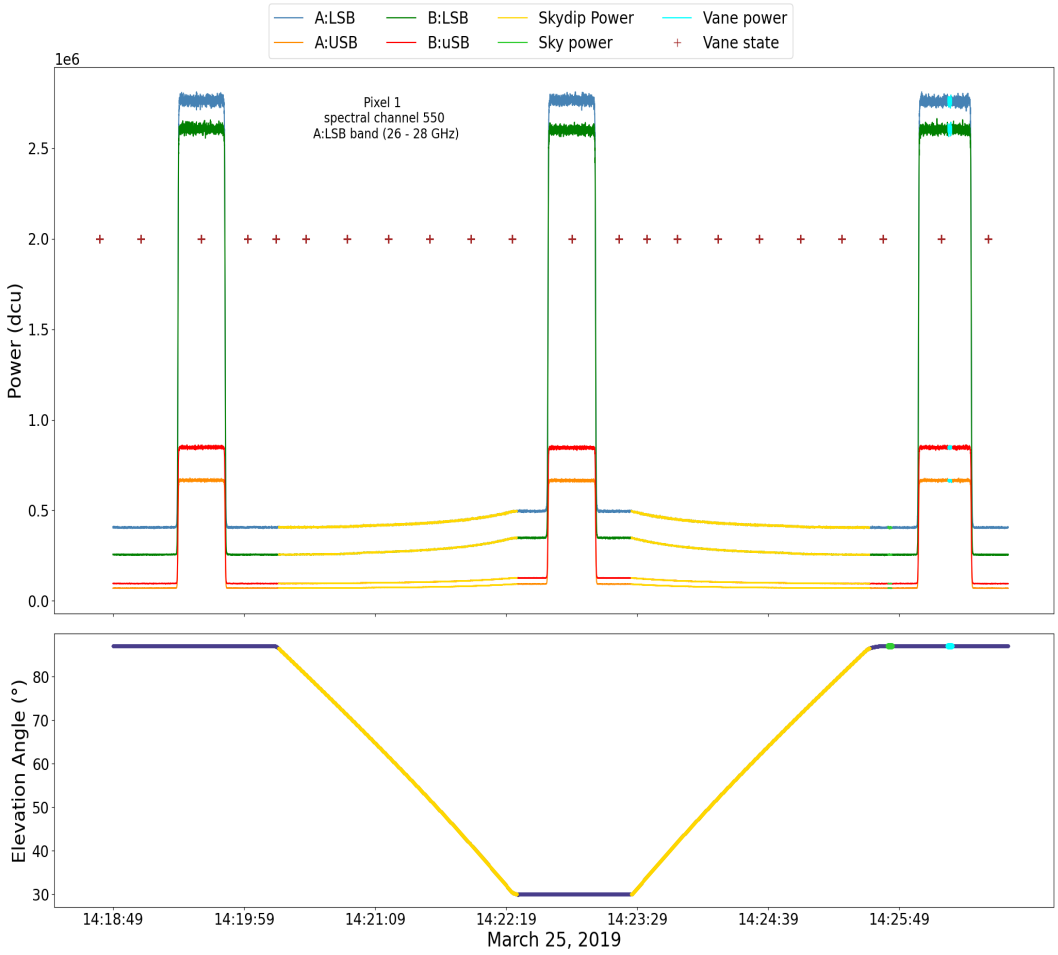

Figure 4.3.9: The power scan for pixel 1 is shown in all 4 spectral bands for spectral channel 550 and their respective useful sections during the scan. The A:LSB, A:USB, B:LSB, and B:USB bands are presented in blue, orange, green, and red lines. The calibration sections are represented in light blue and light green lines, while the load status is represented in a red cross, both of which are positioned over the power data for visualization only. The skydip sections are shown in yellow lines.

Additionally, the sky power is considered at the closest possible elevation angle to the zenith (θ_{za} =0°) found in the recorded data, specifically θ_{ea} =86.5°. Consequently, the sky reference point in Equation 4.3.7 is not directly at the zenith but at θ_{za} =4° in terms of the zenith angle. This distinction is crucial, as

the simulated atmospheric brightness temperature derived from the AM radiative transfer model must now be computed at this adjusted angle, $T_{ATM}(\nu, \theta_{za} = 4°)$, ensuring proper usage as a reference. To determine the antenna temperature values associated with power measurements, Skydip power data, illustrated by the yellow lines, are used, computing it at each point of both Skydips individually. To illustrate the T_{Ant} calculation, spectral channel 550 (26.927734 GHz) of pixel 1 in band A:LSB is selected from the second Skydip scan in Figure 4.3.9 for a point within it at 30° elevation as a reference. The procedure follows these steps:

1. Compute the Y-factor using Equation 3.11.1:

$$Y^{P1,A:LSB} = \frac{P_{load}^{P1,A:LSB}}{P_{sky}^{P1,A:LSB}} = \frac{2756538.25\ dcu}{404865.91\ dcu} = 6.808521 \tag{4.3.10}$$

2. Determine the receiver temperature using Equation 3.11.5:

$$\begin{aligned} T_{Rx}^{P1,A:LSB} &= \frac{T_{load} - Y^{P1,A:LSB} \cdot T_{sky}^{P1,A:LSB}}{Y^{P1,A:LSB} - 1} \\ &= \frac{273.14\ K - 6.808521 \cdot 16.33\ K}{6.808521 - 1} \\ &= 27.88\ K \end{aligned} \tag{4.3.11}$$

Note that the Y-factor and T_{sky} are different for each pixel, band, and spectral channel. Figure 4.3.10 presents the T_{Rx} for all pixels, bands, and spectral channels registered in obsid4386 file. The T_{Rx} generally exhibits smooth behavior, with pronounced noise spikes, particularly in the lower half of band A. Lamb et al. [34] reports that no exact cause has been identified for these spikes; however, they result from the interaction between the polarizers and the corrugated horns. In contrast, specific noise spikes at the edges and center of each sideband, corresponding to spectral channels 1, 513, and 1024 (orange peaks), are common to all pixels, are associated with the DC component and its Nyquist alias, and will therefore be removed in the proposed procedure.

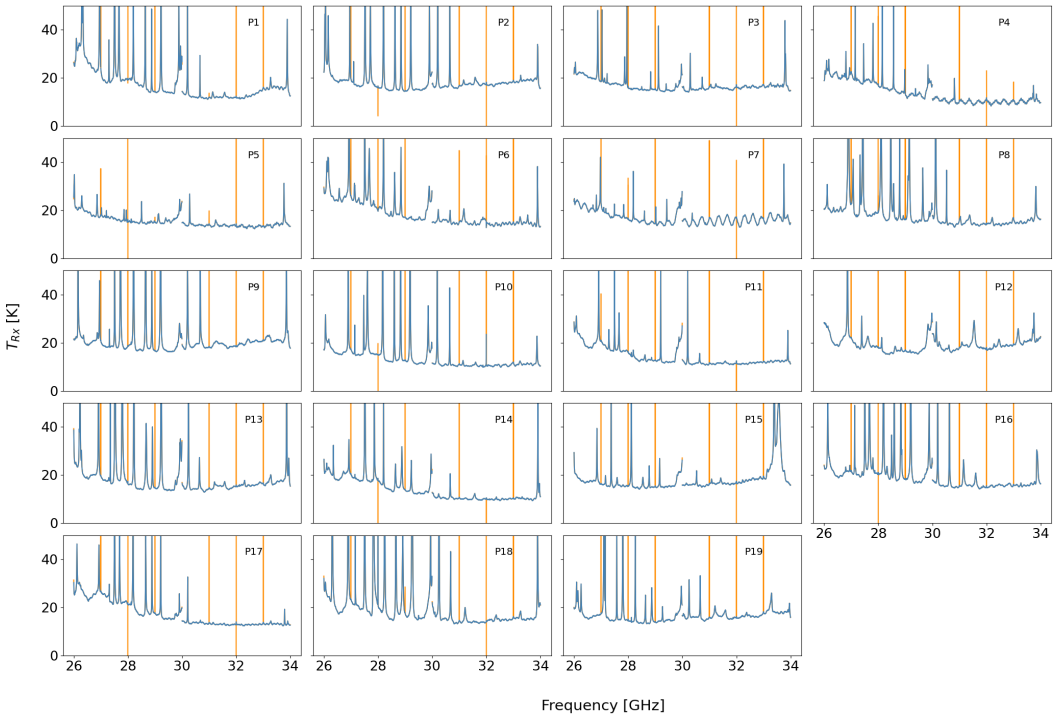

Figure 4.3.10: Receiver temperature for the 18 pixels in all COMAP spectral ranges is shown. The orange spectral channels are not used in the procedure.

3. Apply a first-degree polynomial fit to the reference points to obtain the coefficients. In this case, the reference values are P_{load} =2756538.25 dcu, T^{sys}_{load} =301.03 K, P_{sky} =404865.91 dcu, and T^{sys}_{sky} =44.21 K. The resulting coefficients are the slope m =9157.08625 dcu/K and the Y-intercept P_0 =1.33528798×10^{-2} dcu.

4. Evaluate the antenna temperature using Equation 4.3.9. Substituting the corresponding values, the result is:

$$\begin{aligned} T^{P1,A:LSB}_{Ant_{30°}} &= \frac{P^{P1,A:LSB}_{30°} - P_0}{m} - T^{P1,A:LSB}_{Rx}(\nu) \\ &= \frac{493267\ dcu - 1.33528798 \times 10^{-2}\ dcu}{9157.08625\ dcu/K} - 27.88\ K \\ &= 25.988\ K \end{aligned} \tag{4.3.12}$$

Thus, at an elevation of 30°, the antenna temperature for spectral channel 550 of pixel 1 in band A:LSB reaches 25.98 K. Based on this value, $T_{Ant}(\nu, \theta)$ is obtained for all pixels, bands, and spectral channels within the skydip power sections. The

antenna temperatures from both power sections associated with identical elevation angles are averaged, generating a $T_{Ant}(\nu, \theta)$ sweep between 30.° and 86.5° elevation for each pixel.

Figure 4.3.11 presents the antenna temperature averaged from the skydip for 19 pixels across the entire COMAP frequency range, considering seven elevation angles: 30.°, 40.°, 50.°, 60.°, 70.°, 80.° and 86.5°.

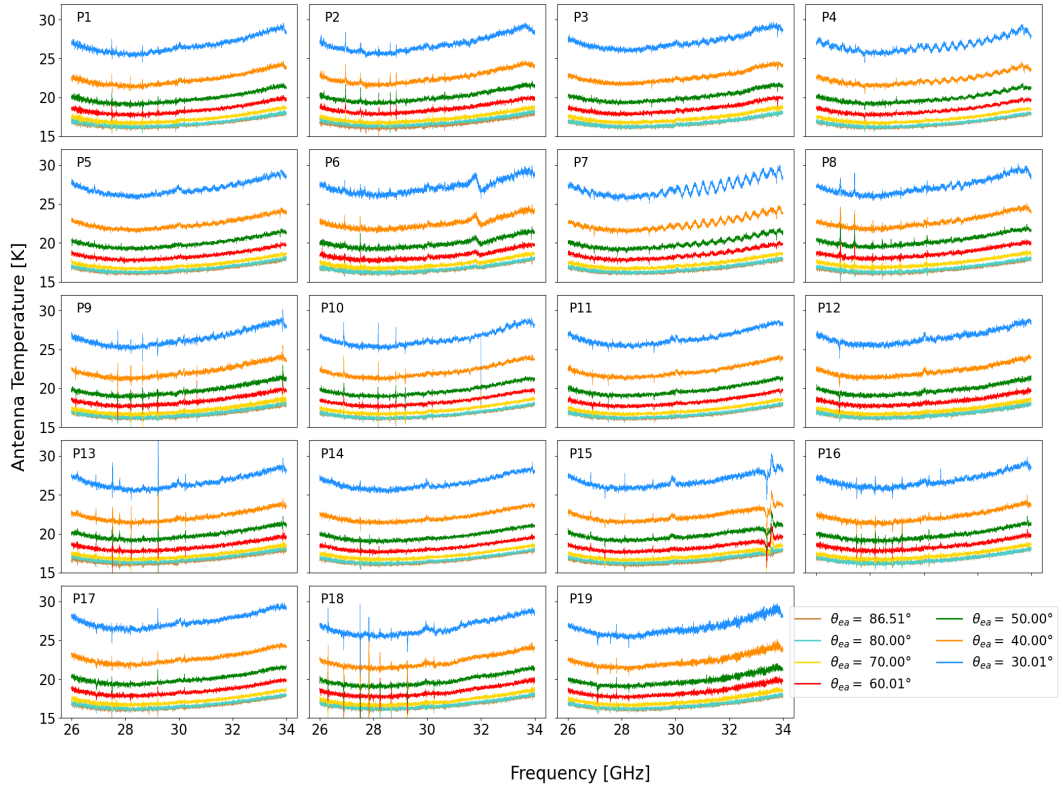

Figure 4.3.11: Antenna temperature from 19-pixels power calibration is shown over the COMAP frequency range. Each pixel presents seven curves corresponding to different elevation angles obtained from the skydip. Standing waves and abrupt drops are displayed at pixels 4, 6, 7, 15, and 18, which are not considered.

The antenna temperature exhibits a range of variation between approximately 15 K and 30 K. Certain pixels, such as P4, P6, P7, P15, P18, and P19, show erratic behavior, characterized by standing waves and abrupt drops within the frequency range of 30 to 34 GHz. Specifically, Foss et al. [25] reported data from feeds 4, 6, and 7 were not used in the final analysis of Session 1. Feeds 4 and 7 were used for engineering testing and did not generate useful data, while feed 6

exhibited significant systematic errors. The antenna temperature changes with the elevation angle; T_{Ant} reaches minimum values when the antenna is positioned at $\theta_{ea} = 86.5°$ and increases as the elevation angle decreases attributed to higher atmospheric contribution and ground spillover effects. It is important to highlight that certain spectral channels were excluded due to their inferior performance relative to the others. Specifically, channels 2 and 3 within the 30 to 32 GHz frequency range (B:LSB) were omitted for pixel 10, while channels 0, 513, and 1024 were discarded for all pixels.

Figure 4.3.12 shows the average of well-behaved pixels: P1, P2, P3, P5, P8, P9, P10, P11, P12, P13, P14, P16 and P17. These are averaged to mitigate noise in the data and enable a comparison with the simulated spectra from the AM radiative transfer model.

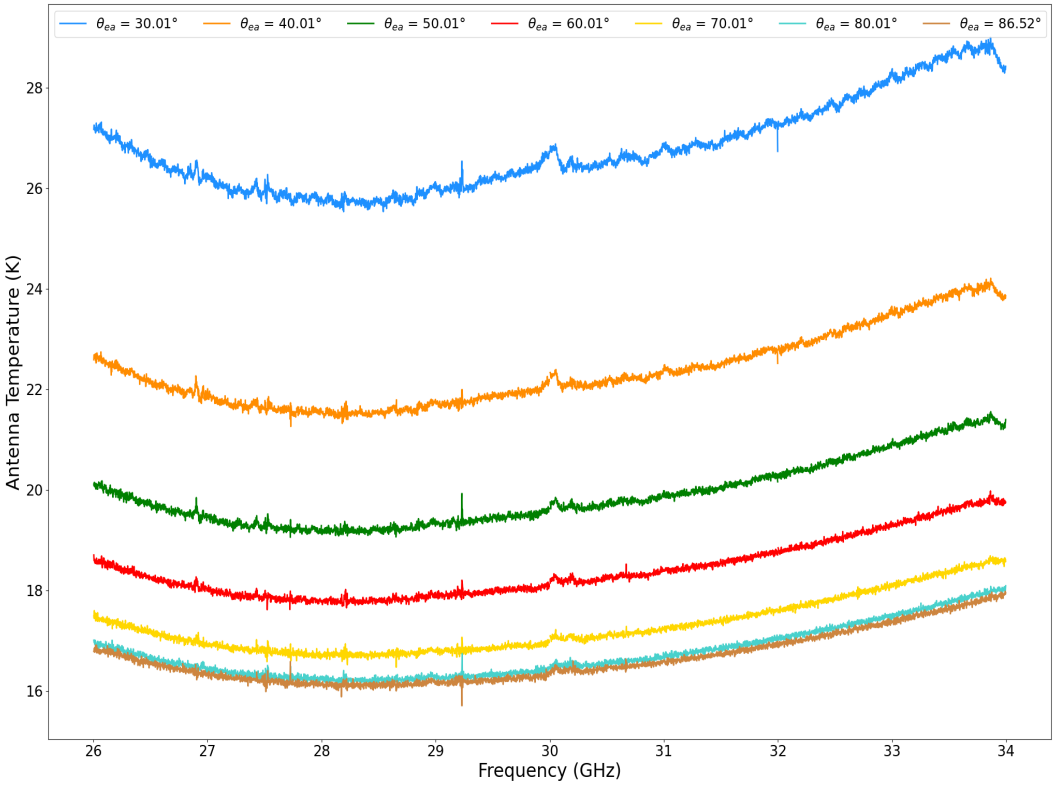

Figure 4.3.12: Averaged antenna temperature over the COMAP frequency range derived from the well-behaved pixels is shown. Seven temperature curves are displayed, each corresponding to a distinct elevation angle, starting at 30° (blue line) up to 80° (light blue line), including 86.5° (brown line).

Figure 4.3.13 compares the averaged antenna temperature (blue line) with the simulated atmospheric brightness temperature spectrum (orange line) from AM radiative transfer model. Each frame corresponds to a specific elevation angle. Notably, an excess temperature compared to the simulation is evident, attributed to a spillover effect.

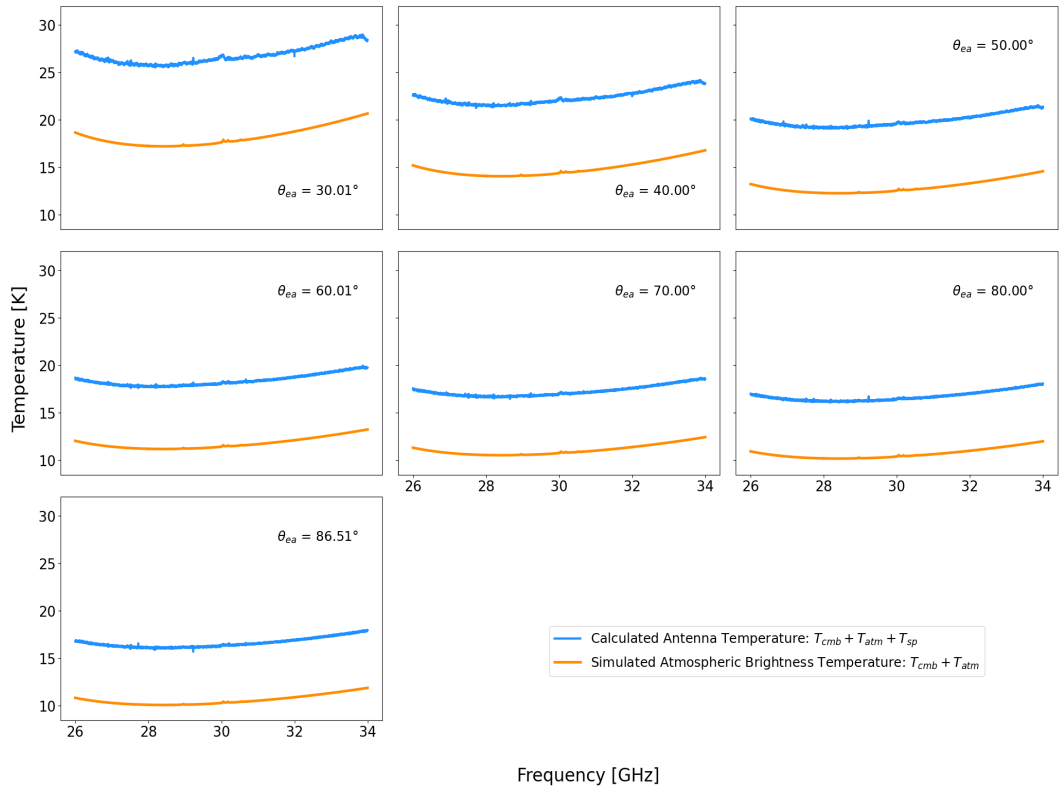

Figure 4.3.13: Comparison between the antenna temperature calculated at seven elevation angles from the power calibration of the averaged pixels and the atmospheric brightness temperature simulated by the AM model. Both temperatures are presented within the COMAP frequency range (26 - 34 GHz). Each panel displays the results obtained at a specific elevation angle, starting at 30° in the top-left panel and progressing in 10° increments up to 96.5° in the seventh panel.

The excess temperature for the seven elevation angles is shown in Figure 4.3.14. It ranges from approximately 9 K at θ_{ea} =30° (first row, first column) and around 6 K at θ_{ea} =86.5° (third row, first column). At 86.5°, the curve around 6 K is fully comparable to Lamb et al. [34], with the only difference being that, in this case, all pixels are averaged, whereas the referenced study presents the excess temperature for two individual pixels when pointing at zenith. Lamb et al. [34] measured

this excess, attributing it to spillover illumination around the primary, combined with ground-reflected signals. Lunde, J. G. S. et al. [38] specifically analyzed and characterized the interaction of these ground signals with the sidelobes, reinforcing the impact of spillover on the observed data. Lunde, J. G. S. et al. [38] combined the antenna radiation pattern simulation with the horizon elevation profile of the OVRO site, finding that ground pickup spillover varies from 0 K at zenith to 8 K at the horizon. Consequently, Figure 4.3.14 presents a result that integrates both contributions and, as Lunde, J. G. S. et al. [38] indicated, demonstrates that spillover decreases with increasing elevation angle. Since temperature exhibits uniform behavior across the frequency range, it is averaged for each evaluated elevation angle, enabling characterization for any elevation angle.

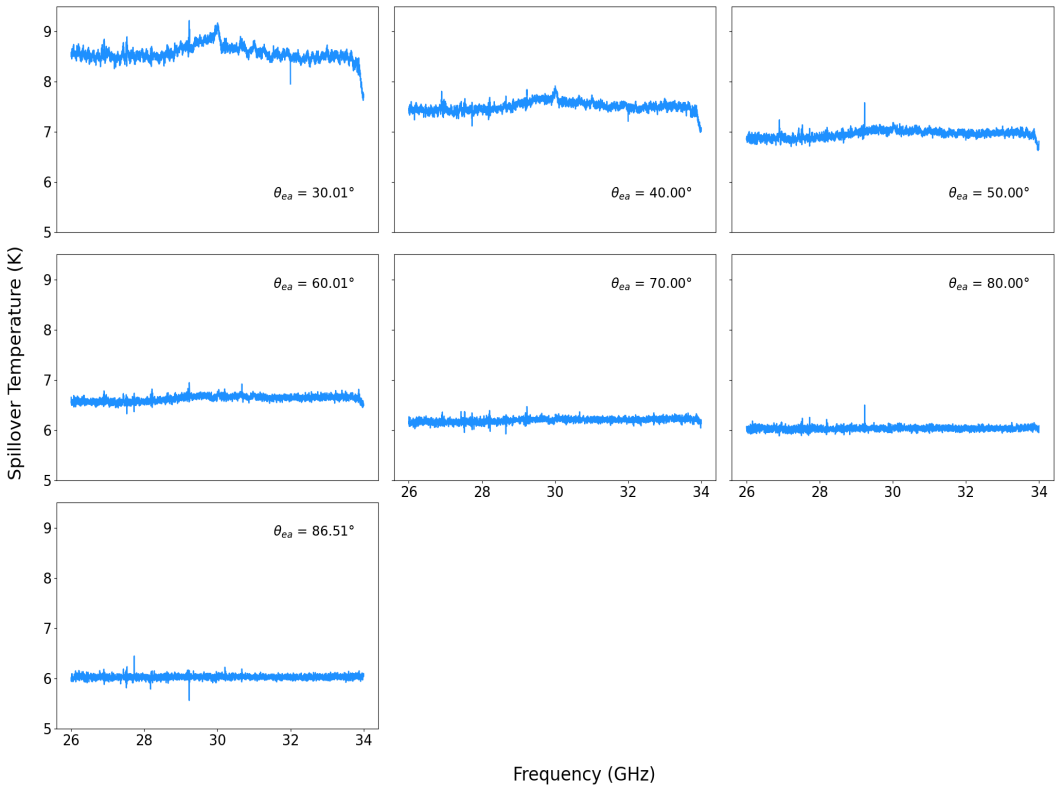

Figure 4.3.14: Ground spillover at different elevation angles.

Figure 4.3.15 illustrates the spillover data and its characterization via an exponential fit:

$$T_{sp} = b \cdot e^{a \cdot X} + c \tag{4.3.13}$$

where, $a = -2.43$, $b = 10.0$, $c = 5.74$ and X is the elevation angle in radians. While Lunde, J. G. S. et al. [38] derived a spillover model through simulations, the present study establishes an alternative model based on experimental measurements, extending its applicability across a broad elevation range.

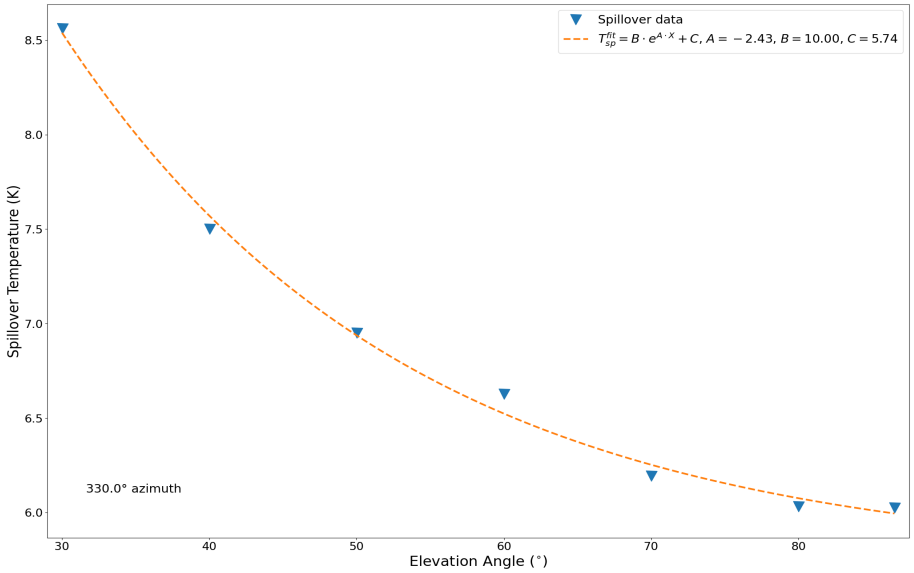

Figure 4.3.15: The exponential fit to the spillover data (blue triangles) as a function of elevation angle at 330° azimuth is shown in orange dashed line.

Subtracting the spillover temperature from the COMAP averaged antenna temperature allows for a comparison with the simulated brightness temperature spectrum, as illustrated in Figure 4.3.16. At this stage, the COMAP calculated brightness temperature $T_B = T_{CMB} + T_{ATM}$, facilitates a direct comparison with the simulated brightness temperature. A strong correlation between the data and the behavior illustrated by the AM radiative transfer model is observed. At low frequencies, the brightness temperature simulation performs adequately with respect to the temperature calculated from the COMAP data, particularly where the 22 GHz water line influences the results. However, at lower elevation angles, the data within the 29 to 30 GHz range exhibit a slight temperature increase relative to the simulation. It is important to note that the COMAP calculated

brightness temperature has been obtained by the skydip process, although results are presented for only seven elevation angles. This approach allows the zenith opacity to be calculated for each COMAP spectral channel.

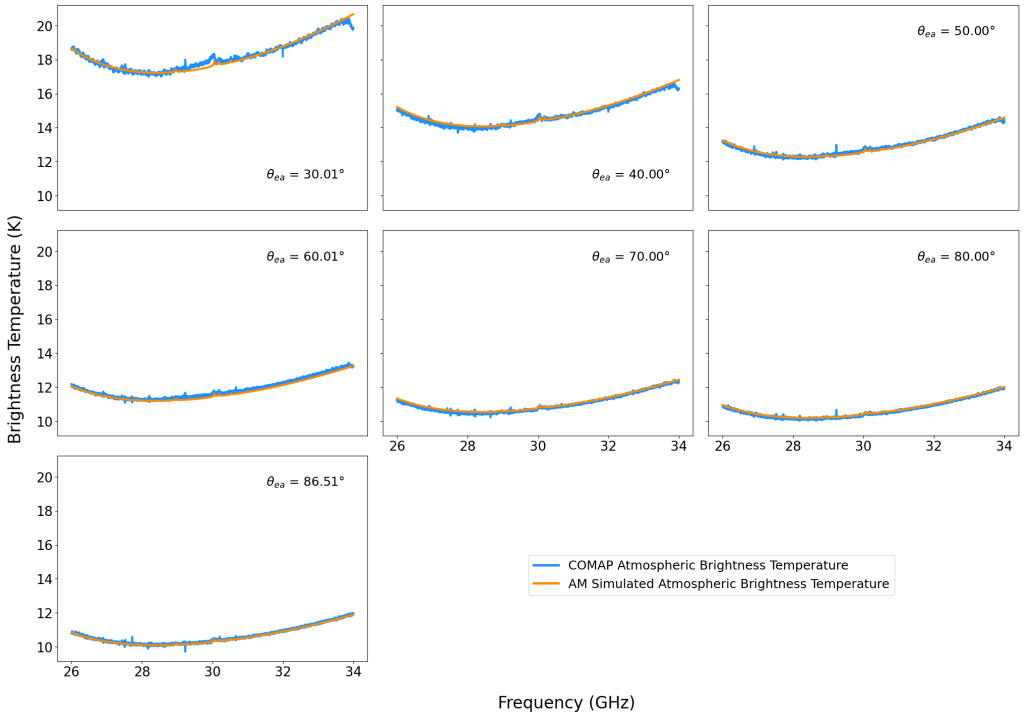

Figure 4.3.16: A comparison of atmospheric brightness temperatures obtained from the COMAP power calibration and the AM model simulation is shown. starting at 30° elevation and increasing to 80° elevation, in steps of 10°, including 86.5° near the zenith.

Figure 4.3.17 displays the calculated brightness temperature for the 26.927 GHz frequency within the range of $1.0 < \text{am} < 2.0$ airmass (or $30° < \theta_{ea} < 86.5°$ elevation angles), accompanied by an exponential "tipping curve" fit to the atmospheric temperature plus CMB. The obtained zenith opacity for 26.927 GHz is τ =0.03013 neper. The point where the fit plateaus is not observed, possibly due to the lack of data below 30° elevation or 2 airmass.

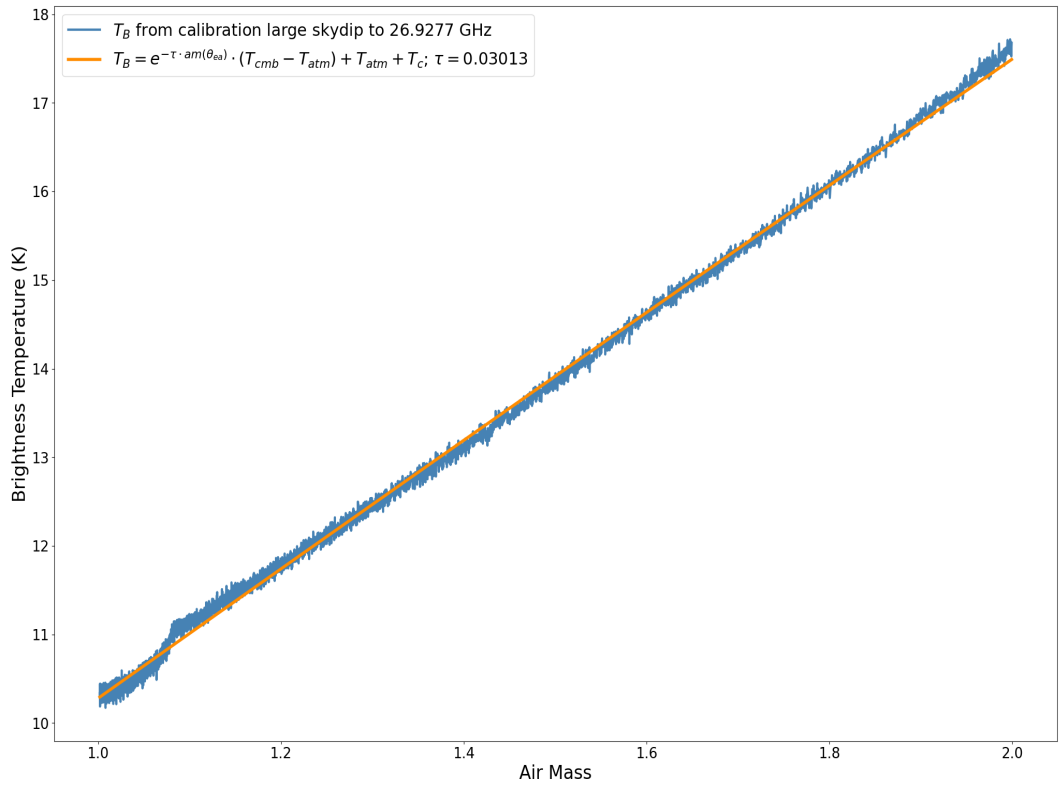

Figure 4.3.17: The atmospheric brightness temperature at 26.927 GHz across 1 and 2 air masses is presented in a blue line. An exponential fit, shown in an orange line, is applied to T_B to determine the atmospheric opacity, yielding τ =0.03013 Neper at 26.927 GHz in 86.5° elevation.

Figure 4.3.18 illustrates the calculated zenith opacity (blue line) from the exponential fit across the COMAP frequency range and compares it with the simulated opacity in the zenith from the AM radiative transfer model. The percentage error between the simulated and calculated opacity across all spectral ranges is 3.92%.

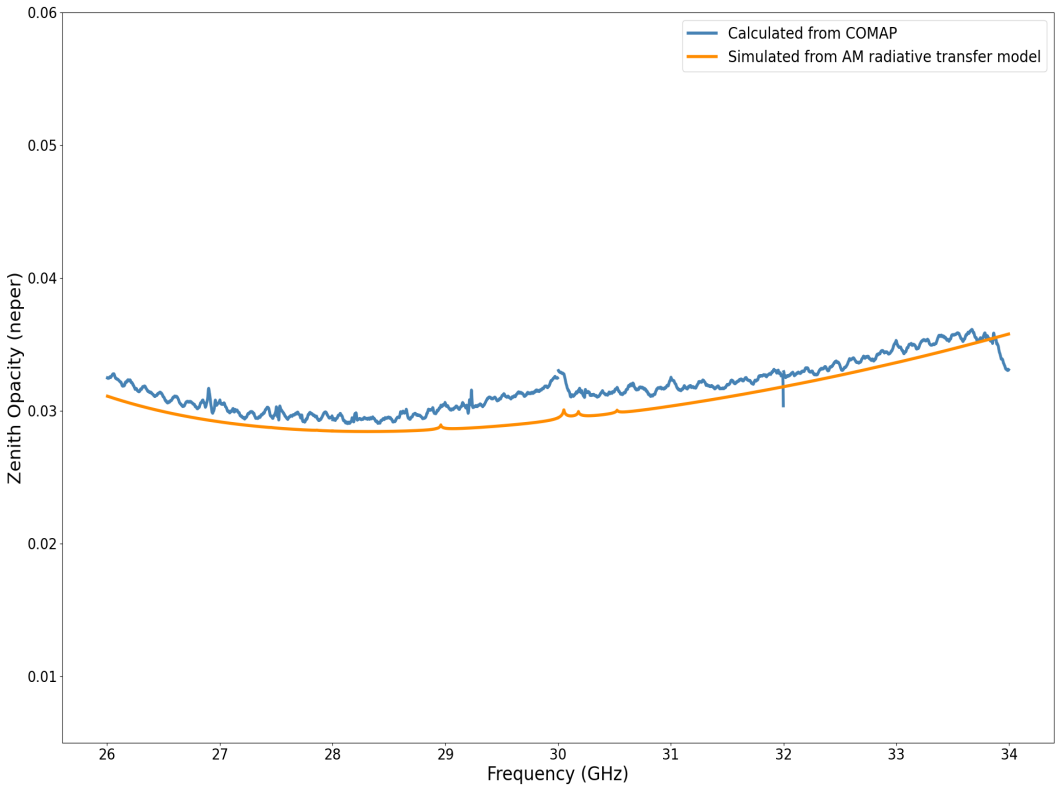

Figure 4.3.18: Calculated and simulated opacity curves for March 25, 2019, at 15:00 hrs, at the OVRO site are shown. The zenith atmospheric opacity, derived from skydip power measurements within the COMAP frequency range, is presented in a blue line. The simulated atmospheric opacity obtained using the AM model is shown in an orange line, for a pwv of 5.7 mm.

This low error indicates a strong agreement between the observed and simulated opacity values, validating the MERRA-2 data and suggesting that the atmospheric parameters it provides, such as temperature, pressure, and water vapor content, accurately represent the actual atmospheric conditions over the site. The consistency between the calculated and simulated opacity further supports the reliability of MERRA-2 atmospheric database as a source for atmospheric modeling.

Since the percentage error between the calculated and simulated opacity is negligible, the same power-to-brightness temperature calibration procedure is applied to the dataset under analysis, but considering a more restricted elevation range, specifically a short skydip power data between 40° and 60° of elevation. Foss et al. [25] reported that data collected during Session 1 at elevations above 65° and below 35° were susceptible to ground contamination through the main beam and sidelobes, leading to their exclusion from the final results. To mitigate this systematic error, short skydip scans were introduced. Accordingly, an assessment is required to determine whether these scans enable the retrieval of zenith atmospheric opacity with an error percentage comparable to that obtained from the long skydip (Figure 4.3.18). The calibration process for the short skydip differs from that applied to the long skydip in terms of sky calibration.

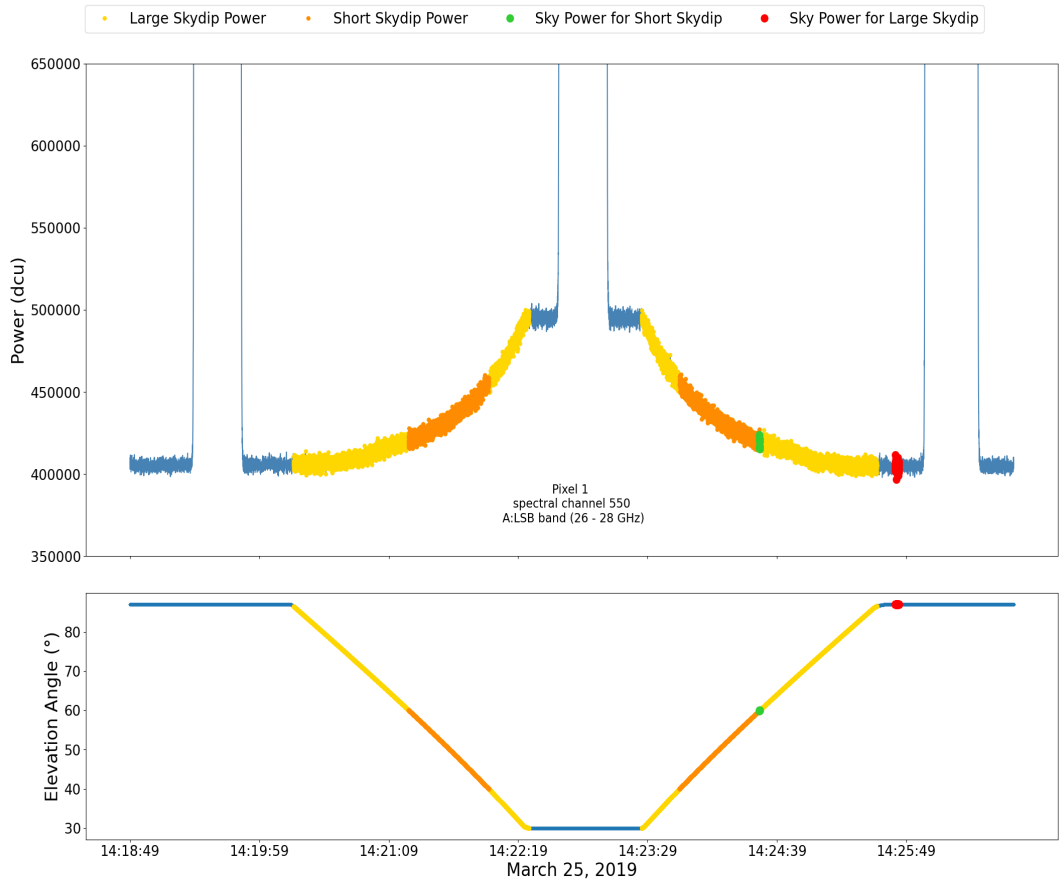

Figure 4.3.19: The upper panel shows the power for spectral channel 500 of pixel 1 in the A:LSB band for file obsid4386. The lower panel presents the elevation angle covered by the radio telescope during the full scan. The long skydip, in yellow, illustrates the power between 30° and 86.5° elevation. The short skydip, in orange, represents the power between 40° and 60°. For comparison, the sky power at 60° and at 86.5° is shown in green and red, respectively.

Unlike the previous case, the 86.5° elevation is no longer considered for either the sky power or the sky temperature. Instead, an elevation of 60° is used, as indicated by green dots in Figure 4.3.19. The spectral channel 550 power for pixel 1 in the A:LSB band is presented to illustrate the new skydip power section, highlighted in orange, in comparison to the long skydip power section, shown in yellow. The previous sky power at 86.5° appears as red dots. Additionally, the elevation angle of pixel 1 is included, depicting the elevation ranges associated with each power section mentioned earlier. Based on these data, the same procedure is applied to derive the zenith atmospheric opacity across the entire COMAP frequency range, as presented in Figure 4.3.20.

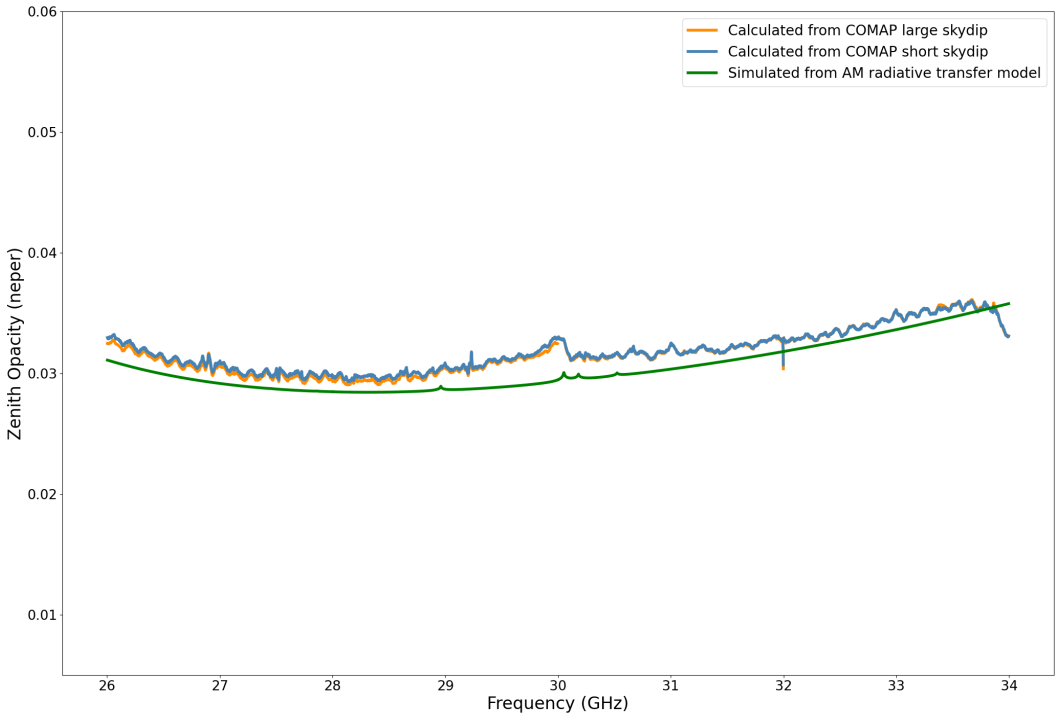

Figure 4.3.20: Calculated and simulated opacity curves for March 25, 2019, at 15:00 hrs, at the OVRO site are shown. The zenith atmospheric opacity across the COMAP frequency range, estimated from the short skydip power data, is shown in blue. For comparison, the opacity derived from the long skydip is also included. Furthermore, the simulated zenith opacity from the AM radiative transfer model is presented, for a pwv of 5.7 mm. The discrepancy between the short skydip-derived opacity and the simulated value is only 4.4%.

The green curve represents the atmospheric opacity simulated using the AM radiative transfer model. The percentage error between the simulated and calculated opacity is 4.4%, representing the difference between both values. As

a reference, the opacity from the long skydip is included in the orange curve. Above 30 GHz, both calculated opacities are nearly identical, while at lower frequencies, some discrepancies are observed. The low error confirms that short skydip measurements can not only be used to validate the MERRA-2 data, but also facilitate atmospheric studies with high precision, as their opacity results exhibit a level of agreement similar to that obtained from long skydip measurements, where the error is 3.92%.

4.3.4 Precipitable Water Vapor over a 24-years Period

Once the MERRA-2 data have been validated using COMAP skydip measurements, the precipitable water vapor is calculated for a 24-year period, from January 1, 2000, to May 31, 2024. To ensure consistency with the validated MERRA-2 data, it is essential to use the same type of files previously employed, specifically Np files, where atmospheric information is distributed across 38 vertical pressure layers. However, in this case, monthly-averaged data are used instead of three-hour averages. The files, identified by the short name M2IMNPASM, are directly obtained from the MERRA-2 platform, totaling 281 monthly files covering the study period. The procedure described in Sections 4.3.1 and 4.3.2 is followed to derive the PWV over the 24 years. Once the water vapor profiles are obtained, Equation 3.12.2 is applied to integrate specific humidity across the pressure layers, computing the PWV at the OVRO site, as represented by the blue line in Figure 4.3.21. The PWV simulated over 24 years using the AM model is also presented in orange points. In the annual cycles, one maximum and one minimum are identified. The analysis shows that the highest values occur between June and August, whereas the lowest are found between December and February. During the 24-year period, the maximum recorded value reached 28 mm of PWV in July 2018, while the minimum was 4 mm in February 2022. A percent error less of 1% is found between the simulated and calculated PWV over the 24-years evaluation. To understand the climate at the OVRO site, the 24-year period is compared with the wettest and driest months. Figure 4.3.22 presents a statistical analysis using a cumulative distribution function (CDF) of pwv as a percentage of observation time. The blue line represents the entire time period, encompassing all months and years. The green line represents the driest months, which include December, January, and February of all years.

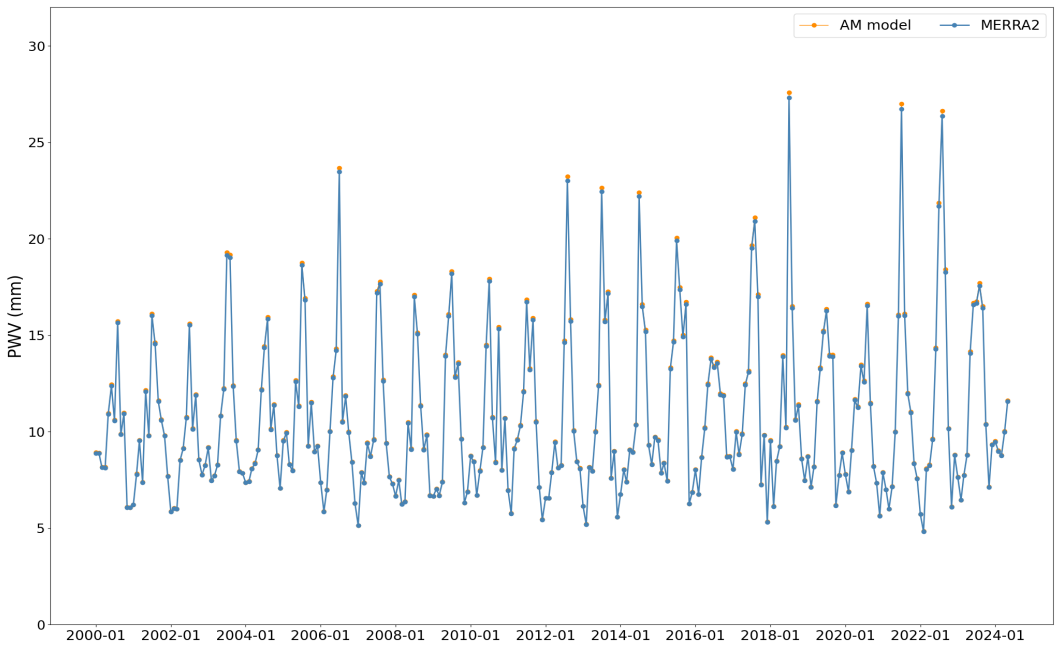

Figure 4.3.21: Variation of precipitable water vapor over a 24-year period at the OVRO site is shown in blue dot-line, derived from MERRA-2 database containing monthly-averaged atmospheric variables. The PWV simulated using the AM radiative transfer model is also displayed in orange dot-line.

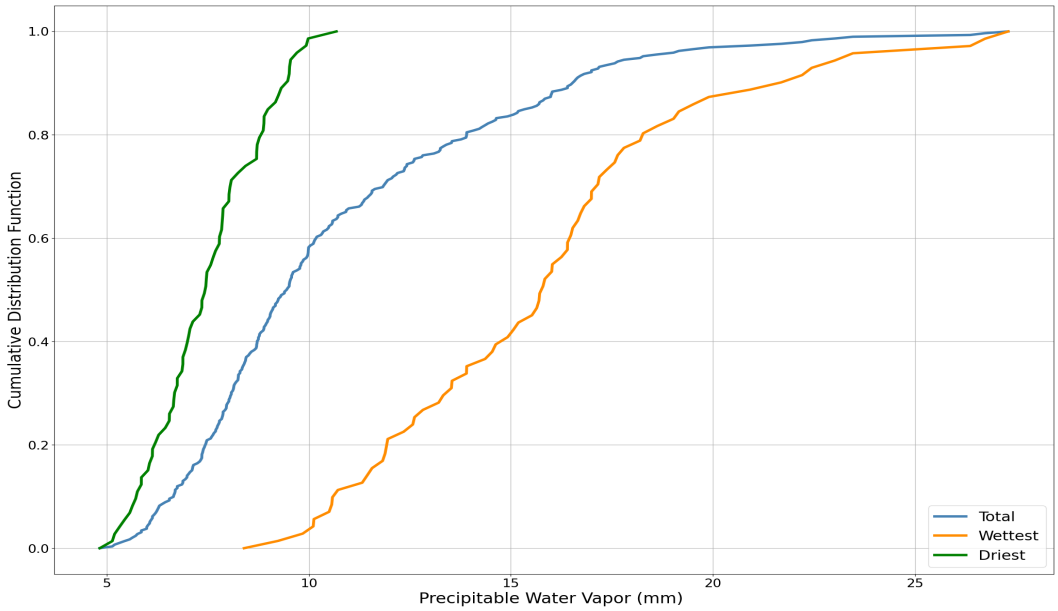

Figure 4.3.22: The cumulative distribution function of PWV values over the 24-year period is represented by a blue line. This curve is compared to the distribution for the driest months, December, January, and February (green line), and the wettest months, June, July, and August (orange line).

The orange line indicates the wettest months, covering June, July, and August of all years. It can be observed that approximately 50% of the observation time corresponds to about 9.5 mm of pwv for the site. In extreme cases, approximately 7.4 mm and 15.7 mm of pwv can be found for the driest and wettest months, respectively. Table 4.3.1 provides additional information on the climatic statistics of PWV data at the OVRO site.

Table 4.3.1: Precipitable water vapor over the OVRO site in different atmospheric conditions.

Observation time (%)	30	50	60	90
Total	8.08	9.45	10.17	16.53
Wettest months	13.32	15.71	16.48	21.69
Driest months	6.68	7.41	7.79	9.47

On Owens Valley, the phenomenon of the Rain Shadow effect plays a significant role in shaping local climate patterns. This effect occurs as moisture-laden air masses are forced to rise over the Sierra Nevada mountains, resulting in precipitation on the western side. However, as the air descends into the Owens Valley, it warms and dries, significantly reducing rainfall. This leads to drier conditions at the OVRO site, particularly during the winter months when the Rain Shadow effect is most pronounced. The data derived from the CDF analysis of PWV further highlight the valley's arid conditions, with the driest months of the year corresponding to the period when the rain shadow effect is strongest, reinforcing the observed patterns of low water vapor. However, during the summer months, the dynamics of the climate in Owens Valley change due to the influence of the southeastern monsoon. This monsoonal flow brings moist air from the Gulf of Mexico and the Pacific Ocean into the region, significantly increasing the moisture content in the atmosphere. These conditions often result in sporadic thunderstorms that lead to rapid increases in PWV, particularly during July and August. The influx of moisture during these monsoonal storms contrasts with the drier winter conditions caused by the Rain Shadow Effect, highlighting the seasonal variability in the valley's atmospheric moisture levels.

Chapter 5

Development of Ultra-Broadband Calibration Loads for the LLAMA Radio Telescope

This chapter presents the development and characterization of calibration loads designed at the CePIA Laboratory of the Universidad de Concepción for the LLAMA project (Chapter 2.2). It begins by introducing the fundamental concept of calibration loads and their intended role within the LLAMA observatory. Subsequently, the specific requirements outlined by the LLAMA project for the construction of these devices are described. The chapter then details the Calibration Loads project's objectives, outlining the distinct areas into which the work was organized. Following this, the results of infrared testing are presented, providing a solid thermal basis that supports progress toward the radiometric characterization. This final section elaborates on the characterization process, the analysis of data, and the findings, which proved to be highly satisfactory.

5.1 Calibration Load: Concept and Utility

A calibration load constitutes a fundamental component in radio astronomy receiving systems, designed to ensure the accuracy of the obtained observational data. Its primary function is to provide a known thermal reference that enables the transformation of radio receiver data into scientifically meaningful units, such as brightness temperature, a key parameter in astronomy, as it represents a direct

measure of the flux from the observed source, as discussed in Section 3.3.
From a functional perspective, calibration loads are foundational for estimating instrumental correction factors, including intrinsic system noise, sensitivity fluctuations, or gain variations in receivers. These parameters are essential for ensuring the reliability of scientific observations, particularly when employing techniques such as the Y-factor method, previously detailed in Section 3.11. Through this technique, thermal loads enable accurate calibration of radio receivers by reducing uncertainties in estimated parameters, ensuring the reliability of observational data.

For the LLAMA project (Chapter 2.2), the Y-factor calibration method requires two thermal loads at significantly different temperatures to enhance the precision of estimated parameters. One load is proposed to operate at ambient temperature, thermally stabilized to the Cassegrain cabin temperature of the telescope, anticipated to maintain approximately 15°C. The second load, intended for higher temperatures, will be designed based on the thermal and resistive properties of the microwave-absorbing material selected as the primary component.
The typical design incorporates a metallic base, often aluminum, onto which the absorbing material is mounted. This configuration allows incident radiation to penetrate the absorber, reflect off the metallic base, and return to the receiver for measurement. This design ensures optimal system response across the evaluated frequency range.
A precise temperature control and monitoring system is vital for maintaining the functionality of the loads. The physical temperatures of the loads must be stringently controlled and tracked. For the hot load, the metallic base will be heated using a regulated heating element, enabling efficient heat transfer to the absorbing material. Temperature values will be monitored via sensors and transmitted to a central computer integrated with LLAMA's control system, ensuring coordinated and accurate operation of the calibration subsystem.
This approach ensures that thermal loads satisfy the stringent requirements for supporting high-quality astronomical observations.

With the foundational concepts and applications of calibration loads established, the next section examines the specific requirements these components must meet to support the LLAMA observatory's scientific objectives.

5.2 LLAMA Requirements

The design and implementation of the calibration subsystem for the LLAMA radio telescope necessitate adherence to stringent material and performance specifications.

1.- Primary material. The calibration loads must consist of a microwave-absorbing material capable of maintaining structural and mechanical stability over a broad temperature range. Following a thorough assessment of potential materials, the absorbent tiles manufactured by *TK Instruments* (UK), known as TK-RAM (Radar Absorbing Material) tiles, were selected. These tiles are composed of polypropylene, a thermoplastic polymer shaped through injection molding to form an array of high-density pyramidal structures. This configuration is designed to enhance electromagnetic wave absorption and effectively reduce reflectivity. The dimensions of the pyramidal elements directly correlate with the frequency range the tiles can cover. Accordingly, two sizes of RAM tiles were selected to meet LLAMA's operational requirements (left panel of Figure 5.2.1). The smaller pyramids, depicted in the right panel of Figure 5.2.1, are effective for frequencies above 150 GHz, although they exhibit increased reflectivity at lower frequencies. Conversely, the larger pyramids, illustrated in the central panel of Figure 5.2.1, operate efficiently from 40 GHz upwards, ensuring superior performance at lower frequencies.

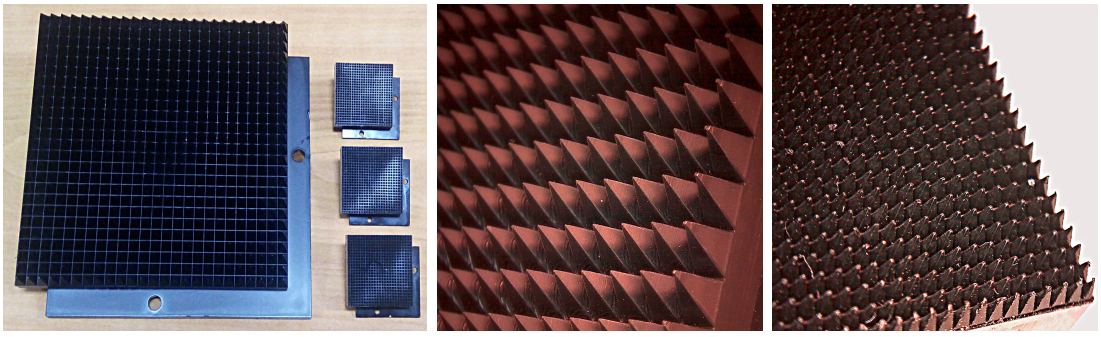

Figure 5.2.1: TK-RAM tiles used as the primary material for the LLAMA observatory's calibration subsystem are shown. The left panel illustrates a size comparison of the large and small RAM tiles. The larger tiles measure 100×100×9.5 mm, while the smaller ones are 25×25×5.7 mm, excluding the pyramidal structures. The central panel provides a microscopic view of the pyramids on the large RAM tiles, with dimensions of 4×4×5.5 mm. Similarly, the right panel displays a microscopic view of the smaller pyramids, measuring 1×1×1.3 mm. Each TK-RAM tile contains a total of 625 pyramids.

Electromagnetic characterization of these materials focused on their reflectivity and return loss to evaluate their effectiveness as microwave absorbers. According to the specifications provided by *TK Instruments*, the smaller RAM tiles achieve reflectivity below -40 dB at frequencies above 150 GHz, while the larger tiles exhibit reflectivity below -30 dB for frequencies starting at 40 GHz. In the W-band (75–110 GHz), the specular reflectivity of the smaller tiles approximates -20 dB, displaying minimal variation with changes in the angle of incidence.
Simulations conducted using HFSS software by Arti Rani [13] further examined the performance of the larger RAM tiles at ambient temperature. Due to the computational demands associated with evaluating the full operational range, the analysis was restricted to two quarter-pyramid pieces arranged in sequence, as shown in panel a) of Figure 5.2.2. These pyramids were modeled within a vacuum waveguide connected to two ports, simulating frequencies between 100 and 500 GHz. The simulation results indicate that the fraction of reflected power remains consistently near -40 dB across the entire evaluated frequency range, as depicted in panel b). Likewise, panel c) illustrates that the portion of power lost during signal propagation, or insertion loss, ranged from -16 dB at 100 GHz to -20 dB at 500 GHz, accounting for the signal's double passage through the material. These results underscore the suitability of the larger RAM tiles for operation across a broad frequency spectrum, with reflective properties and insertion losses well within acceptable limits for submillimeter applications.

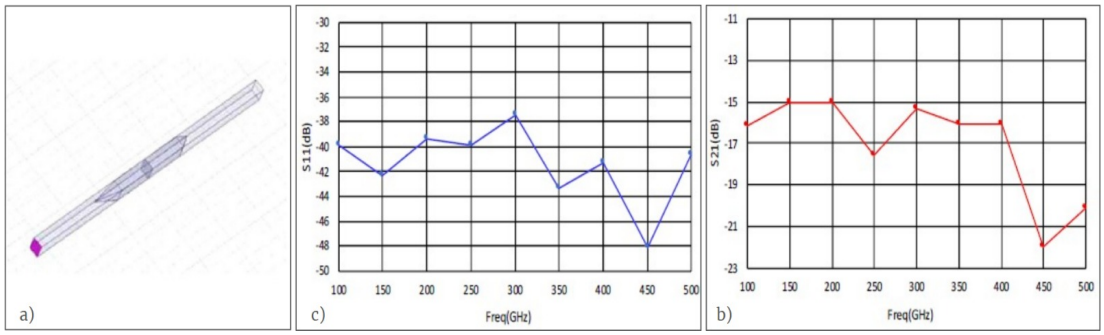

Figure 5.2.2: HFSS simulation of the larger RAM tiles between 100 and 500 GHz. Panel a) shows the arrangement of quarter-pyramids in the simulation, placed within a vacuum waveguide connected to two ports. Panel b) illustrates that the reflected power reaches -40 dB within the evaluated frequency range. Panel c) displays the signal's insertion loss, which ranges from -16 dB to -20 dB as the frequency increases from the lower to the higher evaluation range.

It should also be noted that the material exhibits low thermal conductivity,

approximately 0.5 W/m·K, necessitating significant heating to achieve desired radiometric temperatures. However, the thermal degradation threshold of polypropylene, occurring at temperatures exceeding 100°C, imposes an upper limit on the operational temperature of the tiles.

2.- Dimensions. The effective size of the loads is directly related to the observation frequency bands utilized by LLAMA and the location of the loads in the Nasmyth cabin. The beam projected onto the loads for frequency bands 1, 3, and 9 are 17.2, 8.7, and 6.2 cm at 35 dB, respectively. Consequently, a lower limit for the effective size of the loads is established, which must not be less than 6.2 cm. Note that the term "effective size of the loads" refers to a surface composed exclusively of RAM tiles.

3.- Weight. The ideal weight of each load should be 1 kg, which is considered an acceptable weight for the robotic arm to hold.

4.- Operate at different temperatures. Due to the wide frequency range of LLAMA observatory, at least two calibration loads will comprise the sub-system. A significant temperature difference between loads must be achieved to estimate the instrumental correction factors for the LLAMA receiver. Therefore, at least one load should be used at ambient temperature while the other operates at higher temperatures.

5.- Temperature Stability. The loads must remain stable in temperature during their operation once they are adjusted to a specific temperature.

6.- Temperature Uniformity. The temperature difference across the pyramidal surface of each load must be less than 1°C.

Considering these LLAMA requirements, the calibration loads project and its objectives was established.

5.3 Calibration Loads Project

At the CePIA Laboratory of the Universidad of Concepción, the Calibration Loads project was conceived with the purpose of developing a calibration subsystem for the LLAMA radio telescope. A multidisciplinary team of students from engineering, physics, and astronomy has been instrumental in advancing the project and ensuring its objectives are met by addressing the diverse challenges it

entails. Appendix A provides details of the team members and their contributions, emphasizing their specific roles and the collective impact on the project's success. The following section presents the project's objectives based on the requirements outlined earlier.

5.3.1 Project Objectives

- ***Main Objective***
  Research and develop three calibration loads to characterize the receiver sensitivity of LLAMA Radio-Telescope.

- ***Specific Objectives***

  1. Design, build and characterize a prototype of calibration load operating at 70°C.
  2. Construct and characterize three calibration loads operating at different physical temperatures simultaneously, ranging from ambient temperature to 70°C.
  3. Develop a closed-loop temperature control system based on FPGAs to monitor and regulate the loads temperature.
  4. Implement a data acquisition system using ACS to connect the thermal control system with the LLAMA middleware.
  5. Install the calibration loads in the Nasmyth cabin of the LLAMA radio telescope to verify compliance with the requirements.

Regarding specific objective 1, the design, construction, and IR tests of the prototype load (PL) were presented in the undergraduate thesis of Lilian Basoalto Salazar to obtain the Astronomer degree [14]. The radiometric characterizations of the prototype are shown in this document. For specific objective 2, the construction of final calibration loads follows the same methodology as the prototype. This document includes a preliminary radiometric characterization. In specific objective 3, implementing a temperature control system for the loads, developed by David Arroyo Reyes and presented in his undergraduate thesis to obtain the Electrical Civil Engineer degree [11]. Lastly, specific objective 4 was addressed by Astronomer Paulina Unanue Morales in her Master's thesis in Physics [52]. The specific objective 5 is not presented in this document.

5.4 Calibration Loads for LLAMA

This section provides a general overview of the key aspects related to the design, temperature control, and monitoring of the calibration loads developed for LLAMA. It should be noted that the detailed discussions of these topics have been addressed in the theses referenced in the preceding section.

5.4.1 Design Aspects

Mechanical. The development and design of the calibration loads for LLAMA centered on the concept of encapsulation. Encapsulated loads are essential for maintaining stable temperatures across their effective area, particularly the block containing the RAM tiles. This design reduces heat exchange with the surrounding environment, ensuring the loads achieve and sustain the desired operating temperatures. Any failure in maintaining these conditions would compromise the calibration of LLAMA's astronomical data, leading to potential inaccuracies in subsequent scientific analyses. Therefore, the selection of materials was a critical aspect of the design process.

Figure 5.4.1 illustrates various views of the final design of the small calibration load, created using SolidWorks. The load has a diameter of 146 mm and a height of 100 mm. At its core lies the RAM block, depicted in black, which is surrounded by a durocotton ring. Durocotton, a mechanically robust plastic with low thermal conductivity, helps insulate the RAM tiles.

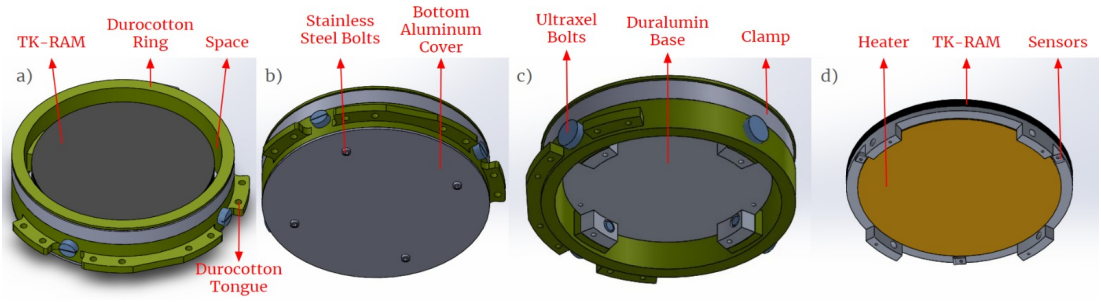

Figure 5.4.1: Illustrations of the mechanical design of the small calibration load, including material specifications chosen to minimize heat transfer from the RAM block to the environment. The figure also highlights the placement of PT100 sensors and the heater, essential for ensuring uniform heat distribution to the RAM block (Credit: Basoalto [14]).

Additionally, the load includes ultraxel bolts, known for their high mechanical strength and temperature resistance. The RAM tiles are covered with a transparent Mylar film, held in place by a metallic clamp not shown in the design. This film is ideal for radiometric studies due to its transparency to microwave radiation, effectively isolating the interior components from the environment. Panel (a) shows the RAM block, 120 mm in diameter and composed of 25 small tiles mounted on a duralumin plate with thermally conductive cement. The plate incorporates four pillars housing ultraxel bolts, as detailed in panels (c) and (d). The plate's machining reduces contact with the durocotton ring, which features rectangular cutouts for connecting both components via ultraxel bolts. Non-contact areas create empty spaces that reduce heat transfer to the environment. Duralumin was selected over standard aluminum (AA1100) for its superior mechanical strength and machinability. Panel (d) reveals the back of the load, where a circular orange heater uniformly warms the duralumin plate, transferring heat to the RAM block. To ensure even heating, a heater covering most of the plate's area was chosen. Surrounding the heater, three PT100 sensors monitor the load's physical temperature during operation. While not visible in the design, mineral wool is layered over the heater to direct heat toward the RAM block and prevent heat loss through the back. An AA1100 aluminum plate secures the wool and fully encloses the load interior, as shown in panel (b). A prototype version of this small load was used for infrared and radiometric evaluations prior to the production of the final versions. Thermal behavior was documented in the author's undergraduate thesis [14], and radiometric testing is presented in Section 5.6.3.
The same design principles and materials were applied to the larger calibration loads, which measure 226 mm in diameter and have a circular form composed of 4 large RAM tiles with an effective area of 200 mm. This larger block supports LLAMA's entire operating frequency range and ensures that the band 1 beam, with a diameter of 17.2 cm, is fully contained within the block.

Thermal Monitoring and Control. To serve as effective calibrators, the Calibration Loads must maintain a stable physical temperature, which necessitates continuous monitoring over time. Figure 5.4.1 illustrates a schematic overview of the thermal monitoring and control system developed by the CePIA Laboratory to achieve this essential requirement. The system includes four principal elements: a temperature measurement subsystem, a heater driver, a control interface, and a

digital module responsible for housing the control strategies. A notable feature of this development is the in-house fabrication of most key components at CePIA, showcasing the laboratory's capabilities.

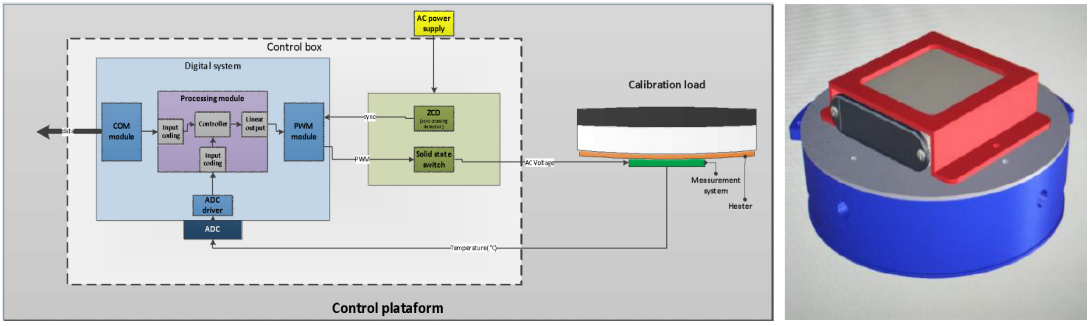

Figure 5.4.2: The left panel presents a schematic of the calibration load control platform, highlighting the components comprising the system (Credit: Arroyo [10]). The right panel displays the small load alongside the conditioning box, which contains the heater control driver (Credit: Arroyo [12]).

The results demonstrate the system's reliability and efficiency, ensuring that the Calibration Loads fulfill their critical role for the LLAMA Observatory, as depicted in Figure 5.4.1. The temperature measurement system achieves a precision of 0.2°C, providing exceptional accuracy. Additionally, a variable voltage controller with linear adjustment, synchronized with the power grid, was implemented to regulate the system.

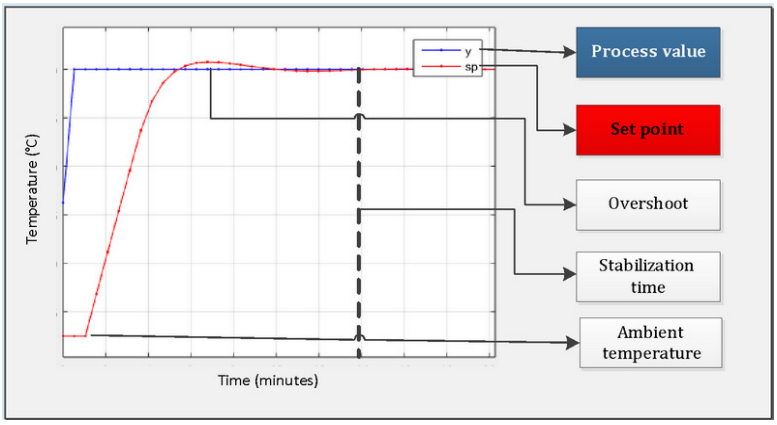

Figure 5.4.3: Temperature response curve illustrating the controlled thermal system's performance, emphasizing its stability and precision (Credit: Arroyo [10]).

Parameter tuning of the controller allows for temperature stabilization within

200 seconds when using a PID loop. In contrast, the natural open-loop system requires approximately 2500 seconds to reach 63.2% of steady-state conditions.

Integration with LLAMA Telescope Control System. The LLAMA Telescope adopts the ALMA Common Software (ACS) architecture as a distributed framework for implementing standardized tools for data acquisition and control systems. This software framework provides mechanisms to encapsulate communication with processes linked to hardware devices, as depicted in Figure 5.4.1. Through the implementation of the DevIO class, it enables efficient interaction with instruments, supporting read and write operations while facilitating the standardized use of properties such as method invocation and alarm transmission.

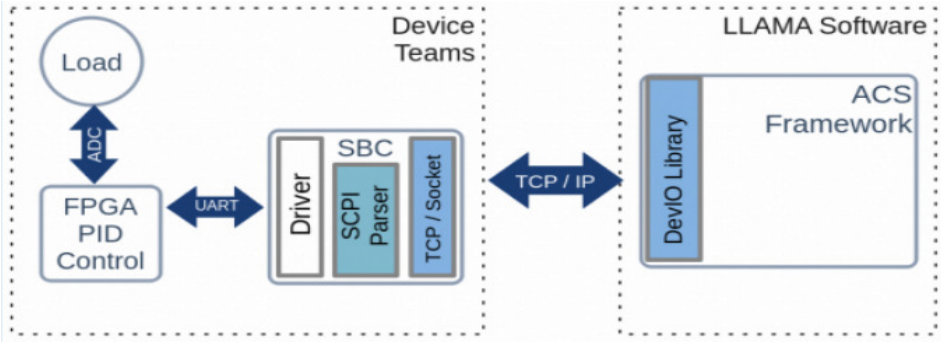

Figure 5.4.4: System communication architecture illustrating the data flow between the main computer, equipped with LLAMA software, and the calibration loads. The system employs a TCP/IP protocol for data access, while a Single Board Computer (SBC) interprets the information and relays requests to the FPGA using a serial communication protocol (Credit: Unanue [52]).

The ACS components for the calibration loads were developed in the C++ programming language. These components integrate the required hardware interface software and testing protocols, enabling the monitoring and control of the three calibration loads via a TCP/IP socket. This system relies on Standard Commands for Programmable Instruments (SCPI) to execute read and write commands. Figure 5.4.1 illustrates the graphical user interface designed to display the temperatures of the three calibration devices.

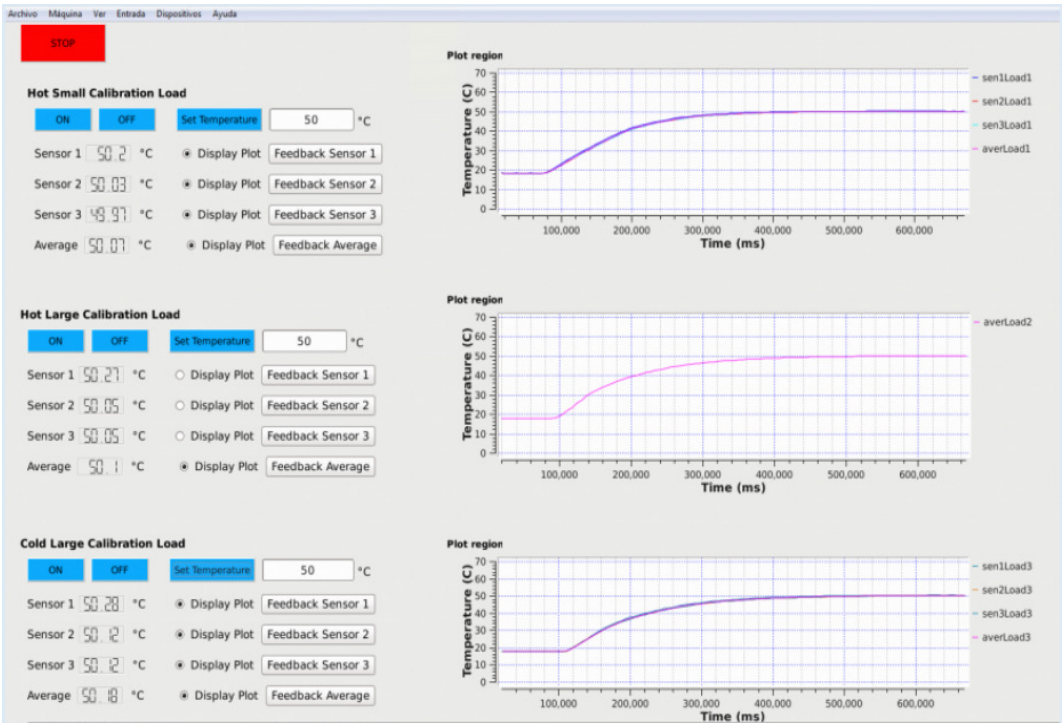

Figure 5.4.5: Graphical user interface for controlling the calibration loads, presenting the temperature settings for each device. The displayed graph indicates a target temperature of 50°C for the loads (Credit: Unanue [52]).

Mechanical Integration in LLAMA. The upper panel in Figure 5.4.1 provides a comprehensive view of the Cassegrain (CASS) cabinet, emphasizing the placement of the three calibration loads alongside the control box developed by CePIA. This box accommodates the thermal regulation system for the loads and incorporates the communication interface linking them to the LLAMA software. The lower panels deliver focused views: the left panel showcases the robotic arm, where the three calibration loads are individually connected to the control box through dedicated cables, while the right panel illustrates the control box securely mounted to the external section of the Cassegrain structure. The system is interconnected via routed cables, ensuring integration with the LLAMA framework.

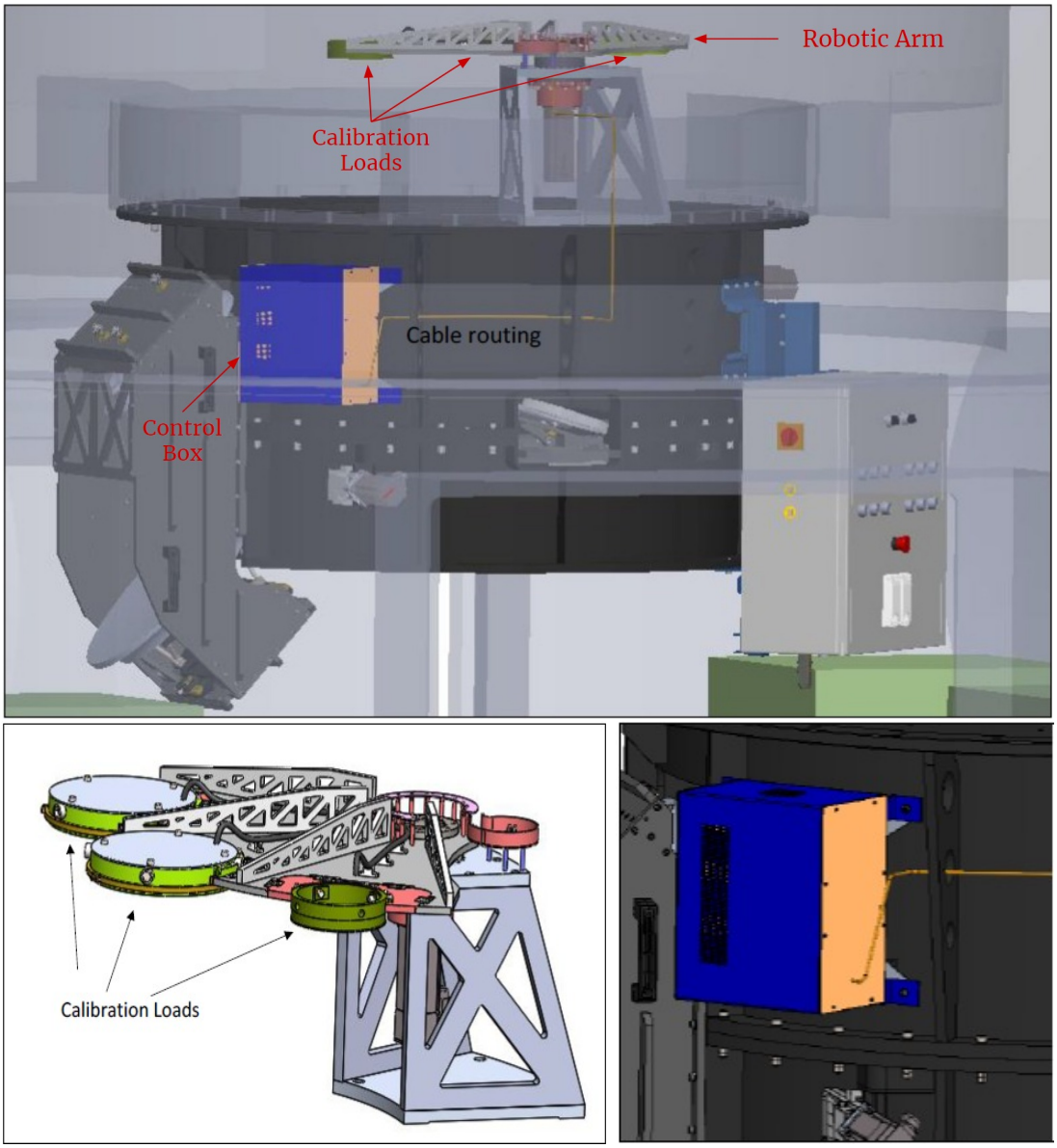

Figure 5.4.6: The upper panel presents an expanded view of the Cassegrain cabin, highlighting the robotic arm with the calibration loads mounted at the top, alongside the control box affixed externally. The lower panels offer detailed perspectives of the calibration loads and the control box (Credit: Rasztocky and Team [46]).

5.4.2 Physical Presentation

This section introduces the four calibration loads designed for LLAMA, of which three are intended for deployment in the radio telescope.

Figure 5.4.7 illustrates the prototype load, constructed in accordance with the mechanical design principles described previously in Section 5.4.1. The left

panel displays the RAM block along with its aluminum base, which forms the fundamental structure of the calibration loads. Directly below the aluminum base resides a circular resistive heater, orange in appearance, responsible for heating the base to a specified temperature. This temperature is continuously monitored by three PT100 sensors positioned at 120° intervals around the aluminum surface, as shown in the central panel. The right panel presents all components enclosed within materials with low thermal conductivity, effectively controlling heat exchange with the external environment. A Mylar sheet is secured over the RAM block using a metal clamp, which serves as an insulator from the exterior to prevent convection on the RAM surface, avoiding thermal gradient issues, and ensuring accurate measurement of the radiation emitted by the RAM tiles.

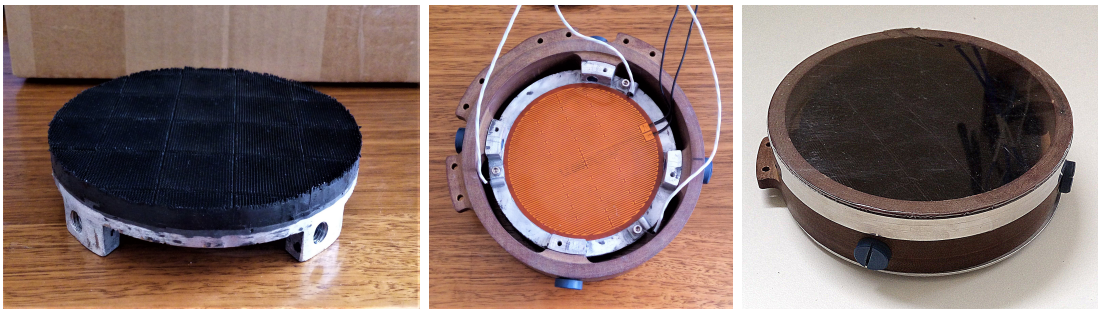

Figure 5.4.7: Prototype Load presentation based on mechanical design. The left panel reveals the base of the prototype, consisting of a RAM block mounted on an aluminum plate. The central panel provides an internal view, highlighting the components beneath the aluminum plate: the orange heater and three PT100 sensors positioned around it. The right panel displays an external view of the load encapsuling the primary base.

Figure 5.4.8 illustrates the complete calibration instrument delivered to LLAMA, comprising three calibration loads and a control unit. The final loads were manufactured based on the same encapsulation design as the prototype but were scaled to different sizes, as shown in the left panel. The smallest load, identifiable by its white clamp, weighs approximately 0.6 kg, meeting LLAMA's design criteria. The larger loads, marked with red and blue clamps, weigh approximately 1.3 kg each, thereby exceeding the specified weight limits. Collectively, the loads have a combined weight of 3.2 kg, which deviates from LLAMA's original requirements. The central panel highlights the rear sections of the loads, where individual compartments house the thermal control drivers. These compartments are connected to the control box via a robust cable equipped with DB9 connectors on both ends. The control box, depicted in the right panel, contains an FPGA

card that implements PID control strategies, a Raspberry Pi 4b, and associated electronic components. This system enables precise thermal regulation of the loads, allowing their physical temperatures to be controlled through a user interface. Additionally, the system facilitates the acquisition of temperature data essential for LLAMA's scientific objectives.

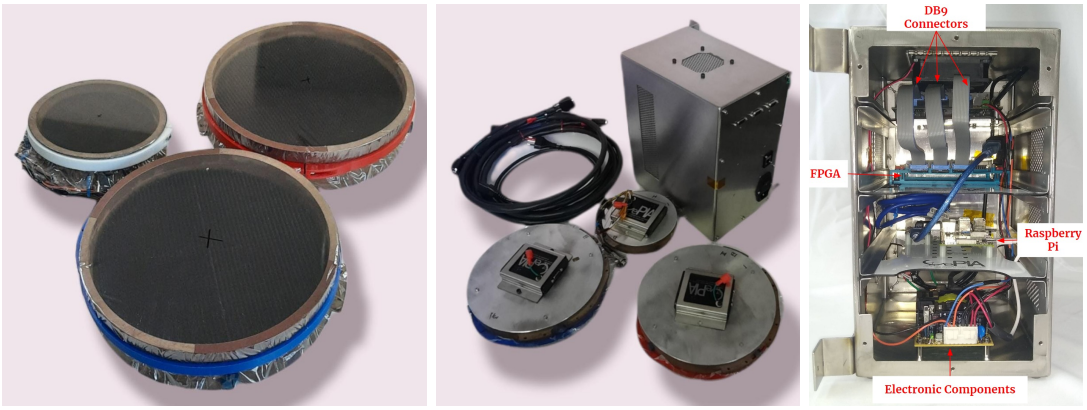

Figure 5.4.8: Presentation of the calibration instrument for LLAMA. The left panel displays the three final calibration loads designed to minimize thermal exchange with the surroundings. The central panel presents the complete system, including the three loads and the control box. The rear view reveals the compartments containing the thermal control drivers, which are connected to the control box using durable cables with DB9 connectors. The right panel shows the interior of the control box, featuring the FPGA and Raspberry Pi, which form the basis of the thermal control and data acquisition system.

Figure 5.4.9 depicts the final calibration loads mounted on the robotic arm positioned atop the Cassegrain cabin of the LLAMA radio telescope. This mechanical integration test was conducted at the ALFA mechanical workshop located in Araraquara, São Paulo, Brazil. The robotic arm, constructed from anodized aluminum, exhibits remarkable mechanical strength. Despite the loads exceeding the specified weight by 200 grams, the test results demonstrate that the arm can support them without significant structural deformations. The loads are positioned facing downward due to their interaction with the LLAMA optical system, which redirects the beam toward the receivers located in the two Nasmyth cabins on either side of the Cassegrain structure. This optical system is situated below the arm and inside the Cassegrain cabin. During calibration procedures, the arm will move horizontally to present each load to the corresponding receivers.

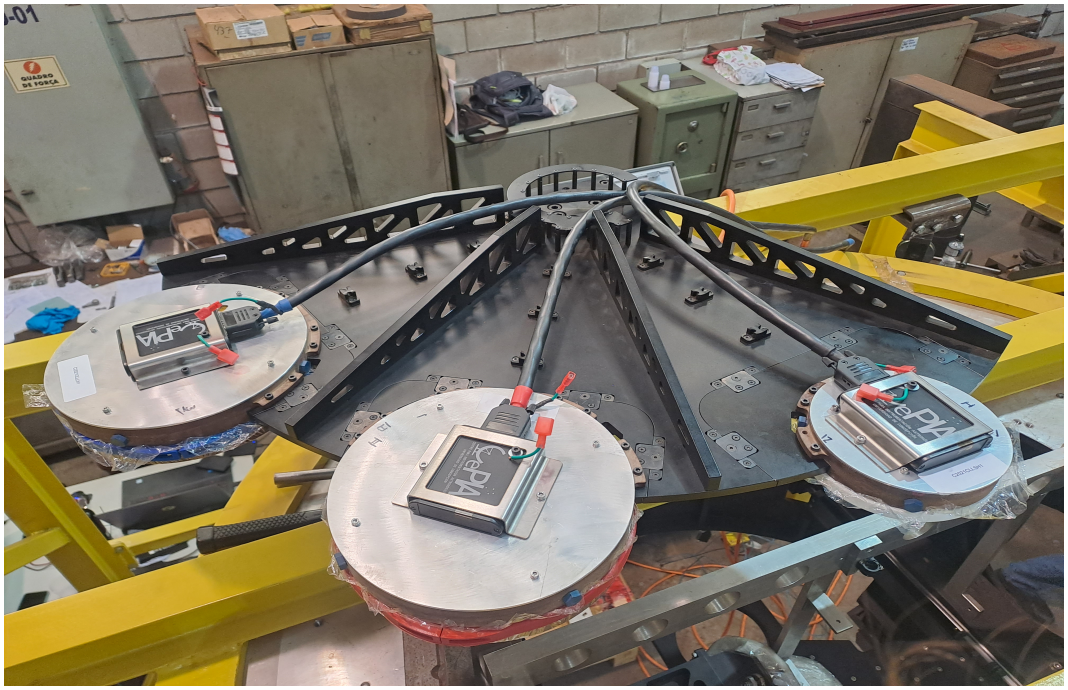

Figure 5.4.9: Final calibration loads mounted on the robotic arm of the Cassegrain cabin of the LLAMA radio telescope.

5.5 Infrared Measurements of Calibration Loads

Infrared measurements of the loads are essential to accommodate radiometric measurements. Therefore, ensuring thermal temperature uniformity across the TK-RAM block of each calibration load is the primary objective to guarantee proper functionality.

This section presents infrared temperature values when the loads have reached a stable infrared state. The infrared measurements are conducted using a GOBI640-GigE camera, sponsored by Dr. Sebastián Godoy, professor of the UdeC Engineering Department, and Mr. Luis Arteaga, Laboratory Manager of the Image and Signal Processing Laboratory of the same department. The IR Camera is presented in Figure 5.5.1 and its respective interface. It is essential to consider that the use of Mylar in this IR stabilization study is significant, as it prevents convection with the surrounding environment, thereby enabling faster and more sustained stabilization over time. Another crucial aspect is that Mylar is not transparent to infrared radiation, which implies that the IR measurements are expected to show a reduction in the actual temperature present on the RAM block. Based on this, it should be noted that the study conducted on the prototype load

was performed without Mylar, as the potential impact of Mylar on the infrared results was unknown at that time.

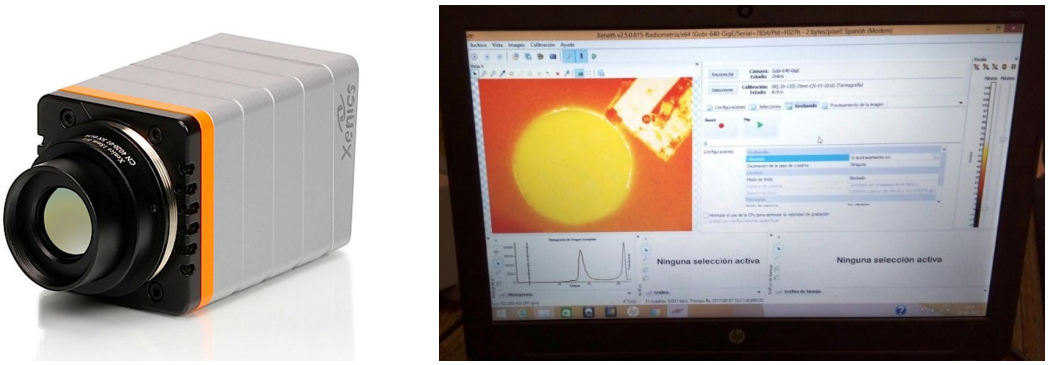

Figure 5.5.1: Right panel: The GOBI640-GigE IR camera used to perform infrared measurements of the calibration loads is shown. Left panel: The user interface of IR camera, which enables access to infrared images and data, is displayed

Therefore, the results presented in the author's thesis [14] do not account for the Mylar effect. An update of the IR data for the prototype has not been possible as all efforts were directed towards the IR and radiometric study of the final loads and also because of the availability of the IR camera. Since this has already been reported, only the final outcome will be provided in this document. Conversely, the infrared study of the final loads did consider the use of Mylar. Figure 5.5.2 displays two IR images of the prototype when set to 70°C using the thermal control, starting from an ambient temperature ∼20°C. The image was captured 14 minutes after the thermal control was activated. The left panel shows the prototype within a temperature range of 17°C tp 63°C. Conversely, the right panel narrows this range significantly to emphasize temperature differences between 57°C and 62°C. The denote Selection A, marked by a black circle at the center of each image, indicates the area where the thermal study is conducted. The diameter of Selection A, measuring ∼87 mm, simulates the beam expected to impinge upon the TK-RAM block from Band 3 of a LLAMA receiver. The average temperature within Selection is 58.94°C, with data dispersion < 1°C with $\sigma = 0.56$°C. The maximum and minimum temperature difference within the selection is 3.5°C. These results are entirely acceptable and meet the requirements established at the beginning of the project. The infrared stabilization study over time of the final calibration loads with mylar is presented. As depicted in Figure 5.5.3, from left to right, the large red load, the large blue load, and the small load can be

observed fixed on an optical table.

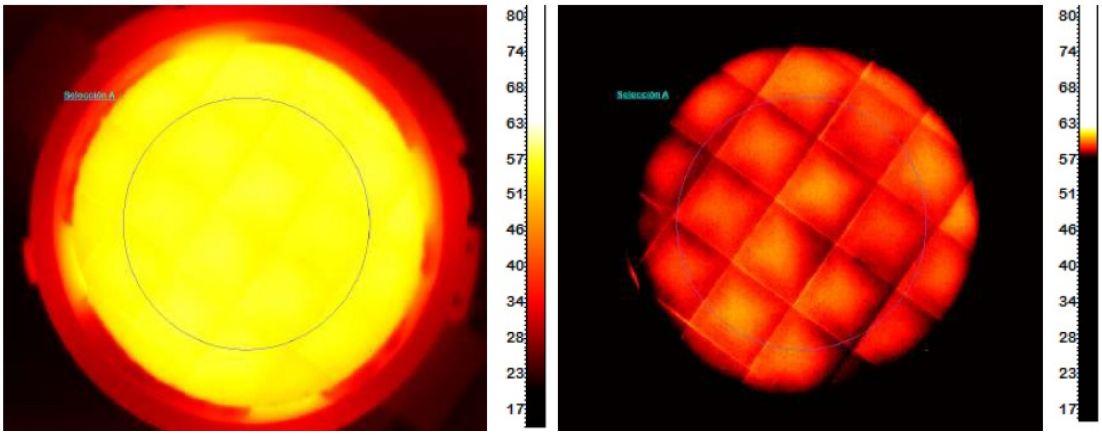

Figure 5.5.2: IR images of the prototype stabilized at 70°C are shown, specifically focusing on Selection A, marked by a black circle. The left panel presents the full temperature range between 17°C and 63°C, while the right panel displays an adjusted range between 57°C and 62°C to better visualize temperature differences. The average temperature of Selection A is 58.94°C.

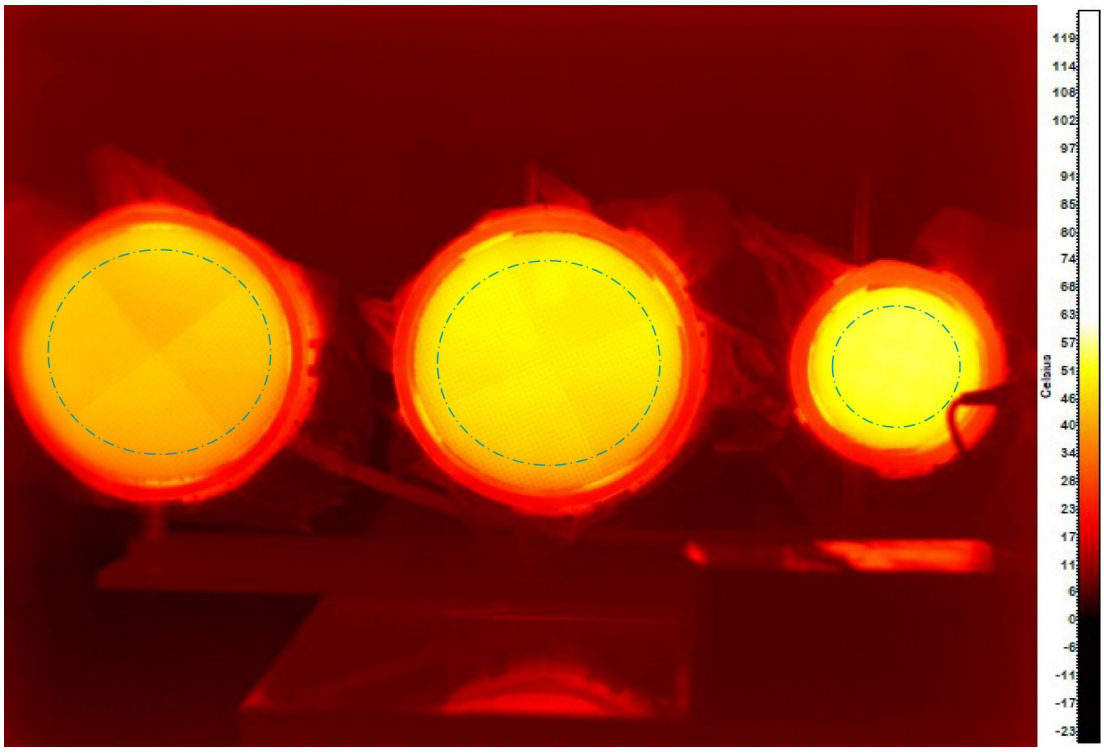

Figure 5.5.3: An infrared image of the three calibration loads during the IR stabilization state over time at a set temperature of 70°C is shown. From left to right, the large red load, the large blue load, and the small load are displayed, each with a circle centered over the RAM block, where the temperature analysis will be conducted.

The loads were stabilized at 70°C from an initial ambient temperature of approximately 20°C. Images were captured after 1 hour of thermal control activation and then every 30 minutes for 3 days, maintaining the positions shown in the figure.

Figure 5.5.4 illustrates the infrared stabilization of the three loads over time. The orange line corresponds to the small load, the large blue load is represented by the light green line, and the red line denotes the large red load.

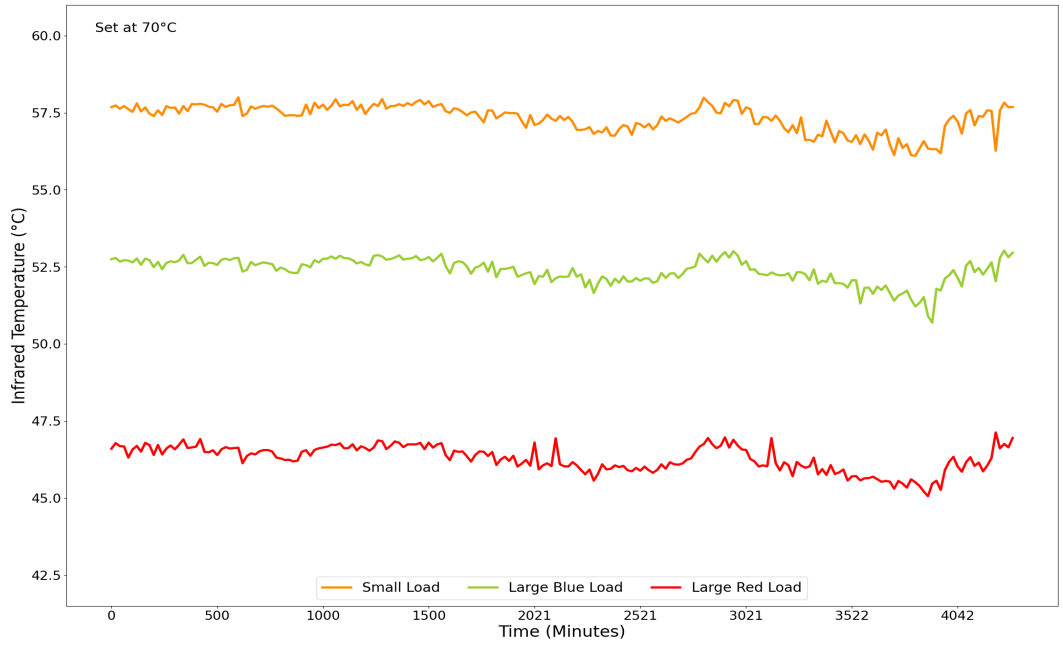

Figure 5.5.4: The IR data of the three final calibration loads during the temperature stabilization study are presented. The study was conducted over 3 days, capturing images every 30 minutes. Each load yielded an average IR temperature of 57.33°C, 52.38°C, and 46.28°C for the small load, the large blue load and the large red load, respectively. Each is associated with an error of less than 1°C.

By time averaging the temperature for each load along with their respective errors, the small load achieves an average of 57.33°C with $\sigma = 0.44$°C, the large blue load stabilizes at 52.38°C with $\sigma = 0.40$°C, while the large red load averages 46.28°C with $\sigma = 0.42$°C. It should be noted that these averaged values include the effect of Mylar, which means the actual temperature over the RAM block should be higher, although the exact value is unknown. Nonetheless, these values are entirely valid and meet one of the project requirements: an associated error of less than 1°C, enabling advancement to the radiometric study.

5.6 Radiometric Measurements of Prototype Load

To conduct the radiometric measurements, several preliminary tasks were necessary: 1) implementing a receiver capable of measuring the power of the blackbodies, 2) calculating beam propagation over blackbodies, 3) developing an automated system to perform the power measurements, and 4) designing and fabricating supports for both the receiver and the automated system. This section provides a detailed description of each task and emphasizes its significance in the overall measurement process.

5.6.1 Previous Considerations

Defining the operating frequency before initiating any task was crucial, ensuring it aligned with the operation frequency range of LLAMA. Due to the availability of components, a 93-GHz receiver was implemented, forming the basis for all subsequent tasks. Figure 5.6.1 illustrates the 93-GHz total power heterodyne receiver schematic. The receiver consists of a Mi-Wave circular corrugated feed horn operating in the W band. Although the manufacturer specifies its operational range as limited to 92–94 GHz, it is considered that its bandwidth might be significantly broader since the W band spans frequencies from 75 to 110 GHz. The signal is subsequently amplified by two low-noise amplifiers (LNAs) developed by NASA's Jet Propulsion Laboratory (JPL), which together achieve a maximum gain of -40 dB centered at 93 GHz. Next, the signal is processed through a Virginia Diodes mixer designed to operate in W-band, with optimal performance when the Millitech x4 local oscillator delivers 3 dBm of input power. Following the mixing stage, the intermediate frequency signal, ranging from DC to 15 GHz, is filtered by two Mini-Circuits low-pass filters with a bandpass from DC to 3 GHz. Finally, the filtered signal is measured using a Keysight power meter. After testing the receiver, a receiver temperature of approximately 540 K was obtained, which is within the acceptable range for maintaining the instrument's operational status, allowing it to be used in the measurements. As this topic is beyond the scope of this thesis, it will not be discussed further in this document. The receiver's performance in radiometric measurements is detailed in the results section 5.6.3.

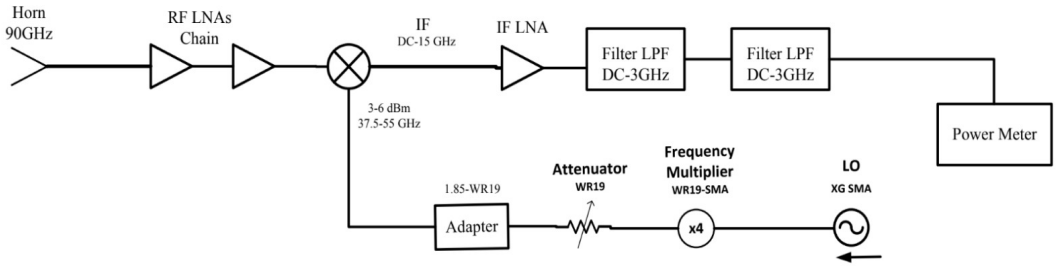

Figure 5.6.1: 93-GHz total power and heterodyne receiver scheme used in the radiometric measurements of the prototype.

Determining the maximum permissible distance between the prototype and the feedhorn is crucial for configuring the automated system. This process requires analyzing the prototype's beam size projection over the RAM block. The Gaussian beam propagation procedure requires understanding 1) the type and inner radius of the feedhorn, 2) the distance from the beam waist to the aperture, and 3) the maximum beam distance. The feedhorn in use is corrugated, so the beam waist size is calculated based on the inner radius $a = 0.75$ cm, using the beam waist Equation from Goldsmith [27]:

$$\begin{aligned} w_0 &= 0.644 \cdot a \\ &= 0.644 \cdot 0.75\ cm \\ &= 0.483\ cm \end{aligned} \tag{5.6.1}$$

where 0.75 cm represents the feedhorn radius, and 0.483 cm denotes the beam waist size specific to this feedhorn. The distance z from the beam waist to the aperture is then calculated using the slant length $R_h = 4.1$ cm, the wavelength $\lambda = 0.323$ cm, and the beam waist w_0, by substituting these parameters into distance Equation according to Goldsmith [27]:

$$\begin{aligned} z &= \frac{R_h}{1 + \left(\frac{\lambda \cdot R_h}{\pi \cdot w_0^2}\right)^2} \\ &= \frac{4.1\ cm}{1 + \left(\frac{0.323\ cm \cdot 4.1\ cm}{\pi \cdot (0.483\ cm)^2}\right)^2} \\ &= 0.963\ cm \end{aligned} \tag{5.6.2}$$

This calculation reveals that the beam waist is located at 0.963 cm inside the feedhorn aperture. It is important to note that R_h is not measured directly; it is estimated based on the feedhorn's design. Subsequently, the beam radius w is calculated for various distances z. By incorporating the wavelength λ and beam waist w_0, these parameters are substituted into beam waist Equation given by Goldsmith [27]:

$$\begin{aligned} w &= w_0 \cdot \left[1 + \left(\frac{\lambda \cdot z}{\pi \cdot w_0^2}\right)^2\right]^{1/2} \\ &= 0.483\ cm \cdot \left[1 + \left(\frac{0.323\ cm \cdot z\ cm}{\pi \cdot (0.483\ cm)^2}\right)^2\right]^{1/2} \end{aligned} \tag{5.6.3}$$

Starting from $z = 0$ cm which corresponds to the beam waist location, the beam radius is evaluated in 1 mm increments until the maximum beam radius is identified. According to [27], a beam diameter equal to four times the beam radius truncates the beam at 34.7 dB, encompassing 99.97 % of the power in the Gaussian beam, a criterion adopted in this thesis. Considering these factors, the maximum beam radius w_{max} selected from the w_0 is:

$$w_{max} = 2.589\ cm \quad at\ \ z = 11.963\ cm \tag{5.6.4}$$

and the maximum illumination diameter $\varnothing_{max}$ over RAM block is:

$$\begin{aligned} \varnothing_{max} &= 4 \cdot w_{max} \\ &= 10.355\ cm \quad at\ \ z = 11.963\ cm \end{aligned} \tag{5.6.5}$$

Consider that a maximum diameter of 10.355 cm at a distance of 11.963 cm is calculated from the w_0 inside of the horn but the effective distance is only 11 cm which corresponds to the distance from the aperture. Remember that the RAM block has a 12 cm diameter but a margin approximated of 0.7 cm by side was allowed for potential design and fabrication errors. Appendix C shows Table C.1 detailing the beam diameters at various distances.

An automated system based on FPGA was developed to continuously monitor the receiver's performance over an extended period without human intervention [9]. The behavior of the receiver directly impacts the accuracy of prototype measurements, influencing the precision of its characterization. The decision to

eliminate manual measurements stems from insights gained during preliminary evaluations of final loads, as detailed in Section 5.7. The current objective is to monitor the receiver temperature more frequently, enabling real-time feedback on measurement status. This approach facilitates the identification of acceptable or not acceptable T_{rx} measurements, allowing the process to be paused for the further investigation if issues arise, thus conserving both time and liquid nitrogen. Proper calibration, according to theoretical guidelines, requires at least two calibrators with known temperatures. In this case, one calibrator is at ambient temperature, while the other is immersed in liquid nitrogen (LN2) at 77 K (or -196.15°C). The system is engineered to sequentially measure the power from both calibrators and the prototype.

Figure 5.6.2 presents four panels providing various perspectives of the automated system. The triangular mirror includes two reflective aluminum plates and a third surface containing a calibrator used at ambient temperature. The dimensions of the mirror were determined by the previously calculated maximum allowable distance.

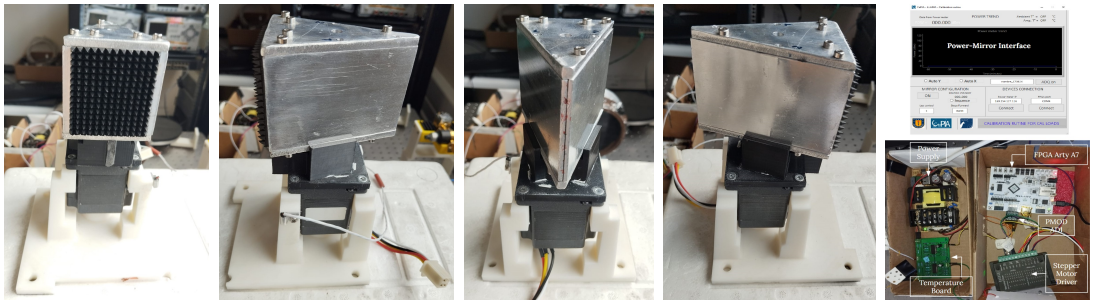

Figure 5.6.2: The FPGA-based automated mirror-motor system is illustrated with multiple perspectives. The first four panels, from left to right, present various views of the mirror, motor, and its supporting structure. In panel 1, the ambient calibrator is attached to one side of the mirror. Panel 5 displays the core components enabling motor movement: the ARTY A7 FPGA board, motor driver, temperature control board, and power supply. The top section of panel 5 shows the control interface based on Python used to operate the mirror system.

The first panel displays a black calibrator constructed from a large RAM piece, cut to dimensions of 5 cm by 6 cm, and mounted on an aluminum plate. The second, third, and fourth panels show the aluminum plates, each measuring 9 cm by 6 cm, polished to a reflective finish. A motor positioned beneath the mirror enables it to rotate 360° counterclockwise. The second panel also illustrates a PT100 temperature sensor bolted on a white pillar, which measures the ambient

load temperature. The power measurements setup was meticulously designed to optimize the alignment and spacing between all components. This configuration ensures that the beam is fully contained within the mirror surface upon reflection and accurately intersects the RAM tiles, guaranteeing precise measurements. Figure 5.6.3 illustrates a design of the different configurations utilized for power measurements, depicting the horn, the mirror, and the prototype, with the center of the horn serving as a reference point. The placement of the mirror relative to the horn and prototype was determined based on the previously calculated maximum allowable distance.

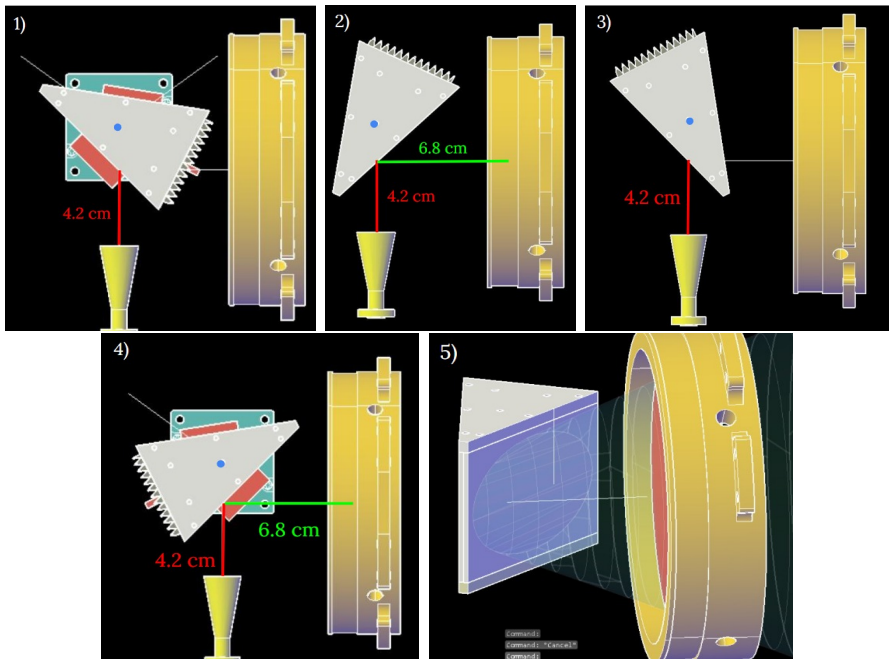

Figure 5.6.3: Illustration of the primary components involved in the power measurement process to ensure the success of the procedure. Panel 1, 2, 3, and 4 show the four main mirror positions: two directed towards the prototype and two towards the LN2 calibrator. All distances are measured relative to the receiver horn. When the mirror reaches its respective position, the horn-to-mirror distance is 4.2 cm, except when pointing at the ambient calibrator, which is measured directly. Panel 5 displays the beam reflected from the mirror to the prototype, demonstrating that the beam remains entirely within the mirror surface, a crucial condition to ensure precise power measurements (Image credits: Jorge Muñoz Mujica, Designer, CePIA).

The mirror aligns with the prototype in panels 2 and 4 and is directed toward the LN2 calibrator in panels 1 and 3. In all configurations, the distance between the horn and the plates remains consistently at 4.2 cm. The prototype and LN2 calibrator are arranged at a 90° angle relative to the center of the horn, with the

plates positioned at a 45° angle. This arrangement ensures that the beam from the horn reflects at a 90° angle toward either the prototype or the LN2 calibrator. Furthermore, the prototype is placed 6.8 cm from the plate, establishing the maximum effective distance of 11 cm between the aperture of the horn and the RAM block. The center of rotation of the mirror is represented by a blue point in the panels. Panel 5 verifies that the beam is fully contained within one of the mirror's surfaces, a crucial confirmation to guarantee the accuracy of the measurements. After establishing the appropriate distances, the liquid nitrogen calibrator is presented in Figure 5.6.4. The first panel depicts the calibrator, constructed from four large RAM tiles fixed to an aluminum plate measuring 26 cm square and 0.5 cm thick. As shown in the second panel, this calibrator is vertically positioned inside a polystyrene box. The box will filled with liquid nitrogen, fully submerging the calibrator, allowing it to reach the LN2 temperature. The third panel shows a 3 cm gap between the calibrator and the inner wall of the box ensures direct contact between the LN2 and the RAM block. The LN2 box is centered concerning one of the mirror plates, as shown in panels 1 and 3 of Figure 5.6.3. In these mirror configurations, the box is positioned 15 cm away from the plate, resulting in a total distance of 19.3 cm from the aperture of the horn. At this distance, the illumination diameter is fully contained within the RAM block submerged in LN2, with a diameter measuring 16.525 cm.

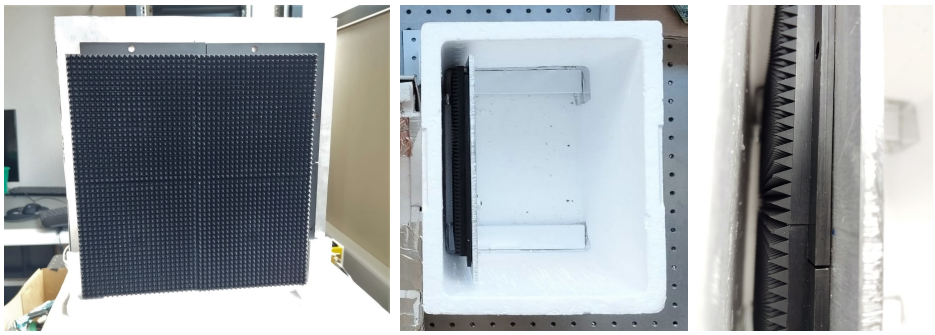

Figure 5.6.4: Calibration device based on RAM tiles. Panel 1 displays the calibrator, which consists of four RAM segments mounted onto an aluminum plate and designed to be submerged in LN2-box. Panel 2 illustrates the calibrator placement inside the expanded polystyrene container, which is pointing to the mirror. Panel 3 provides a broader view, highlighting that the calibrator does not touch the container walls, allowing the calibrator to come into direct contact with the LN2.

Figure 5.6.5 illustrates the setup for measuring power from the prototype, with components arranged on the optical table to maintain the previously calculated distance. The prototype load is positioned on the center-left side of the table, connected via a robust wire from the thermal control system housed in a box containing the FPGA, control driver, and power source. Although this system is visible on the table on the image, it is not present during actual measurements. The automated system is divided into three main parts: the mirror at the center and two boxes on the lower left side of the table containing the FPGA, power source, and additional components. Additionally, a PT100 sensor is also visible next to the prototype. The 93-GHz receiver is set up on top of the table in three sections: the RF section at the center, with the horn facing the mirror, the LO system on the left, and the IF section on the right.

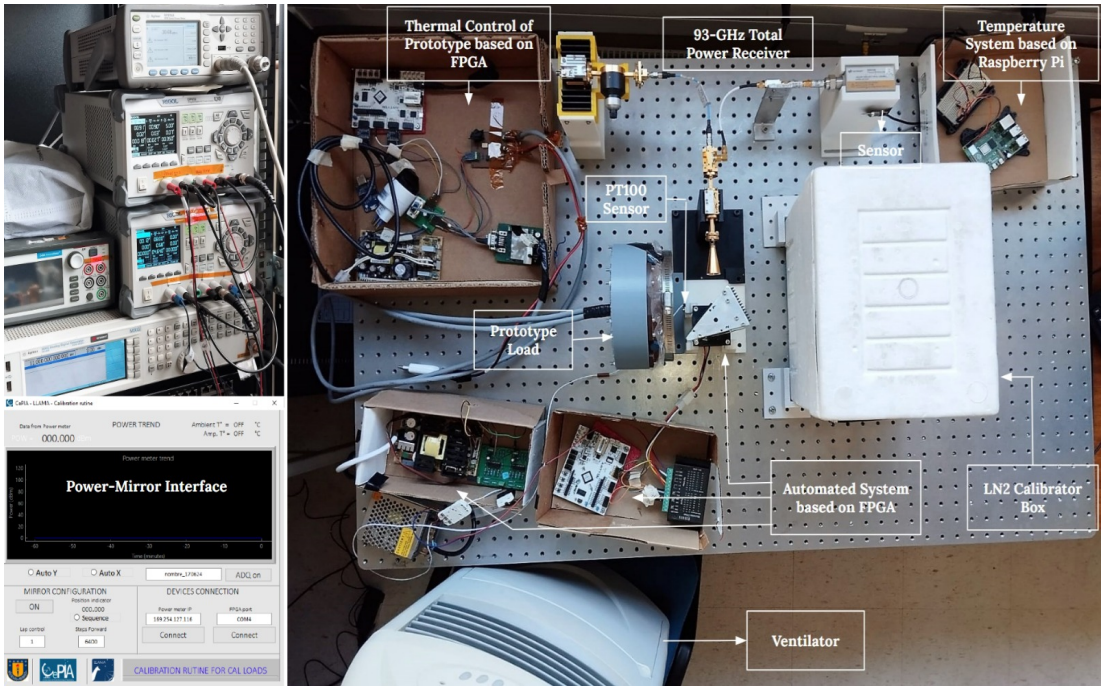

Figure 5.6.5: Radiometric measurement configuration for the prototype. The right panel depicts the setup, which includes a 93-GHz total power receiver, and FPGA-based automated mirror-motor system, the prototype load equipped with its FPGA-based thermal control system, a calibrator submerged in an LN2 container, and a ventilator to minimize frost formation on the container walls. The top left panel presents the supporting instruments required for the receiver operation (Two Rigol Multimeters, an MXG signal generator, and a power meter). The bottom left panel displays the power and mirror positioning interface.

The large white box contains the calibrator submerged in LN2. A ventilator

is used to prevent frost formation on the side wall of the LN2 box in front of the mirror. Lastly, an ambient temperature system based on a Raspberry Pi monitors the room temperature and compares it with the ambient temperature recorded by the PT100 sensor. It is crucial to note that inserting a mirror may affect power measurements due to the emissivity of the aluminum, as discussed in Chapter 4. Therefore, characterizing both sides of the mirror is necessary. This characterization requires the same elements used in the prototype characterization, excluding the prototype itself, and introduces a second LN2 calibrator, distinct from the one previously shown in Figure 5.6.4. Figure 5.6.6 presents a cone-shaped metal calibrator, with its interior lined with black absorber called Eccosorb (as shown in the first panel) and its exterior covered with a copper sheet (as illustrated in the second panel). This calibrator is immersed in liquid nitrogen contained in an expanded polystyrene container, as depicted in the third panel. The calibrator is directly exposed to the receiver, eliminating the need for the mirror in its power measurements.

Figure 5.6.6: Liquid nitrogen direct calibration device utilized in radiometric measurements of prototype. Panels 1 and 2 present different perspectives of the direct cone employed as a calibrator, while Panel 3 displays the expanded polystyrene container designated for the LN2 containment.

Figure 5.6.7 depicts the setup for mirror characterization. In this configuration, the prototype and its associated thermal control system are absent. Instead, the cone (Figure 5.6.6) is positioned in front of the horn and will be submerged in an LN2-filled box placed on the floor beneath the optical table. A metal collector is used to recover LN2 during the measurements.

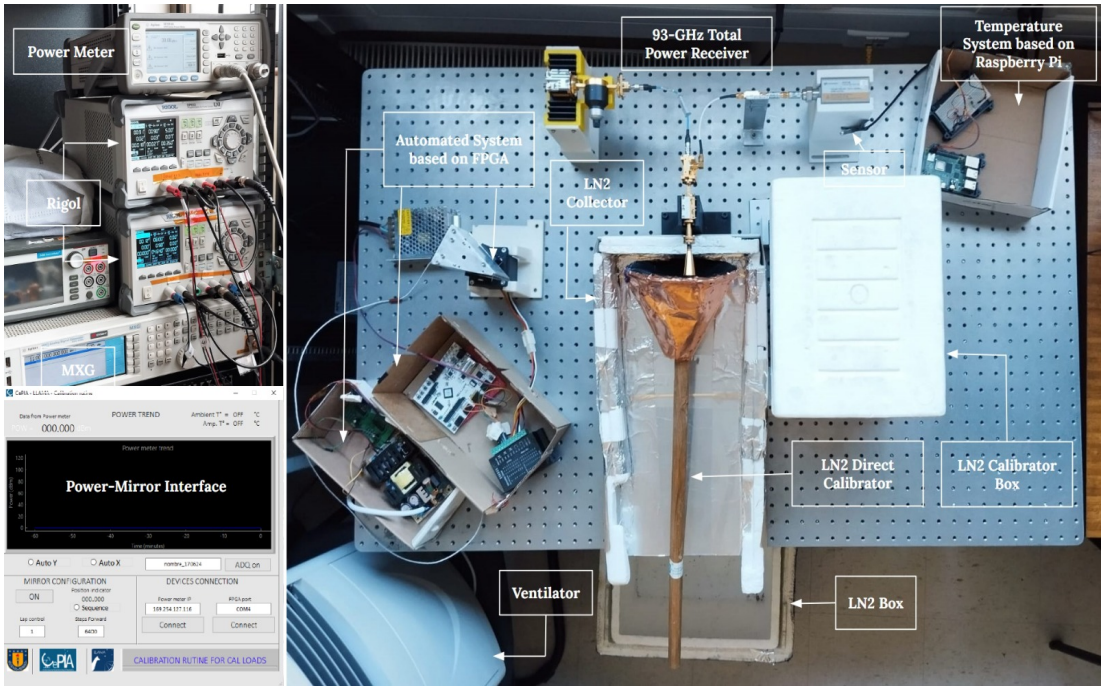

Figure 5.6.7: Mirror characterization setup. The right panel shows the setup, which includes the 93-GHz total power receiver, the automated motor-mirror system based on FPGA, the two LN2 calibrators, a liquid nitrogen collector, and a fan to minimize the frost on the box wall. The top left panel presents the supporting instruments required for the receiver operation (Two Rigol Multimeters, an MXG signal generator, and a power meter). The bottom left panel displays the power and mirror positioning interface.

To ensure accurate power measurements, supports for the primary components: the prototype, receiver, mirror, and LN2 calibrator, were designed and fabricated. Each component needed to be precisely positioned 15 cm high and centered with the horn along the vertical axis. Achieving this alignment was challenging due to the 2.5 cm spacing of perforations on the optical table. The supports were meticulously engineered to maintain the correct height while ensuring the precise distance between components and the horn, allowing the beam to be accurately reflected by the mirror plates without power loss. A deviation of just half a centimeter in the position of the mirror could cause the beam to exit the plate entirely, potentially leading to erroneous measurements.

The procedures for characterizing both the prototype and the mirror are detailed in Section 5.6.2.

5.6.2 Measurement Process for the Characterization of Prototype

This section outlines the measurement method for characterizing both the prototype and the mirror. The prototype characterization requires three essential tasks: **1) Power Stability Measurement Procedure at 40°C, 50°C, 60°C and 70°C.** The decision to start at 40°C, rather than 30°C, was due to the summer ambient temperature being approximately 28°C, rendering it impractical to begin at 30°C. The prototype is maintained at each temperature for about 1 hour, as infrared tests (referenced in Lilian's undergraduate thesis) indicate that the prototype stabilizes within 30 minutes when transitioning from ambient temperature to 70°C. Therefore, the time was standardized not only to ensure stabilization but also to allow for measurements during the stabilization phase at each temperature and, **2) Determining the emissivity of each side of the triangular mirror.**

Figure 5.6.8 illustrates the measurement procedure used to characterize the prototype, corresponding to item 1).

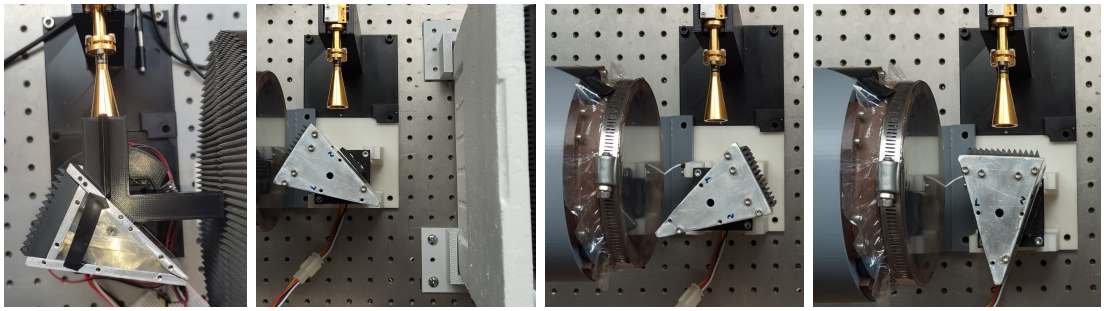

Figure 5.6.8: Various mirror configurations employed for power measurements of the prototype and calibrators, both ambient and LN2. In Panel 1, the manual calibration marks the initial position of the mirror. Panel 2 illustrates the mirror alignment for LN2 measurements, Panel 3 depicts the mirror oriented towards the prototype, and Panel 4 presents the direct measurement of the ambient calibrator.

Panel 1 displays a black piece used to manually establish the initial mirror position, designed as the 0° angle. In Panel 2, the mirror measures the power of the LN2 calibrator using side 2. After remaining stationary for 7 seconds, the mirror transitions to the position depicted in Panel 3, where it faces the prototype and measures its power with side 1, maintaining this position for another 7 seconds. Finally, the mirror brings the ambient calibrator in front of the receiver, as

shown in Panel 4, where it also remains for 7 seconds. This sequence is repeated over several hours until the measurement process is complete. In principle, this procedure must be repeated during 4 hours to achieve the objective 1).
Figure 5.6.9 presents the configurations used during the characterization procedure of the mirror, corresponding to item 2). This procedure is conducted for both aluminum plates, designed as sides 1 and 2, to clearly distinguish which side is being tested. Determining the emissivity of each side individually is essential. Panel 1 shows the ambient temperature calibrator directly presented to the receiver. Panels 2 and 4 depict the measurements of the LN2-immersed calibrator using sides 1 and 2 of the mirror, respectively. Panel 3 illustrates the manual measurement with the LN2 cone. In each configuration, the mirror pauses for 7 seconds in front of the receiver. The mirror rotates 360° counterclockwise, beginning with the ambient load (Panel 1), then measuring the LN2 calibrator with side 1 (Panel 2). After completing one full rotation and returning to the ambient calibrator, the mirror is promptly removed from the center, and the LN2 collector is positioned to enable manual measurement with the LN2 cone (Panel 3). Finally, the mirror is repositioned in front of the receiver to restart measurements. The same procedure is applied for side 2, where the LN2 calibrator is measured with side 2 (Panel 4).

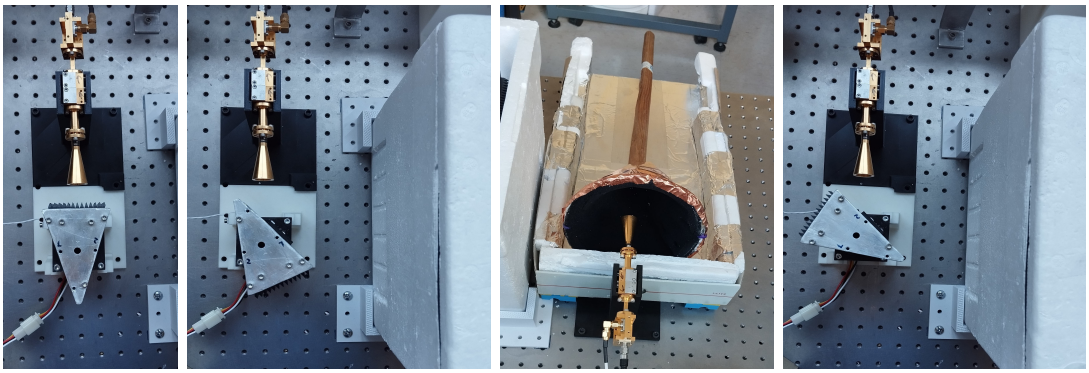

Figure 5.6.9: Different configurations of the measurement system, utilizing the three calibrators to characterize both mirror plates, are displayed. Panels 1 and 3 exhibit the direct measurements of the ambient and LN2 cone calibrators at the receiver. Panels 2 and 4 show the mirror positioned on sides 1 and 2, respectively, with the beam directed toward the calibrator within the LN2 container.

5.6.3 Data Analysis and Results

This section details the analysis and results obtained through the measurement method described in Section 5.6.2. The initial phase involved determining the

emissivity of each mirror side, followed by the characterization of the prototype. The entire testing procedure extended over approximately 12 hours. Throughout this period, the receiver temperature was manually documented in a spreadsheet, enabling a thorough assessment of its performance throughout the procedure.

Figure 5.6.10 presents the parameters essential for calculating the mirror emissivity. The first panel illustrates the power measurements used to characterize side 1 of the mirror. This procedure involves measurements from the ambient calibrator (yellow points), and the LN2-covered cone (light blue points), both taken directly to the receiver, as well as the calibrator immersed in the LN2 container (orange points) observed through the mirror.

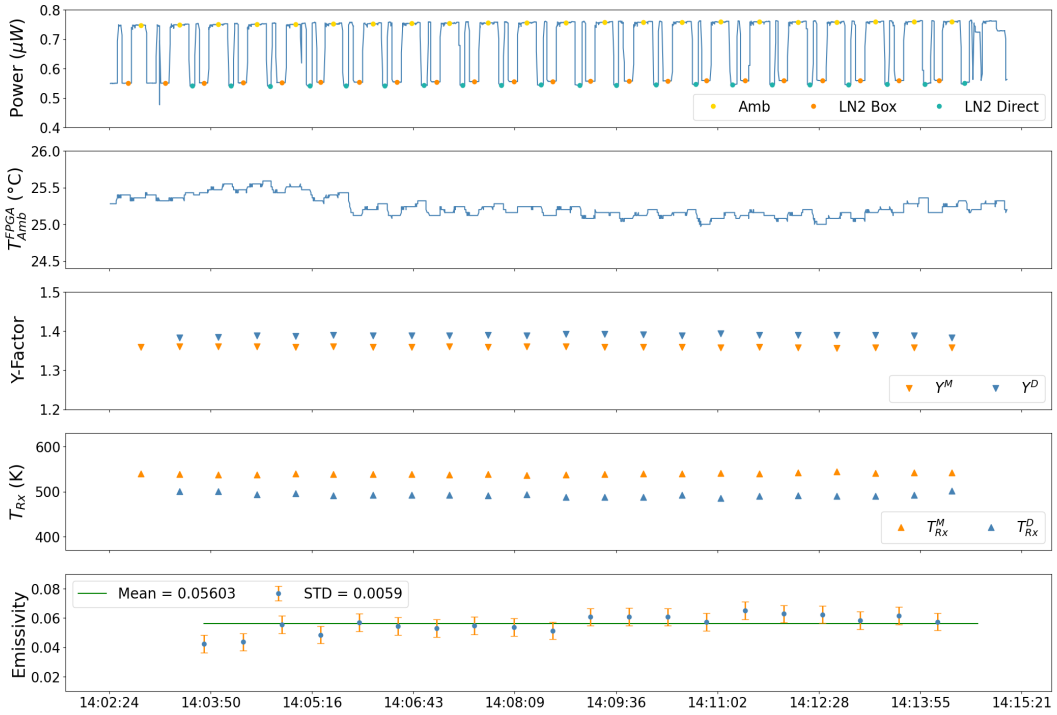

Figure 5.6.10: Main parameters for estimating the side-1 mirror emissivity. Panel 1 shows the power sections of the ambient (Amb) and LN2 calibrators (LN2 box and LN2 Direct). The second panel shows the ambient temperature measured by a PT100 sensor recorded on an FPGA, T^{FPGA}_{Amb}. The third and fourth panels show the y-factor and receiver temperature, respectively, calculated from the direct (red triangles) and through-the-mirror (green triangles) power measurements. The fifth panel presents the side-1 mirror emissivity, estimated to be 0.0564.

The sequence begins with the LN2 box, followed by the ambient calibrator, then the LN2 Direct measurement, and repeats thereafter. A systematic discrepancy in

power between the box and direct measurements is observed, which is attributed to the influence of the mirror on the beam path rather than any variation in receiver performance. This discrepancy directly affects subsequent calculations. The second panel displays the ambient temperature measured by the PT100 sensor. These temperature readings correspond precisely with the temporal sequence of power measurement presented in the first panel. The third panel presents the y-factor (Eq. 3.11.1) derived from the power measurements. The blue triangles indicate direct comparisons between the ambient calibrator and the direct LN2 cone, while the orange triangles represent measurements through the mirror, utilizing the LN2 box power. The y-factor calculated from direct measurements is higher than that obtained through the mirror, consistent with the observed reduction in LN2 power. This behavior is only the mirror effect, without suggesting any alteration in the receiver's stability, which is evidenced by the consistent direct measurements.

Based on the power and y-factor values presented in the previous panels, an equation for the mirror emissivity has been derived:

$$\varepsilon = 1 - \frac{P^M_{LN2}}{P^D_{LN2}} \cdot \frac{\left(Y^M - 1\right)}{\left(Y^D - 1\right)} \tag{5.6.6}$$

where P^M_{LN2} and P^D_{LN2} correspond to the LN2 power measured through the mirror and with the direct cone as shown in the first panel. The variables Y^M and Y^D represent the y-factor values for mirror and direct measurements, respectively, as shown in the second panel. A detailed derivation of emissivity can be found in Appendix D. The calculated emissivity values are shown as blue data points in the fifth panel. These values are averaged, yielding a mirror emissivity of 0.05603 for side 1, with a 10% error given by a standard deviation of 0.0059.

In the fourth panel, the receiver temperature is calculated using the power and ambient temperature data (Equation 3.11.5). The direct T^D_{Rx} values, associated with the y-factor from direct measurements, are presented by blue triangles, while the orange triangles denote the T^D_{Rx} values derived from measurements of LN2 box. As expected, the direct T_{Rx} exceeds the mirror-derived values, owing to the difference in LN2 power between the two sets of measurements. A key motivation for determining the receiver temperature through the power measurements of the calibrator within the LN2 container via the mirror was to maintain consistency with the prototype power measurements, which were also conducted using the

mirror. This approach facilitates the direct use of T_{Rx} values in the calculation of the prototype brightness temperature. However, following the data analysis of the prototype measurements presented in Figures 5.6.12 and 5.6.13, it was decided to use T_{Rx}^{D} for brightness temperature calculations, instead of T_{Rx}^{M}, due to its high variability. From these measurements, an averaged value of T_{Rx}^{D} is reported as 492.65 K. Considering possible temporal variations in system gain or a receiver performance degradation during the measurements, an additional power measurement using the LN2 cone and ambient calibrator was performed at the end of the radiometric measurements, yielding a receiver temperature of 492.71 K. A linear fit between these two temperature values is expressed as:

$$T_{Rx}^{fit}(K) = 8.08065 \cdot 10^{-5} \cdot t + \ 491.5585\ K \tag{5.6.7}$$

where t represents time in minutes.

Figure 5.6.11 shows the full power measurement along $\sim$ 11 hours incorporating the prototype. The panel 1, 2, 3 and 4 illustrates the power behavior when the prototype is set to $40°C$, $50°C$, $60°C$ and $70°C$, respectively. The yellow dots correspond to the ambient calibrator, the sky blue points refer to the submerged calibrator in the LN2 box and the red dots show the prototype. The three calibrators are presented interspersed to the receiver as shown in section 5.6.2. The spaces between continuous measurements indicate that the mirror is not moving. In panel 1, between approximately 16:00 and 17:15 hours, a significant change is seen in the behavior of the cold load; its power has increased too much compared to the powers of the other calibrators. This is because the LN2 condenses on the front side of the box. When the condensed ice is removed, the cold power changes abruptly. From this point on, a ventilator is used to dry the box front (Figure 5.6.5). As a precaution, it is continuously dried with a cloth; thus, the same behavior does not occur again. In panel 3 at 20:50 hrs, a notable increase in the power of the loads is observed, but this is only attributed to variations in the receiver's gain. More information about the receiver's behavior can be found in Figure 5.6.12. The primary objective of these radiometric measurements is to determine the prototype brightness temperature. All power analyses are therefore conducted with this purpose in mind. Whether the power is measured directly at the receiver (P^{D}) or via the triangular mirror (P^{M}) it is consistently governed by power Equation 3.11.2 presented in Section 3.11.

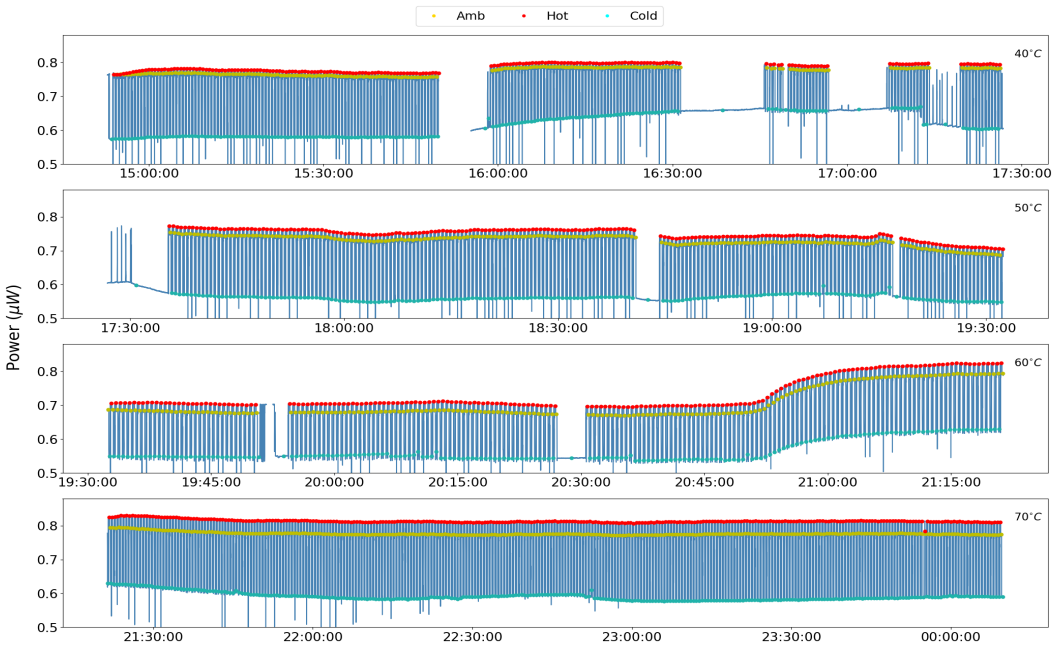

Figure 5.6.11: Power measurement process of the prototype load through the mirror for brightness temperature calibration at various physical temperatures ($40°C$, $50°C$, $60°C$ and $70°C$) over a period of 9 hours and 30 minutes. The prototype load is depicted in red points, while the ambient and LN2 calibrators are shown in yellow and light blue points, respectively. The sequence begins with measuring the LN2 power, followed by the ambient, and then the prototype load, repeating the cycle throughout the entire period. Significant gain variations are observed during the measurement, notably around 20:50 hours. A distinct increase in Cold power is evident between 16:00 and 17:20 hours, attributed to frost formation on the LN2 container wall.

It should be noted that, in these measurements, radiation from the prototype invariably passes through the mirror (P^M_{Load}), and the prototype power is consequently defined as follows:

$$P^M_{Load} = k \cdot \Delta\nu \cdot G \cdot \left(T^D_{Rx} + T^M_{Load}\right) \tag{5.6.8}$$

where "Load" denotes any calibration load, k represents the Boltzmann constant, $\Delta\nu$ is the bandwidth, and G indicates the receiver gain. T^M_{Load} corresponds to the prototype brightness temperature measured through the mirror, while T^D_{Rx} represents the receiver temperature derived from its components. Among these, the LN2 power (P^M_{LN2}) is invariably measured through the mirror, whereas the power of the ambient calibrator (P^D_{amb}) is always measured directly. Therefore,

the calibrators power is given by:

$$P^D_{amb} = k \cdot \Delta\nu \cdot G \cdot \left(T^D_{Rx} + T_{amb}\right) \tag{5.6.9}$$

$$P^M_{LN2} = k \cdot \Delta\nu \cdot G \cdot \left(T^D_{Rx} + T^M_{LN2}\right) \tag{5.6.10}$$

It is essential to note that the calibrators have known temperatures; with T^M_{LN2} is considered unknown, while T_{amb} is continuously monitored by a pt100 sensor via FPGA board. Both power and ambient temperature serves as a reference to calculating T^M_{Load}; thus, this variable is expressed as a function of these parameters. By considering the ratio of load power to ambient power:

$$\begin{aligned}
\frac{P^M_{Load}}{P^D_{amb}} &= \frac{\cancel{k \cdot \Delta\nu \cdot G} \cdot \left(T^D_{Rx} + T^M_{Load}\right)}{\cancel{k \cdot \Delta\nu \cdot G} \cdot \left(T^D_{Rx} + T_{amb}\right)} \\
\Rightarrow \frac{P^M_{Load}}{P^D_{amb}} &= \frac{\left(T^D_{Rx} + T^M_{Load}\right)}{\left(T^D_{Rx} + T_{amb}\right)} \\
\Rightarrow P^M_{Load} \cdot \left(T^D_{Rx} + T_{amb}\right) &= P^D_{amb} \cdot \left(T^D_{Rx} + T^M_{Load}\right) \\
\Rightarrow T^M_{Load} &= \frac{P^M_{Load}}{P^D_{amb}} \cdot \left(T^D_{Rx} + T_{amb}\right) - T^D_{Rx}
\end{aligned} \tag{5.6.11}$$

The load brightness temperature T^M_{Load} has been derived in Equation 5.6.11 using only measurable parameters. As anticipated, the receiver's performance directly influences power measurements, necessitating the inclusion of the receiver temperature. The term $k \cdot \Delta\nu \cdot G$ is assumed constant, implying no gain variations in the receiver at a given time, and is thus eliminated. The relevant parameter is the prototype brightness temperature measured directly at the receiver, T^D_{Load}. Therefore, in addition to Equation 5.6.11, the following expression must be considered from Wilson et al. [56] and Section 3.2.2:

$$T^M_{Load} = \left(1 - \varepsilon\right) \cdot T^D_{Load} + \varepsilon \cdot T_{amb} \tag{5.6.12}$$

This expression illustrates how the load temperature is affected or "attenuated" when measured through a mirror with a specific emissivity (ε). The first term of the equation, $\left(1-\varepsilon\right) \cdot T^D_{Load}$, quantifies the portion of the load's actual temperature that reaches the detector after being partially reflected by the mirror. The second term, $\varepsilon \cdot T_{amb}$, represents the contribution of the ambient temperature emitted by the mirror that influences the measurement. If the mirror is perfectly reflective

($\varepsilon = 0$), the entire contribution arises from the load temperature, resulting in $T^M_{Load} = T^D_{Load}$. Conversely, if the mirror is completely absorptive and emissive ($\varepsilon = 1$), the measurement exclusively reflects the ambient temperature. Solving T^D_{Load} in Equation 5.6.12:

$$T^D_{Load} = \frac{T^M_{Load} - \varepsilon \cdot T_{amb}}{1 - \varepsilon} \tag{5.6.13}$$

where T^M_{Load} is obtained from Equation 5.6.11, and ε represents the emissivity calculated from Equation 5.6.6. To compute T^D_{Load}, it is first necessary to determine T^M_{Load}, which requires the evaluation of the receiver temperature over the entire measurement period.

Figure 5.6.12 details the principal parameters for estimating the brightness temperature of the prototype. The upper panel depicts the prototype power (Hot) in red, alongside the ambient calibrator (Amb) and the LN2-immersed calibrator (Cold), represented in yellow and light blue, respectively. Only the relevant power data are shown, omitting the complete dataset from Figure 5.6.11, to ensure clarity and improve the visualization of power behavior. The central panel shows the ambient temperature recorded by the FPGA board (T^{FPGA}_{Amb}), using data from the PT100 sensor positioned in one corner of the motor-mirror system mount. The ambient temperature varies around 25 and 27°C throughout the measurement process, which is associated with the power measurements of the prototype and each calibrator. In the lower panel, a light green line represents an adjustment to the receiver temperature, calculated from the average T_{Rx} derived from the direct power measurements with the LN2 cone (Panel 3 on Figure 5.6.10). Blue points display the calculated T_{Rx} from power measurements of the calibrator immersed in the LN2 box, taken through the mirror. A high variability in T_{Rx} across the mirror suggests potential receiver performance issues. However, the analysis of LN2 power and the y-factors in Figure 5.6.13 demonstrates the consistency of the y-factor with the power of the LN2-immersed load. This is particularly evident during certain time intervals, such as between 16:00 and 17:00 hours or after 21:00 hours, as well as at peaks around 19:00, 8:00, and 23:00 hours. These discrepancies indicate reliability issues with the LN2 power data, and therefore, such sections should not be used to calculate the prototype brightness temperature. According to Equation 5.6.12, T^M_B would be significantly impacted.

Figure 5.6.14 shows the temperature curves during the entire measurement procedure of the prototype. The prototype physical temperature T_{Ph}, is shown in the orange line, which takes values of 40°C (313.15 K), 50°C (323.15 K), 60°C (333.15 K), and 70°C (343.15 K). The prototype brightness temperature T^{D}_{Load} (Equation 5.6.12), is presented in a blue line, which is calculated using the Equation 5.6.13 determined employing the T^{D}_{Rx} linear fit, the calibrator ambient temperature (T_{amb}), the direct power measurements of ambient calibrator (P^{D}_{amb}) and the mirror power measurements of Load (P^{M}_{Load}) (parameters presented in the third panel on Figure 5.6.12).

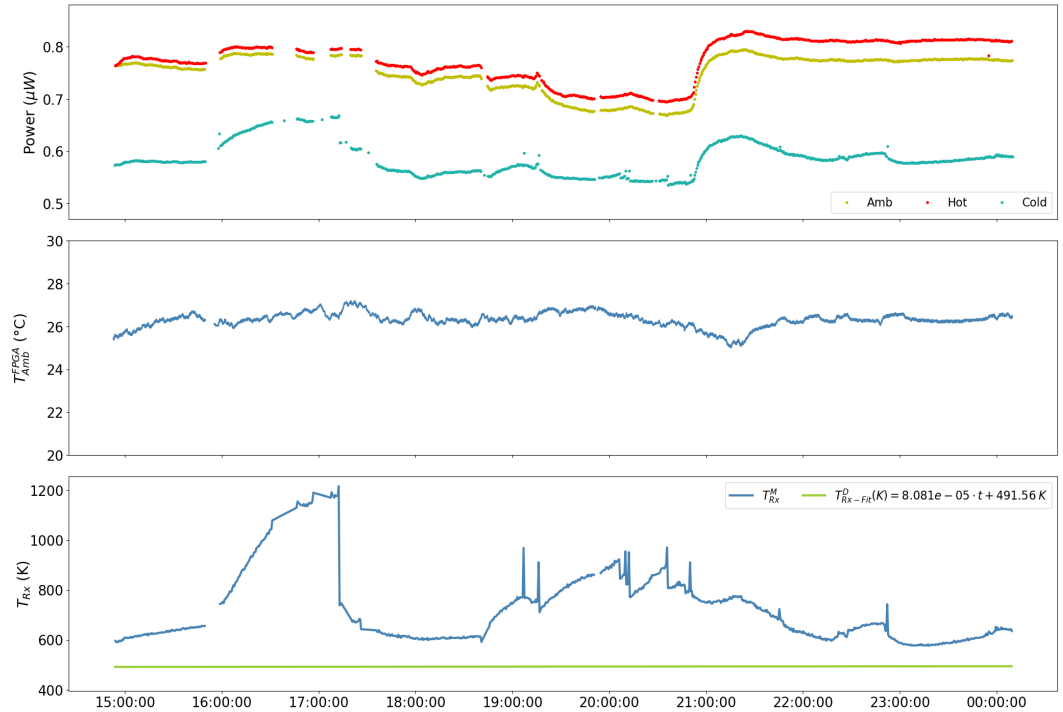

Figure 5.6.12: Key parameters for determining the brightness temperature of final calibration loads set at 40°C, 50°C, 60°C and 70°C. The upper panel displays the power data from the prototype and calibrators. The middle panel presents ambient temperature data near the motor-mirror system and prototype from the PT100 sensor (blue line) and the environment temperature from the DS18B20 sensor (orange line), recorded by the FPGA board. The lower panel shows the receiver temperatures derived from the power and temperature information calibrator powers and ambient temperature. The blue points show the T_{Rx} calculated from the instantaneous measurement of the calibrators, and the green line displays a section of the T_{Rx} linear fit from the measurements directed with the LN2 cone (Figure 5.6.10) for the power measurements of loads.

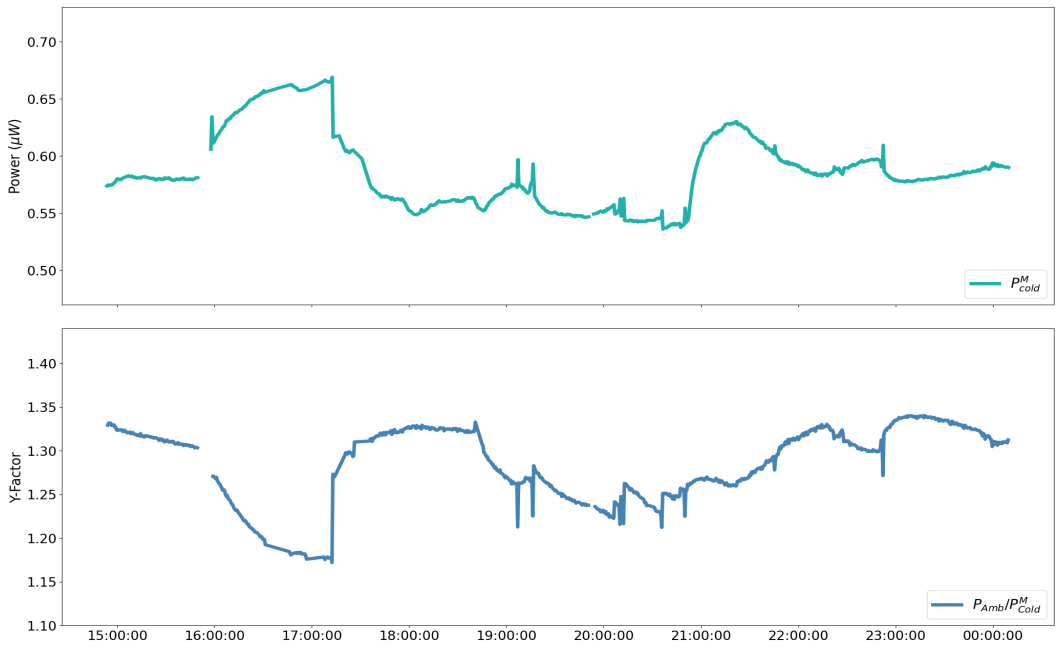

Figure 5.6.13: Y-factor of measurements (second panel) influenced by the Cold power of the calibrator immersed in LN2-container (first panel).

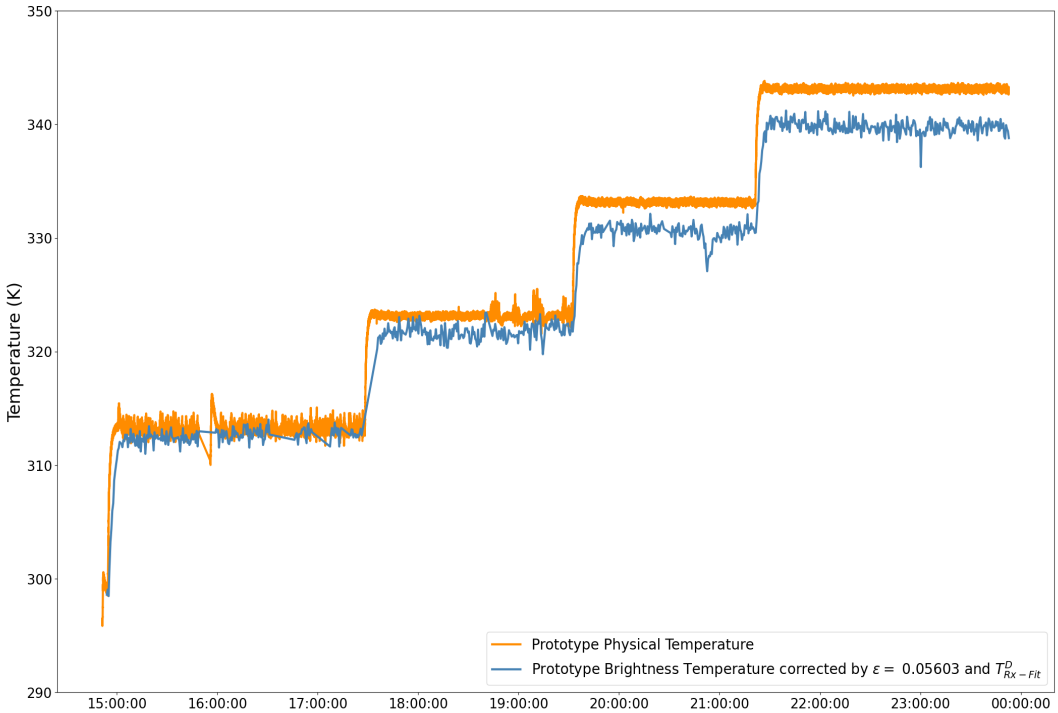

Figure 5.6.14: The brightness temperature of the prototype T^D_{Load} is presented in orange line when set to a physical temperature of 313.15 K ($40°C$), 323.15 K ($50°C$), 333.15 K ($60°C$), and 343.15 K ($70°C$) shown in the blue line.

Both temperatures are presented to illustrate the radiometric behavior of the prototype, demonstrating the expected trend of an increase in T^D_{Load} as T_{Ph} rises. The difference between these temperatures also becomes more pronounced with increasing T_{Ph}, possibly due to environmental radiation contributions during measurements or, less likely, variations in the stability of the measurement system over time. To provide a brightness temperature value, the average of a selected section was taken 30 minutes after the prototype was set to the corresponding physical temperatures. Consequently, when the prototype was adjusted to 313.15 K ($40°C$), the resulting brightness temperature was 312.64 K; at 323.15 K ($50°C$), the average was 321.67 K; at 333.15 K ($60°C$), the value averaged 330.48 K; and finally, at 343.15 K ($70°C$) the brightness temperature reached 339.71 K. It is evident that the difference between temperatures increases progressively, though it does not exceed 3.44 K at 343.15 K ($70°C$), representing a divergence of no more than 1% between the two temperatures. Figure 5.6.15 illustrates a linear relationship between the prototype brightness temperature and its physical temperature (thermal control), depicted by an orange dashed line. This fit is derived by applying linear regression to the four blue points given by:

$$T^P_B = 0.8993 \cdot T_{ph} + 276.51\ K \tag{5.6.14}$$

where T_{ph} is in Kelvin units, and the slope reflects the efficiency of the prototype rather than the direct emissivity of the polypropylene, which constitutes the main material, as one might assume. This occurs because the behavior of the polypropylene is influenced by the thermal properties of the other materials and their response to the supplied physical temperature. Therefore, the efficiency should be understood as the overall behavior of the load as a whole.
Table 5.6.1 provides the prototype calibration data, which correspond to the exact averaged values brightness temperature with respect to its physical temperature. Given that the prototype is not a perfect blackbody, it is expected that the brightness temperature will not exactly match the physical temperature. However, the temperature difference between T^P_B and T^P_{Ph} is not constant, it tends to increase as the prototype reaches higher physical temperatures. This behavior may be attributed to the mirror emissivity and a potential degradation in the receiver performance over the course of the measurements.

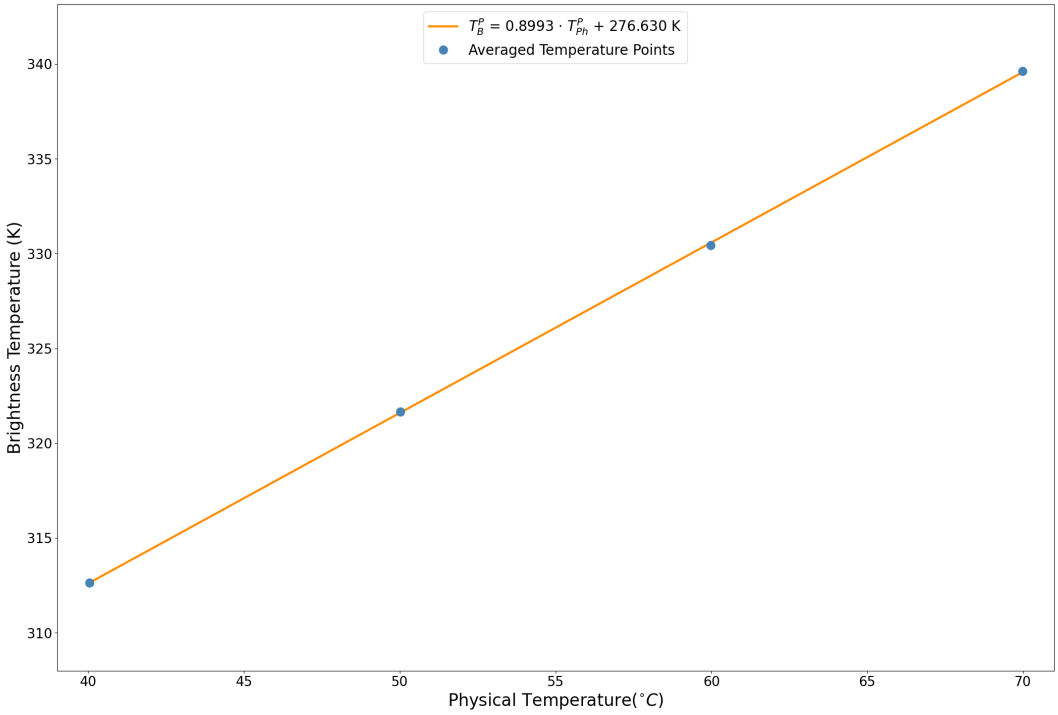

Figure 5.6.15: A linear fit between the brightness temperature and physical temperature for the prototype load is displayed. The blue points represent the data from Table 5.6.1, with the linear fit applied and represented by the orange dashed line.

Table 5.6.1: Calibration data of Prototype. T_{ph}^P correspond to loads physical temperature and T_B^P is referred to loads radiometric temperature.

T_{ph}^P (K)	313.15 (40°C)	323.15 (50°C)	333.15 (60°C)	343.15 (70°C)
T_B^P (K)	312.64	321.67	330.48	339.71
ΔT (K)	0.51	1.48	2.67	3.44
%	0.16	0.45	0.8	1.0

5.7 Radiometric Measurements of the Final Loads

The power measurements of the final loads were conducted manually due to the urgency expressed by the LLAMA committee to have the loads on their facilities. Consequently, these measurements are regarded as preliminary. The following tasks were undertaken in preparation: 1) implementation of a receiver, 2) calculation of the illumination diameter on blackbodies, 3) design and fabrication

of supports, and 4) development of a manual measurement method. These tasks closely parallel those outlined in the prototype measurement process, leading to a similar procedural approach.

As previously mentioned, the receiver determines the operating frequency. In this instance, a 93-GHz direct detection and total power receiver was implemented. Figure 5.7.1 provides a schematic of this receiver. The system includes a Mi-WAVE circular feedhorn operating within the 92 to 94 GHz range, followed by two low-noise amplifiers (LNAs) developed by NASA's Jet Propulsion Laboratory (JPL). The signal is subsequently attenuated by a 520W Mi-WAVE attenuator, re-amplified by another LNA, and then measured by a Virginia Diodes power meter. After testing, the receiver remained operational, with its temperature stabilized around 650 K, a condition deemed suitable for initiating measurements.

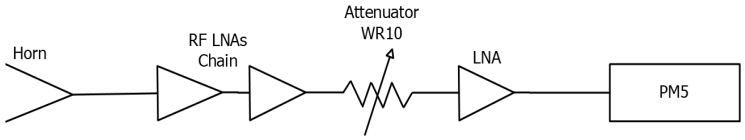

Figure 5.7.1: 93-GHz direct detection and total power receiver scheme used in the preliminary radiometric measurements of final loads.

Given that the operating frequency remains unchanged, the beam propagation calculations: beam waist size, beam waist location, beam size, and illumination diameter are identical to those presented in Section 5.6.1 or Table C.1 in Appendix C. Therefore, these calculations are not reiterated in this section. The distance chosen between the horn aperture and the loads RAM block are 13, 16.3, and 20 cm for the small load, and blue and large red load, respectively. The size of the illumination diameter above the RAM block is 11, 14, and 17 cm in the order mentioned above. In addition to the three final calibration loads previously presented in Figure 5.4.8, the cone submerged in the LN2 box, as shown in Figure 5.6.6, serves as a cold calibrator. Figure 5.7.2 illustrates the LN2 calibrator used in this measurement, which consists of a prototype employed by ALMA, featuring four large RAM tiles bolted to an aluminum plate.

Figure 5.7.3 illustrates the setup employed for the final load measurements. The left panel depicts the primary configuration, with the three loads arranged from left to right as follows: the large hot load with a red clamp, the large cold load

with a blue clamp, and the small hot load with a white clamp.

Figure 5.7.2: The ambient calibrator used to monitor ambient power during radiometric measurements is shown.

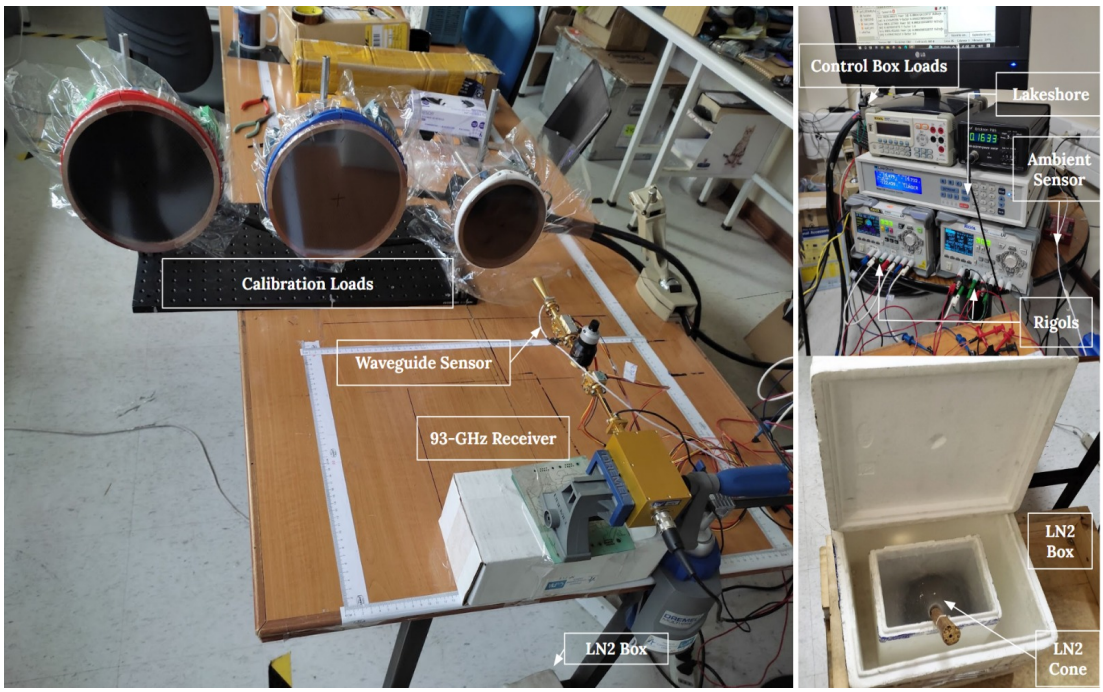

Figure 5.7.3: Setup for radiometric measurements of the final calibration loads at temperatures different. The left panel shows the three loads aligned on an optical table plate: from left to right, the large red, large blue, and small loads. In front of them is the 93-GHz total power receiver. The top-right panel displays two Rigol power supplies for the LNAs of the receiver and a Lakeshore recording the PT100 sensors, which monitor the ambient temperature and the waveguide temperature of the receiver. Behind the instruments, part of the control box for the final loads can be seen, providing power to the loads via a thick black cable connected at the rear of each load. the bottom-left panel shows the cone submerged in the LN2 container.

Each load is mounted on a black optical table using metal brackets as individual

supports. In front of the small load is the 93-GHz receiver, with its LNAs connected to two Rigol power supplies, as shown in the first panel on the right. Positioned above these power supplies is a Lakeshore temperature meter, which continuously records the ambient temperature via a pt100 sensor located at the rear, corresponding to the ambient calibrator described in Figure 5.7.2. A pt100 sensor was bolted to the waveguide after the horn to record the physical temperature variations of the receiver during the measurements. On the floor beneath the receiver, the LN2 box as shown in the lower right panel, with the cone submerged in LN2. The height of the mounting relative to the center of the aperture horn is 15 cm.

5.7.1 Measurement Procedure for Final Loads

The measurement procedure for the final loads is relatively straightforward. Key points include: 1) each load is characterized individually, and 2) calibration is performed at the beginning and end of each load measurement to assess receiver performance.

1.- Hot-Cold Calibration Process. As shown in Figure 5.7.4, the calibration process involves rotating the receiver 90° from its main mounting position, as depicted in Figure 5.7.3. The ambient calibrator is presented for approximately 25 seconds (left panel), followed by the LN2 cone for a similar duration (right panel).

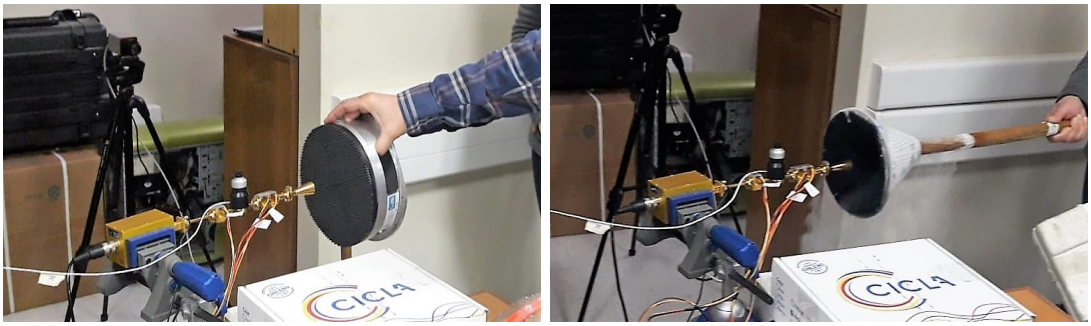

Figure 5.7.4: The calibrators used for the calibration process during power measurements of the final calibration loads set at 40°C, 50°C y 70°C are shown. The left panel presents the ambient calibrator, while the right panel displays the LN2 cone, both measured by the 93-GHz receiver.

2.- Power Measurement Procedure at 70°C. The procedure begins with the calibration sequence described above. As shown in Figure 5.7.5, the receiver is then repositioned to its original orientation to initiate load power measurement.

Panels 1, 2, and 4 show the measurement for the small, blue and large red load, respectively. Although the procedure is described using the term "load" in the singular, the same method applies to all three loads. The load is heated from room temperature to 70°C. The measurement alternates between a load and the ambient calibrator (Panel 3). In all measurements, the ambient calibrator is manually presented every 2 to 5 minutes and held in front of the receiver for about 1 minute. At the end of each measurement, the calibration process is repeated. The entire procedure lasts approximately 60 minutes per load, which allows thermal stability to be achieved in each load (Section 5.5) and the calibration process to be carried out.

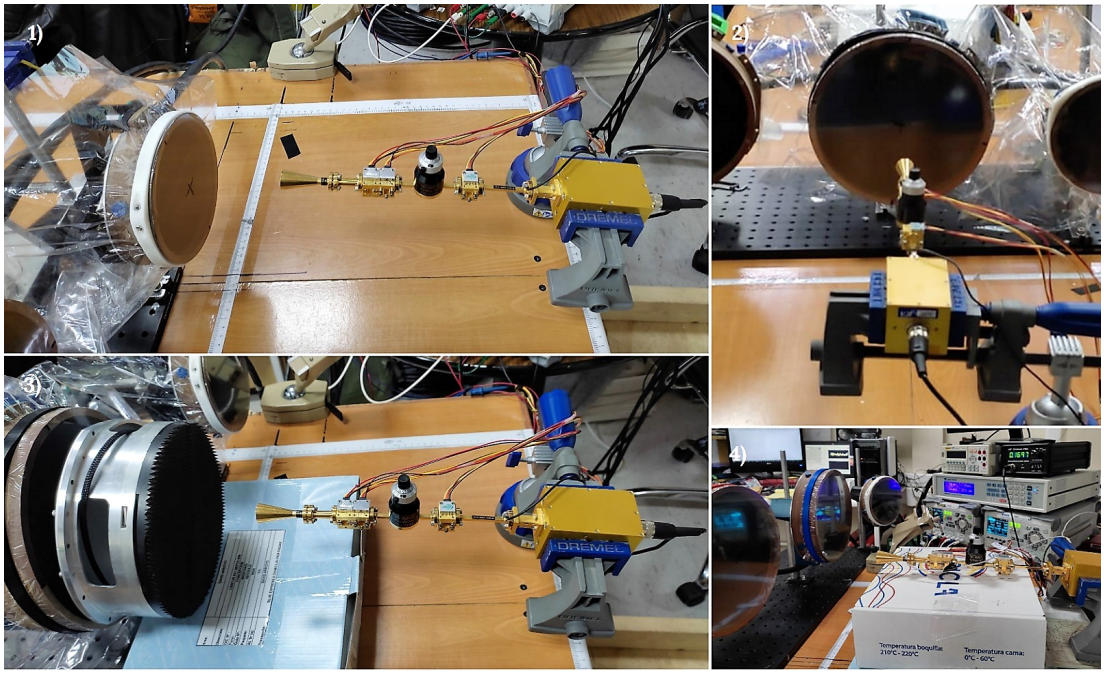

Figure 5.7.5: Power measurements of the final calibration loads set at 40°C, 50°C and 70°C using the 93-GHz receiver. Panels 1, 2, and 4 display the small load, large red load, and blue load, respectively, as measured by the receiver. Panel 3 shows the ambient calibrator positioned in front of one of the loads for measurement.

3.- Power Stability Measurement Procedure at 40°C and 55°C. The procedure begins with the calibration process, which is performed twice. Next, the three loads are simultaneously set to 40°C, allowing a stabilization period of one hour. The measurement sequence starts with the small load, alternating it with the ambient calibrator for 20 seconds of exposure to the receiver, repeating this step four to five times. The same sequence is then applied to the blue load, followed

by the red load. After completing these measurements, a second calibration cycle is conducted. The entire procedure requires approximately 80 minutes. Once this is complete, all loads are adjusted to 55°C, and a stabilization period of 60 minutes is allowed. The measurement process at 55°C follows the same procedure as described for 40°C; however, the order changes: the large red load is presented first, followed by the large blue load, and finally the small load, concluding with two additional calibration cycles.

5.7.2 Data Analysis and Results

This section presents the analysis and results of the power calibration to brightness temperature of the loads at different physical temperatures in relation to the measurement methods described in Section 5.7.1.

5.7.2.1 Stabilization to 40°C.

It begins detailing the procedure for measuring power in loads maintained at different temperatures through thermal control, starting with those set at 40°C. Figure 5.7.6 displays the power measurements for the three loads, including two calibration processes performed at the beginning and the end of the procedure, which spans approximately 80 minutes. The power readings for the small, large blue and large red loads are shown in orange, light green, and red, respectively. The yellow points represent the ambient power, while the light blue points correspond to the LN2 cone. A noticeable power drop occurs when LN2 is presented to the receiver. At the center of the figure, an enlarged view highlights the stabilization state of the three loads between minutes 70 and 88 is presented. Fluctuations in receiver gain are evident throughout the entire measurement process. A degree-3 spline fit, represented by a yellow dashed line, is applied to the averaged ambient power sections, with emphasis on accurately modeling the behavior in the stabilization zone. It is essential to note that the transition phases between different load measurements lack physical significance and are therefore excluded from this analysis. From these power measurements, the temperature is determined using Equation 5.6.11, considering both ambient power and the temperatures of the ambient and receiver.

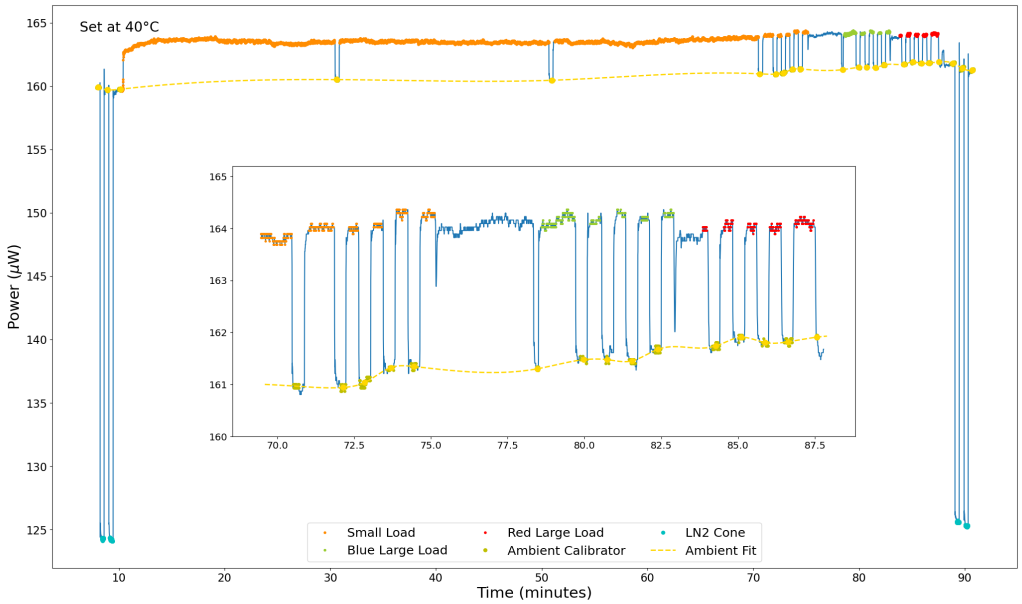

Figure 5.7.6: Power measurements of final calibration loads set at 40°C over time. The power data for the small load are shown as orange points, the large blue load as light green points, and the large red load as red points. Power data for the ambient and LN2 calibrators are presented in light blue and yellow points, respectively. At the beginning and end of the measurements, two calibration sequences are shown to track the receiver performance. The central section of the figure highlights the power stabilization of the loads. Additionally, a yellow dashed line represents a 1-degree spline applied to the ambient power sections, used to estimate this power during the stabilization state.

Figure 5.7.7 displays the loads and calibrators power in the top panel, the ambient and waveguide temperatures in the middle panel, and the receiver temperature calculated from these parameters in the bottom panel. In the initial calibration process (upper panel), two contiguous sections of ambient and LN2 power are selected to calculate receiver temperature. The analysis begins with the first section of ambient and nitrogen power, using the ambient temperature data from the same timeframe indicated in the middle panel. The initial T_{Rx} value is 671.27 K, represented by the first green triangle in the lower panel. The second pair of power measurements yields a T_{Rx} of 673.86 K, indicated by the second green triangle. These values are averaged, resulting in a receiver temperature of 672.57 K for the first calibration, indicated by the orange triangle on the left side of the lower panel. For the final calibration, around 83 minutes, T_{Rx} values of 670.62 K and 668.62 K are obtained. The average receiver temperature for the second calibration process is 669.62 K, indicated by the orange triangle on the right side

of the lower panel. A decrease of 0.44% in the average of T_{Rx} from the beginning to the end of the measurements suggests improved receiver performance over time. A linear fit between the averaged T_{Rx} values is applied, shown as a blue dashed line in the lower panel, providing the T_{Rx} for each load measurement point. It is also important to emphasize that the waveguide temperature exhibits temperature drops at the beginning and end of the measurement, corresponding to the moments when the LN2 cone is presented to the receiver. This temperature behavior aligns with the power fluctuations observed in the upper panel.

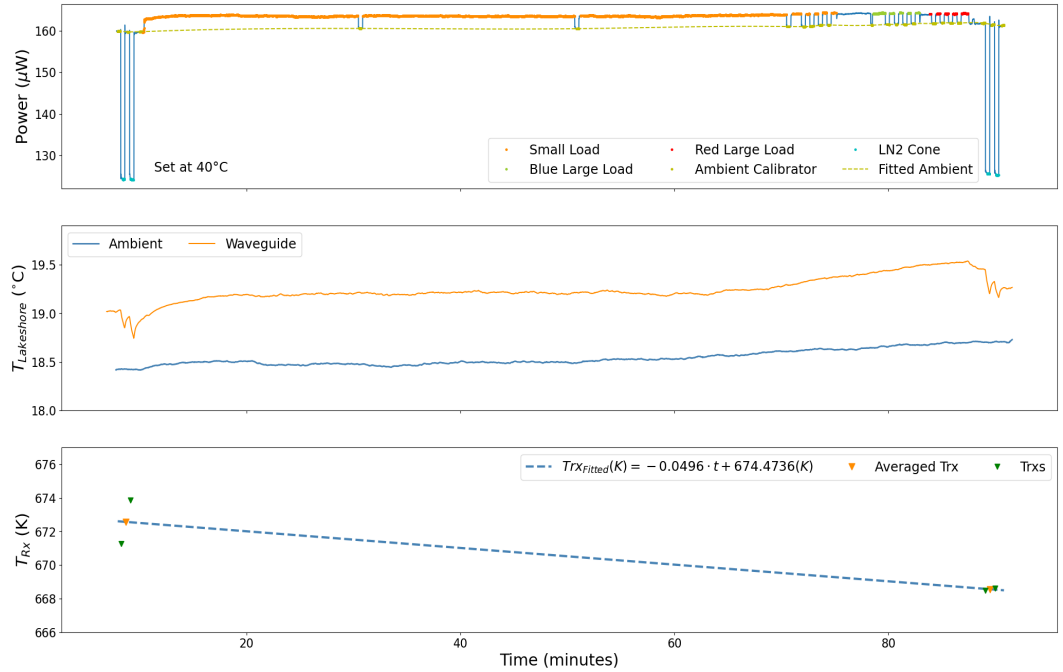

Figure 5.7.7: The upper panel displays the power data from loads set at 40°C and the calibrators. The middle panel presents temperature data from the ambient environment (blue line) and waveguide (orange line), which were recorded by Lakeshore. The lower panel shows the receiver temperatures (green triangles) derived from the calibrator powers and ambient temperature during the first and second calibration processes. These values are averaged and represented by orange triangles. A linear fit (blue dashed line) was applied to the averaged values to estimate T_{Rx} at the moment of power stabilization of the loads.

Figure 5.7.8 presents the brightness temperature of three final loads, calculated using Equation 5.6.11 during the stabilization state at 40°C. It is crucial to note that Equation 5.6.11 is applied instead of Equation 5.6.12, as these measurements were conducted directly, without the involvement of additional systems, such as the motor-mirror mechanism described in Section 5.6.1. The orange points

represent the brightness temperature of the small load, while the light green points correspond to the large blue load, and the red points indicate the brightness temperature of the large red load. A yellow line represents the ambient temperature measured by the Lakeshore sensor T_{amb}^{LS}, which fluctuates around 18.6°C (Figure 5.7.7). This physical temperature aligns with the averaged brightness temperatures sections calculated for the ambient calibrator, depicted as pink points in the figure. Based on the reliability of the experimental procedure and data analysis applied it is expected that the calculated ambient brightness temperature and the measured ambient physical temperature would be consistent, as, theoretically, a blackbody should always satisfy the condition $T_{Ph} = T_B$. The five sections of each load presented in Figure 5.7.8 are averaged to provide a brightness temperature value when the loads are set at 40° C and have already stabilized. The average value for the small load is 309.51 K (36.352°C), 307.81 K (34.662°C) for the large blue load, and 305.11 K (31.962°C) for the large red load.

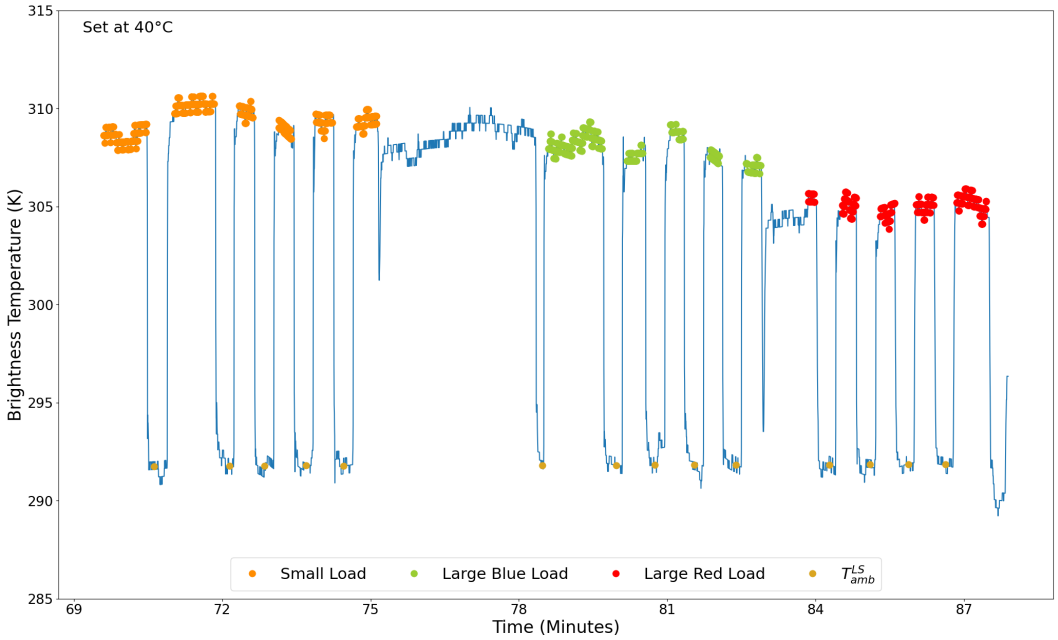

Figure 5.7.8: Brightness temperature of the calibration loads stabilized to 40°C respecting the time, calculated from Equation 5.6.11. The orange points correspond to the small load, while the light green points represent the large blue load, and the red points show the large red load. The ambient temperature in the yellow line overlaps with the pink points, corresponding to the ambient brightness temperature, to show that in a calibrator, T_{Ph} is according to T_B.

5.7.2.2 Stabilization to 55°C

The procedure advances with the measurements of the final loads, stabilized at 55°C, as illustrated in Figure 5.7.9. In accordance with the previously defined color scheme, the sequence begins with the large red load, depicted by red points, followed by the large blue load in light green, and concludes with the small load in orange points. The ambient and liquid nitrogen calibrators are marked by yellow and light blue points, respectively. Two calibrations are carried out at the start and the end of the measurement sequence. A power increase becomes apparent 91 minutes into the process, following stabilization at 40°C. A detailed view between minutes 149 and 16, located at the center of the figure, highlights the stabilization state of the loads.

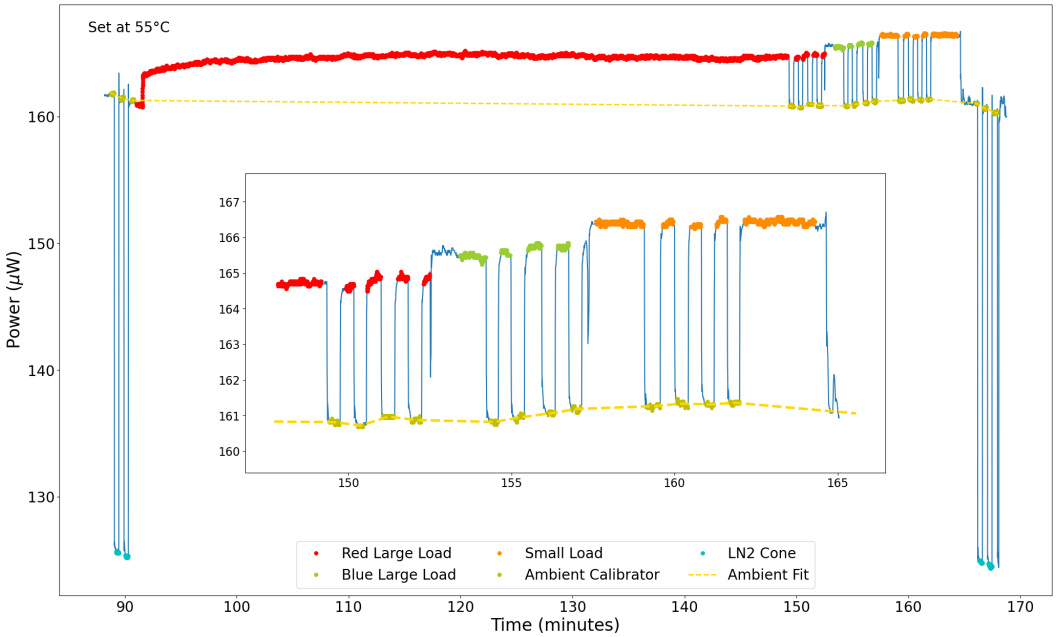

Figure 5.7.9: Power measurements of final calibration loads set at 55°C over time. The power data for the large red load are shown as red points, the small load as orange points, and the large blue load as light green points. Power data for the ambient and LN2 calibrators are presented in light blue and yellow points, respectively. At the beginning and end of the measurements, two calibration sequences are shown to track the receiver performance. The central section of the figure highlights the power stabilization of the loads. Additionally, a yellow dashed line represents a 1-degree spline applied to the ambient power sections, used to estimate this power during the stabilization state.

The ambient calibrator is presented four times with each load, where the

corresponding sections are averaged, and a first-degree spline is applied to capture the gain variations in the receiver during this period. The small load displays a significantly higher power output compared to the other two loads, resulting in a pronounced difference in brightness temperature as shown below. Figure 5.7.10 presents the power data for the final loads, incorporating both calibration procedures and the corresponding adjustments to the ambient power. It should be noted that the first two calibration pairs, near minute 90, correspond to the final calibration of the 40°C measurements. The middle panel illustrates both ambient and waveguide temperatures, with four clear decreases in the waveguide temperature coinciding with the introduction of the LN2 calibrator.

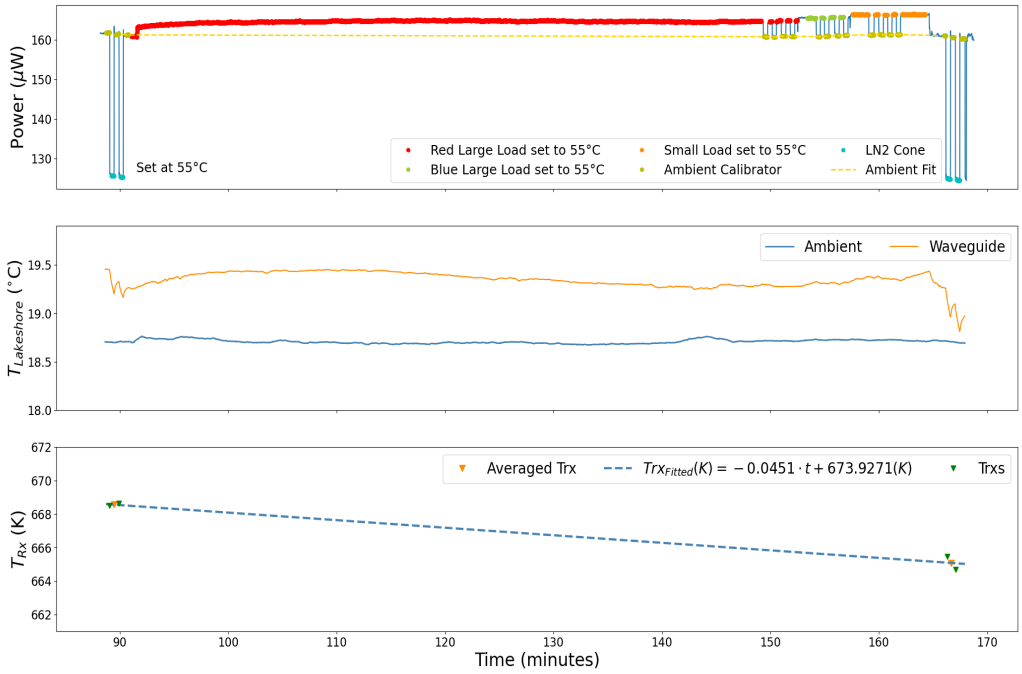

Figure 5.7.10: Key parameters for determining the brightness temperature of final calibration loads set at 55°C. The upper panel displays the power data from loads and calibrators. The middle panel presents temperature data from the ambient environment (blue line) and waveguide (orange line), recorded by Lakeshore. The lower panel shows the receiver temperatures (green triangles) derived from the calibrator powers and ambient temperature during the first and second calibration processes. These values are averaged and represented by orange triangles. A linear fit (blue dashed line) was applied to the averaged values to estimate T_{Rx} at the moment of power stabilization of the loads.

The behavior of the waveguide temperature aligns closely with the overall power variations, while ambient temperature fluctuations are observed at the beginning

and near 140-150 minutes, likely caused by the laboratory door being left open during testing. However, no direct effect on the load power is detected. The lower panel depicts the receiver temperature derived from the power measurements presented in the upper panel. The mean T_{Rx} for the first two calibration processes reaches 668.56 K. The last two calibration pairs, involving ambient and LN2 power measurements, yield receiver temperatures of 665.47 K and 664.69 K, shown in green triangles, averaging 665.08 K, represented by an orange triangle. Producing a 0.5% performance improvement from the beginning of measurements to the end. A dashed blue line shows a linear fit to the averaged T_{Rx} values. Figure 5.7.11 displays the brightness temperatures of the three loads at 55°C, computing using Equation 5.6.11, based on the adjusted ambient calibrator power and the receiver temperature. The large red, large blue, and small loads are represented by red, light green, and orange points, respectively.

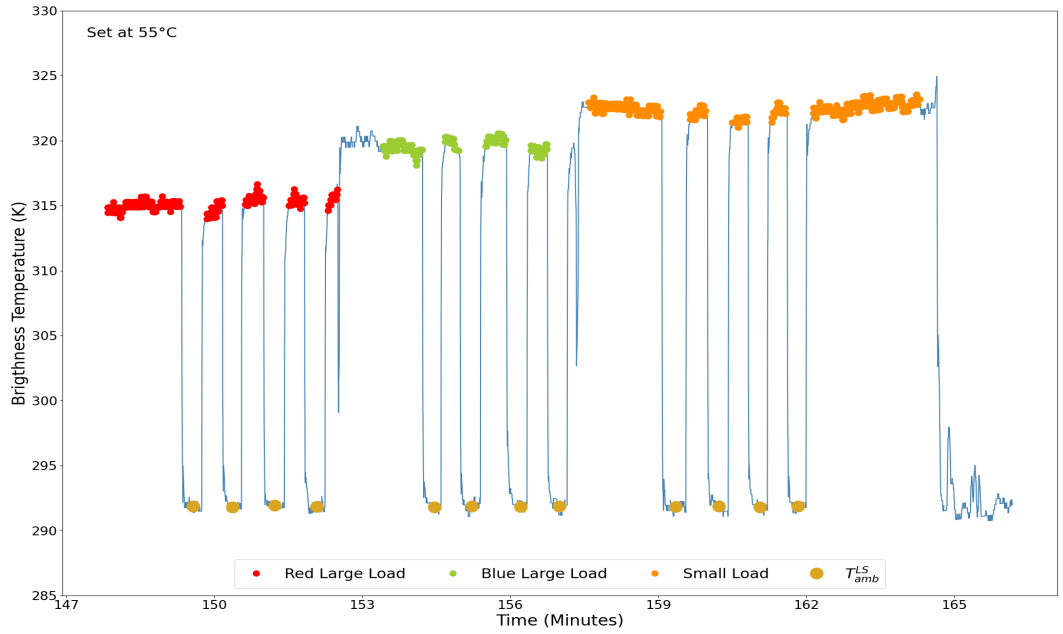

Figure 5.7.11: Brightness temperature of the calibration loads stabilized to 55°C respecting the time, calculated from Equation 5.6.11. The red points correspond to the large red load, while the light green points represent the large blue load, and the orange points show the small load. The ambient temperature in the yellow line overlaps with the pink points, corresponding to the ambient brightness temperature, to show that in a calibrator, T_{Ph} is according to T_B.

The ambient temperature recorded by the Lakeshore sensor, T^{LS}_{amb}, is represented by a yellow line, fluctuating around 18.7°C (Figure 5.7.10), overlaid with the

averaged brightness temperature sections for the ambient calibrator, demonstrating consistent behavior between both measurements. The sections of each load presented in Figure 5.7.11 are averaged to determine the stabilized brightness temperature at 55°C. The large red load yields an average of 315.28 K (42.128°C), the large blue load 319.60 K (46.452°C), and 322.48 K (49.333°C) for the small load.

5.7.2.3 Stabilization to 70°C

This section analyzes the power stabilization curves for the three calibration loads set at 70°C. Each load was independently measured to obtain the desired stabilization curves. Figure 5.7.12 illustrates the power measurement for the three loads as they stabilize from ambient temperature to 70°C.

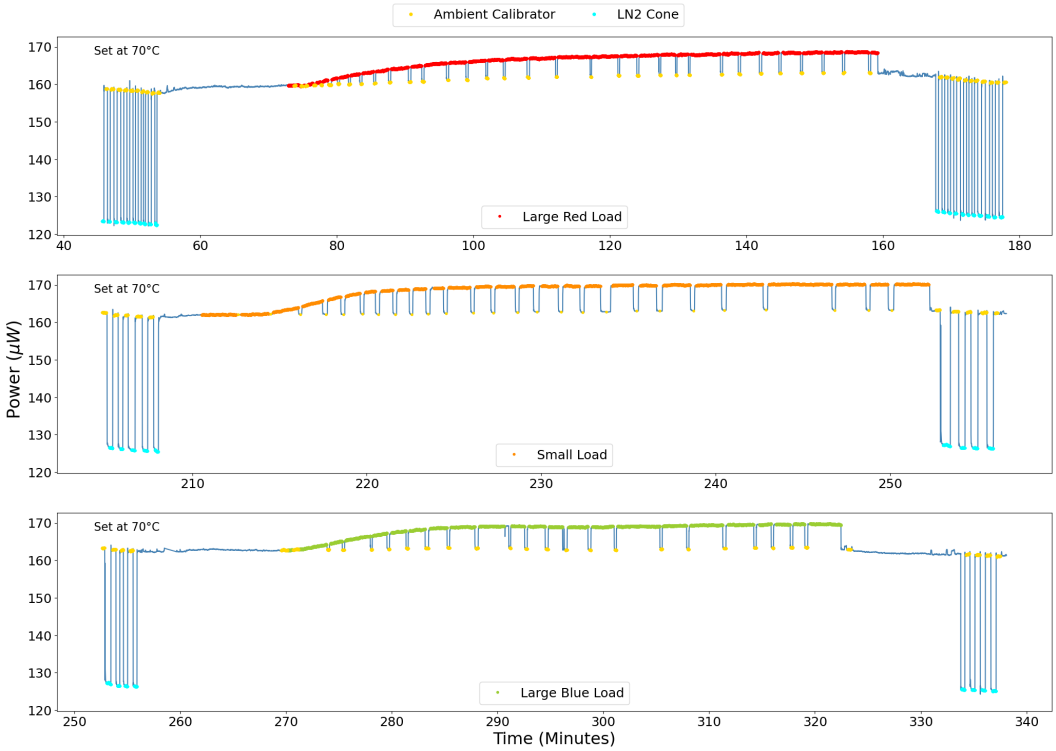

Figure 5.7.12: Power measurements for the calibration loads set to 70°C over time. The upper panel shows the power data of the large red load in red points, the middle panel displays the power data of the small load in orange points, and the lower panel corresponds to the large blue load in light green points. The ambient calibrator data are shown in yellow points, and the LN2 calibrator data are presented in light blue points. Calibration processes at the beginning and end of each measurement track receiver performance.

The power of the large red load is represented by red points, the small load by orange points, and the large blue load by light green points. Power data for the ambient calibrator and LN2 cone are shown in yellow and light blue points, respectively. Calibration was conducted at the beginning and end of each measurement procedure. The final calibrations of the receiver during the small load measurement, between minutes 250 and 260, are also used as the initial calibrations for the large blue load measurement. The measurements were taken sequentially, reflected in the distinct x-axes of each panel, starting with the large red load, followed by the small load, and concluding with the large blue load. Consistent scales were applied across all panels to allow a direct comparison of the power variations during the three measurements.

Figure 5.7.13 provides a zoomed-view of the central section of Figure 5.7.12, highlighting the power measurements of the loads alongside the ambient calibrator.

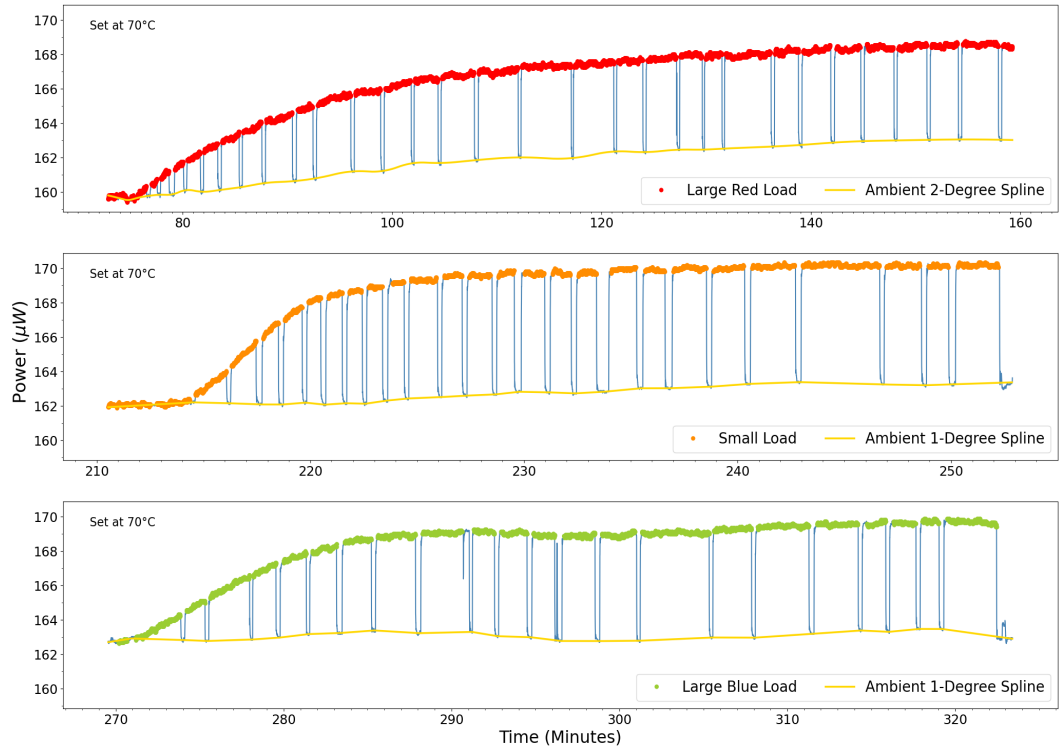

Figure 5.7.13: Zoomed-in view of the central section of Figure 5.7.12, focusing on the power measurement processes of the three calibration loads set to 70°C from ambient temperature. The upper, middle and lower panels show the power of the large red load, small load, and large blue load, represented by red, orange, and light blue points, respectively. The yellow line denotes the fit for the ambient calibrator.

The first panel displays the large red load power along with a 2-degree spline fitted to the ambient calibrator power. In the middle panel, the small load power is shown in orange points, with a 1-degree spline fit to the ambient power. The large blue load power is presented in light blue points, accompanied by a 1-degree spline for the ambient power. The large red load exhibits a slower stabilization in power compared to the other two loads. Conversely, the small load shows a steep power slope, indicating rapid stabilization. Overall, the receiver gain remains stable during the measurement of the three loads, as evidenced more clearly in Figure 5.7.15, where the receiver temperature is presented.

Figure 5.7.14 presents three panels showing the temperatures recorded by the Lakeshore using PT100 sensors. The blue lines indicate the ambient temperature during the three power measurement procedures of the loads, which is crucial for calculating T_{Rx} and T^{D}_{Load}. In the central panel, five points represent manually recorded ambient temperature data, as no data was saved by Lakeshore at that time.

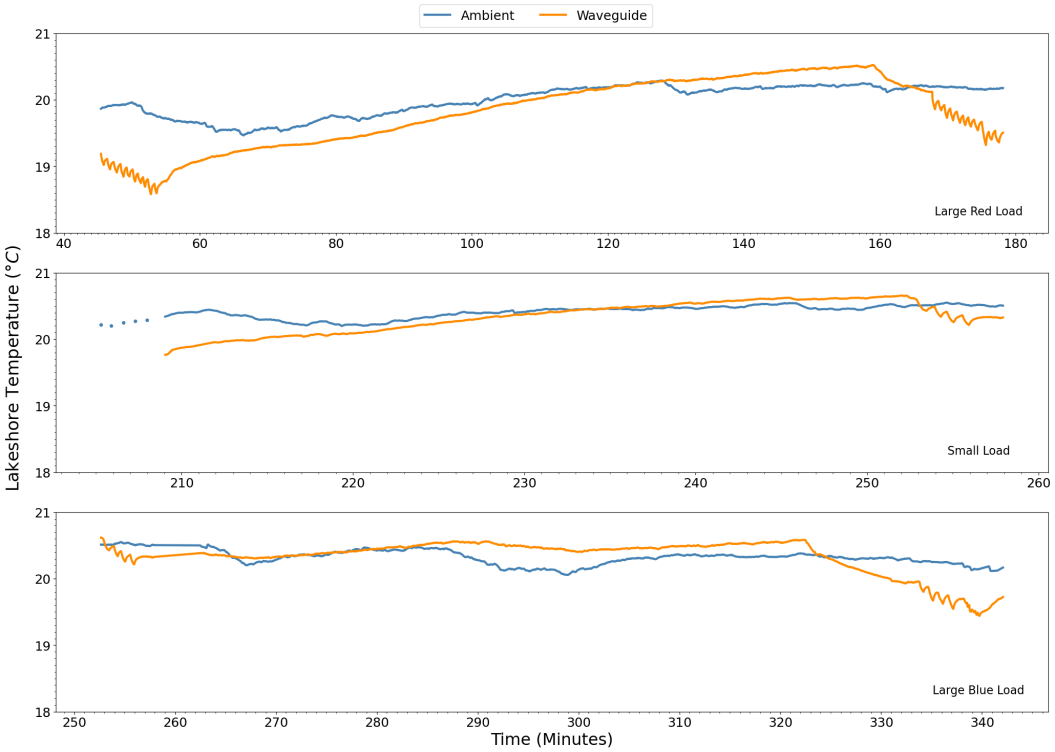

Figure 5.7.14: Temperature data recorded by the Lakeshore using PT100 sensors are shown. Blue lines denote ambient temperature, while orange lines represent the waveguide temperature. Each panel corresponds to a specific measurement period for one of the loads.

On average, the ambient temperature during the entire measurement process remained at 20.2°C, with variations of less than 1°C. The orange line corresponds to the temperature of the receiver waveguide, showing descending power peaks at the beginning and end of the measurements, a characteristic behavior when the LN2 cone is present. A sharp temperature drop is observed in the third panel near minute 320, just before the final calibration process. This drop is attributed to the receiver proximity to the LN2 container, not to any change in the receiver performance.

Figure 5.7.15 presents the receiver temperature calculated using the variables from the calibration processes conducted at the beginning and end of the power measurements (Figure 5.7.12), incorporating ambient temperature (Figure 5.7.14). These parameters are applied in Equation 3.11.5 through the y-factor technique. Each panel shows the power measurements for individual loads.

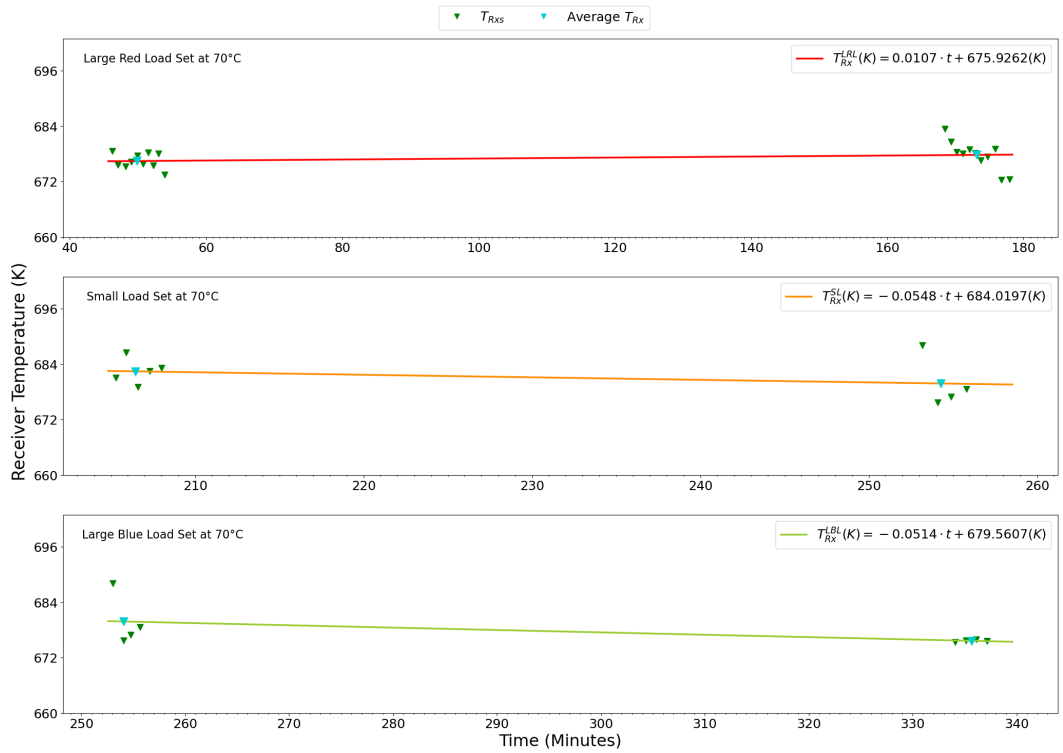

Figure 5.7.15: Receiver temperature during the power measurement of three calibration loads at 70°C. Each panel illustrates the individual T_{Rx} values, represented by green triangles, obtained from each hot-cold power pair taken at the beginning and end of the measurements (Figure 5.7.12). Averaging these values for each calibration process provides an averaged T_{Rx} value, shown as light blue triangles. For each measurement process, a linear fit represented by T_{Rx}^{LRL}, T_{Rx}^{SL} and T_{Rx}^{LBL} is applied to each pair of averaged T_{Rx} values.

The green triangles represent the T_{Rx} values obtained from individual hot-cold power measurements, paired with the corresponding ambient temperature average at the time of each hot-cold measurement. The averaged T_{Rx} values for each calibration process are displayed as cyan triangles in all panels. It is important to note that the T_{Rx} values from the second calibration process in the central panel are the same to those in the first calibration process of the lower panel. Three linear fits are applied to the averaged T_{Rx} values; represented by T_{Rx}^{LRL}, T_{Rx}^{SL} and T_{Rx}^{LBL}, indicated by the red, orange and light green lines, respectively, corresponding to the colors of each load. Power data is intrinsically correlated with the receiver's performance, making it essential to evaluate T_{Rx} variations over time during the measurements. For the first measurement, corresponding to the large red load, the initial T_{Rx} values, recorded approximately at 50 minutes, exhibit an average of 676.46 K. Subsequently, during the second set of measurements, around 173 minutes, the average increases to 677.79 K, indicating a 0.2% degradation in the receiver's performance. Regarding the second measurement, associated with the small load, the initial T_{Rx} values, obtained near 206 minutes, yield an average of 682.47 K. Later, during the second set, around 254 minutes, the average decreases to 679.84 K, reflecting a 0.39% improvement in the receiver's performance. The measurement for the large blue load begins immediately after the final T_{Rx} set, using the corresponding average as the initial value. In the final set, recorded approximately at 336 minutes, the average is 675.65 K, showing an additional 0.62% improvement. This behavior is also observed in the slopes derived from the adjustments applied to T_{Rx}. In all three cases, the slopes are negligible, while the negative signs in the second and third panels reflect an improvement in the receiver's performance.

In Figure 5.7.16, the brightness temperature and stabilization curves for the three loads set at 343.15 K (70°C) are presented. The brightness temperature, calculated using Equation 5.6.11, accounts for the power of each load, the ambient calibrator power, ambient temperature, and receiver temperature. The T_B of the large red, small, and large blue loads are represented by red, orange, and light green lines, respectively. An exponential fit T_{Load}^{SC}, described by:

$$T_{Load}^{SC} = a \cdot \left(1 - e^{-t/b}\right) + c \tag{5.7.1}$$

is applied to the brightness temperature data for each load to determine the

stabilization time t, indicated by the blue lines. In previous figures, the data and calculated parameters are shown with the x-axis indicating the time at which power measurements were taken, but this time, a correction is applied to ensure the stabilization curves start at minute zero for a clearer visualization of the stabilization time for each load. The differences in stabilization times are evident. The small load displays a more rapid temperature rise compared to the large red load, which approaches its maximum temperature more slowly.

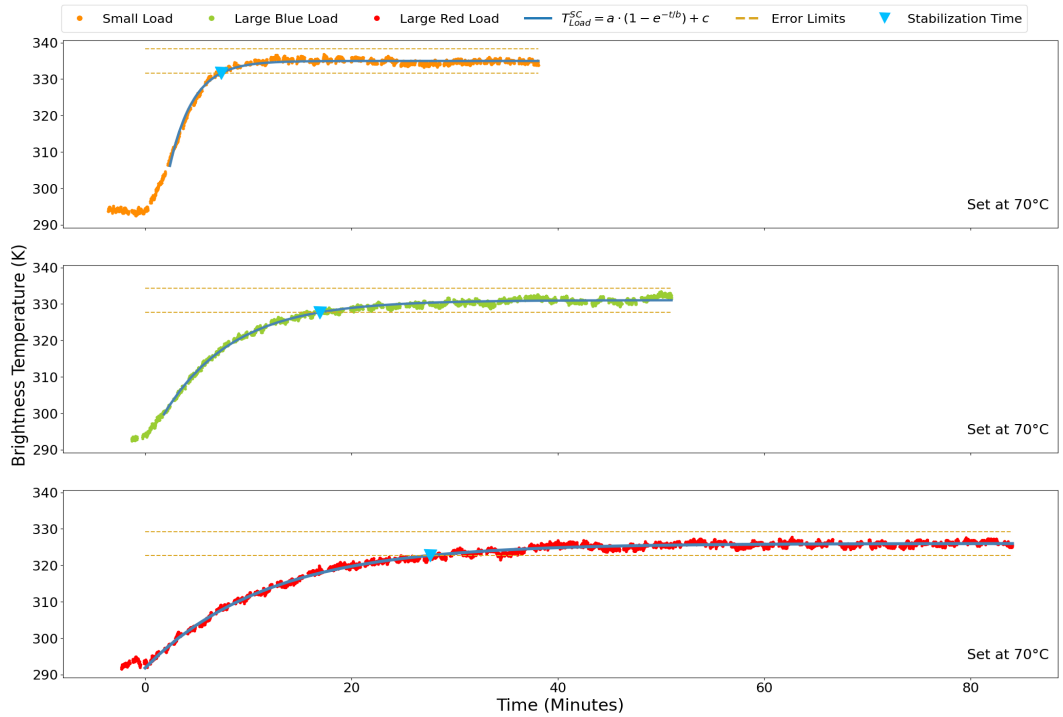

Figure 5.7.16: The brightness temperature and stabilization curve for three loads set at 343.15 K (70°C) are presented. The T_B are depicted in red for the large red load, orange for the small load, and light green for the large blue load. The stabilization curves, showing temperature evolution over time, are indicated by blue lines.

Each stabilization curve converges to a specific temperature value, with an associated error margin of 1% as required by the scientific specifications set at the outset of the LLAMA project. These values correspond to 325.95 K ± 3.26 K for the large red load, 334.95 K ± 3.34 K for the small load, and 331.0 K ± 3.31 K for the large blue load. The brightness temperature curves upper and lower error limits are depicted as dashed grey lines. The stabilization time is defined as the moment when the stabilization curve intersects the lower error boundary.

These intersection points are indicated by yellow triangles and correspond to 28 minutesfor the large red load, 8 minutes for the small load, and 17 minutes for the large blue load. Once the stabilization time has been terminated, the remaining temperature data points are averaged to yield a unique brightness temperature value for each load when set to 343.15 K (70°C). Table 5.7.1 presents the resulting temperatures, which are 325.43 K (52.282°C) for the large red load, 334.67 K (61.517°C) for the small load, and 332.31 K (59.157°C) for the large blue load. It is evident that the temperature difference progressively increases across the three loads. The most extreme case is observed in the large red load, where at 343.15 K (70°C), a difference of 17.72 K is noted compared to its brightness temperature. Although this may seem significant, it represents only a 5% of difference between T_B relative to T_{ph}. Figure 5.7.17 shows the linear fits applied to the experimental brightness temperature values obtained by setting the loads to different physical temperatures. The points corresponding to the large red load (LRL), represented by inverted blue triangles, are modeled using the linear fit shown in red, described by:

$$T_B^{LRL} = 0.6773 \cdot T_{ph} + 278.02\ K \tag{5.7.2}$$

The data associated with the small load (SL), represented by circular markers, are fitted with the linear curve displayed in orange, defined by:

$$T_B^{SL} = 0.8388 \cdot T_{ph} + 276.08\ K \tag{5.7.3}$$

Finally, the experimental values of the large blue load (LBL), represented by rightward-facing triangles, are fitted with the green line described by:

$$T_B^{LBL} = 0.8165 \cdot T_{ph} + 275\ K \tag{5.7.4}$$

where in all three equations, T_{ph} is expressed in Kelvin. This is because the thermal control system operates directly using these units. It can be stated that these curves enable the determination of the brightness temperature for any load by inputting a physical temperature value into the control and monitoring system, ranging from ambient temperature to 343.15 K (70°C), and not limited to the temperatures previously tested. It is important to note that the slope of each curve reflects the efficiency of the calibration loads rather than the direct emissivity of the polypropylene, which constitutes the main material, as one might

assume. This occurs because the behavior of the polypropylene is influenced by the thermal properties of the other materials and their response to the supplied physical temperature. Therefore, the efficiencies should be understood as the overall behavior of the loads as a whole.

Table 5.7.1: Calibration data for the final calibration loads, represented as SL (small load), LBL (large blue load), and LRL (large red load). T_{ph} denotes the physical temperature, while T_B refers to the radiometric temperature corresponding to T_{ph}. ΔT corresponds to the percentage differences between T_B and T_{ph}.

T_{ph} (K)	T_B (K)					
	SL	ΔT_{SL} (%)	LBL	ΔT_{LBL} (%)	LRL	ΔT_{LRL} (%)
313.15 (40°C)	309.50	1.2	307.81	1.7	305.11	2.6
328.15 (55°C)	322.48	1.7	319.60	2.6	315.28	3.9
343.15 (70°C)	334.67	2.5	332.31	3.2	325.43	5.2

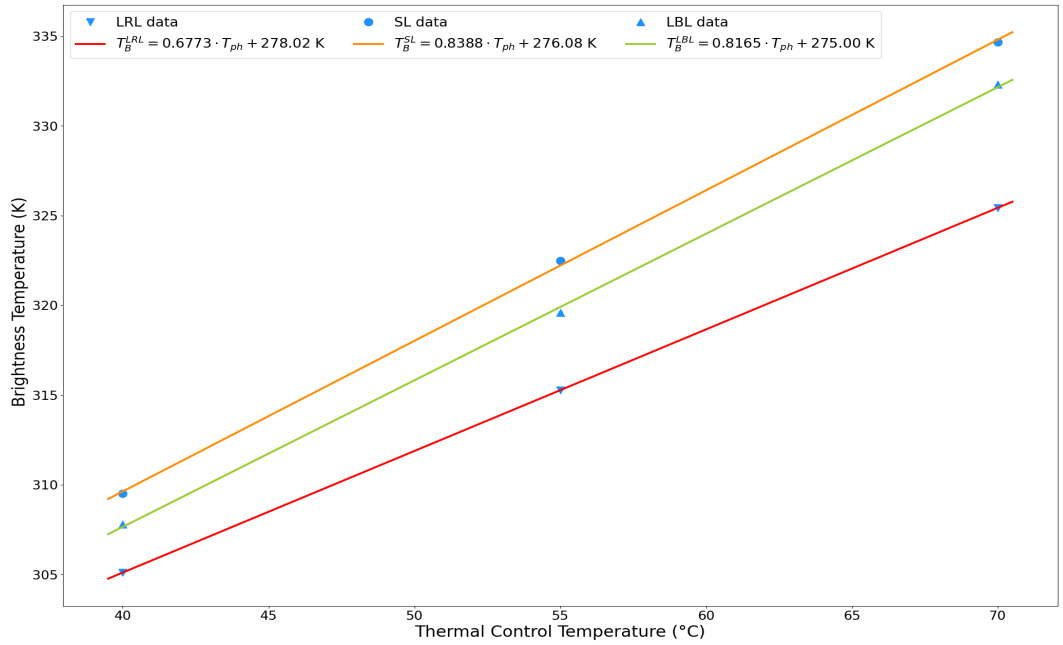

Figure 5.7.17: Three linear fits between the brightness temperature and the physical temperature for the final calibration loads are shown. The blue points represent the data presented in Table 5.7.1. The red line corresponds to the linear fit for the large red load, the orange line represents the small load, and the light green line refers to the large blue load.

Chapter 6

Discusion

This chapter discusses the key observational and instrumental factors evaluated in this thesis within the framework of the COMAP and LLAMA projects.
The design, development, and integration of the calibration loads for the LLAMA telescope represent an innovative contribution to the field of high-precision astronomical instrumentation. The implementation of an encapsulated calibration load design was key to ensuring efficient thermal control and minimizing heat exchange with the environment. This, along with the use of suitable materials ensured mechanical robustness, thermal stability, and uniformity in the temperature of the RAM block, all fundamental to ensuring precision in brightness temperature measurements. One of the most innovative features of the system is its ability to operate at different physical temperatures, achieved through a thermal control system based on FPGA developed at the CePIA laboratory. This system was distinguished by its precision of 0.2°C and rapid stabilization times, owing to the use of PID controllers. The integration of the ACS software and SCPI protocols facilitates the interoperability and operation of the loads. This approach ensures that the system can easily integrate with other subsystems of LLAMA telescope. Although the loads slightly exceeded the specified weight by 200 grams, mechanical tests validated the structural solidity of the design and the robotic arm, which allowed meeting the functional requirements of the radio telescope.
The analysis of infrared measurements performed on the calibration loads highlights several key aspects for evaluating their thermal performance and potential areas for improvement. First, the measurements met the established

tolerance margins when the loads were set to 70°C, achieving a standard deviation over time of less than 1°C, which demonstrates the effectiveness of the encapsulated design in achieving thermal stability. The use of Mylar in the final loads limited the measurements by blocking infrared radiation, which reduced the temperature recorded by the IR camera compared to the RAM block. Although this effect was considered in the results, the lack of exact data for the block restricts a fully precise interpretation. Furthermore, differences in the thermal behavior of the three final calibration loads were observed, which can be attributed to the size and uncertainty in their manufacturing, suggesting that the ideal conditions are not uniform for all the loads. The results validate the use of the GOBI640-GigE infrared camera and the experimental setup adopted for all calibration loads. Further, studies are suggested to precisely quantify the impact of the Mylar on the measurements.

The methodology used for the radiometric evaluation of the prototype involved a hybrid procedure comprising an FPGA-based triangular mirror with automatic movement and a manually presented calibration cone, aimed at obtaining power measurements of the prototype and various calibrators. During the procedure, three fundamental parameters were analyzed: the emissivity of the mirror, the stability of the receiver, and the brightness temperature of the prototype. The analysis performed determined that the emissivity of the mirror for one of its faces was 0.05603 with a 10% dispersion. This result demonstrates the impact of the mirror in reducing power when observing one of the sources through it, compared to direct measurements. This effect was consistent throughout the procedure and suggests that it is due to the optical properties of the mirror and not variations in the receiver's performance. Moreover, the low emissivity value confirms its high reflectivity, which aligns with the theory of the opaque body and previous studies. The stability of the receiver was key in the radiometric analysis of the prototype. The results indicated that the receiver temperature calculated with the direct cone was smaller and more consistent than those derived through the mirror. This reflects the differences in liquid nitrogen power observed with and without the mirror, highlighting the impact of the mirror's optical properties on the accuracy of the calculation. Consequently, the receiver temperature calculated with direct measurements is the one used to infer the brightness temperature. The average value obtained for the receiver temperature at the beginning of the measurements with the prototype was 492.65 K, with

a 1% variation during the 12-hour procedure, which was corroborated by an additional measurement at the end of the experiment, yielding a value of 492.71 K. This result suggests that there was no degradation in the receiver's performance during the measurements. The radiometric analysis performed to determine the brightness temperature of the prototype revealed important behaviors related to its performance and how external factors influence it in the measurement system. The emissivity of the mirror introduced a systematic modification in the brightness temperature measurements by attenuating the radiation from the prototype and adding contributions from the ambient temperature. Since the emissivity value of the mirror is known, this effect is corrected before determining the final brightness temperature of the prototype. The analysis shows that the brightness temperature is systematically lower than its physical temperature, which is expected since the prototype is not a perfect black body. However, the difference between these temperatures is not constant, increasing with higher physical temperature values. For example, at T_{ph} of 343.15 K (70°C), T_B reached only 339.71 K, with a difference of 3.44 K, while at T_{ph} of 313.15 K (40°C), this difference was only 0.51 K.This suggests that ambient radiation may be coupled during prolonged measurements. These results indicate a linear relationship between the T_{ph} and T_B temperatures.The slope of this adjustment, with a value of 0.9, is crucial as it represents the efficiency of the prototype load when supplied with energy. The erratic behavior of the LN2 power measured with the mirror during the prototype measurements demonstrates the importance of mitigating factors that interfere with the correct measurement of the LN2 box surface, such as condensation. The introduction of a fan and manual drying of the surface were effective measures to improve the data quality, though not sufficient to allow its use. A possible factor is that the mirror's angle position during the measurements may have moved physically by a few fractions of a degree, generating erratic LN2 power measurements with the mirror.

The methodology employed for the radiometric evaluation of the final calibration loads is a manual procedure consisting of a calibration cone immersed in LN2 and an ambient calibrator, which were alternately presented to the receiver system to record their powers. The radiometric results obtained in this study show a high degree of consistency between the evaluated physical temperatures and the calculated brightness temperatures.This behavior was observed in the three thermal stabilization scenarios analyzed (40°C, 55°C, and 70°C). At 40°C, the

measurements demonstrated the ability of the loads to reach a stable brightness temperature state, with values ranging from 305.11 K for the large red load to 309.51 K for the small load. During this process, a 0.44% improvement in the receiver's performance was noted between the initial and final calibrations. The analysis at 55°C showed similar results, with average brightness temperatures of 315.28 K, 319.60 K, and 322.48 K for the large red, large blue, and small loads, respectively. Additionally, an increase in the temperature differences between the physical temperature and the brightness temperature was observed, as evidenced with the prototype load, although in this case, these differences did not exceed 3%. For this measurement, the receiver system was highly stable with only a 0.5% variation between the start and end of the measurements. Finally, the measurements at 70°C showed the same previous behavior, with results giving average brightness temperatures of 325.43 K, 332.31 K, and 334.67 K for the large red, large blue, and small loads, respectively. Although the largest difference of 17.7 K corresponds to the large red load, it represents only a 5% error relative to its physical temperature.

A noteworthy aspect at 70°C is the difference in the stabilization times of the loads. While the small load reached stability in 8 minutes, the large blue and large red loads required 17 and 28 minutes, respectively. This behavior is related to the physical properties of each load, such as heat capacity and efficiency in heat transfer from the main block. The results obtained in this temperature range allowed the modeling of the stabilization curves through exponential adjustments, achieving 1% precision in the brightness temperature estimates. The radiometric results obtained were independently modeled for each load using a linear fit, enabling the prediction of brightness temperature behavior as a function of physical temperature within the evaluated range. A significant finding is that its slope represents the efficiencies of each calibration load when supplied with energy, ranging from 0.7 for the large red load to 0.8 for the small load. It is worth emphasizing that this linear model serves as a crucial tool for users of the LLAMA project's calibration loads, as it facilitates continuous and precise calibration without requiring additional experimental measurements.

The evaluation of the receiver performance in the COMAP Project is based on advanced simulations that model critical parameters such as atmospheric

brightness temperature and spillover. These models, developed and validated in this thesis, were based on the use of the AM radiative transfer model to simulate atmospheric brightness temperature and an exponential model to estimate spillover as a function of elevation angle. The obtained results allowed the analysis of the merit figures merit of COMAP system. The study of the receiver temperature revealed high temporal stability, with very small variations across spectral bands. A 95% of the T_{Rx} values were between 10 and 31 K, with a mean of 17.7 K. These results are consistent with those reported by Foss et al. [25], who identified T_{Rx} ranges between 10 and 30 K. As expected, the system temperature showed a strong dependence on PWV and elevation angle. The values of T_{sys} ranged from 28 to 56 K for 95% of the data, being lower under reduced PWV conditions, such as in the scans obsid8983 (PWV = 4.113 mm) and obsid4386 (PWV = 5.779 mm). These results confirm the importance of including parameters like atmospheric brightness temperature and spillover to improve calculation accuracy. Our results are comparable to those reported by [25], which ranged from 34 to 60 K, although their calculations include a fixed spillover contribution, and it does not vary by elevation angle. The sensitivity values of the system were evaluated between 100 and 400 mK, with 95% of the data in the range of 146–260 mK, with a mean of 203 mK. For a single-pixel receiver operating at a typical spectral channel of 27.025 GHz in the A:LSB band, the sensitivity reaches 263.85 mK. When employing the full 19-pixel array, this value decreases by a factor of 6.57, reaching 40.15 mK. This reduction underscores the advantage of a multi-pixel array in detecting weak signals. The temporal stability analysis through the Allan variance revealed optimal integration times between 5 and 21 seconds, including all pixels, with a mean of 14 seconds. Since the sensitivity required for the project is high, the scans will always have a combination of white noise and gain fluctuations. In particular, Foss et al. [25] highlights $1/f$ noise induced by gain fluctuations, atmospheric fluctuations, and standing waves. The aperture efficiency was assessed for all pixels in the array at the central frequencies of the COMAP bands: 26, 29, 31, and 33 GHz. The measured values range from 0.27 to 0.51, with an average of 0.38. In general, efficiency decreases with frequency. This trend, observed in most pixels, is primarily attributed to coma, an optical aberration that affects those farther from the optical axis, leading to an asymmetric radiation distribution in the focal plane. However, certain discrepancies were identified, particularly in pixels 7 and 16, which exhibited higher-than-expected efficiency at 31 GHz. The measured

values fall within the predicted range reported by Lamb et al. [34], which estimates aperture efficiencies between 0.35 and 0.5 for COMAP frequencies.

From an observational perspective, the validation of the MERRA-2 atmospheric database was achieved through a consistent methodological approach. First, simulating atmospheric brightness temperature using the AM radiative transfer model with MERRA-2 database for the OVRO site enabled precise calibration of COMAP long skydip power measurements to antenna temperature across the full spectral range. The atmospheric brightness temperature derived from skydip data was obtained by subtracting the spectral atmospheric brightness temperature simulated by the AM model to the measured antenna temperature at all COMAP frequencies. A temperature excess emerged from this comparison, attributed to spillover contributions from the surroundings, which was modeled using an exponential curve within the 30°–86.5° elevation range. Applying an exponential tipping-curve fit to the measured atmospheric brightness temperature allowed for the calculation of zenith atmospheric opacity across the entire COMAP frequency range. Subsequently, this was compared with the simulated spectral zenith opacity from the AM radiative transfer model, yielding a percent error of only 4%. These results validate the MERRA-2 atmospheric database as a reliable tool for characterizing astronomical sites of interest. The same calibration procedure was applied to a short skydip scan between 40° and 60° elevation from the same scan studied, demonstrating that such scans can also be used for routine atmospheric studies by obtaining atmospheric brightness temperature and zenith opacity across the COMAP frequency range, with a percent error of just 4.4%. A key outcome of the validation is the ability to perform a direct atmospheric analysis on the OVRO site using the MERRA-2 database. A 24-year study revealed that PWV levels peak in summer (June–August) and reach their lowest values in winter (December–February). These results are crucial for observation planning, as lower PWV levels during winter enhance the detection of faint signals. Statistical analysis showed that PWV remains around 9.5 mm for approximately 50% of the time, varying between 7.4 mm in drier periods and 15.7 mm in wetter conditions. These variations result from the shadow effect of rain in the Owens Valley. During winter, colder temperatures reduce the capacity of the atmosphere to retain moisture, further lowering the PWV. In summer, higher temperatures increase the air's ability to hold water vapor, leading to elevated PWV levels.

Chapter 7

Conclusion

We have presented a comprehensive analysis of the observational and instrumental factors that play an important role in the calibration of radiotelescopes' data within high-level projects such as COMAP and LLAMA.

This study focused on the development and characterization of calibration sources for the LLAMA radio telescope. The encapsulated design of the loads, featuring well-defined thermomechanical properties, ensures high precision and reliability in radiometric measurements. The incorporation of Mylar to minimize convection with the surrounding environment proved to be an effective strategy for speeding up and maintaining thermal stabilization. These calibration loads stand out from other existing black bodies, as these sources allow for the configuration of different physical temperatures, ranging from ambient to 70°C, through a thermal control system based on FPGA technology. This capability enabled more precise brightness temperature calibration by providing multiple temperature and power measurements. Additionally, they stand out for their data acquisition, control, and monitoring system, based on ACS software and SCPI protocols, enhances integration with the LLAMA radio telescope platform. The data characterization methodology implemented, based on the Y-factor technique and the general power equation, allowed for the effective characterization of the calibration instruments, modeling a linear relationship between physical temperature and brightness temperature, which will facilitate its use for LLAMA users. Overall, the calibration loads meet the technical requirements established by LLAMA, ensuring integration with the radio telescope system.

The performance of the COMAP receiver was successfully studied by analyzing various power scans at different dates and times. The study was achieved owing to the implementation of an atmospheric brightness temperature model and a spillover model, which enabled the accurate use of sky temperature values in the calibration of power data from the scans. The results demonstrated a robust and consistent performance in line with existing literature. The stability of the receiver stands out, assessed through temperature measurements across the entire COMAP frequency range, determined using the Y-factor technique and known-temperature calibrators. As expected, the system temperature exhibited a strong dependence on atmospheric variations and the elevation angle at which observations were conducted with the radio telescope. The 19-pixel COMAP array proved to be a highly sensitive system, significantly reducing the time required for detecting weak signals, such as CO, from years to days compared to single-pixel receivers. Aperture efficiency decreased with increasing frequency, aligning with expected behavior. Lamb et al. [34] states that this phenomenon does not affect data processing.

The validation of the MERRA-2 atmospheric database through the calibration of COMAP skydip measurements to brightness temperature proved successful. Implementing the AM radiative transfer model with MERRA-2 data was essential for deriving simulated zenith atmospheric opacity and brightness temperature across the entire COMAP frequency range, enabling the calibration of skydip power data. Applying a tipping-curve fit to the brightness temperature computed from COMAP measurements played a key role in determining the calculated zenith atmospheric opacity throughout the spectral range. This approach allowed for a direct comparison between simulated opacity from the AM model and calculated values, achieving a mean squared error of only 4%. Therefore, the MERRA-2 atmospheric database serves as a reliable tool for astronomical site evaluation. Furthermore, the calibration of short skydip power measurements to brightness temperature was also validated as a reliable method for atmospheric assessments, achieving a 4.4% error margin. A spillover model dependent on elevation angle were successfully derived from the long and short skydip calibration procedure. As a result of this, a 24-year atmospheric study at the OVRO site, using PWV as an indicator, was conducted directly with MERRA-2 data, revealing that PWV remained close to 9.5 mm for approximately 50% of the observation time.

References

[1] Atacama large millimeter/submillimeter array alma. URL https://www.almaobservatory.org/en/image-gallery/?images-tags=technology&pg=29.

[2] Large latin american millimeter/submillimeter array llama. URL https://www.llamaobservatory.org/.

[3] Rutherford Appleton Laboratory (RAL Space). URL https://www.ralspace.stfc.ac.uk/Pages/Blackbody-calibration-targets.aspx.

[4] Zax Millimeter Wave Corporation. URL https://www.ralspace.stfc.ac.uk/Pages/Blackbody-calibration-targets.aspx.

[5] Emmerson & Cumming Anechoic Chambers. URL https://www.ecanechoicchambers.com/.

[6] Thomas keating ltd, 2008. URL https://www.terahertz.co.uk/tk-instruments/products/calibratedthermaltargets/loadsystem.

[7] Murk A. and Renker M. Alma calibration device prototype calibration load test report fend-40.06.04.00-005-a-rep version: A. Technical report, Atacama Large Millimeter Array ALMA, 2007.

[8] Murk A. and Renker M. Alma calibration device thermal and physical optics simulation of calibration targets fend-40.06.00.00-098-b-rep version: B. Technical report, Atacama Large Millimeter Array ALMA, 2008.

[9] Alarcon P. Control de espejo para cargas de calibración con Stepper Motor. Internal Contactor, 2024.

[10] David Arroyo. Internal Contact.

[11] David Arroyo. Fase inicial de desarrollo de una plataforma de control de temperatura para cargas de calibración para el radiotelescopio LLAMA [Tesis de Pregrado, Internal Contact], 2016.

[12] David Arroyo. Empaques tarjetas electrónicas del sistema de control Proyecto Cargas de Calibración LLAMA. Internal Contact., 2020.

[13] Arti Rani. Final Report Calibration Load for LLAMA Project: October 2018. internal contact, 2018.

[14] Lilian Basoalto. Desarrollo de Fuentes de Calibración para Instrumentos de Calibración Submilimétrica [Tesis de Pregrado, Internal Contact], 2018.

[15] Michael G. Bosilovich, Franklin R. Robertson, Lawrence Takacs, Andrea Molod, and David Mocko. Atmospheric water balance and variability in the merra-2 reanalysis. *Journal of Climate*, 30(4):1177 – 1196, 2017. doi: 10.1175/JCLI-D-16-0338.1. URL https://journals.ametsoc.org/view/journals/clim/30/4/jcli-d-16-0338.1.xml.

[16] Charles L. Braun and Sergei N. Smirnov. Why is water blue? *Journal of Chemical Education*, 70(8):612, 1993. doi: 10.1021/ed070p612. URL https://doi.org/10.1021/ed070p612.

[17] Bernard F. Burke, Francis Graham-Smith, and Peter N. Wilkinson. *AN INTRODUCTION TO RADIO ASTRONOMY Fourth Edition*. Cambridge University Press, 2019. ISBN 978-1-107-18941-6. doi: 10.1017/9781316987506.

[18] R. Bustos, M. Rubio, A. Otárola, and N. Nagar. Parque astronómico de atacama: An ideal site for millimeter, submillimeter, and mid-infrared astronomy. *Publications of the Astronomical Society of the Pacific*, 126(946): 1126, dec 2014. doi: 10.1086/679330. URL https://dx.doi.org/10.1086/679330.

[19] Kieran A. Cleary, Jowita Borowska, Patrick C. Breysse, Morgan Catha, Dongwoo T. Chung, Sarah E. Church, Clive Dickinson, Hans Kristian Eriksen, Marie Kristine Foss, Joshua Ott Gundersen, Stuart E. Harper, Andrew I. Harris, Richard Hobbs, Håvard T. Ihle, Junhan Kim, Jonathon Kocz, James W. Lamb, Jonas G. S. Lunde, Hamsa Padmanabhan, Timothy J. Pearson, Liju Philip, Travis W. Powell, Maren Rasmussen, Anthony C. S. Readhead, Thomas J. Rennie, Marta B. Silva, Nils-Ole Stutzer, Bade D. Uzgil, Duncan J. Watts, Ingunn Kathrine Wehus, David P. Woody, Lilian Basoalto, J. Richard Bond, Delaney A. Dunne, Todd Gaier, Brandon Hensley, Laura C. Keating, Charles R. Lawrence, Norman Murray, Roberta Paladini, Rodrigo Reeves, Marco P. Viero, and Risa H. Wechsler. Comap early science. i. overview. *The Astrophysical Journal*, 933(2):182, July 2022. ISSN 1538-4357. doi: 10.3847/1538-4357/ac63cc. URL http://dx.doi.org/10.3847/1538-4357/ac63cc.

[20] Marshall H. Cohen. The owens valley radio observatory: Early years. *Engineering and Science,*, 1994. URL https://calteches.library.caltech.edu/3774/1/Cohen.pdf.

[21] James J. Condon and Scott M. Ransom. *Essential Radio Astronomy*. Princeton University Press, 41 William Street, Princeton, New Jersey 08540, 2016. ISBN 978-0-691-13779-7.

[22] Fernando Cortés, Rodrigo Reeves, and Ricardo Bustos. Analysis of the distribution of precipitable water vapor in the chajnantor area. *Radio Science*, 51(7):1166–1175, 2016. doi: https://doi.org/10.1002/2015RS005929. URL https://agupubs.onlinelibrary.wiley.com/doi/abs/10.1002/2015RS005929.

[23] Cortés, F., Cortés, K., Reeves, R., Bustos, R., and Radford, S. Twenty years of precipitable water vapor measurements in the chajnantor area. *A&A*, 640: A126, 2020. doi: 10.1051/0004-6361/202037784. URL https://doi.org/10.1051/0004-6361/202037784.

[24] Charles Elachi and Jakob van Zyl. *Introduction to the Physics and Techniques of Remote Sensing Third Edition*. Wiley, 2021. ISBN 9781119523123.

[25] Marie K. Foss, Håvard T. Ihle, Jowita Borowska, Kieran A. Cleary, Hans Kristian Eriksen, Stuart E. Harper, Junhan Kim, James W. Lamb, Jonas G. S. Lunde, Liju Philip, Maren Rasmussen, Nils-Ole Stutzer, Bade D. Uzgil, Duncan J. Watts, Ingunn K. Wehus, David P. Woody, J. Richard Bond, Patrick C. Breysse, Morgan Catha, Sarah E. Church, Dongwoo T. Chung, Clive Dickinson, Delaney A. Dunne, Todd Gaier, Joshua Ott Gundersen, Andrew I. Harris, Richard Hobbs, Charles R. Lawrence, Norman Murray, Anthony C. S. Readhead, Hamsa Padmanabhan, Timothy J. Pearson, Thomas J. Rennie, and (COMAP Collaboration). Comap early science. iii. co data processing. *The Astrophysical Journal*, 933(2):184, jul 2022. doi: 10.3847/1538-4357/ac63ca. URL https://dx.doi.org/10.3847/1538-4357/ac63ca.

[26] Ronald Gelaro, Will McCarty, Max J. Suárez, Ricardo Todling, Andrea Molod, Lawrence Takacs, Cynthia A. Randles, Anton Darmenov, Michael G. Bosilovich, Rolf Reichle, Krzysztof Wargan, Lawrence Coy, Richard Cullather, Clara Draper, Santha Akella, Virginie Buchard, Austin Conaty, Arlindo M. da Silva, Wei Gu, Gi-Kong Kim, Randal Koster, Robert Lucchesi, Dagmar Merkova, Jon Eric Nielsen, Gary Partyka, Steven Pawson, William Putman, Michele Rienecker, Siegfried D. Schubert, Meta Sienkiewicz, and Bin Zhao. The modern-era retrospective analysis for research and applications, version 2 (merra-2). *Journal of Climate*, 30(14):5419 – 5454, 2017. doi: 10.1175/JCLI-D-16-0758.1. URL https://journals.ametsoc.org/view/journals/clim/30/14/jcli-d-16-0758.1.xml.

[27] Paul F. Goldsmith. *Quasioptical Systems: Gaussian Beam Quasioptical Propagation and Applications*. IEEE Press, Pscataway, NJ 0885-1331, 1998.

[28] Richard T. Hall and Jerome M. Dowling. Pure Rotational Spectrum of Water Vapor. *The Journal of Chemical Physics*, 47(7):2454–2461, 10 1967. ISSN 0021-9606. doi: 10.1063/1.1703330. URL https://doi.org/10.1063/1.1703330.

[29] Richard Hills. Status of the calibration "loads" for alma. Technical report, Atacama Large Millimeter Array ALMA, 2007.

[30] Ramsey L. Karim, David DeBoer, Imke de Pater, and Garrett K. Keating. A wideband self-consistent disk-averaged spectrum of jupiter near 30 ghz and its implications for nh3 saturation in the upper troposphere. *The Astronomical Journal*, 155(3):129, feb 2018. doi: 10.3847/1538-3881/aaaab2. URL https://dx.doi.org/10.3847/1538-3881/aaaab2.

[31] K.I. Kellermann, E.N. Bouton, and S.S. Brandt. *Open Skies: The National Radio Astronomy Observatory and Its Impact on US Radio Astronomy*. Historical & Cultural Astronomy. Springer International Publishing, 2020. ISBN 9783030323455. URL https://books.google.cl/books?id=c1juDwAAQBAJ.

[32] J. W. Kooi, J. J. A. Baselmans, A. Baryshev, R. Schieder, M. Hajenius, J. R. Gao, T. M. Klapwijk, B. Voronov, and G. Gol'tsman. Stability of heterodyne terahertz receivers. *Journal of Applied Physics*, 100(6):064904, 09 2006. ISSN 0021-8979. doi: 10.1063/1.2336498. URL https://doi.org/10.1063/1.2336498.

[33] John D. Krauss. *Radio Astronomy Second Edition*. Cygnus-Quasar Books, P.O. Box 353 Durham, N.H. 03824, 1988. ISBN 1-882484-00-2.

[34] James W. Lamb, Kieran A. Cleary, David P. Woody, Morgan Catha, Dongwoo T. Chung, Joshua Ott Gundersen, Stuart E. Harper, Andrew I. Harris, Richard Hobbs, Håvard T. Ihle, Jonathon Kocz, Timothy J. Pearson, Liju Philip, Travis W. Powell, Lilian Basoalto, J. Richard Bond, Jowita Borowska, Patrick C. Breysse, Sarah E. Church, Clive Dickinson, Delaney A. Dunne, Hans Kristian Eriksen, Marie Kristine Foss, Todd Gaier, Junhan Kim, Charles R. Lawrence, Jonas G. S. Lunde, Hamsa Padmanabhan, Maren Rasmussen, Anthony C. S. Readhead, Rodrigo Reeves, Thomas J. Rennie, Nils-Ole Stutzer, Marco P. Viero, Duncan J. Watts, Ingunn Kathrine Wehus, and (COMAP Collaboration). Comap early science. ii. pathfinder instrument. *The Astrophysical Journal*, 933(2):183, jul 2022. doi: 10.3847/1538-4357/ac63c6. URL https://dx.doi.org/10.3847/1538-4357/ac63c6.

[35] Yoonjae Lee, Brian Ellison, Peter Huggard, Mark Harman, Abdelhakim Boughriet, Wojciech Bartynowski, Matthew Oldfield, Nigel Morris, Peter Hekman, and Gie Han Tan. ALMA front-end verification using dry cold load. In Wayne S. Holland and Jonas Zmuidzinas, editors, *Millimeter, Submillimeter, and Far-Infrared Detectors and Instrumentation for Astronomy V*, volume 7741, page 77412K. International Society for Optics and Photonics, SPIE, 2010. doi: 10.1117/12.857302. URL https://doi.org/10.1117/12.857302.

[36] Ming-Shuai Li, Rui Li, Na Wang, and Xing-Wu Zheng. Research and application of reanalysis data for radio astronomical site testing. *Research in Astronomy and Astrophysics*, 20(12):200, dec 2020. doi: 10.1088/1674-4527/20/12/200. URL https://dx.doi.org/10.1088/1674-4527/20/12/200.

[37] Jonas Gahr Sturtzel Lunde. Low-level data analysis, calibration, and ground modeling with comap. Published Master's Thesis, Institute of Theoretical Astrophysics, University of Oslo, 2021. URL http://www.publiclibraryofscience.org.

[38] Lunde, J. G. S., Stutzer, N.-O., Breysse, P. C., Chung, D. T., Cleary, K. A., Dunne, D. A., Eriksen, H. K., Harper, S. E., Ihle, H. T., Lamb, J. W., Pearson, T. J., Philip, L., Wehus, I. K., Woody, D. P., Bond, J. R., Church, S. E., Gaier, T., Gundersen, J. O., Harris, A. I., Hobbs, R.,

Kim, J., Lawrence, C. R., Murray, N., Padmanabhan, H., Readhead, A. C. S., Rennie, T. J., Tolgay, D., and (COMAP Collaboration). Comap pathfinder – season 2 results - i. improved data selection and processing. *A&A*, 691:A335, 2024. doi: 10.1051/0004-6361/202451121. URL https://doi.org/10.1051/0004-6361/202451121.

[39] Jonathan Mittaz. Instrument noise characterization and the allan/m-sample variance, 2016. URL https://research.reading.ac.uk/fiduceo/wp-content/uploads/sites/129/2020/12/noise_and_allan_variance_report.pdf.

[40] K. O'Neil. Single-Dish Calibration Techniques at Radio Wavelengths. In Snezana Stanimirovic, Daniel Altschuler, Paul Goldsmith, and Chris Salter, editors, *Single-Dish Radio Astronomy: Techniques and Applications*, volume 278 of *Astronomical Society of the Pacific Conference Series*, pages 293–311, December 2002. doi: 10.48550/arXiv.astro-ph/0203001.

[41] Ossenkopf, V. The stability of spectroscopic instruments: a unified allan variance computation scheme. *A&A*, 479(3):915–926, 2008. doi: 10.1051/0004-6361:20079188. URL https://doi.org/10.1051/0004-6361:20079188.

[42] Scott Paine. The am atmospheric model, September 2024. URL https://doi.org/10.5281/zenodo.13748391.

[43] Juan R. Pardo, José Cernicharo, and Eugene Serabyn. Atmospheric transmission at microwaves (atm): an improved model for millimeter/submillimeter applications. *IEEE Transactions on Antennas and Propagation*, 49:1683–1694, 2001. URL https://api.semanticscholar.org/CorpusID:54693832.

[44] Dennis V. Perepelitsa. Johnson noise and shot noise. *MIT Departament of Physics*, 2006. URL http://web.mit.edu/dvp/Public/noise-paper.pdf.

[45] Simon J. E. Radford and Jeffery B. Peterson. Submillimeter atmospheric transparency at maunakea, at the south pole, and at chajnantor. *Publications of the Astronomical Society of the Pacific*, 128(965):075001, jun 2016. doi: 10.1088/1538-3873/128/965/075001. URL https://dx.doi.org/10.1088/1538-3873/128/965/075001.

[46] Emiliano Rasztocky and CALLOADS Team. Calloads and electronic box location. llama-nacosaiv1-09-04.01.01-020-01-mem. Technical report, Large Latin American Millimeter Array LLAMA, 2020.

[47] Emiliano Rasztocky, Matías Rolf Hampel, Rodrigo Reeves, Jacques R.D. Lepine, and Gustavo Esteban Romero. Design of the tertiary optical system for the Large Latin American Millimeter Array radio telescope. *Journal of Astronomical Telescopes, Instruments, and Systems*, 10(4):044001, 2024. doi: 10.1117/1.JATIS.10.4.044001. URL https://doi.org/10.1117/1.JATIS.10.4.044001.

[48] Rebecca J. Ross and William P. Elliott. Tropospheric water vapor climatology

and trends over north america: 1973–93. *Journal of Climate*, 9:3561–3574, 12 1996. ISSN 0894-8755. doi: 10.1175/1520-0442(1996)009<3561:TWVCAT>2.0.CO;2.

[49] M.L. Salby. *Fundamentals of Atmospheric Physics*. Number v. 61 in Fundamentals of Atmospheric Physics. Elsevier Science, 1996. ISBN 9780126151602. URL https://books.google.cl/books?id=xWQ0G-_UTBoC.

[50] Junna Sugiyama, Haruki Nishino, and Akito Kusaka. Precipitable water vapour measurement using GNSS data in the Atacama Desert for millimetre and submillimetre astronomical observations. *Monthly Notices of the Royal Astronomical Society*, 528(3):4582–4590, 01 2024. ISSN 0035-8711. doi: 10.1093/mnras/stae270. URL https://doi.org/10.1093/mnras/stae270.

[51] Mengistu Tsidu, T. Blumenstock, and F. Hase. Observations of precipitable water vapour over complex topography of Ethiopia from ground-based GPS, FTIR, radiosonde and ERA-Interim reanalysis. *Atmospheric Measurement Techniques*, 8(8):3277–3295, 2015. doi: 10.5194/amt-8-3277-2015. URL https://amt.copernicus.org/articles/8/3277/2015/.

[52] Paulina Unanue. Software Distribuido de Control para Cargas de Calibración en Radio Astronomía [Internal Contact]. Master's thesis, Universidad de Concepcion, 2023.

[53] Valeria, L., Martínez-Ledesma, M., and Reeves, R. Satellite-based atmospheric characterization for sites of interest in millimeter and sub-millimeter astronomy. *A&A*, 684:A186, 2024. doi: 10.1051/0004-6361/202347773. URL https://doi.org/10.1051/0004-6361/202347773.

[54] Moufeng Wan, Kefei Zhang, Suqin Wu, Zhen Shen, Peng Sun, and Longjiang Li. New models for vertical distribution and variation of tropospheric water vapor—a case study for china. *Atmosphere*, 13(12), 2022. ISSN 2073-4433. doi: 10.3390/atmos13122039. URL https://www.mdpi.com/2073-4433/13/12/2039.

[55] J.W. Waters. 2.3. absorption and emission by atmospheric gases. In M.L. Meeks, editor, *Astrophysics*, volume 12 of *Methods in Experimental Physics*, pages 142–176. Academic Press, 1976. doi: https://doi.org/10.1016/S0076-695X(08)60684-5. URL https://www.sciencedirect.com/science/article/pii/S0076695X08606845.

[56] Thomas Wilson, Kristen Rohlfs, and Susanne Hüttemeister. *Tools of Radio Astronomy Sixth Edition*. Springer, 2013. ISBN 978-3-642-39949-7. doi: 10.1007/978-3-642-39950-3.

[57] D. Woody. Comap memo #15 measuring comap pathfinder system temperature and aperture efficiency. page 2, 2018.

[58] Pavel A. Yagoubov, Axel Murk, Richard Wylde, Graham Bell, and Gie Han Tan. Calibration loads for alma. *2011 International Conference on*

Infrared, Millimeter, and Terahertz Waves, pages 1–2, 2011. URL https://api.semanticscholar.org/CorpusID:1741688.

Appendix A

Calibration Load Team

The Calibration Load Project would not have been accomplished without the dedicated support of a multidisciplinary team.

Sponsor of the Project:

Rodrigo Reeves Díaz, Ph.D. in Electrical Civil Engineering. Director of the CePIA Laboratory and a faculty member of the Department of Astronomy at the University of Concepción. Principal investigator and supervisor of the project.

Postgraduate Student:

Lilian Basoalto Salazar, Astronomer, B.Sc. in Physics. Guided the research and project development. Organized and planned activities within the thermo-mechanical area. Actively participated in the physical development (design, manufacturing, and assembly) and characterization (setup preparation, measurements, and data analysis) of the infrared and radiometric testing of the prototype from scratch, as well as the final calibration loads.

Project Permanent Collaborators:

Fernando Cortés Guerrero, M.Sc. in Physics, Astronomer, B.Sc. in Physics. Actively contributed to the thermo-mechanical area of the project. Played an essential role in the physical development (design, manufacturing, and assembly) of the prototype from scratch and the final calibration loads. Conducted in preparing the setups and assisted infrared and radiometric measurements of the prototype load.

Katherine Cortés Urbina, Ph.D. and M.Sc. in Physics, Physical Engineer, B.Sc. in Applied Physics. Responsible for developing and implementing the receivers for radiometric measurements of the prototype and final calibration loads. Played an active role in the prototype design. Participated in preparing the setups for radiometric measurements of all calibration loads.

David Arroyo Reyes, Electronic Civil Engineer. Project coordinator at the CePIA Laboratory. Developed and implemented the closed-loop temperature control system based on FPGA for all calibration loads. Responsible for the development of the control box for the final calibration loads.

Paulina Unanue Morales, M.Sc. in Physics, Astronomer. Developed and implemented the control, monitoring, and data acquisition system based on ACS control software to achieve integration between the LLAMA software and the thermal control system for the final calibration loads.

Members of the CePIA Laboratory technical team:

Patricio Alarcón Díaz, Industrial Instrumentation and Control Engineer. Designed and implemented the automated motor-mirror measurement system based on FPGA for the radiometric measurements of the prototype.

Jorge Muñoz Mujica, Designer at CePIA Laboratory. Designed and fabricated mechanical supports and 3D-printed components for the radiometric testing of the prototype and final calibration loads. Designed and manufactured the mylar supports for all the loads. Collaborated in the design of the automated motor-mirror measurement system based on FPGA for radiometric measurements of the prototype.

Nicolás Lastra, Mechanical Civil Engineer. Collaborated in the design and fabrication of mylar supports for the prototype and final calibration loads. Also contributed to the design of the automated motor-mirror measurement system based on FPGA for the radiometric measurements of the prototype.

Cristian Calquín, Electronic Civil Engineer. Implemented the PCB cards for the temperature control and monitoring system of the final calibration loads. Physically updated one of the PCB cards for the FPGA-based temperature control system of the prototype. Collaborated in the development of the control box for the final calibration loads.

Calibration Load Project Temporary Collaborators:

Lilian Mora, Mechanical Engineer. Actively participated in the design of the prototype from scratch. Manufactured and machined custom mechanical parts for performing the mechanical and infrared tests of the prototype.

Arti Rani, Ph.D. in Radiation Thermometry. Carried out the electromagnetic simulation in HFSS of the RAM components.

Vicente Montecinos, Electronic Technician and Electronic Civil Engineering UdeC Student. Developed and implemented a temperature control system based on a Raspberry Pi for the radiometric testing of the prototype.

Appendix B

COMAP Receiver Performance

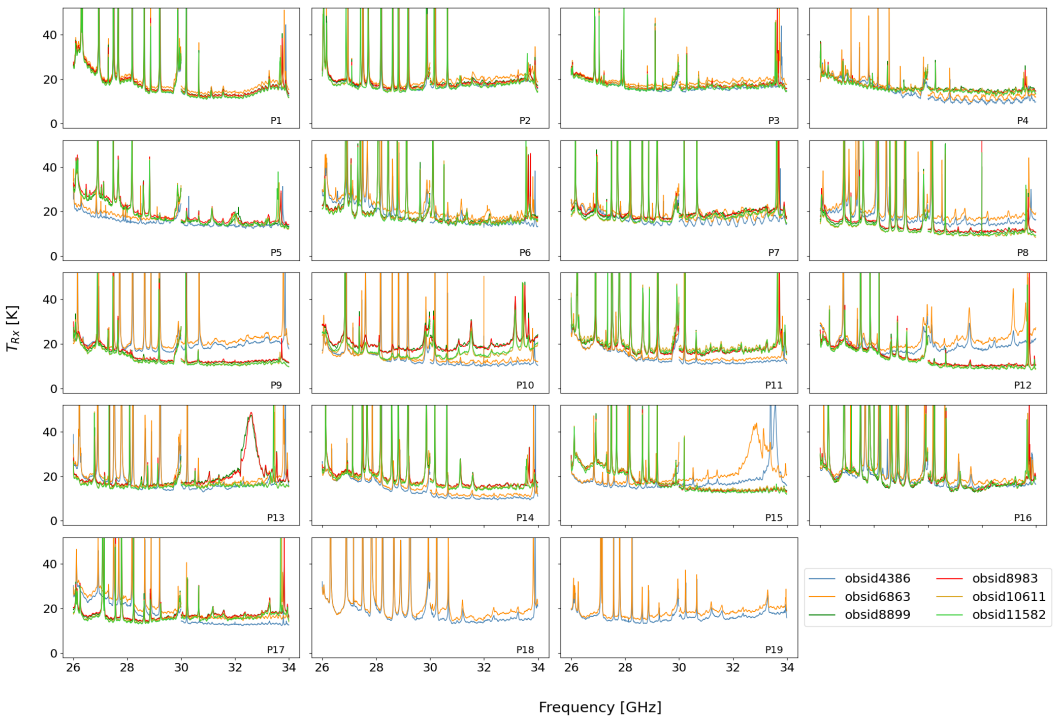

Figure B.1: Receiver temperature across the entire spectral frequency range of COMAP for each individual scan is shown.

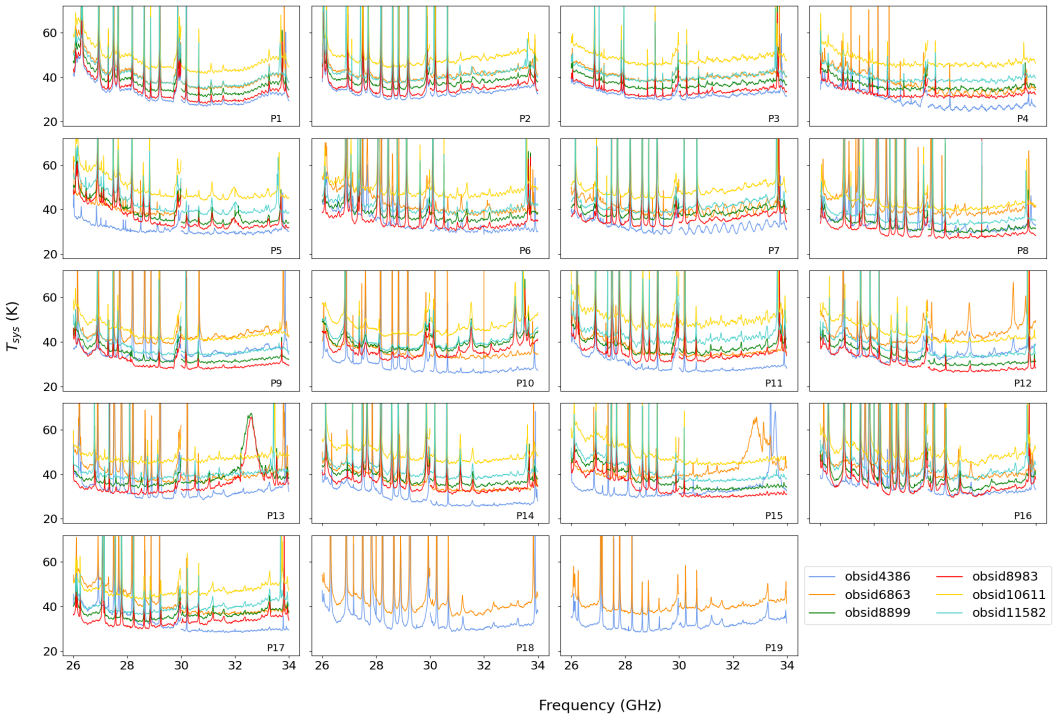

Figure B.2: System temperature across the entire spectral frequency range of COMAP for each individual scan is shown.

Appendix C

Gaussian Beam Diameters

Table C.1: The primary variables involved in the Gaussian beam calculations are presented, with the analysis centered at a frequency of 93 GHz. The first and fifth columns display the distance (z) between the beam waist of the horn, w_0, and the RAM block of the Load, spanning from 0.0 cm to 28 cm. The second and sixth columns indicate the beam radius w_0 for the corrugated horn utilized in the receivers. The third and seventh columns provide the illumination diameters $\varnothing$ over a 35 dB range on the RAM block of the Load. All measurements are reported in centimeters.

z	$w_{0_{bc}}$	$\varnothing_{bc}$		z	$w_{0_{bc}}$	$\varnothing_{bc}$
0.0	0.4766	1.9062		15.0	3.2669	13.0675
1.0	0.5230	2.0920		16.0	3.4802	13.9207
2.0	0.6425	2.5700		17.0	3.6937	14.7749
3.0	0.8031	3.2123		18.0	3.9075	15.6299
4.0	0.9848	3.9393		19.0	4.1214	16.4857
5.0	1.1780	4.7120		20.0	4.3355	17.3421
6.0	1.3778	5.5113		21.0	4.5497	18.1989
7.0	1.5817	6.3269		22.0	4.7641	19.0562
8.0	1.7884	7.1534		23.0	4.9785	19.9140
9.0	1.9969	7.9874		24.0	5.1930	20.7720
10.0	2.2067	8.8268		25.0	5.4076	21.6304
11.0	2.4175	9.6701		26.0	5.6222	22.4890
12.0	2.6291	10.5164		27.0	5.8370	23.3479
13.0	2.8413	11.3650		28.0	6.0517	24.2069
14.0	3.0539	12.2155				

Appendix D

Deduction of Emissivity

According to the general power equation provided by Equation 3.11.3, the liquid nitrogen power measured directly P^D_{LN2} and through the mirror P^M_{LN2} is expressed as follows:

$$P^M_{LN2} = k \cdot \Delta\nu \cdot G \cdot \left(T^M_{Rx} + T^M_{LN2}\right) \tag{D.1}$$

$$P^D_{LN2} = k \cdot \Delta\nu \cdot G \cdot \left(T^D_{Rx} + T^D_{LN2}\right) \tag{D.2}$$

In this context, a receiver temperature is determined both through the mirror (T^M_{Rx}) and directly (T^D_{Rx}). It is also assumed that the temperature of liquid nitrogen measured through the mirror (T^M_{LN2}) differs from the value obtained during direct measurement (T^M_{LN2}). Furthermore, the $k \cdot \Delta\nu \cdot G$ term can be disregarded under the assumption of no gain variations. By dividing Equations D.1 and D.2, this simplification is applied:

$$\frac{P^M_{LN2}}{P^D_{LN2}} = \frac{T^M_{Rx} + T^M_{LN2}}{T^D_{Rx} + T^D_{LN2}} \tag{D.3}$$

The resulting expression is mathematically developed to derive the receiver temperatures as outlined in Equation 3.11.5, leading to the isolation of T^M_{LN2}:

$$\frac{P^M_{LN2}}{P^D_{LN2}} = \frac{\dfrac{T_{amb} - Y^M \cdot T^M_{LN2}}{Y^M - 1} + T^M_{LN2}}{\dfrac{T_{amb} - Y^D_{L-A} \cdot T^D_{LN2}}{Y^D_{L-A} - 1} + T^D_{LN2}}$$

$$= \frac{\dfrac{T_{amb} - \cancel{Y^M \cdot T^M_{LN2}} + \cancel{Y^M \cdot T^M_{LN2}} - T^M_{LN2}}{Y^M - 1}}{\dfrac{T_{amb} - \cancel{Y^D_{L-A} \cdot T^D_{LN2}} + \cancel{Y^D_{L-A} \cdot T^D_{LN2}} - T^D_{LN2}}{Y^D_{L-A} - 1}}$$

$$\frac{P^M_{LN2}}{P^D_{LN2}} = \left(\frac{T_{amb} - T^M_{LN2}}{Y^M - 1}\right) \cdot \left(\frac{Y^D_{L-A} - 1}{T_{amb} - Y^D_{L-A}}\right)$$

$$\frac{P^M_{LN2}}{P^D_{LN2}} \cdot \frac{\left(Y^M - 1\right) \cdot \left(T_{amb} - T^D_{LN2}\right)}{Y^D_{L-A} - 1} = T_{amb} - T^M_{LN2}$$

Solving T^M_{LN2}:

$$T^M_{LN2} = T_{amb} - \frac{P^M_{LN2}}{P^D_{LN2}} \cdot \left(\frac{Y^M - 1}{Y^D_{L-A} - 1}\right) \cdot \left(T_{amb} - T^D_{LN2}\right) \tag{D.4}$$

Equation 3.2.9 is then employed to define the liquid nitrogen temperature measured through the mirror as a function of the mirror's emissivity:

$$T^M_{LN2} = T^D_{LN2} + \varepsilon \cdot \left(T_{amb} - T^D_{LN2}\right) \tag{D.5}$$

Equations D.4 and D.5 are equated to solve for the emissivity:

$$T^D_{LN2} + \varepsilon \cdot \left(T_{amb} - T^D_{LN2}\right) = T_{amb} - \frac{P^M_{LN2}}{P^D_{LN2}} \cdot \left(\frac{Y^M - 1}{Y^D_{L-A} - 1}\right) \cdot \left(T_{amb} - T^D_{LN2}\right)$$

$$\Rightarrow \varepsilon \cdot \left(T_{amb} - T^D_{LN2}\right) = T_{amb} - T^D_{LN2} - \frac{P^M_{LN2}}{P^D_{LN2}} \cdot \left(\frac{Y^M - 1}{Y^D_{L-A} - 1}\right) \cdot \left(T_{amb} - T^D_{LN2}\right)$$

$$\varepsilon = \frac{1}{\left(T_{amb} - T^D_{LN2}\right)} \cdot \left[T_{amb} - T^D_{LN2} - \frac{P^M_{LN2}}{P^D_{LN2}} \cdot \left(\frac{Y^M - 1}{Y^D_{L-A} - 1}\right) \cdot \left(T_{amb} - T^D_{LN2}\right)\right] \tag{D.6}$$

By simplifying the expression to its most reduced form, the emissivity is found as a function of the liquid nitrogen powers, P_{LN2}^{M} and P_{LN2}^{D}, which are directly obtained through the power meter:

$$\Rightarrow \varepsilon = 1 - \frac{P_{LN2}^{M}}{P_{LN2}^{D}} \cdot \frac{\left(Y^{M} - 1\right)}{\left(Y^{D} - 1\right)} \tag{D.7}$$